Open Access Dissertations

Theses and Dissertations

January 2014

MASS SPECTROMETRIC INVESTIGATIONS OF STRUCTURALLY DIAGNOSTIC ION-MOLECULE REACTIONS AND OF MOLECULAR STRUCTURES OF ASPHALTENES

James Riedeman
Purdue University

Follow this and additional works at: https://docs.lib.purdue.edu/open_access_dissertations

PURDUE UNIVERSITY
GRADUATE SCHOOL
Thesis/Dissertation Acceptance

This is to certify that the thesis/dissertation prepared

By James Steven Riedeman

Entitled MASS SPECTROMETRIC INVESTIGATIONS OF STRUCTURALLY DIAGNOSTIC
ION-MOLECULE REACTIONS AND OF MOLECULAR STRUCTURES OF
ASPHALTENES

For the degree of Doctor of Philosophy

Is approved by the final examining committee:

Hilkka I. Kenttämaa
_____
Chair
P. V. Ramachandran

Mahdi Abu-Omar

Alexander Wei

To the best of my knowledge and as understood by the student in the *Research Integrity and Copyright Disclaimer (Graduate School Form 20)*, this thesis/dissertation adheres to the provisions of Purdue University's "Policy on Integrity in Research" and the use of copyrighted material.

Approved by Major Professor(s): Hilkka I. Kenttämaa
_____

Approved by: R. E. Wild   12-04-2014
                    Head of the Graduate Program   Date

MASS SPECTROMETRIC INVESTIGATIONS OF STRUCTURALLY DIAGNOSTIC

ION-MOLECULE REACTIONS AND OF MOLECULAR STRUCTURES OF

ASPHALTENES

A Dissertation

Submitted to the Faculty

of

Purdue University

by

James Steven Riedeman

In Partial Fulfillment of the

Requirements for the Degree

of

Doctor of Philosophy

December 2014

Purdue University

West Lafayette, Indiana

For my beloved grandmother,

Grace Maria Taddeo.

Without your wisdom and unending love I would not have become who I am today.

ACKNOWLEDGEMENTS

First and foremost, I would like to express my gratitude to my graduate research advisor, Professor Hilkka I. Kenttämaa. Her guidance and encouragement were critical to my success. Upon entering graduate school at Purdue, I had initially intended to join a research group engaging in total synthesis. It was my first meeting with Hilkka that ultimately changed my perspective. Her approach to research and dedication to the success of her students crystallized my appreciation for her group. The freedom I have been given to conduct research was pivotal to my success and taught me to think as an independent scientist. It has truly been an honor to be her student.

There are numerous members of the Kenttämaa research group, past and present, who have been instrumental in my success. Dr. Vanessa Gallardo, Dr. Matthew Hurt, Dr. David Borton, and Christopher Marcum contributed to my training and provided me with skills that helped jump start my research. Dr. Benjamin Owen, Dr. Fanny Widjaja, Dr. Laura Haupert, and Dr. Nelson Vinueza, and Dr. Enada Archibold were exemplary scientists who I strived to model in my own efforts. Dr. Tiffany Jarrell, Dr. Ashley Wittrig, Huaming Sheng, Alex Dow, Weijuan Tang, Guannan Li, and Dr. Linan Yang were all contemporaries in the group, with whom I enjoyed collaborating on research and undertaking the challenges of graduate school. I will always be grateful for their support and friendships. The newer additions to the research group have been a pleasure to work

with, i.e. Chunfen Jin, Hanyu Zu, Ravi Yerabolu, John Kong, Priya Murria, Raghavendhar Kotha, Xueming Dong, and Laurance Cain. Your eagerness for learning has been a source of inspiration for me as I have witnessed the greatness in all of you.

I also would like to acknowledge several persons within and outside of this research group who have been invaluable during my studies. Dr. Sabir Aqueel helped initiate me into the group and taught me a multitude of lab techniques that benefited me throughout the remainder of my graduate career. Dr. Nelson Vinueza was truly a source of comfort and wisdom whenever I needed it. I would also like to thank members of the Jonathan Amy Facility for Chemical Instrumentation of Purdue University: Mark Carlsen, Tim Selby, Randall Replogle, and Dr. Hartmut Hedderich. I am ever so gracious for the advice and support I received from them which was essential to the successful completion of my research projects. The Purdue IT professionals Konrad Klewier, Pat Patterson, and Phillip Wyss were also commendable people to work with who helped me several times throughout my graduate studies.

I would also like to thank the friends that I have made during my time at Purdue, Dr. Tiffany Jarrell, Chunfen Jin, Alex Dow, Raghavendhar Kotha, Naveen Kadasala, Hari Khatri, Dr. Chad Keyes, Clifford Jack, Dr. Nelson Vinueza, Dr. Sabir Aqueel, Dr. Nadine Njoya, Scott Cole, Dr. Fanny Widjaja, Colby Adolph, and the rest of the Kenttämaa research group. The friendship and memories we made together were instrumental in getting me through the last four years. You are all responsible for the fun and enjoyable moments that filled my life during my graduate career.

Also, I must thank my family for their unconditional support during my life. My sister Mary Riedeman sparked my interest in chemistry while I was still studying Computer

Information Systems at the University of Indianapolis. Without your guidance I might have wound up on a totally different path in life less satisfying than the one I ultimately pursued. My father Jim Riedeman, who supported me during my college years and molded me into the man I am today. I always had a place to come home to that would be filled with love and good cooking. He taught me to cherish the simpler things in life, like family, which should never be taken for granted. My brother Thomas Riedeman, for his love and support and virtuous ways that I strive to exemplify every day in my own life.

Finally, I must acknowledge the most gracious and loving person I have ever had the pleasure of knowing, my grandmother, Grace Maria Taddeo, for whom I dedicate this thesis. Her love and support are insurmountable and were unequivocally the most important factors to my success in life. After my mother passed away when I was a child she made a promise to care for me and my sister. She cared for us as if we were her own and never cast any doubts about our futures. Without you I would not be where I am today.

TABLE OF CONTENTS

LIST OF TABLES

Table   Page

LIST OF FIGURES

LIST OF SCHEMES

ABSTRACT

Riedeman, James Steven. Ph.D., Purdue University, December 2014. Mass Spectrometric Investigations of Structurally Diagnostic Ion-Molecule Reactions and of Molecular Structures of Asphaltenes. Major Professor: Hilkka I. Kenttämaa.

Tandem mass spectrometry (MS/MS) has proven to be a powerful tool for the molecular-level characterization of components of complex mixtures due to its ability to study ionized molecules with high sensitivity, selectivity and specificity. By combining MS/MS with liquid chromatography (LC) to enable front end separation of complex mixtures, trace level analysis of components in these mixtures is possible. Hence, LC-MS/MS has proven invaluable in the separation and characterization of saturated, alkyl aromatic, and polycyclic aromatic hydrocarbon constituents of crude oil. The most common MS/MS method involves collision-activated dissociation of mass-selected ions. Additionally, MS/MS strategies utilizing functional-group or isomer specific ion-molecule reactions have been recognized as a fast and efficient way to identify specific analytes among mixture components. However, the mechanisms of many gas-phase reactions, including dissociation and ion-molecule reactions, are not easily deciphered using MS alone. Thus, density functional theory (DFT) calculations may be used in combination with MS/MS data to derive reaction pathways leading to the formation of intermediate and product ions. Knowledge of the structures of these intermediate and product ions and pathways to their formation may be used to develop new mass spectrometry methodologies

for elucidation of structures of unknown components in mixtures and to identify better reagents for functional-group and isomer specific ion-molecule reactions.

This thesis focuses on the development of MS/MS strategies utilizing ion-molecule reactions, synthetic model compounds, and DFT calculations to elucidate the structures of ions and reaction pathways for a variety of gas-phase ion processes. Chemical ionization with aluminum (III) chloride followed by collision-activated dissociation (CAD) was examined as a method to distinguish epimeric 1,6-anhydrosugars which are commonly found in the pyrolysis products of cellulosic biomass. The use of dimethylamine in ion-molecule reactions with protonated *N*-oxides was investigated as a method to distinguish secondary and tertiary *N*-oxides from amines and other heteroatom-containing analytes. Additionally, MS/MS analysis was combined with Raman spectroscopy for the detailed characterization of asphaltenes derived from crude oil deposits. Crude oil deposition in oil transfer pipelines is perpetuated by the presence of polynuclear aromatic hydrocarbon structures, such as asphaltenes, whose molecular architectures are still not fully understood. The molecular structures of asphaltenes were explored by comparing the fragmentation behavior of ionized synthetic model compounds to that of genuine ionized asphaltenes isolated from Maya crude oil. Finally, rearrangement of the molecular ion of diphenylmethane leading to cleavage of methyl radical was examined by studying the fragmentation products of ^{2}H- and ^{13}C-labeled derivatives of diphenylmethane ions and through the use of DFT calculations since diphenylmethane is a common carbon skeleton in numerous therapeutic drugs whose dissociation mechanisms were not fully understood previously.

CHAPTER 1. INTRODUCTION AND OVERVIEW

1.1 <u>Introduction</u>

The first use of mass spectrometry (MS) was reported in 1913 by J. J. Thomson[1] who discovered the electron and its mass-to-charge (m/z) ratio. Meanwhile, numerous scientific fields have benefited from the use of MS. The unparalleled sensitivity, speed, low detection limits, and diverse applicability[2] of MS have made it a popular analytical method among chemists, biologists, engineers, and physicists, as well as many others.

At its core, mass spectrometry is composed of four basic events: evaporation, ionization, separation, and detection.[3] MS requires that ions be evaporated into the gas phase in order to be manipulated by magnetic and/or electric fields used to influence their trajectories. Evaporation and ionization often occur nearly simultaneously in contemporary ionization sources. The gas-phase analyte ions are separated as a function of some physical parameter related to the ions' m/z value, such as momentum, time-of-flight, frequency of motion, or kinetic energy. Typically, high vacuum is required to provide the collision-free paths needed for manipulating the ions' trajectories. Finally, the separated gas-phase ions are detected by an electron multiplier, Faraday cup, or various other techniques dependent on the type of mass separation being used. The detector generates a useable signal that is proportional to the ions' abundances. The ion abundances and m/z values are recorded by a computer data station and transformed into a mass spectrum wherein the ions' m/z values

are plotted along the x-axis and their abundances (relative or absolute) are plotted on the y-axis.

The measurement of stable ions' m/z values provides valuable information about the ions, such as their mass. Moreover, a careful analysis of the mass spectrum may provide some elemental composition information. For instance, a stable molecular ion ($M^{+\bullet}$) possessing an even m/z value will contain zero or an even number of nitrogen atoms. Molecular ions of analytes with an odd number of nitrogen atoms will possess an odd m/z value. Additionally, characteristic isotope patterns may be used to identify the presence of other elements (e.g., Br would produce an M+2 peak with 49.5% abundance relative to the abundance of M, corresponding to the natural abundance of ^{79}Br and ^{81}Br). By using a mass analyzer capable of highly accurate mass measurements wherein m/z ratios can be determined very accurately, unique elemental compositions can be identified for ions.[4,5]

In addition to elemental composition information obtained from the mass spectrum, tandem mass spectrometry (MS^n) may be used to elucidate structures of ions.[6] Tandem mass spectrometry involves at least two stages of mass separation wherein an ion of interest is selected via one stage of mass separation and probed via dissociation or other reactions. The product ions are analysed by an additional stage of mass separation.[7] MS^n experiments can utilize fragmentation reactions of ions or reactions between ions and neutral molecules[8] (more specifically, neutral molecules that react differently with certain isomeric forms[9] of an ionized analyte or only react with specific functional groups[10] in an ion). Both approaches were utilized in this dissertation.

1.2 <u>Thesis Overview</u>

The research in this dissertation focusses on stereospecific and functional-group selective gas-phase ion-molecule reactions, mass spectrometric investigations of the molecular structures of asphaltenes, and the dissociation processes of ionized aromatic hydrocarbons. Chapter 2 briefly discusses the principles of the instrumentation, experimental methods, and the computational chemistry methods used in these studies. Fundamental principles of linear quadrupole ion trap (LQIT) mass spectrometers are discussed in this chapter.

Chapter 3 describes the synthetic procedures used to produce the asphaltene model compounds and ^{2}H- and ^{13}C-labeled derivatives of diphenylmethane which were used in the studies summarized in chapters 7 and 8, respectively. Chapter 4 discusses the use of a novel reagent, dimethylamine, for the identification of protonated secondary and tertiary *N*-oxide ions via their ion-molecule reactions in the gas phase. Chapter 5 is devoted to the use of ion-molecule reactions combined with collision-activated dissociation (CAD) to differentiate epimeric 1,6-anhydrosugars by studying differences in the CAD spectra of their gas-phase complexes with the aluminum(III) ion.

The remaining chapters (6 through 8) detail analytical investigations into the molecular structures of asphaltenes and the dissociation mechanisms of ionized aromatic hydrocarbons. Chapter 6 details the characterization of asphaltenes derived from crude oil deposits by using Raman spectroscopy and mass spectrometry to unveil information about the size of their polynuclear aromatic core structure and the total number of carbons in their alkyl side chains. Chapter 7 discusses CAD of molecular ions of synthetic asphaltene model compounds that were compared to the CAD spectra of Maya asphaltene ions.

Chapter 8 discusses rearrangements of the molecular ion of a simple aromatic hydrocarbon,

diphenylmethane, upon CAD.

1.3 <u>References</u>

1.   Thomson, J. *Rays of Positive Electricity and their Application to Chemical Analysis*; Longmans, Green, & Co.: London, 1913.

2.   McLuckey, S. A.; Wells, J. M. *Chem. Rev.* **2001**, *101*, 571.

3.   de Hoffman, E.; Stroobant, V. *Mass Spectrometry, Principles and Applications*; 2nd Ed.; John Wiley and Sons, Ltd.: New York, 2002.

4.   McLafferty, F. W. *Interpretation of Mass Spectra*; 4th ed.; University Science Books: Sausalito, CA, 1993.

5.   Zubarev, R. A.; Håkansson, P.; Sundqvist, B. *Anal. Chem.* **1996**, *68*, 4060.

6.   Busch, K. L.; Glish, G. L.; McLuckey, S. A. *Mass Spectrometry/Mass Spectrometry: Techniques and Aplications of Tandem Mass Spectrometry*; VCH Publishers: New York, 1988.

7.   de Hoffmann, E. *J. Mass Spectrom.* **1996**, *31*, 129.

8.   Brodbelt, J. S. *Mass Spectrom. Rev.* **1997**, *16*, 91.

9.   Stirk, K. M.; Kiminkinen, L. K. M.; Kenttamaa, H. I. *Chem. Rev.* **1992**, *92*, 1649.

10.   Eberlin, M. N. *J. Mass Spectrom.* **2006**, *41*, 141.

CHAPTER 2. INTRODUCTION AND EXPERIMENTAL CONSIDERATIONS

2.1 <u>Introduction</u>

Mass spectrometry is an analytical tool that has become ubiquitous in a variety of research areas, such as those relating to pharmaceuticals,[1] biotechnology,[2] and petroleum.[3,4] The popularity of mass spectrometry has grown as a result of its high specificity, sensitivity, speed, and versatility.[5] Mass spectrometry has been used to obtain accurate molecular weights of asphaltenes,[6] monitor enzymatic reactions,[7] characterize peptide sequences,[8] and structurally elucidate individual components in complex mixtures.[9]

Mass spectrometers are composed of three basic parts, namely, ionization source, mass analyzer, and detector. Analysis of compounds by mass spectrometry requires that they be introduced into the gas phase. Ionization of analytes may occur before, during, or after their evaporation. Next, the gas-phase ions enter the analyzer region of the mass spectrometer where they are separated according to their mass-to-charge ratios. Finally, the separated ions are detected, generating a signal that is sent to a data system where their mass-to-charge ratios and abundances are recorded to produce a mass spectrum.

Typically, mass analyzers fall into one of two major categories: scanning mass analyzers or trapping mass analyzers. Scanning instruments, such as time-of-flight and quadrupole mass spectrometers, pass a stream of ions through different parts of the

instrument where they are being manipulated using electric or magnetic fields. Conversely, trapping instruments, such as quadrupole ion traps (QIT) and Fourier transform ion cyclotron resonance (FT-ICR) mass spectrometers, confine ions in a specific area of the instrument where various manipulations occur at different times.

In addition to single-stage mass spectral analysis (MS^1), which may be useful in providing molecular weight and elemental composition information on ions, tandem mass spectrometry (MS^2) can provide structural information via fragmentation reactions and/or ion-molecule reactions for mass-selected ions.[10,11] Dissociation of ions is typically achieved via activating collisions with an inert gas. Ion-molecule reactions involve introduction of a reagent gas into the ion trap after ion isolation followed by a pre-determined reaction time. Further, isolation of the product ions of these reactions followed by dissociation or ion-molecule reactions (MS^3) may be used to provide additional structural information. Multiple stages of ion isolation/reactions followed by mass analysis is known as multiple-stage tandem mass spectrometry (MS^n).[12]

Trapping instruments were primarily used for the work presented in this dissertation, specifically, a linear quadrupole ion trap (LQIT) mass spectrometer. Density functional theory (DFT) calculations were used as necessary to facilitate the interpretation of experimental results. Principles of LQITs have been discussed in the literature.[13,14] Some fundamental and experimental aspects of the instrumentation and methods employed in the research discussed in this thesis are discussed in this chapter.

<center>2.2 <u>Ionization Methods</u></center>

Mass spectrometry involves the manipulation of ions in magnetic and/or electric fields in a mass spectrometer, thus, ionization is a critically important step. Several methods of ionization exist, such as electron ionization (EI),[15] chemical ionization (CI),[16-18] fast atom bombardment (FAB),[19] matrix-assisted laser desorption ionization (MALDI),[20] electrospray ionization (ESI),[21] and atmospheric pressure chemical ionization (APCI).[22] Each method of ionization has unique advantages and disadvantages that are dependent on the nature of the analyte, such as the presence of specific functional groups. Only the ionization methods employed in the work presented in this dissertation will be discussed below.

<center>2.2.1 Electron Ionization</center>

Electron ionization (EI) is the oldest ionization technique for mass spectrometry, dating back to 1918 when it was first introduced by A. J. Dempster. It has colloquially been called electron impact ionization.[15] Ionization by EI involves bombarding neutral analyte molecules with high energy electrons (typically 70 eV) in the gas phase, which causes an electron to be ejected, resulting in the formation of a radical cation (molecular ion; Scheme 2.1). Energy in excess of the ionization energy for the analyte can internally excite the newly formed ion, thus inducing fragmentation.

<center>$M + e^- \rightarrow M^{+\bullet} + 2e^-$ (where M = analyte molecule)</center>

<center>Scheme 2.1 Electron ionization of an analyte molecule.</center>

An advantage of EI is its great reproducibility, which has led to the development of

extensive mass spectral libraries.[23]

2.2.2 Chemical Ionization

Chemical ionization (CI) generates analyte ions via chemical reactions with

specific reagent ions.[16-18] These reactions may involve proton transfer, proton abstraction,

adduct formation, or charge exchange, etc. Pressures and/or reaction times employed in CI

are generally greater than for EI to ensure multiple collisions between analytes and reagent

ions. CI typically generates ions possessing much less excess energy than EI, which allows

for the generation of stable molecular ions ($M^{+\bullet}$) or pseudo-molecular ions (notably MH^+)

without causing excessive fragmentation.[24,25]

In the work presented in this dissertation, CI was utilized to generate molecular ions

($M^{+\bullet}$) and protonated molecules (MH^+) via charge exchange and proton transfer,

respectively. Most of the work presented in this dissertation utilized charge exchange. A

typical CI reaction sequence is shown in Scheme 2.2.

$$R^{+\bullet} + M \rightarrow R + M^{+\bullet} \text{ (where R = reagent)}$$
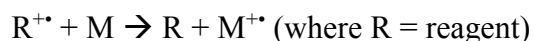
Scheme 2.2 Chemical ionization of an analyte molecule (M).

The difference between generating molecular ions by EI and by CI via charge exchange is

that the molecular ions $M^{+\bullet}$ generated by CI possess a narrow internal energy distribution

determined by the enthalpy of reaction of the reagent ion and the neutral analyte.[26] The

exothermicity of the charge exchange reaction is determined by the recombination energy

(RE) of the reagent ion minus the ionization energy of the neutral analyte. Hence, the approximate amount of internal energy imparted into the analyte ion may be reduced by choosing a reagent ion with RE close to the IE of the analyte.

2.2.3 Electrospray Ionization

The development of electrospray ionization (ESI) in 1989 by Fenn[21] expanded the applicability of MS to many compounds that were previously not amenable to MS due to their high molecular weight or thermal lability. ESI is considered a "soft" ionization method since it typically does not cause much or any fragmentation. ESI involves the transfer of preformed ions from solution into the gas phase by passing the solution through a metal needle with a high DC voltage (typically ± 3-5 kV) applied to it. An illustration of the ESI process can be seen in Figure 2.1.
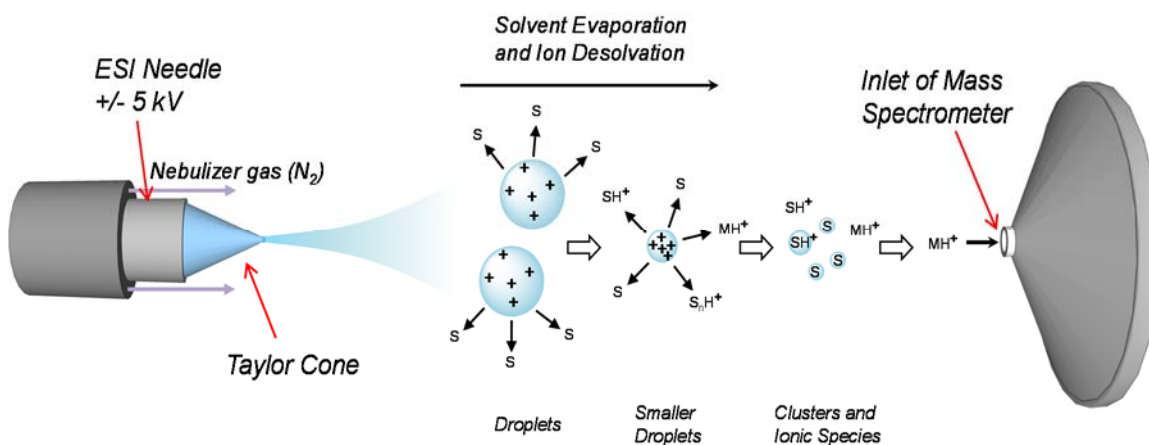
Figure 2.1 Illustration of the ESI process for producing gas-phase positively charged analyte ions. The letters "S" and "M" denote solvent and analyte molecules, respectively.

Nitrogen gas is also utilized at the tip of the ESI needle to assist nebulization of the solution and begin the desolvation process of analyte ions (MH^+). Due to the high voltage, a Taylor cone forms[27-29] at the tip of the ESI needle resulting in the production of multiply charged fine droplets. As solvent evaporates from these droplets, the residual charges migrate to the surface of the droplet and experience greater repulsion as the droplet becomes smaller. Eventually, Coulombic forces overcome the surface tension of the droplet at a point known as the Rayleigh stability limit.[30,31] The droplet forms a distorted prolate ellipsoid with progeny jets which eject progeny droplets that are much smaller than the parent droplet from which they formed.[32,33] The charge-to-volume ratio increases with every iteration of this process. Thus, the rate at which new progeny droplets reach the Rayleigh stability limit also increases. These droplets divide many times until all solvent has evaporated, leaving only gas-phase ions.

The generation of gas-phase ions from progeny droplets in ESI has been proposed to occur by two competing mechanisms: the ion evaporation model[34,35] and the charge residue model.[36] These two mechanisms are depicted in Figure 2.2. According to the ion evaporation model, as the charged droplets attain the Rayleigh limit, the charge on their surface becomes sufficiently large to cause desolvated ions or scarcely solvated ions to be ejected from the droplet. Conversely, according to the charge residue model, the highly charged droplets shrink due to solvent evaporation until the strength of the electric field at the droplet surface location with the highest curvature is large enough to form a Taylor cone. Smaller droplets are emitted from the Taylor cone and the process repeats until droplets form that contain a single analyte ion. This analyte ion is eventually released into the gas phase by evaporation of the solvent.[37]

Solvent evaporation
and droplet fission

Surface electric field ejects
analyte ion from droplet

Solvent evaporation

Droplet fission

Ion Evaporation Model

Solvent evaporation
and droplet fission

Ion evaporation

Charge Residue Model
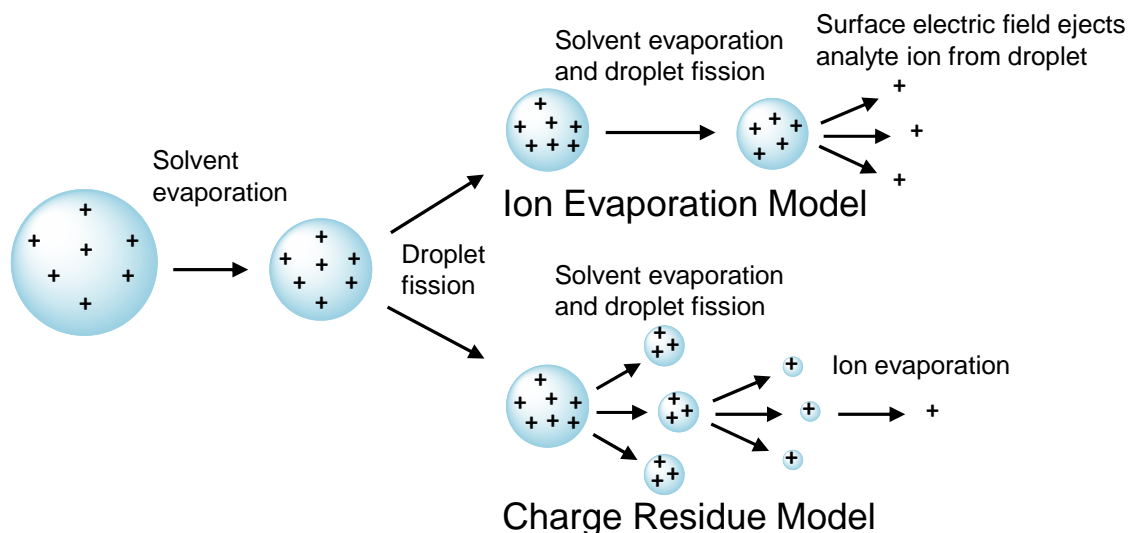
Figure 2.2 Illustration of the two competing ion generation models for ESI.

Small molecules typically form ions possessing a single charge, most notably protonated molecules (MH^+) in positive ion mode or deprotonated molecules ($[M-H]^-$) in negative mode. The formation of these ions depends on their precursor molecules' basic or acidic properties in solution. ESI is also capable of forming multiply charged ions for larger molecules possessing multiple acidic or basic functionalities, such as biopolymers[38] and proteins.[39] Additionally, the study of noncovalent complexes is also possible by ESI. This is of high interest because the binding affinities of small ligands to proteins may be examined with the aid of ESI of their complexes.[40,41]

2.2.4 Atmospheric Pressure Chemical Ionization

Atmospheric pressure chemical ionization (APCI) is another common ionization technique that is considered "soft" yet not as gentle ESI.[22,42] In APCI, analyte ions are

formed through a series of gas-phase reactions involving ionized nitrogen drying gas, ambient oxygen, water vapor, and/or solvent molecules. A typical cascade of reactions resulting in the formation of gas-phase protonated analyte ions is shown in Scheme 2.3.

Ionization of drying gas via corona discharge:

$N_2 + e^- \rightarrow N_2^{+\bullet} + 2e^-$
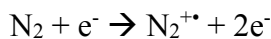
Charge exchange with solvent molecules:

$H_2O + N_2^{+\bullet} \rightarrow H_2O^{+\bullet} + N_2$
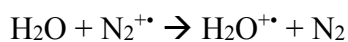
Proton transfer between ionized and neutral solvent:

$H_2O + H_2O^{+\bullet} \rightarrow H_3O^+ + HO^{\bullet}$
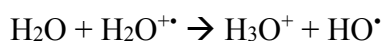
Protonation of analyte molecules:

$M + H_3O^+ \rightarrow MH^+ + H_2O$
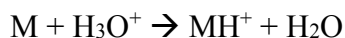
Scheme 2.3 Gas-phase ionization processes occurring during and after a corona discharge

APCI can be used to generate pseudo-molecular ions (i.e., MH^+, $[M-H]^+$) and also molecular ions depending on the solvent or reagent used.[24,43,44] Figure 2.3 shows an illustration of an APCI source. In APCI, the solution containing the dissolved analyte flow through a capillary within a ceramic heater (typically $250 - 500$ °C) where it is nebulized by nitrogen gas running coaxial to the capillary and vaporized. Solvent and analyte vapor exit the APCI source probe and are exposed to a corona discharge plasma which is generated by applying a high voltage (3-6 kV) to the corona discharge needle.
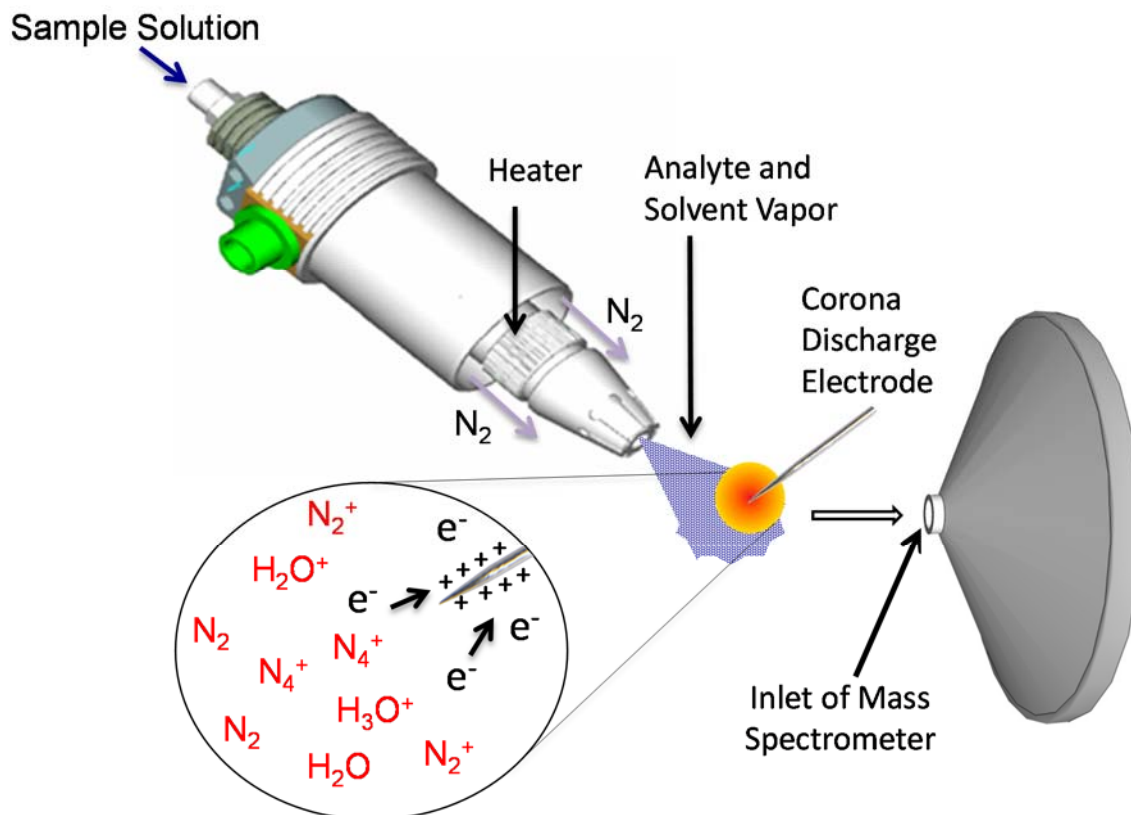
Figure 2.3 Illustration of APCI source operating in positive ion mode.

Due to the high frequency of ion-molecule collisions in APCI, high ionization efficiency of analyte ions is achieved.[42]

2.3 Linear Quadrupole Ion Trap (LQIT) Mass Spectrometry

Linear quadrupole ion traps have grown in popularity since their inception[13,14] as a result of their versatility and high sensitivity. The principles of operation are similar to the 3-D quadrupole ion traps[45,46] (QIT); however, LQITs have many advantages over 3-D QITs. The ion trapping capacity of the LQITs is sixteen times greater than for QITs and the trapping efficiency is also greatly improved.[13] Additionally, the larger capacity for storing

ions and improved ejection efficiency of the LQITs have made them suitable as front-end analyzers for other types of mass spectrometers, such as LQIT-FT-ICR[47] and LQIT-Orbitrap.[48]

The LQIT mass spectrometers used for the work presented in this dissertation are Thermo Scientific LTQ[13,49] mass spectrometers equipped with an ESI or APCI source and coupled with Thermo Scientific Surveyor Plus HPLC systems. A Dell Optiplex workstation (Microsoft Windows XP operating system) running Xcalibur 2.1 software was used to control instrument functions and acquire and process data. A schematic of a LQIT mass spectrometer is shown in Figure 2.4.
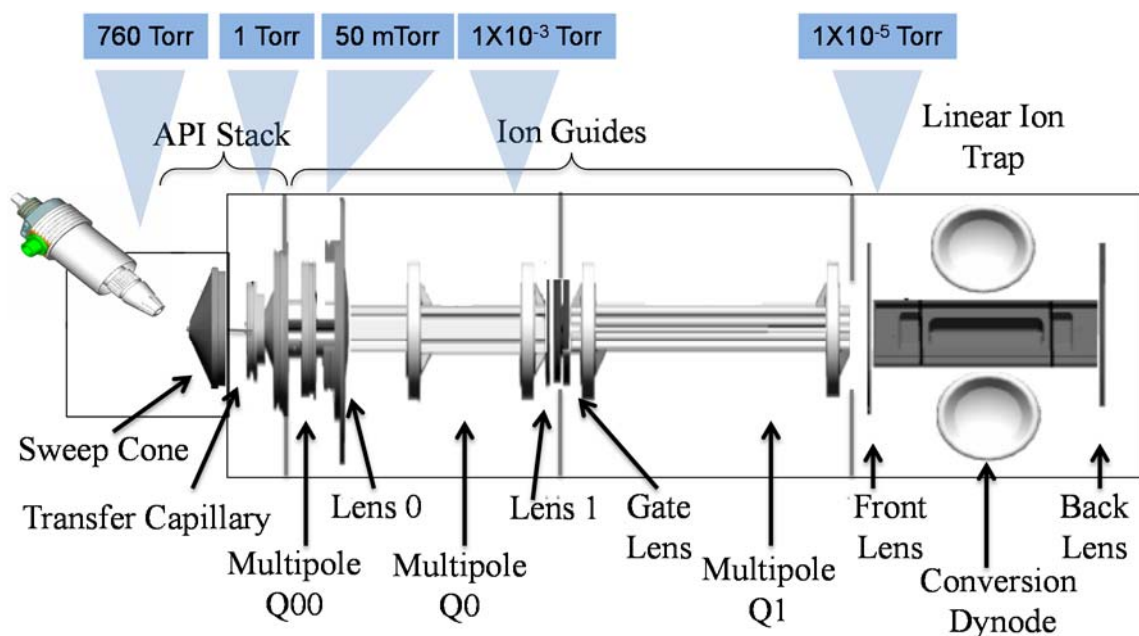
Figure 2.4 Schematic of the Thermo Scientific LTQ mass spectrometer, including operating pressures for each region of the instrument.

The LQIT can be divided into three sections: 1) the atmospheric pressure ionization (API) stack, 2) the ion optics region, and 4) the mass analyzer region, where the linear quadrupole ion trap and ion detection system are located. The instrument was differentially pumped, thus, each region operated at a different pressure. Pressure in the API stack region after the sweep cone was maintained at ~ 1 Torr by two Edwards E2M30 rotary-vane mechanical pumps pumping at a rate of 650 L/min and monitored by a convectron gauge. The ion optics and mass analyzer regions were maintained by a Leybold T220/150/15S triple-inlet turbomolecular pump. The first inlet (25 L/s) maintained the pressure in the region housing the multipole Q00 at 0.5 – 100 mTorr. The second inlet (300 L/s) evacuated the differentially pumped region housing the multipole Q0 which was partially sealed from the previous higher pressure region by a lens aperture (lens 0). The pressure in this region was maintained at 1 mTorr. The third inlet (400 L/s) maintained the pressure in the mass analyzer region at 1 x 10^{-5} Torr, as monitored by an ion gauge. This vacuum region, which housed the multipole Q1 and the linear quadrupole ion trap, was also partially sealed from the higher pressure regions of the instrument by a lens aperture (lens 1).

Generation of ions occurred under ambient conditions in the Ion Max API source shown in Figure 2.5. ESI and APCI source probes could be easily interchanged in the Ion Max API source. A read-back voltage from the Ion Max source informed the LQIT instrument which type of source probe was installed. Position adjusters for x, y, and z movements of the source probe facilitated position optimization for optimal ESI spray and ion plume location.
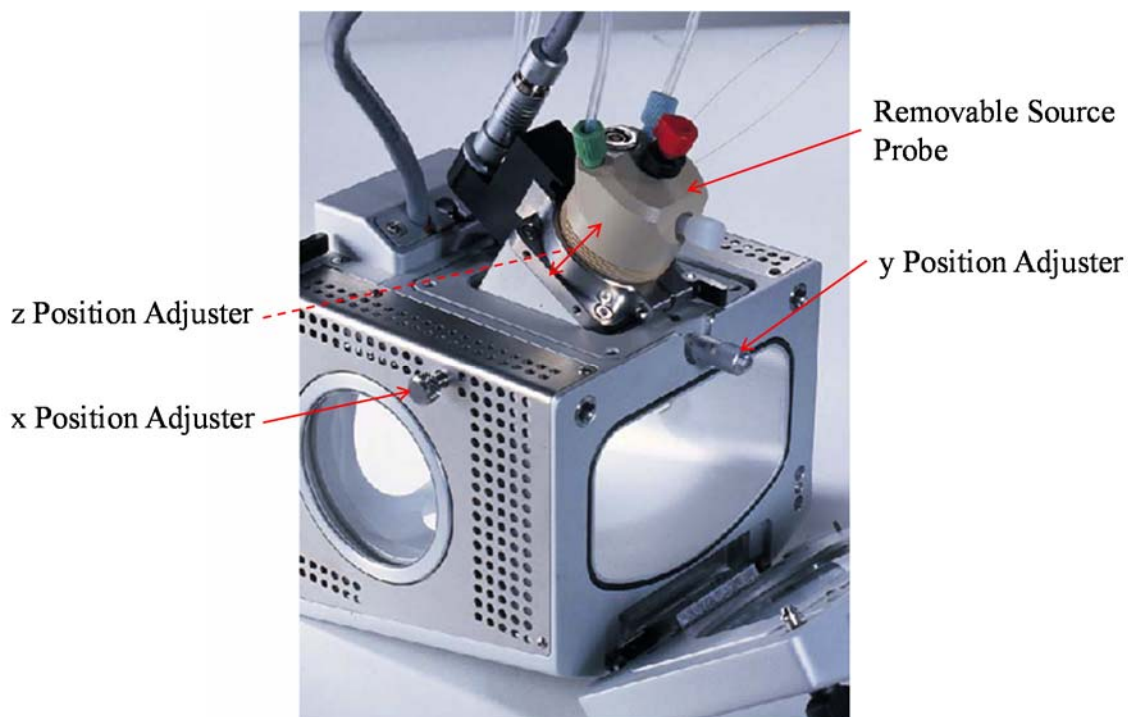
Figure 2.5 Photo of the Ion Max API source equipped with an ESI source probe. Source probe position adjusters are indicated for the x, y, and, z movements.
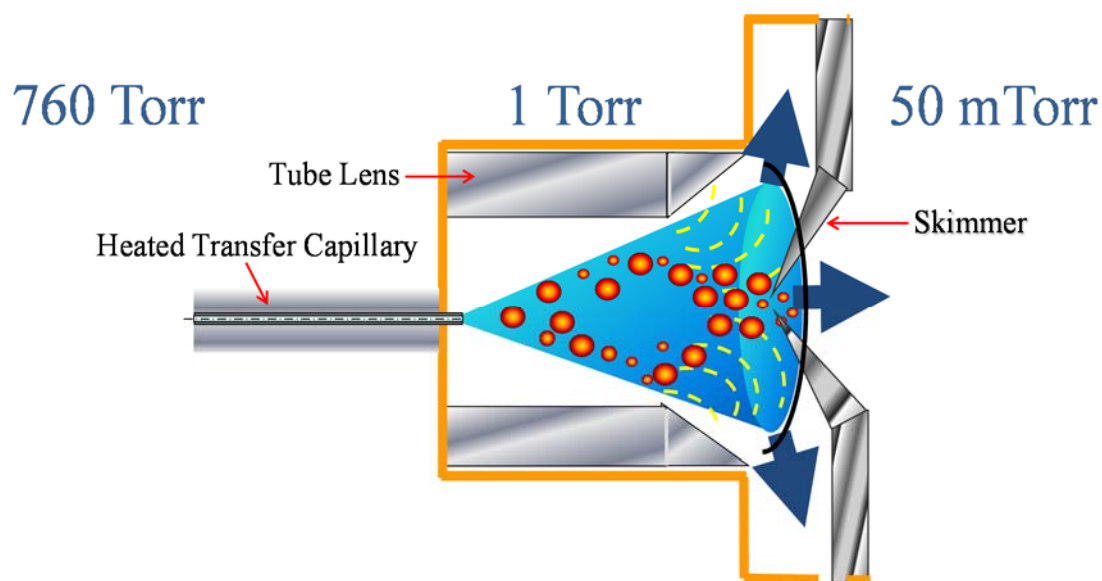
Figure 2.6 Illustration of the API stack region consisting of the heated transfer capillary, tube lens, and skimmer cone.

Ions are generated in the Ion Max API source via APCI or ESI and drawn into the mass spectrometer through a heated (typically 250 – 300 °C) transfer capillary aided by a negative pressure gradient (760 Torr → 1 Torr) as shown in Figure 2.6. Ions and residual neutral molecules, such as those of the solvent, exit the transfer capillary and expand as they enter the much lower pressure (~1 Torr) region before the skimmer cone. A like-polarity DC voltage applied to a circular lens, called the tube lens, serves to focus the emerging ions through the small circular orifice of the skimmer cone. The DC voltage applied to the tube lens creates a mass bias, with ions of higher m/z values requiring a higher voltage to be focused than ions with lower m/z values. Additionally, higher DC voltages applied to the tube lens increases ions' kinetic energies which may cause ions to fragment via collisions with residual solvent molecules and N_2 gas in the API stack. Thus, the DC voltage applied to the tubes lens needs to be tuned for optimal transmission of ions through the skimmer cone without causing fragmentation. The skimmer cone has no voltage applied to it and is positioned off-axis relative to the transfer capillary to block neutral molecules from progressing further into the mass spectrometer. After passing through the skimmer cone, ions are guided by ion optics, which direct them into the LQIT mass analyzer. The ion optics consist of two square-rod quadrupoles (Q00 and Q0) and a cylindrical-rod octupole (Q1) which serve as ion guides. Two lenses (0 and 1) serve as vacuum baffles between different pressure regions of the instrument and focus ions as they pass through the mass spectrometer.
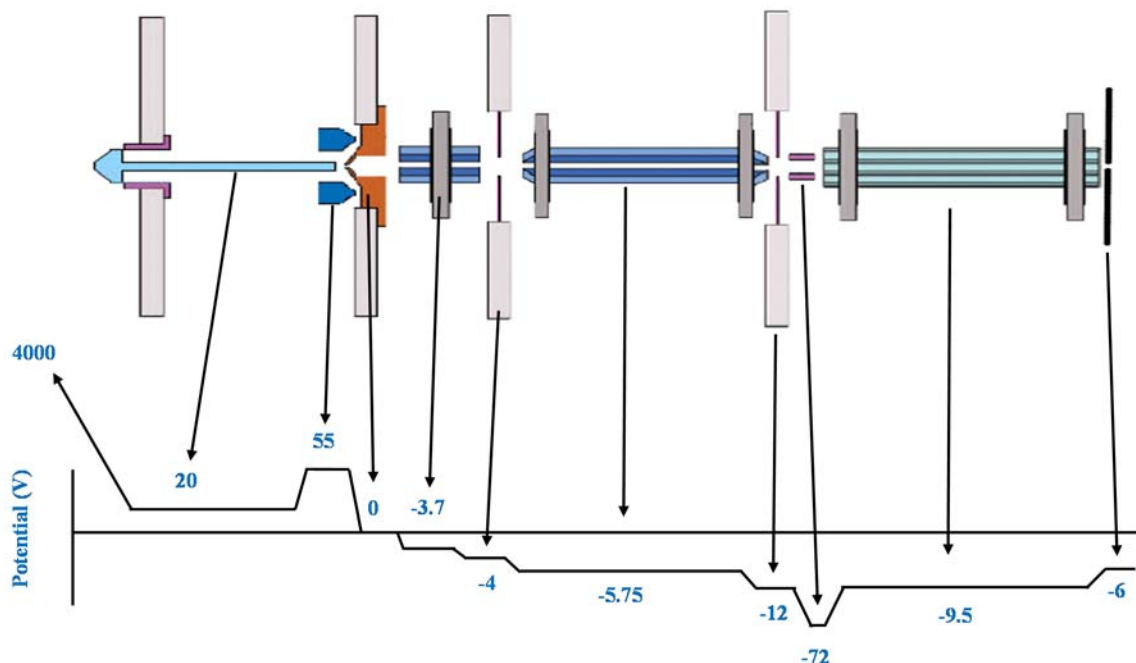
Figure 2.7 Typical DC voltages applied to the different ion optical elements for transmission of ions.

Ions emerging from quadrupole Q00 typically have lower kinetic energies than ions generated and accelerated in vacuum sources due to the higher pressure in the API stack which reduces ions' kinetic energies via multiple collisions with residual solvent molecules. Thus, a downhill potential gradient is needed to transmit the ions further into the instrument towards the LQIT mass analyzer (Figure 2.7).

Ions enter the LQIT after passing through a front lens (Figure 2.4). The LQIT consists of four hyperbolic rods that are each divided into three sections: front, center, and back, as shown in Figure 2.8. The front and back sections are 12 mm long in the z-direction. The center section is 37 mm long. Two of the rods in the center section, called x-rods, have 0.25 x 30 mm slits which allow ions to be ejected from the trap in the x-direction for detection by two pairs of conversion dynodes and electron multipliers. The fundamental

aspects of ion trapping, activation, and detection in the LQIT are discussed in the following sections.
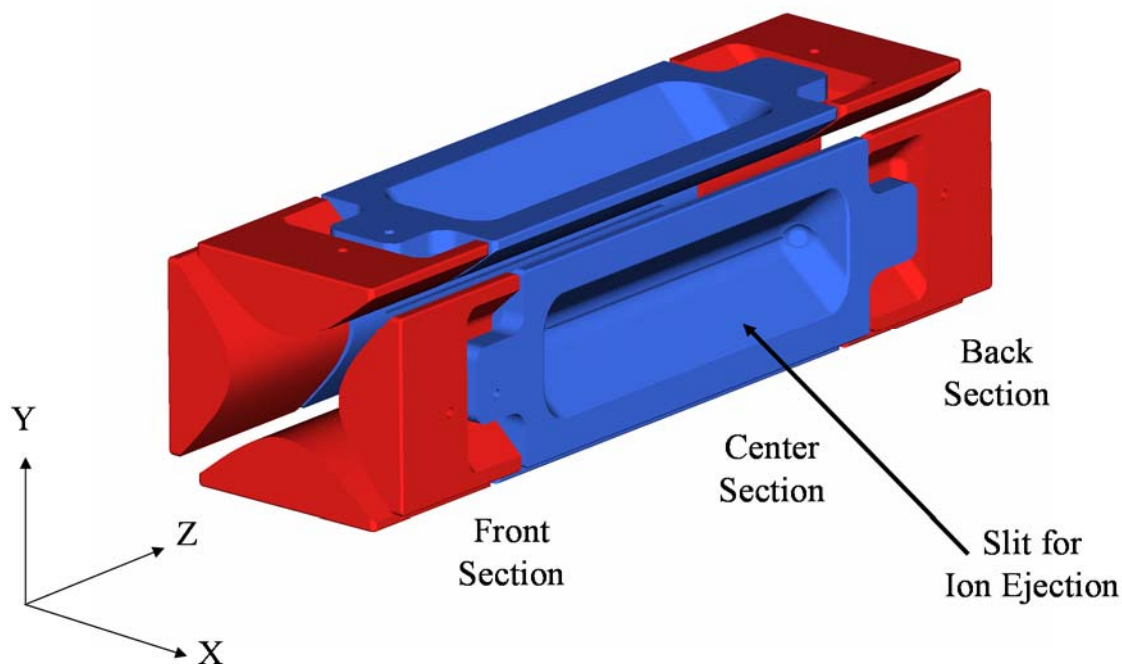
Figure 2.8 Schematic of the linear quadrupole ion trap.

2.3.1 Ion Motion in the LQIT

Ions are trapped axially and radially in the linear quadrupole ion trap through a combination of RF and DC voltages applied to the hyperbolic rods. Applied quadrupolar RF fields are similar to those used in quadrupole mass filters.[45,46,50] Ions are trapped radially (in x-y plane) through the use of two phases of the main RF voltage applied to the rods which has constant frequency (1.2 MHz) but variable amplitude ($\pm$5 kV peak-to-peak). RF voltage on adjacent rod pairs 180° out-of-phase. Thus, adjacent rods have identical RF

amplitude applied to them but opposite polarity while opposing rods have the same polarity

and RF amplitude. This creates a quadrupolar field that is weakest in the center of the trap.

A supplementary RF voltage is applied to the x-rods in addition to the main RF voltage for

excitation, isolation, and ejection of ions. The supplementary RF voltage is a dipolar (180°

out-of-phase) RF voltage of variable frequency (5-500 kHz) and amplitude (±80 V peak-

to-peak). Additionally, different DC voltages (±100 V) are applied to the three sections of

the ion trap to confine ions axially.

2.3.1.1 Radial Motion

The forces that confine ions radially (x-y plane) are identical to those used in a

quadrupole mass filter.[45,46,50] RF and DC voltages are applied to the four hyperbolic rods

to yield the following potentials (Φ_0):

$$\pm\Phi_0 = \pm(U - Vcos\Omega t) \tag{2.1}$$

where U is the applied DC voltage, V is the zero-to-peak amplitude of the RF voltage, Ω is

the angular frequency ($2\pi v$) of the main RF field, and t is time. The application of these

voltages creates a quadrupolar electric field in the space between the four hyperbolic rods.

When ions are injected into the LQIT along the z-axis, they are subjected to the following

forces in the x- and y- directions due to these potentials:

$$F_x = m\frac{d^2x}{dt^2} = -ze\frac{d\Phi}{dx} \tag{2.2}$$

$$F_y = m\frac{d^2y}{dt^2} = -ze\frac{d\Phi}{dy} \tag{2.3}$$

where the potential in the x-y direction can be written as

$$\Phi_{(x,y)} = \frac{\Phi_0(x^2 - y^2)}{r_0^2} = \frac{(U - V\cos\Omega t)(x^2 - y^2)}{r_0^2} \tag{2.4}$$

where m is the mass of the ion, e is the elementary charge, z is the number of charges of the ion, and r_0 is the radius of a circle inscribed within the space between the four rods. Rearrangement of these equations leads to the following equations of ion motion:

$$\frac{d^2x}{dt^2} + \frac{2ze}{mr_0^2}(U - V\cos\Omega t)x = 0 \tag{2.5}$$

$$\frac{d^2y}{dt^2} - \frac{2ze}{mr_0^2}(U - V\cos\Omega t)y = 0 \tag{2.6}$$

These equations are similar to the general form of the Mathieu equation,

$$\frac{d^2u}{dt^2} + (a_u - 2q_u\cos2\xi)u = 0 \tag{2.7}$$

Thus, by performing a change of variables where

$$\xi = \frac{\Omega t}{2} \tag{2.8}$$

the equations of motion can be expressed in terms of the Mathieu equation:

$$a_u = \frac{8zeU}{mr_0^2\Omega^2} \tag{2.9}$$

$$q_u = \frac{4zeV}{mr_0^2\Omega^2} \tag{2.10}$$

wherein

$$a_u = a_x = -a_y \tag{2.11}$$

$$q_u = q_x = -q_y \tag{2.12}$$

The variables a_u and q_u are the Mathieu stability parameters. For a particular ion to have a stable trajectory within the quadrupolar field, its a_u and q_u values must fall within the stability region defined by the Mathieu stability diagram. The most well-defined and widely used overlap region of the Mathieu stability diagram is shown in Figure 2.9.
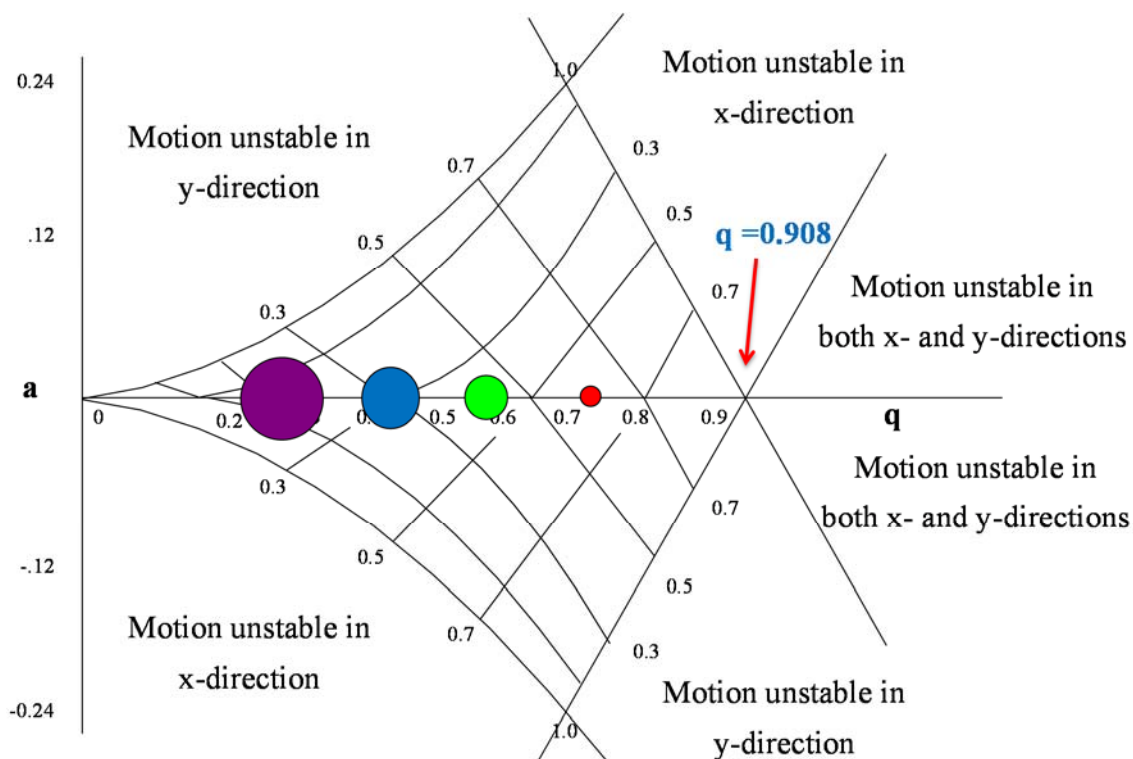
Figure 2.9 The most well defined and widely used region of the Mathieu stability diagram. The colored circles represent ions of varying *m/z* values with the larger circles corresponding to ions of larger *m/z* than the smaller circles. The spatial distribution of ions in *q*-space is indicated. Ions possess stable trajectories within the overlap region.

The LQIT is usually operated with $a_u = 0$ so that a larger range of ions may be trapped simultaneously.

Each ion of a unique *m/z* value oscillates at a specific frequency called the secular frequency (ω_u). The secular frequency can be calculated using the following equation:

$$\omega_u = \frac{1}{2}\beta_u\Omega \tag{2.13}$$

where ω_u is the angular frequency of the RF field applied to the rods and β_u is the Dehmelt approximation for a q_u value less than 0.4, which can be expressed using the following equation:

$$\beta_u = \sqrt{\left(a_u + \frac{1}{2} q_u^2 \right)} \tag{2.14}$$

The value of β_u must be between 0 and 1 for an ion to have a stable trajectory in the ion trap.[46] Thus, the maximum secular frequency an ion is capable of having is one half of the angular frequency ω_u. Additionally, the secular frequency of an ion is proportional to its q_u value but inversely proportional to its m/z value. Thus, ions with lower m/z will oscillate at higher secular frequencies and possess larger q_u values.

Ions confined in the trapping area of the LQIT exist in a pseudopotential well with a well depth (D_u) given by:

$$D_u = \frac{q_u V}{4} \tag{2.15}$$

D_u is known as the Dehmelt pseudopotential well.[46] As ions with lower m/z values have higher q_u values than ions with higher m/z values, they will exist in deeper pseudopotential wells.[51] The depth of the pseudopotential well is an important factor in determining an appropriate q_u value (RF voltage) to use for resonant excitation or ejection of a particular ion of interest.

2.3.1.2 Axial Motion

Ion motion in the LQIT is confined axially (z-direction) by the application of DC potentials to the front and back lenses and the front and back sections of the trap that are of the same polarity as the trapped ions.[49] Application of these repulsive potentials to the front and back sections of the trap causes ions to be trapped axially in the center of the trap. An illustration of the DC potential well is shown in Figure 2.10. Fringe fields created by the DC potentials on the front and back lenses are also reduced by the DC potentials applied to the front and back sections of the trap. Also, more efficient ejection of ions through the x-rods is achieved by maintaining the ions' position in the center of the trap.[13]
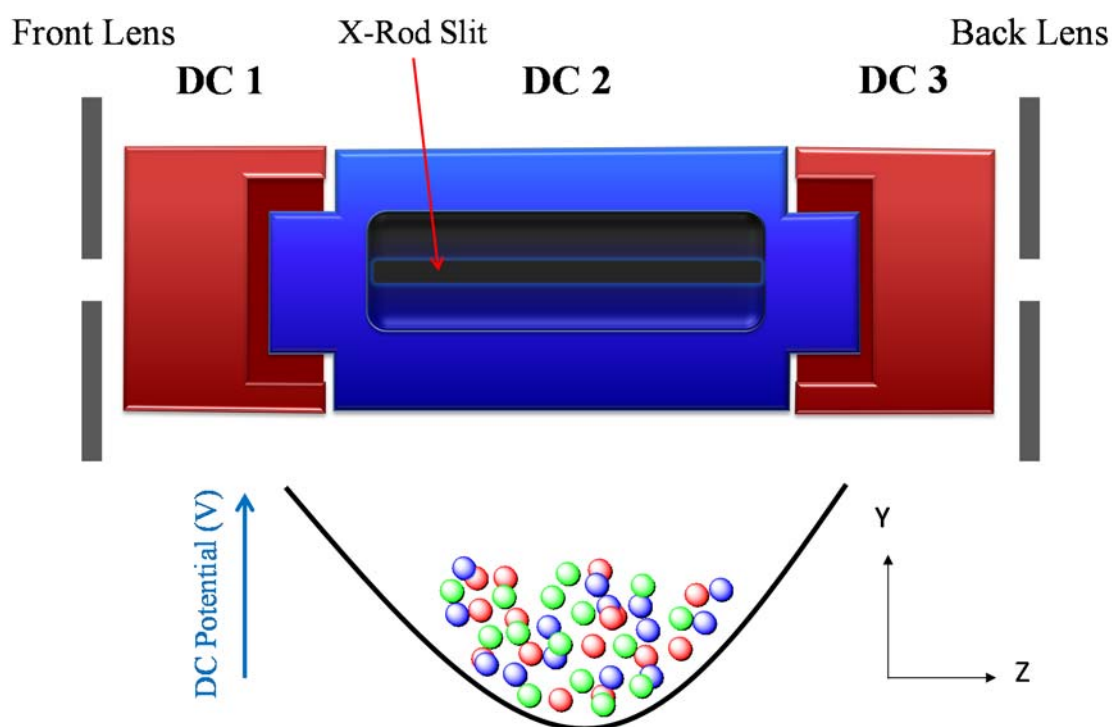
Figure 2.10 Potential energy well created through the application of a greater DC potential (V) on the front and back sections (DC 1 and DC 3) than the center section (DC 2) of the ion trap with illustration of ions confined in the z-direction.

Another crucial factor for the efficient trapping of ions in the LQIT is the use of an inert buffer gas (helium is the gas of choice for the Thermo Scientific LTQ).[52] The downward potential gradient used to draw ions into the trap from the API source causes them to gain a significant amount of kinetic energy. The constant presence of a buffer gas (~3 mTorr) serves to cool the ions as they enter the trap through multiple low energy collisions. These collisions transfer energy from the incumbent ions and allow the ions to be trapped more efficiently by the DC and RF potentials as well as to concentrate the ions into the center of the trap (along the z-direction). Sensitivity, mass accuracy, and mass spectral resolution are improved through the use of a buffer gas in the LQIT.

2.3.2 Ion Ejection and Detection

Ions were detected by an external electron multiplier after being ejected from the LQIT using a technique known as the "mass selective instability scan".[53] As stated above, the LQIT generally operates with an a_u value of zero; thus, ejection of ions is achieved by ramping the amplitude of the main RF voltage applied to the rods of the ion trap. According to equation 2.10, as the main RF voltage is increased, the q-values of ions increases and the ions are ejected when their q-value exceeds 0.908, which is called stability limit ($a = 0$, $q = 0.908$). This technique was originally used in QITs to eject ions for detection.[53] However, ejecting ions by this method has undesirable side effects since the ions exit the trap in an unsystematic manner. As an improvement, the LQIT uses resonance ejection described below which gives better resolution, mass range, and sensitivity.[54]

Resonance ejection of ions is achieved by applying a supplementary RF voltage to the x-rods of the LQIT which facilitates dipolar excitation of ions in the x-direction. The supplementary RF voltage is lower in amplitude and frequency than the main RF voltage (~400 kHz; ~5 – 50 V). As the main RF voltage is increased, ions come into resonance with the supplementary RF voltage as their secular frequency (Eq. 2.13) matches that of the supplementary RF. Ions gain additional kinetic energy from the supplementary RF voltage which increases the amplitude of their motion in the x-direction causing them to be ejected from the trap through the slits in the x-rods (Figure 2.10). The Thermo Scientific LTQ mass spectrometer uses the mass selective instability scan with resonant ejection at q = 0.880 as shown in Figure 2.11. In addition to above stated improvements using resonant ejection, higher scan speeds are also possible while maintaining unit resolution.[55]
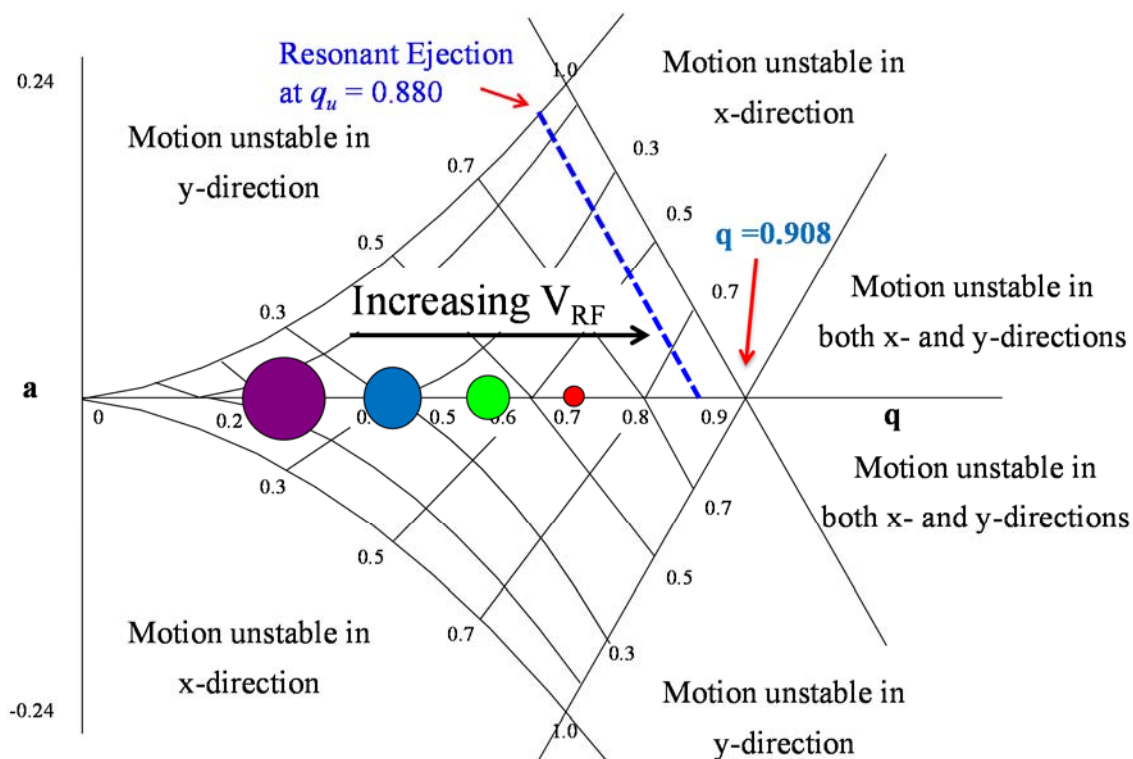
Figure 2.11 Increasing the main RF voltage (V_{RF}) brings ions into resonance with the supplementary RF frequency which facilitates resonant ejection of ions from the trap at q_u = 0.880.

Upon ejection of ions from the trap through the x-rods, they are detected by two detection systems on both sides of the mass analyzer. A depiction of the ion ejection and detection event is shown in Figure 2.12 for the Thermo Scientific LTQ mass spectrometer. Upon exiting the x-rods, the ions are attracted to the conversion dynodes that are held at -15 kV (for positive ions). The ions strike the conversion dynode and multiple secondary particles (neutral molecules, electrons, or negative ions) are generated. They are directed toward the electron multiplier (due to the concave shape of the conversion dynode) for detection. Every particle that strikes the inside wall of the electron multiplier causes one or more electrons to be ejected from the surface. The ejected electrons accelerate into the cathode, drawn by the increasingly positive potential gradient. Every newly generated

electron that strikes the inner surface of the cathode causes the emission of more electrons, thus amplifying the current at the end of the cathode where the electrons are collected by the anode. The resulting current is proportional to the number of secondary particles striking the cathode. The measured current is assigned to a particular *m/z* value, and reported as ion abundance, thus, generating a mass spectrum.
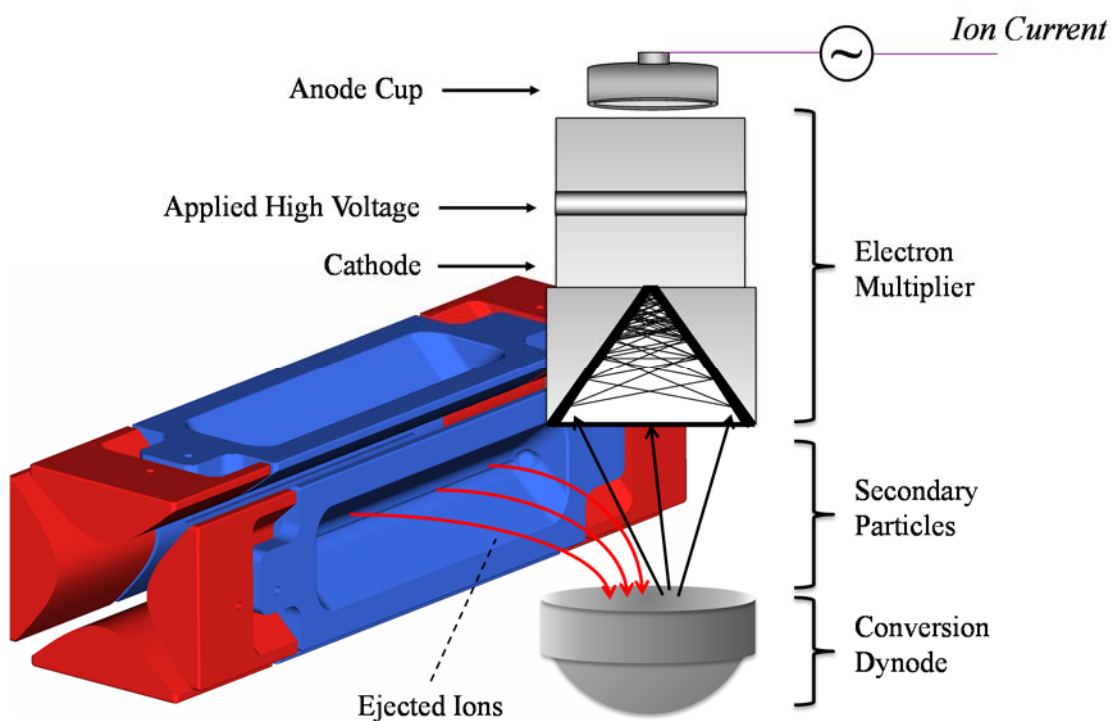
Figure 2.12 Ion detection set-up consists of a conversion dynode and an electron multiplier. Ions exiting the trap through slits in the x-rods are attracted to the conversion dynode and converted into secondary particles. These secondary particles strike the inner cathode surface of an electron multiplier, resulting in a cascade emission of electrons thus amplifying the signal that is measured at the anode cup.

2.3.3 Tandem Mass Spectrometry (MS^n)

Tandem mass spectrometry (MS^n) involves multiple stages of ion isolation followed by fragmentation or other reactions. In an LQIT, these multiple stages do not occur in separate regions of the mass spectrometer but instead they all occur in the trap and are separated in time. An MS/MS (MS^2) experiment is performed by isolating an ion of interest and subjecting it to fragmentation or other reactions followed by ejection and detection of the product ions.[12] An MS^3 experiment involves isolation of one of the product ions from the MS^2 experiment and subjecting it to further reactions followed by detection. Repeating this process by adding additional stages of ion isolation followed by fragmentation or other reactions facilitates structural characterization of ions. In this dissertation, MS^n experiments involving collision-activated dissociation (CAD) and ion-molecule reactions are discussed.

2.3.3.1 <u>Ion Isolation</u>

A prerequisite to tandem mass spectrometric analysis is ion isolation. The LQIT achieves this by ramping RF voltage in conjunction with resonance ejection to remove all unwanted ions from the trap, leaving only the ion(s) of interest. As discussed above, increasing the main RF voltage causes the q_u value to increase for all ions. Ions of different m/z values possess different secular frequencies at a given RF voltage (equation 2.10). A graphical representation of the ion isolation process can be seen in Figure 2.13. First, the RF voltage is increased to give the ion of interest a q_u value of 0.830. This results in the ejection of many ions with lower m/z values than the ion of interest. Next, a broadband

waveform called the isolation waveform (tailored waveform) is used to excite all remaining ions via resonant ejection, with the exception of the ion of interest. This is accomplished in a Thermo Scientific LTQ by applying a $5 - 500$ kHz multi-frequency waveform with sine components spaced every 0.5 kHz, with a notch at $q_u = 0.830$, the q_u value of our ion of interest.[13] Immediately following isolation, the q_u value of the isolated ion(s) is adjusted to 0.250 (this may also be adjusted manually in the Xcalibur software) for MS/MS experiments.
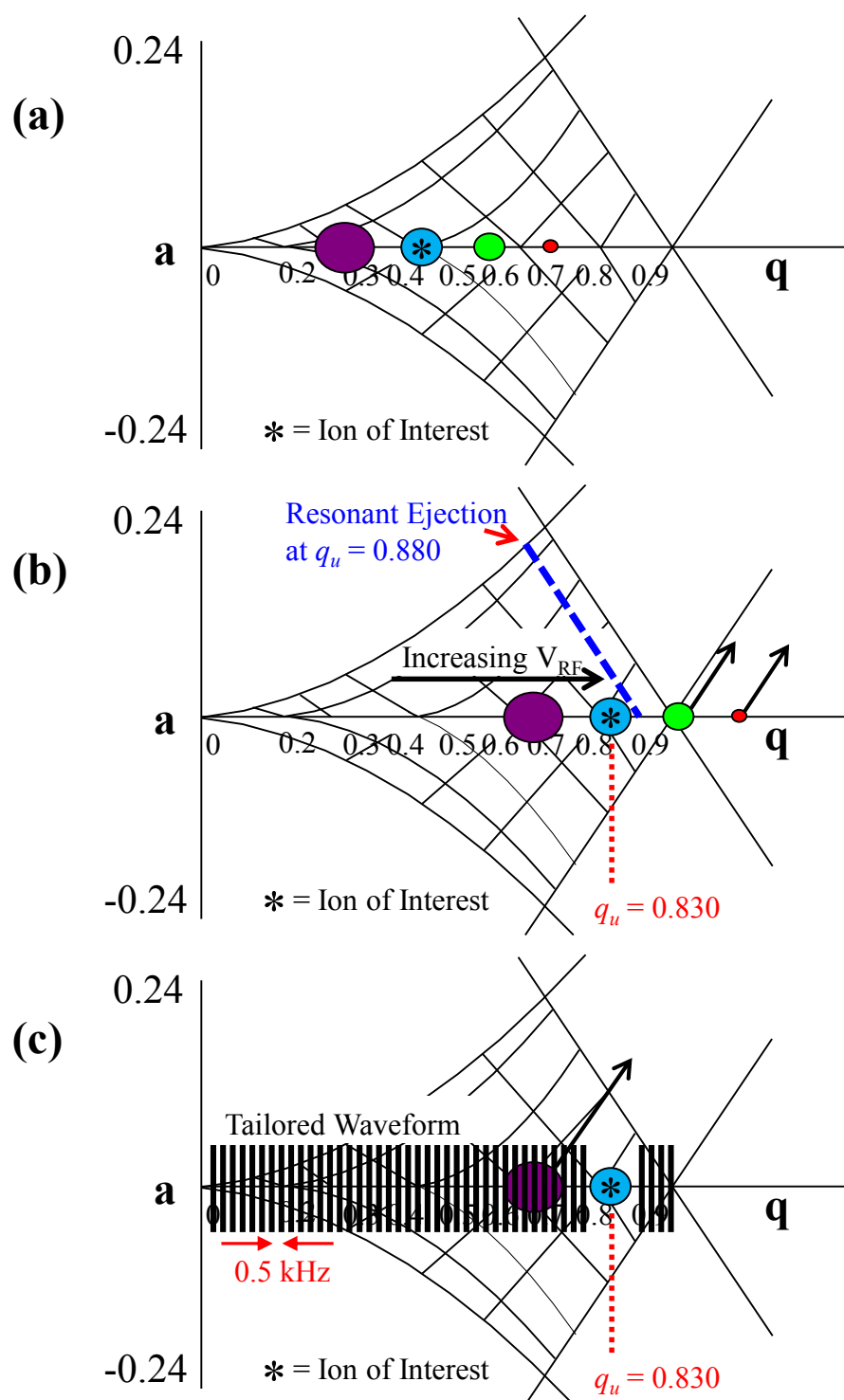
Figure 2.13 (a) Ions trapped in the LQIT. (b) Ramping the main RF voltage gives the ion of interest a q_u value of 0.830; many lower m/z ions are ejected from the LQIT. (c) A tailored waveform is applied that spans the secular frequencies of all ions except the ion of interest to eject all remaining unwanted ions from the trap.

2.3.3.2 <u>Collision-Activated Dissociation (CAD)</u>

Collision-activated dissociation in LQIT involves heating ions through multiple low energy inelastic collisions with the ever-present helium buffer gas in the trap.[56] CAD can be categorized into "slow" or "fast" regimes, dependent upon the rate that energy is deposited into the ion.[57] For the purposes of the work presented in this dissertation, only the "slow" heating method was used and, therefore, will be discussed further. By default, isolated ions are stored at a low q_u value of 0.250. The low q_u value is a compromise between efficient energy deposition for CAD and efficient trapping of product ions. Higher q_u values prevent low m/z ions (fragments) from being trapped. At a q_u value of 0.250, fragment ions with a m/z value approximately 25% of the precursor ion's m/z and lower will not be trapped. This is often referred to as the low-mass cutoff (LMCO). A supplementary RF voltage (typically <1 V peak-to-peak) at the secular frequency of the ion is applied to the x-rods for 30 ms (user defined) to increase the ion's kinetic energy by dipolar excitation. This is often referred to as a "tickle" voltage since the energy deposited is not enough to eject the ion. As the kinetic energy of the ion increases, it undergoes several energetic collisions with the helium buffer gas present in the trap. These collisions convert part of the ion's kinetic energy into internal energy (rovibrational energy). The internal energy of the ion increases gradually through multiple collisions until the dissociation threshold of the ion is met and the ion dissociates. Since only the secular frequency of the precursor ion is excited during resonance excitation, the product ions that are formed will not be excited further after fragmentation, which prevents further fragmentation of the fragment ions.

The Thermo Scientific LTQ also offers a feature to bypass the LMCO in CAD experiments, pulsed q collision-activated dissociation (PqCAD).[58] This activation method utilizes a larger q_u value (typically $q_u > 0.6$) and a greater RF voltage (~$1 - 2$ V) during excitation and a shorter activation time (typically 100 μs) than conventional CAD. Upon activation of the precursor ion, the main RF voltage is quickly dropped to a low value, lowering the q_u value as a result and thus trapping many of the lower m/z product ions. One consequence of PqCAD is that dissociation of the precursor ion is less efficient as a result of premature ejection of the precursor ion due to the larger tickle voltage used.[59]

2.3.4 Ion-Molecule Reactions

The use of gas-phase reactions between isolated ions and neutral molecules in tandem mass spectrometry has become a powerful technique for solving an array of complex analytical problems.[60-62] Ion-molecule reactions (IMRs) may occur readily in the gas-phase provided the kinetic energies of the ion and neutral molecule are sufficiently low to allow for a long-lived collision complex.[63] Gas-phase reactions occurring in mass spectrometers are unhindered by solvent and behave as isolated systems due to the high vacuum. This results in an energy profile that is different from those describing IMRs occurring in solution (Figure 2.14).

The Brauman double-well potential energy surface model can be used to describe IMRs occurring in the gas phase for both negative and positive ions.[64,65] An illustration of the double-well potential energy surface for a reaction between a neutral molecule and a positive ion can be seen in Figure 2.15. According to this model, IMRs proceed by formation of a reactant complex between the neutral molecule and the ion via ion-dipole

and ion-induced dipole forces (solvation energy).[66] The solvation energy afforded upon formation of the reactant complex may be sufficient to overcome barriers along the reaction coordinate leading to formation of products. Since the reaction is occurring in high vacuum, the total energy of the system is conserved, thus, the overall reaction must be exothermic to occur. The rates for these reactions are controlled by the difference in energy between the transition states and the separated reactants (ΔE). In solution, the potential energy of the system is lowered due to the solvation energy afforded by the presence of solvent (Figure 2.14). Ion-molecule reactions occurring in the gas phase are typically faster than those occurring in solution. This is partially a result of the higher concentration of molecules in the solution phase which may hinder the approach of reactants.

Another factor controlling the rates of gas-phase IMRs is the entropy of the transition state, as shown in Figure 2.15. For reactions where the orientation of the ion and neutral molecule is very specific, as is common for rearrangements involving ring-closure, the transition state is considered "tight" (low entropy) and may proceed slowly or not at all. Conversely, reaction pathways possessing a "loose" transition state have many available orientations to proceed to products, such as simple bond cleavages, thus, these reactions are entropically more favorable.

$$A + BC^+ \quad \underset{k_{-1}}{\overset{k_1}{\rightleftarrows}} \quad AB^+ + C$$

Solvation lowers energy of the system

[A----B----C]$^+$

Potential Energy

Separated Reactants

Separated Products

Reaction Coordinate
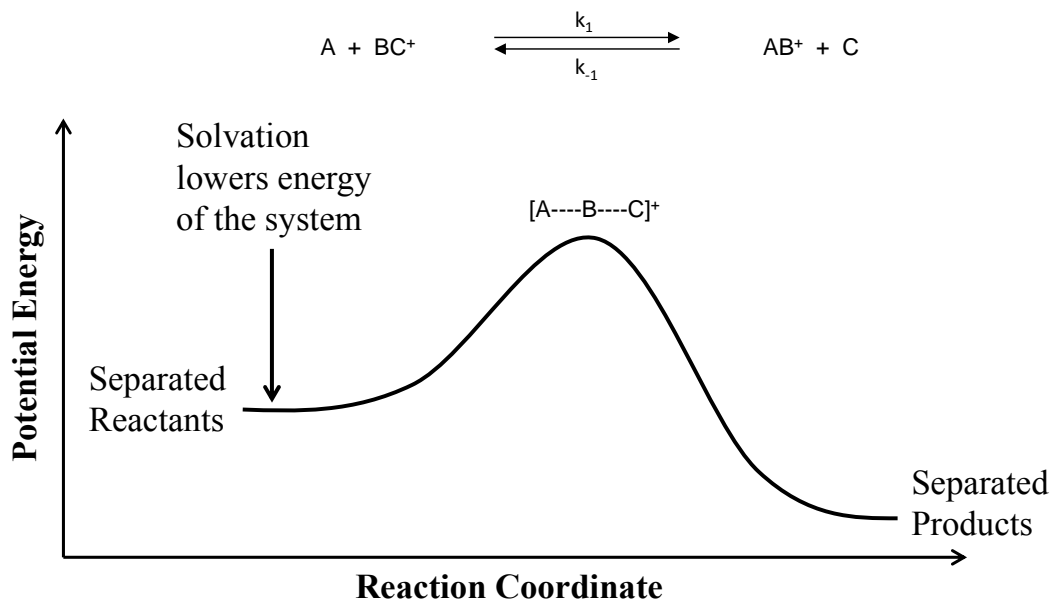
Figure 2.14 Potential energy surface for ion-molecule reactions occurring in solution. Solvation energy afforded by the presence of solvent lowers the energy of the separated reactants and products relative to that of the transition state.

$$A + BC^+ \underset{k_{-1}}{\overset{k_1}{\rightleftarrows}} A\text{----}BC^+ \underset{k_{-2}}{\overset{k_2}{\rightleftarrows}} AB^+\text{----}C \underset{k_{-3}}{\overset{k_3}{\rightleftarrows}} AB^+ + C$$

Separated Reactants

ΔE

Solvation Energy

[A----B----C]$^+$

Separated Products

Potential Energy

Reactant Complex

Product Complex

Reaction Coordinate
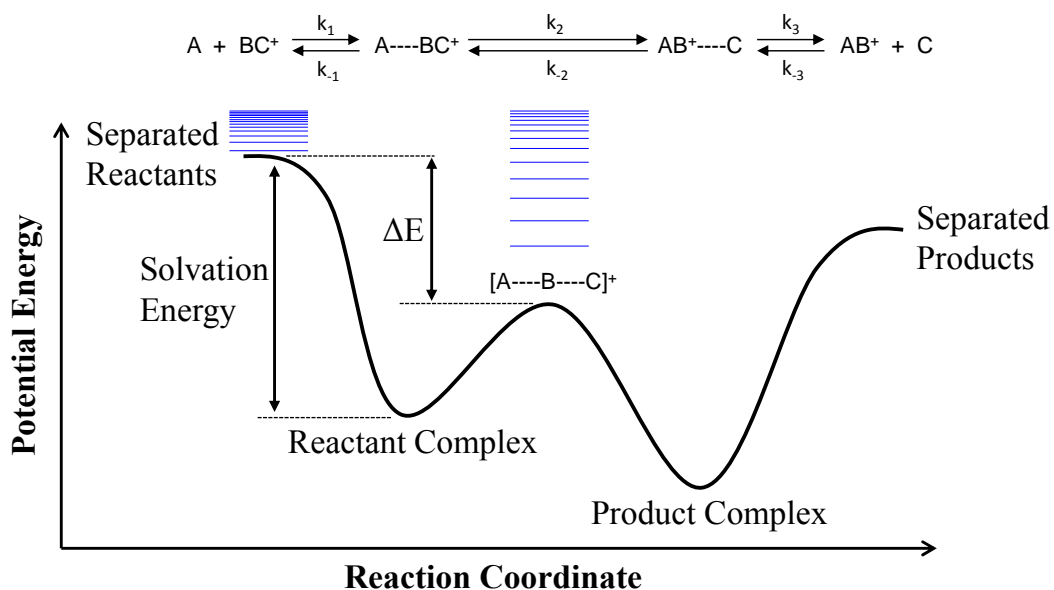
Figure 2.15 The Brauman double-well potential energy surface for a simple ion-molecule reaction in the gas phase, including an illustration of the energy-levels spacing for the transition state complex [A----B----C]$^+$ and separated reactants.

In order to study IMRs in the LQIT, a multiported pulsed valve reagent inlet system was developed during this thesis research.[67] A schematic of the pulsed valve inlet system is shown in Figure 2.16. In this setup, reagents were introduced into the ion trap by using series 9 pulsed valves mounted sequentially on stainless steel tubing. Each pair of pulsed valves was used for introducing a single reagent into the LQIT. The space in the tubing between the pair of pulsed valves behaves as a vacuum baffle. Each steel tube contains a tee connector with a Swagelok Ultra-Torr fitting, which houses a rubber septum for introducing reagents into the steel tubing. A vacuum valve (Figure 2.16) on the steel tube nearest to the space containing the reagent was opened to pump the reagent away after the completion of an experiment. The steel tube contains two pulsed valves (labeled 1 and 2; Figure 2.16), which are opened one at a time to introduce the reagent contained within the steel tube into the vacuum region of the LQIT. The valves were manually controlled using a waveform generator which sent an electronic signal to a pulse/delay generator. The pulse/delay generator controlled the timing and width of each pulsed valve event, which were optimized for each reagent. More volatile reagents required shorter pulses than reagents with high boiling points.

Reagents were introduced by first opening the pulsed valve nearest to the space in the steel tube containing the reagent (i.e., the steel tube between pulsed valve 1 and the vacuum valve as shown in Figure 2.16) for a set amount of time. This allows the reagent to flow into the space between the pair of pulsed valves (i.e., between valves 1 and 2). The amount of time the pulsed valve was open was determined by the width of the electronic pulse received by the pulsed valve driver from the pulse/delay generator. Next, the pulsed valve that interfaces with the LQIT (pulsed valve 2) was opened for a set amount of time

to allow the reagent to flow into the vacuum region of the LQIT where it can interact with ions in the trap.
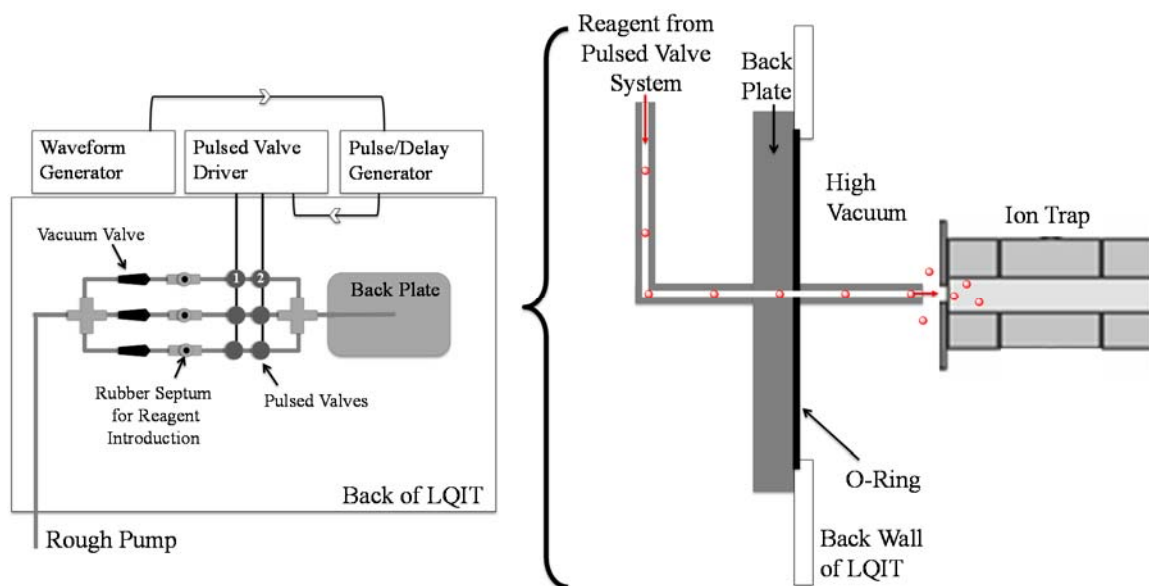
Figure 2.16 Pulsed valve reagent introduction system coupled with a LQIT.

2.3.5 High-Performance Liquid Chromatography/Mass Spectrometry (HPLC/MS)

Tandem mass spectrometry is a powerful method for studying mixtures; however, there are instances where prior separation of analytes is necessary, such as the analysis of isomers or complex mixtures. With the advent of atmospheric pressure ionization techniques, such as ESI and APCI, HPLC coupled with MS has become an important tool for structure elucidation of analytes in mixtures.[68,69] Additionally, coupling HPLC with mass spectrometry allows trace levels of analytes to be identified from mixtures without the need for sample preparation.

A Thermo Scientific Surveyor Plus HPLC system consisting of a quaternary pump, autosampler, thermostatted column compartment, and photodiode array (PDA) was used for the work presented in this dissertation. Analytes were separated using a reversed phase 300 X 7.8 mm Phenomenex Rezex ROA-organic acid analytical column that was maintained at 60 °C during the LC separation. A mobile phase consisting of 0.1% formic (v/v) in water was used for all separations. The volume of sample solution loaded onto the column was 25 μL. Separation was accomplished by using a flow rate of 400 μL min^{-1} and isocratic elution.

2.4 Density Functional Theory (DFT) Calculations

Density functional theory (DFT) is currently the most successful approach to calculating the electronic structures of molecules. DFT has found widespread application in the fields of chemistry, biology, and physics.[70-72] In chemistry, DFT can be used to predict molecular structures, vibrational frequencies, ionization energies, spin densities, reaction pathways, etc. In this dissertation, DFT was primarily used to predict minimum energy structures and transition state structures involved in a variety of chemical transformations occurring in the gas phase. The mechanisms of dissociation and rearrangement reactions of gas-phase ions may be elucidated with the use of DFT calculations. Furthermore, gas-phase ion-molecule reactions occurring between neutral molecules and ions can be studied mechanistically using DFT. A brief introduction to DFT functionals and basis sets is presented here with implications for performing DFT calculations that are chemically relevant for the systems being investigated in this thesis.

2.4.1 DFT Background

The main premise of DFT is that the energy of a molecule can be determined from its electron density. The theory was originally derived from two theorems[73] proved by Hohenberg and Kohn in 1964:

Theorem I: For any system of interacting particles in an external potential $V_{ext}(\vec{r})$, the density is uniquely determined (i.e., the external potential is a unique functional of the density $\rho(\vec{r})$).

Theorem II: A universal functional for the energy $E[\rho]$ can be defined in terms of the density such that:

$$\rho(\vec{r}) \geq 0 \quad and \quad \int \rho(\vec{r})\delta\vec{r} = N \tag{2.16}$$

therefore

$$E_0 \leq E[\rho] \tag{2.17}$$

where $E[\rho]$ is the energy functional deriving from the electron density. In other words, given the charge density, the Hamiltonian operator can be uniquely determined and with this the wave functions ψ of all states and all material properties can be calculated. Thus, the electron density determines the positions and charges of the nuclei and thus determines the Hamiltonian.

At the heart of DFT is the electron density. It is defined as the integral over the spin coordinates of all electrons and all spatial variables $(\vec{x} \equiv \vec{r}, s)$, with the exception of one:

$$\rho(\vec{r}) = N \int \dots \int |\Psi(\vec{x}_1, \vec{x}_2, \dots, \vec{x}_N)|^2 \, d\vec{x}_1 d\vec{x}_2 \dots d\vec{x}_N \tag{2.18}$$

Thus, the density function $\rho(\vec{r})$ determines the probability of finding N electrons within a volume $d\vec{r}$. The function $\rho(\vec{r})$ is non-negative and incorporates the three spatial variables which vanish at infinity and integrates to the total number of electrons N:

$$\rho(\vec{r} \to \infty) = 0 \qquad (2.19)$$

$$\int \rho(\vec{r})\delta\vec{r} = N \qquad (2.20)$$

For any particular atom, the gradient of $\rho(\vec{r})$ possesses a discontinuity resulting in a cusp at the atomic nucleus due to the unbounded electron-nucleus Coulomb potential[74]:

$$\lim_{r_iA \to 0} [\nabla_r + 2Z_A]\bar{\rho}(\vec{r}) = 0 \qquad (2.21)$$

where Z is the nuclear charge and $\bar{\rho}(\vec{r})$ is the spherical average of $\rho(\vec{r})$.

2.4.1.1 <u>Functionals</u>

As discussed above, the electron density can be used to determine the Hamiltonian from which the wave function can be determined and energy eigenvalues. However, solving the Schrödinger equation is challenging in most cases due to the electron-electron interaction term in the Hamiltonian. Thus, in 1965, Kohn and Sham[75] simplified the Hamiltonian operator by constructing it as a sum of one-electron operators representing a system of non-interacting electrons. Although such a system is fictitious since electrons do interact, it makes solving the Schrödinger equation easier and produces an overall ground state density that is identical to the same system where the electrons do interact. The

Hamiltonian for such a system is expressed as a sum of one-electron operators which have eigenfunctions that are Slater determinants of the one-electron eigenfunctions.[75] The total energy is expressed as a functional (a function of a function) of the charge density by

$$E[\rho] = T_S[\rho] + \int \delta r v_{ext}(r)\rho(r) + V_H[\rho] + E_{xc}[\rho] \qquad (2.22)$$

where T_s is the kinetic energy of the non-interacting electrons , derived from the Kohn-Sham orbitals, υ_{ext} is the external potential, V_H is the Hartree (Coulomb) energy, and E_{xc} is the exchange-correlation energy functional. E_{xc} includes the effects of quantum mechanical electron-electron repulsion, the kinetic energy difference between the fictitious non-interacting electron system and the real system of interacting electrons, and a correction for the classical self-interaction (interaction of an electron with itself) energy. DFT often makes a local approximation for the exchange-correlation energy functional $E_{xc}[\rho]$ which often gives inaccurate descriptions of the vibration frequencies, bond lengths, and atomization energies of molecules.[76] On the other hand, hybrid functionals provide a scheme for improving the accuracy of these molecular properties.

Hybrid functionals utilize a portion of the exact exchange energy from the self-consistent field exchange used in Hartree-Fock theory and combine it with *ab initio* calculations of the exchange-correlation energy.[77-80] A popular hybrid functional used for the work presented in this dissertation is the Becke 3-parameter Lee-Yang-Parr (B3LYP) functional. This method uses the Becke88[78] (B) exchange functional combined with the Lee-Yang-Parr[81] (LYP) correlation functional using a 3-parameter functional expression which smoothly converts the Kohn-Sham system of non-interacting electrons into the real

interacting system.[79] The B3LYP functional shows correct asymptotic behavior of the energy density at long range and LYP is designed to calculate the full correlation energy.

2.4.1.2 Basis Sets

A basis set is a set of mathematical functions (basis functions) from which the wave function is constructed.[82] In DFT calculations, molecular orbitals (MOs) are expressed as linear combinations of basis functions. The atomic orbitals (AOs) used to construct the MOs are described effectively with Slater-type orbitals[83] (STOs) since they correctly exhibit the exponential decay of electron density with distance and the appropriate radial shape near the atomic nucleus. However, STOs are computationally laborious. As a result, the advent of approximating the STOs using a linear combination of Gaussian-functions, called primitives, became a common practice due to the ease at which they can be calculated.[84] This led to a large reduction in computational cost.[85] The linear combination of Gaussian primitives (functions) to approximate the AO is described as a "contracted" basis function. The molecular orbitals are then formed as a linear combination of AOs ϕ by

$$\varphi_i = \sum_{k=1}^{n} c_k \, \phi_k \tag{2.23}$$

where φ_i represents the i-th molecular orbital, c_k is the coefficients for the k-th AO, and ϕ_k is the k-th AO for n number of orbitals. Utilizing a similar contraction scheme, the AOs are formed as a linear combination of Gaussian functions by

$$\phi_k = \sum_{w=1}^{b} d_{wy} g_w \tag{2.24}$$

where the constants d_{wy} are the contraction coefficients and g_w are the Gaussian functions used to construct the AOs. One of the first minimal basis sets to come from this type of contraction scheme was STO-3G (Slater-type orbital-3 Gaussians). STO-3G uses a linear combination of three Gaussian primitives to approximate the Slater-type orbital which itself is an approximation of the AO. For lithium, this would imply two functions (1s and 2s), each constructed as a linear combination of three Gaussians. As an example, the 1s AO of lithium would be expressed by

$$\phi_{1s} = \sum_{w=1}^{b} d_{w,1s} g_w \tag{2.25}$$

where

$$g_w = \left(\frac{2}{\pi}\right)^{\frac{3}{4}} \alpha_w^{3/4} e^{-\alpha_w r^2} \tag{2.26}$$

is the 1s Gaussian function and b is the number of Gaussians used in the contraction. With the addition of more Gaussians, the approximation of the atomic orbitals is improved. However, a better method to approximate the shapes of the AOs is to 'decontract' these contracted basis sets by adding more Gaussian primitives to each STO (basis function). A basis set that incorporates two basis functions for each AO with each function comprised

of N Gaussian primitives is called a double-ζ (double-zeta) basis set. A basis set constructed of three basis functions is called a triple- ζ basis set and so forth. The advantage of multiple-ζ basis sets is that with increasingly larger basis sets composed of many basis functions, the approximation of the wave function improves and thus, the accuracy of the calculation.

In terms of chemical bonding, the valence shell orbitals have the highest variability and are the most influential in bond formation. For this reason, split-valence basis sets were developed to add more flexibility to the valence shell orbitals. For these basis sets, the core orbitals are comprised of a single basis function while the valence orbitals are comprised of multiple basis functions. Some of the most popular split-valence basis sets were developed by John Pople and coworkers.[86] These include the widely used 3-21G, 6-31G, and 6-311G basis sets. The contraction scheme for the 6-311G basis set for approximating the AOs of lithium can be seen in Figure 2.17.
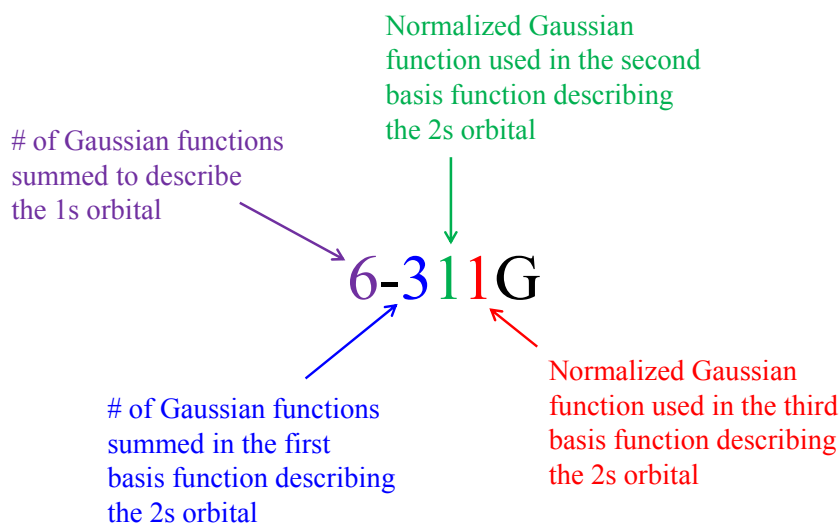
Figure 2.17 Notation for the 6-311G basis set used to approximate the AOs of lithium.

Split valence basis sets describe molecular bonding more accurately by allowing the electron density to modify its spatial extent more appropriately for a particular chemical environment. The contracted minimum basis sets do not offer this kind of flexibility which is why only split basis sets were used for the work presented in this dissertation.

2.5 <u>References</u>

1.   Goodlett, D. R.; Gale, D. C.; Guiles, S.; Crowther, J. B. In *Encyclopedia of Analytical Chemistry*; John Wiley & Sons, Ltd: 2006.

2.   Finehout, E. J.; Lee, K. H. *Biochem. Mol. Biol. Educ.* **2004**, *32*, 93.

3.   Marshall, A. G.; Rodgers, R. P. *Proc. Natl. Acad. Sci. U. S. A.* **2008**, *105*, 18090.

4.   Mullins, O. C.; Sheu, E. Y.; Hammami, A.; Marshall, A. G. *Asphaltenes, Heavy Oils, and Petroleomics*; 1 ed.; Springer, 2007.

5.   McLuckey, S. A.; Wells, J. M. *Chem. Rev.* **2001**, *101*, 571.

6.   Klein, G. C.; Kim, S.; Rodgers, R. P.; Marshall, A. G.; Yen, A.; Asomaning, S. *Energy Fuels* **2006**, *20*, 1965.

7.   Zechel, D. L.; Konermann, L.; Withers, S. G.; Douglas, D. J. *Biochemistry* **1998**, *37*, 7664.

8.   Pappin, D. J. C.; Hojrup, P.; Bleasby, A. J. *Curr. Biol.*, *3*, 327.

9.   Jarrell, T. M.; Marcum, C. L.; Sheng, H.; Owen, B. C.; O'Lenick, C. J.; Maraun, H.; Bozell, J. J.; Kenttamaa, H. I. *Green Chem.* **2014**, *16*, 2713.

10.   Amundson, L. M.; Eismin, R. J.; Reece, J. N.; Fu, M.; Habicht, S. C.; Mossman, A. B.; Shea, R. C.; Kenttämaa, H. I. *Energy Fuels* **2011**, *25*, 3212.

11.   Watkins, M.; Winger, B.; Shea, R.; Kenttämaa, H. *Anal. Chem.* **2005**, *77*, 1385.

12.   de Hoffmann, E. *J. Mass Spectrom.* **1996**, *31*, 129.

13.   Schwartz, J. C.; Senko, M. W.; Syka, J. E. *J. Am. Soc. Mass Spectrom.* **2002**, *13*, 659.

14.   Hager, J. W. *Rapid Commun. Mass Spectrom.* **2002**, *16*, 512.

15.   Dempster, A. J. *Phys. Rev.* **1918**, *11*, 316.

16.   Vestal, M. L. *Chem. Rev.* **2001**, *101*, 361.

17.   Munson, M. S. B.; Field, F. H. *J. Am. Chem. Soc.* **1966**, *88*, 2621.

18.   Munson, B. *Int. J. Mass Spectrom.* **2000**, *200*, 243.

19.   Barber, M.; Bordoli, R. S.; Sedgwick, R. D.; Tyler, A. N. *J. Chem. Soc., Chem. Commun.* **1981**, 325.

20.   Karas, M.; Hillenkamp, F. *Anal. Chem.* **1988**, *60*, 2299.

21.   Fenn, J. B.; Fau, M. M.; Fau, M. C.; Fau, W. S.; Whitehouse, C. M. *Science* **1989**, *246*, 64.

22.   Carroll, D. I.; Dzidic, I.; Stillwell, R. N.; Haegele, K. D.; Horning, E. C. *Anal. Chem.* **1975**, *47*, 2369.

23.   Gross, J. In *Mass Spectrometry*; Springer Berlin Heidelberg: 2011, p 249.

24.   Owen, B. C.; Gao, J.; Borton, D. J.; Amundson, L. M.; Archibold, E. F.; Tan, X.; Azyat, K.; Tykwinski, R.; Gray, M.; Kenttämaa, H. I. *Rapid Commun. Mass Spectrom.* **2011**, *25*, 1924.

25.   Kebarle, P.; Verkerk, U. H. *Mass Spectrom. Rev.* **2009**, *28*, 898.

26.   Harrison, A. G. *Chemical Ionization Mass Spectrometry*; CRC press, 1992.

27.   Taylor, G. *Proc. R. Soc. A* **1964**, *280*, 383.

28.   Taylor, G. *Proc. R. Soc. A* **1965**, *291*, 145.

29.   Taylor, G. *Proc. R. Soc. A* **1969**, *313*, 453.

30.   Rayleigh, L. *Philos. Mag.* **1882**, *14*, 184.

31.   Gomez, A.; Tang, K. *Phys. Fluids* **1994**, *6*, 404.

32.   Marginean, I.; Znamenskiy, V.; Vertes, A. *J. Phys. Chem. B* **2006**, *110*, 6397.

33.   Znamenskiy, V.; Marginean, I.; Vertes, A. *J. Phys. Chem. A* **2003**, *107*, 7406.

34.   Cole, R. B. *J. Mass Spectrom.* **2000**, *35*, 763.

35.   Kerbarle, P.; Peschke, M. *Anal. Chim. Acta* **2000**, *406*, 11.

36.   Thomson, B. A.; Iribarne, J. V. *J. Chem. Phys.* **1979**, *71*, 4451.

37.   Dole, M.; Mack, L. L.; Hines, R. L.; Mobley, R. C.; Ferguson, L. D.; Alice, M. B. *J. Chem. Phys.* **1968**, *49*, 2240.

38.   Whitehouse, C. M.; Dreyer, R. N.; Yamashita, M.; Fenn, J. B. *Anal. Chem.* **1985**, *57*, 675.

39.   Palmblad, M.; Ramström, M.; Markides, K. E.; Håkansson, P.; Bergquist, J. *Anal. Chem.* **2002**, *74*, 5826.

40.   Peschke, M.; Verkerk, U. H.; Kebarle, P. *J. Am. Soc. Mass Spectrom.* **2004**, *15*, 1424.

41.   Loo, J. A. *Mass Spectrom. Rev.* **1997**, *16*, 1.

42.   Sunner, J.; Nicol, G.; Kebarle, P. *Anal. Chem.* **1988**, *60*, 1300.

43.   Weston, D. J. *Analyst* **2010**, *135*, 661.

44.   Kostiainen, R.; Kaupilla, T. J. *J. Chromatogr. A* **2009**, *1216*, 685.

45.   March, R. E. *J. Mass Spectrom.* **1997**, *32*, 351.

46.   March, R. E. *Quadrupole Ion Trap Mass Spectrometry*; Wiley: Hoboken, N.J., 2005.

47.   Syka, J. E. P.; Marto, J. A.; Bai, D. L.; Horning, S.; Senko, M. W.; Schwartz, J. C.; Ueberheide, B.; Garcia, B.; Busby, S.; Muratore, T.; Shabanowitz, J.; Hunt, D. F. *J. Proteome Res.* **2004**, *3*, 621.

48.   Makarov, A.; Denisov, E.; Kholomeev, A.; Balschun, W.; Lange, O.; Strupat, K.; Horning, S. *Anal. Chem.* **2006**, *78*, 2113.

49.   Bier, M. E.; Syka, J. E. P. U.S., 1995.

50.   March, R. E. *Int. J. Mass Spectrom. Ion Proc.* **1992**, *118-119*, 71.

51.   Todd, J. F. *Mass Spectrom. Rev.* **1991**, *10*, 3.

52.   Stafford, G. C.; Kelley, P. E.; Syka, J. E. P.; Reynolds, W. E.; Todd, J. F. J. *Int. J. Mass Spectrom. Ion Proc.* **1984**, *60*, 85.

53.   Stafford Jr, G. C.; Kelley, P. E.; Syka, J. E. P.; Reynolds, W. E.; Todd, J. F. J. *Int. J. Mass Spectrom. Ion Proc.* **1984**, *60*, 85.

54.   Kaiser Jr, R. E.; Graham Cooks, R.; Stafford Jr, G. C.; Syka, J. E. P.; Hemberger, P. H. *Int. J. Mass Spectrom. Ion Proc.* **1991**, *106*, 79.

55. Williams, J. D.; Cox, K. A.; Cooks, R. G.; McLuckey, S. A.; Hart, K. J.; Goeringer, D. E. *Anal. Chem.* **1994**, *66*, 725.

56. McLuckey, S. A. *J. Am. Soc. Mass Spectrom.* **1992**, *3*, 599.

57. Sleno, L.; Volmer, D. A. *J. Mass Spectrom.* **2004**, *39*, 1091.

58. Schwartz, J. C.; Syka, J. E.; Quarmby, S. T. *Proceedings Amer. Soc. MS, San Antonio, Texas* **2005**.

59. Murrell, J.; Despeyroux, D.; Lammert, S.; Stephenson Jr, J.; Goeringer, D. *J. Am. Soc. Mass Spectrom.* **2003**, *14*, 785.

60. Brodbelt, J. S. *Mass Spectrom. Rev.* **1997**, *16*, 91.

61. Osburn, S.; Ryzhov, V. *Anal. Chem.* **2012**, *85*, 769.

62. Gronert, S. *Chem. Rev.* **2001**, *101*, 329.

63. Gislason, E.; Mahan, B. H.; Tsao, C. W.; Werner, A. S. *J. Chem. Phys.* **1969**, *50*, 5418.

64. Brauman, J. I. *J. Mass Spectrom.* **1995**, *30*, 1649.

65. Moylan, C.; Brauman, J.; Hase, W.; JAI Press Inc: New York: 1994.

66. Bowers, M. T. *Gas Phase Ion Chemistry*; Academic Press, 1979; Vol. 1.

67. Jarrell, T.; Riedeman, J.; Carlsen, M.; Replogle, R.; Selby, T.; Kenttämaa, H. *Anal. Chem.* **2014**, *86*, 6533.

68. Thomson, B. A. *J. Am. Soc. Mass Spectrom.* **1998**, *9*, 187.

69. Ermer, J.; Vogel, M. *Biomed. Chromatogr.* **2000**, *14*, 373.

70. Laird, B. B.; Ross, R. B.; Ziegler, T. **1996**.

71. Causá, M.; Putz, M. V.; Mingos, D. *Applications of Density Functional Theory to Biological and Bioinorganic Chemistry*; Springer, 2013.

72. Tozer, D. J.; Peach, M. J. G. *Phys. Chem. Chem. Phys.* **2014**, *16*, 14333.

73. Hohenberg, P.; Kohn, W. *Phys. Rev.* **1964**, *136*, B864.

74. Kato, T. *Commun. Pur. Appl. Math.* **1957**, *10*, 151.

75.   Kohn, W.; Sham, L. J. *Phys. Rev.* **1965**, *140*, A1133.

76.   Perdew, J. P.; Ernzerhof, M.; Burke, K. *J. Chem. Phys.* **1996**, *105*, 9982.

77.   Becke, A. D. *J. Chem. Phys.* **1996**, *104*, 1040.

78.   Becke, A. D. *Phys. Rev. A* **1988**, *38*, 3098.

79.   Becke, A. D. *J. Chem. Phys.* **1993**, *98*, 5648.

80.   Becke, A. D. *J. Chem. Phys.* **1993**, *98*, 1372.

81.   Lee, C.; Yang, W.; Parr, R. G. *Phys. Rev. B* **1988**, *37*, 785.

82.   Cramer, C. *Essentials of Computational Chemistry: Theories and Models*; John Wiley & Sons, 2004.

83.   Slater, J. C. *Phys. Rev.* **1930**, *36*, 57.

84.   Boys, S. F. *Proc. R. Soc. A* **1950**, *200*, 542.

85.   Krishnan, R.; Binkley, J. S.; Seeger, R.; Pople, J. A. *J. Chem. Phys.* **1980**, *72*, 650.

86.   Ditchfield, R.; Hehre, W. J.; Pople, J. A. *J. Chem. Phys.* **1971**, *54*, 724.

CHAPTER 3. SYNTHESIS OF ASPHALTENE MODEL COMPOUNDS AND ^{2}H-
AND ^{13}C-LABELED DERIVATIVES OF DIPHENYLMETHANE

3.1 <u>Introduction</u>

A useful approach to characterizing individual unknown constituents within complex

mixtures by mass spectrometry is to study the fragmentation behavior of ions of relevant

model compounds with known structures and compare this to the fragmentation behavior

of analyte ions isolated from the ionized sample of interest.[1] Appreciable agreement

between the fragmentation behavior of the analyte ion and the ionized model compound

may indicate that specific functional groups within the model structure are also present in

the analyte ion of interest. This requires an ionization method be used that is capable of

ionizing the sample and model compound. A valid ionization method must produce one

ion type containing the intact analyte molecule without aggregation or fragmentation for

all analytes present in order to yield a mass spectrum free of convolution.[2]

When specific model compounds are not readily available, synthesis is required. This

chapter discusses the synthesis procedures used to produce a multitude of asphaltene model

compounds and ^{2}H- and ^{13}C-labeled derivatives of diphenylmethane used in the CAD

experiments discussed in chapters 7 and 8 of this dissertation, respectively.

3.2 General Experimental Conditions

Most of the commercially available reagents were obtained from Sigma-Aldrich (St. Louis, MO) or Alfa Aesar (Ward Hill, MA) and used as received. The synthesized compounds were purified by column chromatography on a Teledyne Isco CombiFlash® Rf200 chromatography system equipped with a photo-diode array detector, capable of measuring UV-vis absorbance in the 200-780 nm wavelength range. Normal-phase silica gel was used for all separations. New compounds were characterized by ^{1}H NMR, ^{13}C NMR, and high resolution mass spectrometry (HRMS). The melting point range was measured for all solid compounds. Thin-layer chromatography (TLC) was used to monitor the progress of reactions. UV light (254 nm) was used to visualize components on the developed TLC plates. $CDCl_3$ (Cambridge Isotope Laboratories) was used as the NMR solvent. NMR spectra were acquired on a Bruker ARX (at 400 MHz for ^{1}H and 100 MHz for ^{13}C) instrument and the chemical shifts are reported relative the residual solvent peak. The spectra data are reported using the following format: chemical shift (δ) (multiplicity, J values in Hz, integration). The following abbreviations were used to describe the multiplicity: s = singlet, d = doublet, t = triplet, quin = quintet, sex = sextet, dd = doublet of doublets, dt = doublet of triplets, m = multiplet. High resolution mass spectra are reported in units of m/z and were acquired on an LTQ-Orbitrap XL. Mass (M) resolution (R) for these measurements was 30000 (M/ΔM). Samples were dissolved in carbon disulfide (CS_2) solvent and ionized by APCI operating in positive ion mode to yield the molecular ion ($M^{+\bullet}$) which was observed for all model compounds.

3.3 <u>Synthesis of Asphaltene Model Compounds</u>

Asphaltenes are the heaviest fraction of crude oil whose structural elucidation has proven difficult. They are a complex mixture of aromatic hydrocarbons that are not easily separated. Thus, the model compound approach is a useful strategy for deducing detailed molecular-level characteristics of asphaltenes. However, the lack of commercially available asphaltene model compounds necessitates synthesis. A total of 11 asphaltene model compounds were synthesized according to the procedures described below. Figure 3.1 shows the structures and labels for each of the synthesized asphaltene model compounds studied in Chapter 7 of this dissertation.
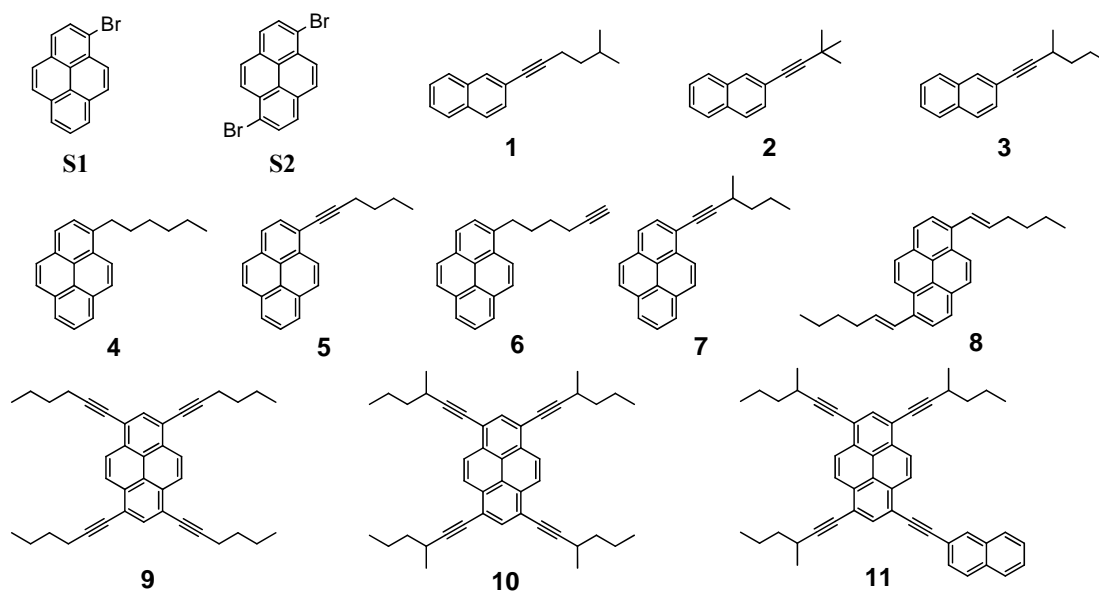
Figure 3.1 Synthesized precursors **S1** and **S2** and asphaltene model compounds **1-11**.

Procedure 1. General procedure for the Sonagashira[3] cross-coupling reaction. A 1:1 mixture of THF/diisopropylamine (20 mL) was added to a 200 mL round bottom three-neck flask equipped with a magnetic stirring bar. Argon was bubbled through the mixture for 20 minutes while stirring. Aryl bromide (0.72 mmol), PPh₃ (80 mg, 0.31 mmol), Pd(PPh₃)₄ (116 mg, 0.10 mmol), CuI (18 mg, 0.09 mmol), and alkyne (1.10 mmol) were added to the mixture and refluxed for 12 hours. The mixture was cooled to room temperature and diluted with 10 mL of chloroform. The reaction mixture was washed with 10 mL of a 10 % HCl aqueous solution and then washed twice with 10 mL of a saturated NaCl solution. The organic phase was dried over Na₂SO₄ and placed under vacuum to remove solvent. The crude product was eluted through a column of silica gel with a 9:1 hexanes/EtOAc solvent mixture to afford the cross-coupled product.
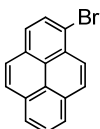
S1

Compound S1. A 500 mL round bottom flask was charged with pyrene (1 g, 4.944 mmol), dichloromethane (100 mL), and a magnetic stirring bar. The reaction vessel was equipped with a dripping column containing bromine (204 μL, 3.961 mmol) dissolved in dichloromethane (40 mL). The solution was stirred vigorously at room temperature while the bromine in dichloromethane solution was added drop wise over the course of 5 hours. The reaction was stirred at room temperature for 3 days. Solvent was removed under vacuum and the solid product was recrystallized in a minimum amount of ethanol to afford compound **S1** as a brown solid (1.13 g, 81% yield). ¹H NMR δ (CDCl₃): 8.35 (d, J = 9.2

Hz, 1H); 8.16-8.12 (m, 2H); 8.07 (d, J = 9.6 Hz, 1H); 8.01 (d, J = 6.8 Hz, 1H); 7.98-7.89 (m, 3H). ^{13}C NMR δ (CDCl$_3$): 131.2, 131.0, 130.6, 130.1, 129.7, 129.0, 127.8, 127.5, 127.1, 126.5, 126.0, 125.8, 125.6, 125.5, 125.0, 124.1, 120.0.

S2
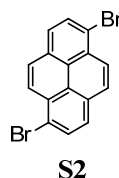
Compound S2. To a 500 mL three-neck round bottom flask equipped with an overhead stirrer was added pyrene (7.7 g, 38.1 mmol) dissolved in dichloromethane (300 mL). A dripping column containing bromine (12.2 g, 76.3 mmol) dissolved in dichloromethane (50 mL) was affixed to the reaction vessel. The pyrene solution was vigorously stirred while bromine solution was added drop wise over the course of 2 days. The reaction mixture was stirred another 2 days and then placed under vacuum to remove solvent. The crude product was recrystallized in a minimum amount of toluene to afford 1,6- and 1,8-dibromopyrene (**S2**) as a mixture of isomers (12.7 g, 93% yield). ^{1}H NMR δ (CDCl$_3$): 8.54 (s, 1H); 8.47 (d, J = 9.2 Hz, 1H); 8.26 (d, J = 8 Hz, 2H); 8.10 (d, J = 8.8 Hz, 1H); 8.03 (d, J = 8.4 Hz, 3H). ^{13}C NMR δ (CDCl$_3$): 131.03, 131.00, 128.88, 127.90, 127.83, 126.64, 126.35, 126.15, 121.08.
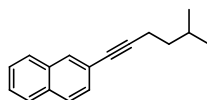
1

Compound 1. (New compound) A 1:1 mixture of THF/diisopropylamine (20 mL) was added to a 200 mL round bottom three-neck flask equipped with a magnetic stir bar. Argon was bubbled through the mixture for 20 minutes while stirring. 2-Bromonaphthalene (150 mg, 0.72 mmol), PPh$_3$ (80 mg, 0.31 mmol), Pd(PPh$_3$)$_4$ (68 mg, 0.10 mmol), CuI (18 mg, 0.09 mmol), and 5-methyl-1-hexyne (145 μL, 1.10 mmol) were added to the mixture and refluxed for 12 hours. The mixture was cooled to room temperature and diluted with 10 mL of chloroform. The reaction mixture was washed with 10 mL of a 10 % HCl aqueous solution and then washed twice with 10 mL of a saturated NaCl solution. The organic phase was dried over Na$_2$SO$_4$ and solvent evaporated under vacuum. The crude product was eluted through a column of silica gel with a 9:1 hexanes/EtOAc solvent mixture to yield a pale yellow oil (134 mg, 83 % yield). ^{1}H NMR δ (CDCl$_3$): 7.89 (s, 1H); 7.73 (m, 3H); 7.43 (m, 3H); 2.45 (t, J = 7.2 Hz, 2H); 1.79 (quin, J = 6.8 Hz, 1H); 1.53 (q, J = 7.2 Hz, 2H); 0.95 (d, J = 6.8 Hz, 6H). ^{13}C NMR δ (CDCl$_3$): 133.2, 132.6, 131.1, 128.9, 127.9, 127.7, 126.4, 126.3, 121.6, 91.0, 80.9, 37.9, 27.5, 22.4, 17.7. HRMS-APCI (R=30000) (m/z): [M$^{+\bullet}$] calcd for C$_{17}$H$_{18}$, 222.1409; found 222.1402.
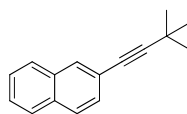
2

Compound 2. (New compound) The same general procedure used for synthesis of compound **1** was used for producing compound **2**. Compound **2** was produced as a pale

yellow solid (131 mg, 87 % yield). ^{1}H NMR δ (CDCl$_3$): 7.89 (s, 1H); 7.73 (m, 3H); 7.43 (m, 3H); 1.35 (s, 9H). ^{13}C NMR δ (CDCl$_3$): 133.2, 132.5, 131.1, 129.0, 127.8, 127.8, 127.7, 126.4, 126.3, 121.6, 99.0, 79.5, 31.2, 28.2. HRMS-APCI (*R*=30000) (m/z): [M$^{+•}$] calcd for C$_{16}$H$_{16}$, 208.1252; found 208.1246. Melting point range: 63-65 °C.

3
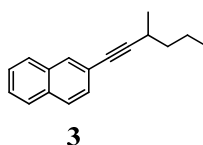
Compound 3. (New compound) The same general procedure used for synthesis of compound **1** was used for producing compound **3**. Compound **3** was produced as a viscous yellow oil (129 mg, 80 % yield). ^{1}H NMR δ (CDCl$_3$): 7.90 (s, 1H); 7.74 (m, 3H); 7.44 (m, 3H); 2.70 (sex, *J* = 6.4 Hz, 1H); 1.52 (m, 4H); 1.28 (d, *J* = 6.8 Hz, 3H); 0.97 (t, *J* = 6.4 Hz, 3H). ^{13}C NMR δ (CDCl$_3$): 133.2, 132.6, 131.1, 129.0, 127.9, 127.8, 127.7, 126.4, 126.3, 121.6, 95.4, 81.1, 39.4, 26.5, 21.3, 20.8, 14.1. HRMS-APCI (*R*=30000) (m/z): [M$^{+•}$] calcd for C$_{17}$H$_{18}$, 222.1409; found 222.1402.

4
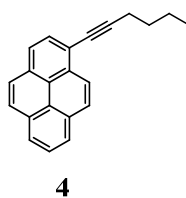
Compound 4. (New compound) Procedure 1 was used for synthesis of compound **4** from 1-bromopyrene. Compound **4** was produced as a yellow oil (209 mg, 73 % yield). ^{1}H NMR δ (CDCl$_3$): 8.53 (d, *J* = 9.2 Hz, 1H); 8.03 (m, 8H); 2.64 (t, *J* = 7.2 Hz, 2H); 1.74 (quin, *J*

= 6.8 Hz, 2H); 1.60 (sex, J = 7.2 Hz, 2H); 1.01 (t, J = 7.2 Hz, 3H). ^{13}C NMR δ (CDCl$_3$): 131.9, 131.4, 131.2, 130.7, 129.7, 128.0, 127.7, 127.3, 126.2, 125.5, 125.4, 124.6, 124.5, 124.5, 119.0, 96.5, 79.7, 31.2, 22.3, 19.8, 13.9. HRMS-APCI (R=30000) (m/z): [M$^{+\bullet}$] calcd for C$_{22}$H$_{18}$, 282.1409; found 282.1405.
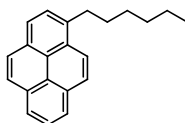
5

Compound 5. In a 50 mL round bottom three-neck flask were added a 1:1 mixture of Et$_2$O/methanol (10 mL), compound **4** (50 mg, 0.177 mmol), and Pd/C (10 wt % on C) (10 mg). The reaction flask was fixed with a hydrogen balloon and vacuum line connected via a flow adapter. Five purge/vacuum cycles were performed and then the mixture was stirred under hydrogen atmosphere for 12 hours at room temperature. The reaction mixture was filtered through celite to remove the catalyst and solvent evaporated under vacuum to yield **5** as a tan solid (50 mg, 99 % yield). ^{1}H NMR δ (CDCl$_3$): 8.26 (d, J = 9.6 Hz, 1H); 8.13 (m, 2H); 8.07 (m, 2H); 7.98 (m, 3H); 7.84 (d, J = 8.0 Hz, 1H); 3.31 (t, J = 7.6 Hz, 2H); 1.83 (quin, J = 8.0 Hz, 2H); 1.47 (m, 2H); 1.33 (m, 4H); 0.89 (t, J = 7.2 Hz, 3H). ^{13}C NMR δ (CDCl$_3$): 137.5, 131.6, 131.1, 129.8, 128.7, 127.7, 127.4, 127.2, 126.6, 125.9, 125.2, 124.9, 124.7, 123.7, 33.8, 32.1, 32.0, 29.7, 22.8, 14.3. HRMS-APCI (R=30000) (m/z): [M$^{+\bullet}$] calcd for C$_{22}$H$_{22}$, 286.1722; found 286.1722. Melting point range: 95-96 °C.
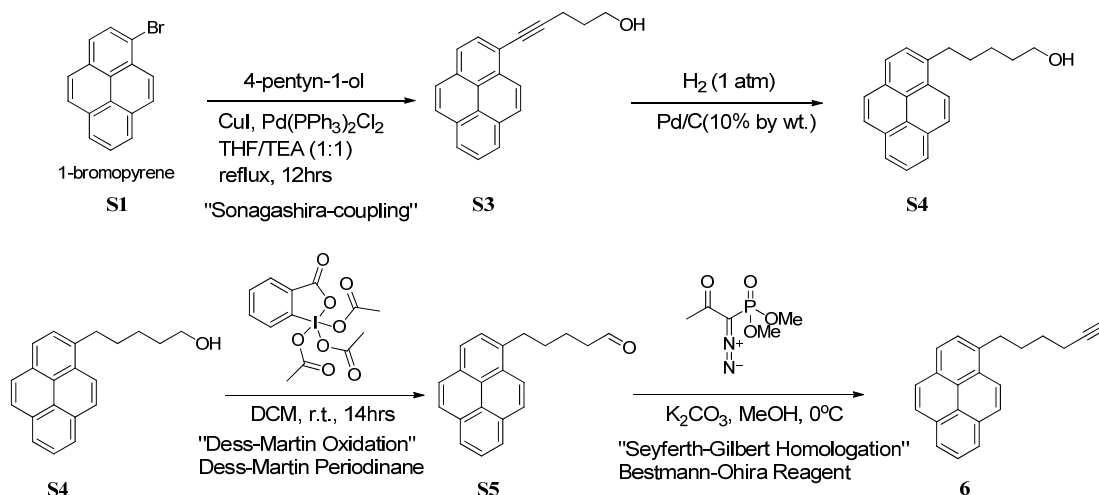
Scheme 3.1 Synthesis of compound **6**

Compound 6. (New compound) To a solution of 1-bromopyrene (**S1**) (250 mg, 0.889 mmol) and THF/TEA (1:1) (20 mL) were added Pd(PPh₃)₂Cl₂ (83 mg, 0.118 mmol), CuI (23 mg, 0.121 mmol), PPh₃ (31 mg, 0.118 mmol), and 4-pentyn-1-ol (124 µL, 1.631 mmol). The reaction mixture was refluxed for 12 hours while stirring. The mix was then cooled to room temperature and diluted with 10 mL chloroform. The resulting mixture was washed with 10 mL of a 10% HCl aqueous solution and washed twice with a saturated NaCl solution. The organic phase was dried over Na₂SO₄ and solvent evaporated under vacuum. The crude product was eluted through a column of silica gel with a 3:1 hexane/EtOAc solvent mixture and solvent evaporated under vacuum to yield **S3** as a brown solid (204 mg, 81 % yield). **S3** was immediately added to a 1:1 Et₂O/methanol (20 mL) mixture containing Pd/C (10 wt % on C) (35 mg). **S3** was hydrogenated according the procedure described above (synthesis of compound **5**) to yield **S4** as a light brown solid (207 mg, quantitative). A solution of **S4** (262 mg, 0.908 mmol) and dichloromethane (20 mL) was cooled to 0 °C and then charged with Dess-Martin periodinane (539 mg, 1.271 mmol) for

the Dess-Martin[4] oxidation. The reaction mixture was slowly allowed to reach room temperature while stirring for 14 hours. To this solution was added 10 mL of a 5 mmol NaCO$_3$ solution. The product was extracted with chloroform. The organic phase was poured over sodium thiosulfate and solvent evaporated under vacuum to yield **S5** as a yellow solid (260 mg, quantitative). **S5** was immediately added to a methanol (20 mL) solution containing Ohira-Bestmann reagent (163 μL, 1.088 mmol) and K$_2$CO$_3$ (251 mg, 1.816 mmol) for the Seyferth-Gilbert homologation reaction.[5,6] The reaction mixture was stirred at room temperature for 8 hours and then extracted with ether. Solvent was removed under vacuum and the crude product was eluted through a column of silica gel by using a 9:1 hexane/EtOAc solvent mixture. The purified product was evaporated under vacuum to yield compound **6** as a white solid (118 mg, 46 % yield). ^{1}H NMR δ (CDCl$_3$): 8.29 (d, J = 9.2 Hz, 1H); 8.17 (m, 2H); 8.11 (m, 2H); 8.00 (m, 3H); 7.88 (d, J = 8.0 Hz, 1H); 3.37 (t, J = 7.6 Hz, 2H); 2.29 (dt, J = 7.2, 2.8 Hz, 2H); 2.01 (m, 3H); 1.73 (quin, J = 7.6 Hz, 2H). ^{13}C NMR δ (CDCl$_3$): 136.7, 131.6, 131.1, 130.0, 128.8, 127.7, 127.4, 126.7, 125.9, 125.3, 125.2, 125.0, 124.9, 124.8, 123.5, 84.5, 73.0, 33.1, 31.0, 28.6, 18.5. HRMS-APCI (R=30000) (m/z): [M$^{+\bullet}$] calcd for C$_{22}$H$_{18}$, 282.1409; found 282.1404. Melting point range: 54-56 °C.
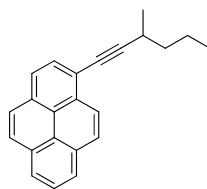
7

Compound 7. (New compound) Procedure 1 was used for the synthesis of compound **7** from 1-bromopyrene (**S1**). A mixture of 1-bromopyrene (**S1**) (50 mg, 0.178 mmol) as the aryl bromide and 3-methyl-1-hexyne (36 μL, 0.266 mmol) as the alkyne was added to a 500 mL round bottom flask, heated to reflux, and stirred by a magnetic stirring bar for 12 hours yielding compound **7** upon work-up as a yellow oil (46 mg, 88% yield). ^{1}H NMR δ (CDCl$_3$): 8.56 (d, J = 9.2 Hz, 1H); 8.20 (s, 1H); 8.18 (s, 1H); 8.08 (d, J = 2.4 Hz, 4H); 8.04 (m, 2H); 8.00 (d, J = 7.6 Hz, 1H); 2.91 (m, 1H); 1.71 (m, 2H); 1.63 (m, 2H); 1.43 (d, J = 5.6 Hz, 3H); 1.04 (t, J = 6.4 Hz). ^{13}C NMR δ (CDCl$_3$): 131.7, 131.2, 131.0, 130.5, 129.5, 127.8, 127.5, 127.3, 127.2, 126.0, 125.7, 125.6, 125.2, 124.8, 124.3, 100.8, 91.3, 39.3, 29.6, 21.3, 20.7, 14.0. HRMS-APCI (R=30000) (m/z): [M$^{+\bullet}$] calcd for C$_{23}$H$_{20}$, 296.1565; found 296.1560.
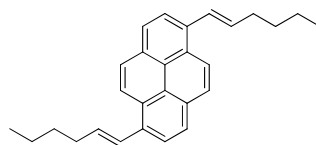
8

Compound 8. (New compound) A three-neck round bottom flask equipped with a septum, reflux condenser, drying tube, and stirring bar was charged with a mixture of 1,6- and 1,8-dibromopyrene (**S2**) (400 mg, 1.111 mmol), Pd(OAc)$_2$ (25 mg, 0.111 mmol), PPh$_3$ (44 mg, 0.168 mmol), tetrabutylammonium bromide (358 mg, 1.110 mmol), sodium acetate (228

mg, 2.779 mmol), and 1-hexene (833 µL, 6.661 mmol) in DMF (10 mL). The system was purged with argon and heated up to 125 °C then stirred for 3 hours. The reaction mixture was cooled to room temperature and diluted with water (10 mL) after TLC indicated a complete reaction. The organic phase was extracted three times with ether and the combined extracts were washed with brine (2 × 10 mL) followed by washing with water (10 mL) to remove traces of DMF. The organic phase was eluted through celite to remove palladium catalyst and purified by flash column chromatography by using a 9:1 hexane/EtOAc solvent mixture. The solvent was evaporated under vacuum to afford compound **8**, a yellow oil, as a mixture of 1,6- and 1,8 isomers (175 mg, 86% yield). ^{1}H NMR δ (CDCl$_3$): 8.40 (d, J = 6.4 Hz, 1H); 8.33 (d, J = 9.2 Hz, 1H); 8.15-8.09 (m, 4H); 7.99-7.96 (m, 2H); 7.42 (d, J = 15.6 Hz, 2H); 6.51-6.41 (m, 2H); 2.46-2.41 (m, 4H); 1.61 (quin, J = 6.8 Hz, 4H); 1.52-1.45 (m, 4H); 1.01 (t, J = 7.2 Hz, 6H). ^{13}C NMR δ (CDCl$_3$): 135.5, 134.8, 132.5, 130.0, 129.9, 128.0, 127.2, 127.0, 126.9, 126.7, 125.2, 125.1, 125.0, 124.9, 124.7, 124.5, 123.9, 123.8, 123.0, 122.6, 33.4, 31.6, 22.3, 14.0. HRMS-APCI (R=30000) (m/z): [M$^{+\bullet}$] calcd for C$_{28}$H$_{30}$, 366.2348; found 366.2351.

9
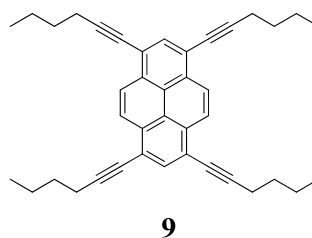
Compound 9. (New compound) Procedure 1 was used for the synthesis of compound **9** by using 1,3,6,8-tetrabromopyrene (200 mg, 0.386 mmol), Pd(OAc)$_2$ (26 mg, 0.116 mmol), PPh$_3$ (30 mg, 0.116 mmol), CuI (22 mg, 0.116 mmol), and 1-hexyne (195 µL, 1.699 mmol).

It afforded compound **9** as an orange solid (165 mg, 82% yield). ^{1}H NMR δ (CDCl$_3$): 8.57 (m, 4H); 8.40 (m, 1H); 8.16 (d, J = 9.6 Hz, 1H); 2.64 (t, J = 6.8 Hz, 8H); 1.75 (quin, J = 6.8 Hz, 8H); 1.62 (sex, J = 7.2 Hz, 8H); 1.03 (t, J = 7.2 Hz, 12H). ^{13}C NMR δ (CDCl$_3$): 133.8, 131.5, 126.4, 124.2, 119.4, 97.0, 79.1, 31.2, 22.3, 19.8, 13.9. HRMS-APCI (R=30000) (m/z): [M$^{+\bullet}$] calcd for C$_{40}$H$_{42}$, 522.3287; found 522.3277. Melting point range: 82-84 °C.

10
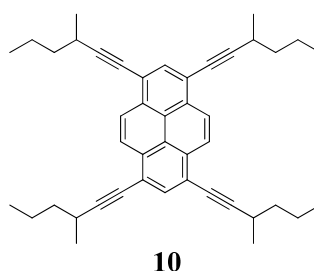
Compound 10. (New compound) Procedure 1 was used for the synthesis of compound **10** by using 1,3,6,8-tetrabromopyrene (100 mg, 0.193 mmol), Pd(PPh$_3$)$_2$Cl (72 mg, 0.103 mmol), PPh$_3$ (85 mg, 0.324 mmol), CuI (20 mg, 0.103 mmol), and 3-methyl-1-hexyne (159 μL, 1.174 mmol). It afforded compound **10** as a pale yellow solid (71 mg, 64% yield). ^{1}H NMR δ (CDCl$_3$): 8.54 (s, 4H); 8.16 (s, 2H); 2.89 (m, 4H); 1.67 (m, 16H); 1.42 (d, J = 6.8 Hz, 12H); 1.04 (t, J = 6.8 Hz, 12H). ^{13}C NMR δ (CDCl$_3$): 133.8, 131.4, 126.4, 124.2, 119.4, 101.4, 79.2, 39.5, 27.0, 21.5, 21.0, 14.2. HRMS-APCI (R=30000) (m/z): [M$^{+\bullet}$] calcd for C$_{44}$H$_{50}$, 578.3913; found 578.3912. Melting point range: 93-94 °C.
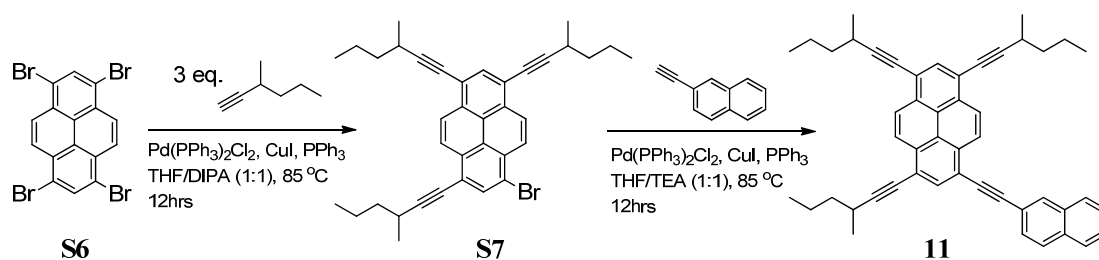
Scheme 3.2 Synthesis of compound **11**

Compound 11. (New compound) Into a sealed tube were added a solution of 1,3,6,8-tetrabromopyrene (**S6**) (24 mg, 0.046 mmol) in THF/DIPA (1:1) (3 mL), Pd(PPh$_3$)$_2$Cl$_2$ (6 mg, 0.025 mmol), CuI (5 mg, 0.025 mmol), and PPh$_3$ (20 mg, 0.078 mmol). Then, 3-methyl-1-hexyne (21 μL, 0.153 mmol) was added to the mixture while stirring and the solution was heated in a silicone bath at 85 °C for 6 hours. The reaction mixture was diluted with chloroform (5 mL) and washed with 5 mL of a 10% HCl aqueous solution. The organic layer was washed with a 10% sodium bicarbonate solution followed by washing with brine and then with water. Next, the organic layer was dried over sodium sulfate and concentrated. The product was purified by flash column chromatography by using a mixture of hexane/ethyl acetate (9:1) to give the trisubstituted intermediate **S7** as an orange solid (18 mg, 69% yield). Next, a solution of **S7** (18 mg, 0.032 mmol), Pd(PPh$_3$)$_2$Cl$_2$ (6 mg, 0.008 mmol), CuI (2 mg, 0.008 mmol), PPh$_3$ (2 mg, 0.008 mmol), and 2-ethynylnaphthalene (10 mg, 0.066 mmol) in THF/TEA (1:1) (3 mL) were added to a sealed tube and heated to 85 °C while stirring for 12 hours. The reaction was cooled to room temperature, diluted with chloroform and worked up using the same procedure that was used for purifying **S7** to afford compound **11** as a reddish orange solid (15 mg, 75% yield). ^{1}H NMR δ (CDCl$_3$): 8.73 (d, J = 9.2 Hz, 1H); 8.63 (d, J = 9.2 Hz, 1H); 8.59 (s, 2H); 8.34

(s, 1H); 8.24 (s, 1H); 8.18 (s, 1H); 7.90 (d, J = 8.4 Hz, 3H); 7.76 (d, J = 8.4 Hz, 1H); 7.54 (t, J = 4.0 Hz, 2H); 2.90 (sex, J = 6.8 Hz, 3H); 1.67 (m, 12H); 1.43 (dd, J = 6.8, 4.4 Hz, 9H); 1.04 (m, 9H). ^{13}C NMR δ (CDCl$_3$): 133.9, 133.8, 133.3, 133.1, 132.0, 131.7, 131.5, 131.4, 129.0, 128.6, 128.3, 128.0, 126.9, 126.8, 126.4, 126.3, 124.3, 124.2, 120.8, 119.8, 119.6, 118.3, 101.7, 96.1, 79.2, 79.1, 39.5, 27.0, 21.5, 21.0, 14.2. HRMS-APCI (R=30000) (m/z): [M$^{+\bullet}$] calcd for C$_{49}$H$_{46}$, 634.3600; found 634.3586. Melting point range: 131-132 °C.

3.4 Synthesis of ^{2}H- and ^{13}C-Labeled Diphenylmethane Compounds
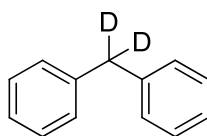
(1,1-^{2}H$_2$)Diphenylmethane. The synthesis procedure for production of (1,1-^{2}H$_2$)Diphenylmethane was modified from an earlier method.[7] A solution of lithium aluminum deuteride (45 mg, 1.1 mmol) in dry ether (2 mL) was stirred under argon atmosphere for 10 min as aluminum chloride (157 mg, 1.2 mmol) in dry ether (2 mL) was added drop wise. The mixture was stirred for 5 min followed by addition of a solution of benzophenone (195 mg, 1.1 mmol) in dry ether (2 mL). The reaction mixture was stirred for 45 min under argon atmosphere and then quenched with 2 mL of deuterium oxide followed by the addition of 2 mL 6 N sulfuric acid. The product mixture was diluted with water (5 mL) and extracted four times with ether (4 × 4 mL). The ethereal extracts were combined and washed with 5 mL of a 10 % (wt.) sodium bicarbonate solution followed by

two water washes (2 × 5 mL). The organic phase was dried over calcium chloride and solvent evaporated under vacuum yielding 118 mg (1,1-^{2}H$_2$)diphenylmethane (65 % yield).
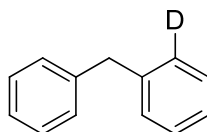
(2-^{2}H$_1$)Diphenylmethane. In a dry 50 mL three-neck flask were added 2-bromodiphenylmethane (118 mg, 0.48 mmol), sodium hydroxide (19 mg, 0.48 mmol), Pd/C (5 mg, 10 wt. % on C), and 5 mL anhydrous methanol. The reaction flask was equipped with a deuterium gas filled balloon and vacuum line connected via two-way adapter. Atmosphere within the vessel was evacuated followed by purging with deuterium gas from the balloon. This process was repeated five times followed by closing the vacuum line and opening the vessel to deuterium gas. The reaction mixture was stirred vigorously under deuterium atmosphere at room temperature until TLC indicated that the reaction was complete (1 hr). The product mixture was eluted through celite and then diluted with water (5 mL). The resulting solution was extracted four times with ether (4 × 5mL). The combined ethereal extracts were washed with a 10 % HCl solution (5 mL) followed by a wash with 10 % (wt.) sodium bicarbonate solution (5 mL) and three washes with water (3 × 5 mL). The organic phase was dried over sodium sulfate and solvent evaporated under vacuum to yield 72 mg (2-^{2}H$_1$)diphenylmethane (89 % yield).
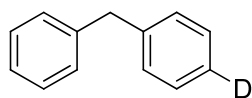
(4-²H₁)Diphenylmethane. The same general procedure used for synthesis of (2-²H₁)diphenylmethane was used for the synthesis of (4-²H₁)diphenylmethane except that 2-bromodiphenylmethane was replaced with 4-bromodiphenylmethane (80 mg, 93 % yield).
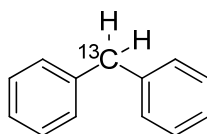
(1-¹³C)Diphenylmethane. The same general procedure used for the synthesis of (1,1-²H₂)diphenylmethane was used for the synthesis of (1-¹³C)diphenylmethane except that benzophenone was replaced with benzophenone-(*carbonyl*-¹³C) and LiAlH₄ was substituted for LiAlD₄ (44 mg, 87 % yield).
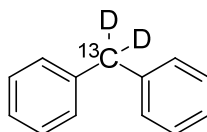
(1-¹³C,1,1-²H₂)Diphenylmethane. The same general procedure used for the synthesis of (1,1-²H₂)diphenylmethane was used for the synthesis of (1-¹³C,1,1-²H₂)diphenylmethane except that benzophenone was replaced with benzophenone-(*carbonyl*-¹³C) (53 mg, 95 % yield).

3.5 <u>References</u>

1. Jarrell, T. M.; Jin, C.; Riedeman, J. S.; Owen, B. C.; Tan, X.; Scherer, A.; Tykwinski, R. R.; Gray, M. R.; Slater, P.; Kenttämaa, H. I. *Fuel* **2014**, *133*, 106.

2. Cooks, R.; Busch, K.; Glish, G. *Science* **1983**, *222*, 273.

3. Sonogashira, K. *J. Organomet. Chem.* **2002**, *653*, 46.

4. Dess, D. B.; Martin, J. C. *J. Org. Chem.* **1983**, *48*, 4155.

5. Seyferth, D.; Marmor, R. S.; Hilbert, P. *J. Org. Chem.* **1971**, *36*, 1379.

6. Gilbert, J. C.; Weerasooriya, U. *J. Org. Chem.* **1982**, *47*, 1837.

7. Ofosu-Asante, K.; Stock, L. M. *J. Org. Chem.* **1990**, *55*, 3409.

CHAPTER 4. ION/MOLECULE REACTIONS OF DIMETHYLAMINE WITH
PROTONATED ANALYTES FACILITATE THE IDENTIFICATION OF
SECONDARY AND TERTIARY *N*-OXIDE FUNCTIONALITIES IN A LINEAR
QUADRUPOLE ION TRAP MASS SPECTROMETER

4.1 Introduction

Methods for the rapid detection of *N*-oxide functionalities in unknown molecules

in complex mixtures are of great current interest for several reasons. For example, the

oxidation of the amino functional group is a common metabolic pathway for many

nitrogen-containing pharmaceuticals.[1,2] In some cases, the degradation products containing

the *N*-oxide functionality have been shown to be genotoxic.[3,4] Further, amine-based

surfactants persisting in the environment are known to form *N*-oxides upon aerobic

biodegradation.[5] These *N*-oxides have been found to be particulary toxic to photobacteria

and crustacea living in aquatic ecosystems.[5]

NMR and FT-IR are viable techniques for the identification of unknown

compounds but require fairly pure samples. NMR detects ^{15}N but its natural abundance is

only 0.37% of that of ^{14}N, which makes this a very insensitive technique for the detection

of *N*-oxides. FT-IR has a good sensitivity but cannot distinguish tertiary *N*-oxides from

primary or secondary *N*-oxides.[6] On the other hand, tandem mass spectrometry has

excellent sensitivity and can be used to analyze complex mixtures without prior

purification.[7,8] Collision-activated dissociation (CAD) commonly employed in tandem

mass spectrometry experiments have been used extensively to probe the structures of

ionized compounds. However, CAD of protonated N-oxides does not in general produce functional group specific fragmentation that can be used to distinguish protonated N-oxides from other ionized nitrogen-containing compounds.[9]

Tandem mass spectrometric methods based on ion-molecule reactions have been demonstrated to be particularly useful for the identification of specific functional groups in ionized analytes.[10-16] For example, aliphatic and aromatic tertiary N-oxide functionalities can be identified in protonated analytes via their reactions with tris(dimethylamino)borane (TDMAB) (Scheme 4.1) in a Fourier-transform ion cyclotron resonance (FT-ICR) mass spectrometer.[10] This reaction occurs via a proton transfer/nucleophilic substitution mechanism which forms a boron-derivatized N-oxide (adduct-$(CH_3)_2NH$).[10] This method was recently adapted to a linear quadrupole ion trap (LQIT) equipped with an external reagent-mixing manifold that allows TDMAB to be introduced through the helium buffer gas inlet into the ion trap.[15] However, due to the low boiling point of TDMAB (147-148 ºC), it is difficult to pump out of the manifold after the experiment is over. Additionally, TDMAB has a high calculated proton affinity[10] (PA = 230), which facilitates unwanted proton transfer reactions with ionized analytes for as long as it resides in the instrument. Thus, a more volatile reagent, dimethylamine (DMA), was tested for the identification of tertiary N-oxides. Its proton affinity[17] (PA = 222 kcal mol^{-1}) is lower than that of TDMAB and it has a boiling point (BP) an order of magnitude lower (7-9 ºC) than TDMAB.
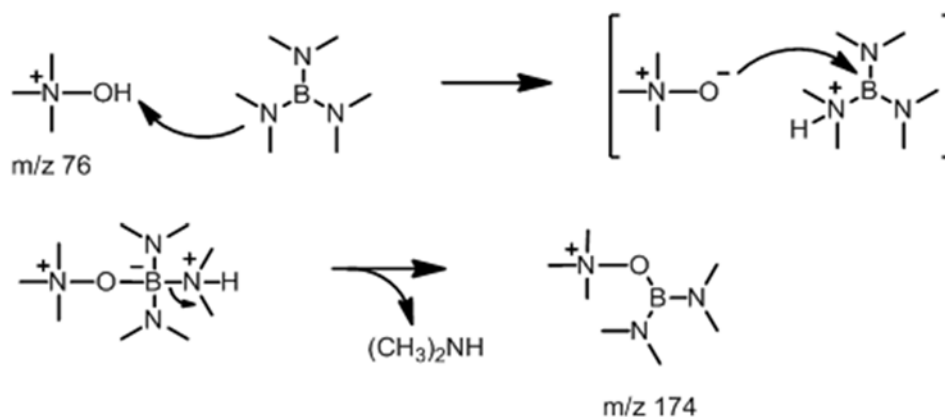
Scheme 4.1 Ion-molecule reaction between protonated trimethylamine *N*-oxide and TDMAB.

4.2 <u>Experimental</u>

N-oxides (>95%), dimethylamine (>99%) as a pressurized gas in a cyclinder, and 2-(3-benzoylphenyl)propionic acid (≥ 98%) were purchased from Sigma-Aldrich. Acetonitrile and methanol were purchased from OmniSolv (99.9%). Ethanol was purchased from Koptec and meets USP specifications. Ethyl acetate and diethyl ether were purchased from Macron and meet ACS reagent requirements. Propionaldehyde was purchased from Alfa Aesar (97%). All chemicals were used without further purification.

Mass spectrometric data were collected using a Thermo Scientific linear quadrupole ion trap (LQIT) mass spectrometer (LTQ, Thermo Scientific, San Jose, CA, USA) utilizing an electrospray ionization (ESI) source operating in positive-ion mode. The trapping region of the instrument was maintained at ~10^{-5} Torr by a triple-inlet turbomolecular pump, as measured by an ion gauge.

Samples were dissolved in methanol (1 mg/mL) and introduced into the ESI source via a syringe pump at a flow rate of 10 μL/min. A tee connector combined 50/50 (v/v)

methanol/water from a Finnigan Surveyor MS Pump Plus with the sample at a flow rate of 200 μL/min to facilitate formation of a stable ESI spray. Source conditions were as follows: 275 ^{0}C capillary temperature, sheath gas flow of 60 arbitrary units), auxillary gas flow of 30 (arbitrary units), 2 kV spray voltage, 18 V capillary voltage, and 50 V tube lens voltage. The automated tuning feature of the instrument was used to optimize the ion optics for ions (m/z 50 to m/z 500).

The reagent inlet system has been described previously.[18] The neutral reagent DMA was introduced into the trapping region of the LQIT using two Series 9 pulsed valves with an exit orifice of 0.060 inch (Parker Hannifin Corp., Cleveland, OH). A single pulsed valve pair was utilized for the introduction of DMA into the trapping region of the mass spectrometer. DMA was introduced via a gas regulator equipped with a hose and needle through a rubber septum into a single pulsed valve channel. The channel was filled to one atmosphere with DMA. DMA was introduced into the instrument by first opening the pulsed valve connected to the sample channel (i.e., pulsed valve A, Figure 4.1) for 500 μs to allow the reagent to flow into the space between the pulsed valves (i.e., between A and B). Next, the pulsed valve that interfaces with the trapping region of the LQIT (i.e., pulsed valve B), was opened for 900 μs to let the reagent enter the mass spectrometer. A 20 ms delay was set between open events of pulsed valves A and B.
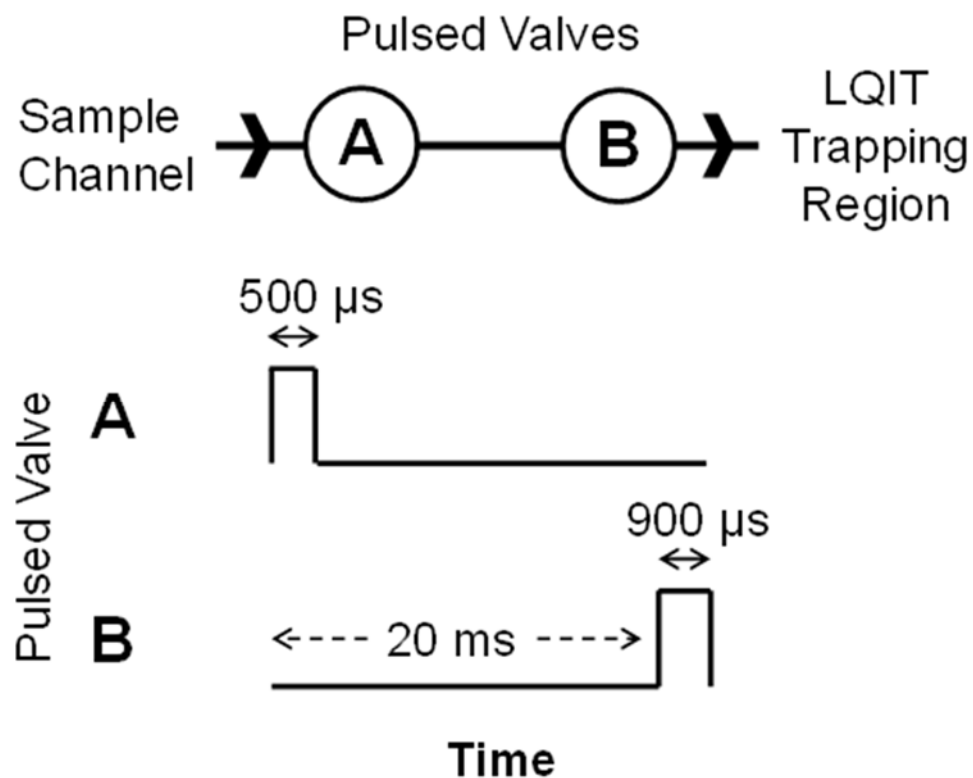
Figure 4.1 Shown here are the parameters used for the pulsed valve experiments. The pulse width of A is the time the pulsed valve is open. When pulsed valve A is opened, DMA flows from the sample channel into the space between pulsed valves A and B. The pulse width of B is the time the pulsed valve is open to the trapping region of the LQIT. The dashed arrow represents the delay from the start of the sequence to the time when the pulsed valve opens.

The experiments were performed utilizing the scan features of the LTQ Tune Plus interface (Xcalibur 2.1 version). Analyte ions were isolated using a 2 Dalton window with a q value of 0.25 and then allowed to react with DMA for 500 ms before being ejected from the trap and detected.

All geometries and zero-point energies were calculated at the B3LYP/6-31++G(d,p) level of theory by using the Gaussian 09 suite of programs.[19] Frequency calculations were performed to verify all stationary points as energy minima and to provide zero-point

vibrational energy corrections. Minimum energy structures do not have imaginary frequencies. Proton affinities were computed as the energy difference between the molecule of interest and the same molecule with one additional proton. This method was found to be reasonably accurate when comparing the difference (Δ) between calculated proton affinities and the experimental values available in literature for 5,5-dimethyl-1-pyrroline *N*-oxide (Δ = 0.23 kcal mol^{-1}), pyridine *N*-oxide (Δ = 2.2 kcal mol^{-1}), nitrosobenzene (Δ = 2.1 kcal mol^{-1}), and trimethylamine *N*-oxide (Δ = 1.5 kcal mol^{-1}).

Hydrogen-bonding energies were calculated using the standard energy difference method.[20] The hydrogen bond energy between a hydrogen bond donor and acceptor is calculated by

$$\Delta E_{int}^{CP}(AD) = E_{AD}^{AD} - E_{A}^{AD} - E_{D}^{AD} \tag{4.1}$$

where $\Delta E_{int}^{CP}(AD)$ is the hydrogen-bonding energy including counterpoise correction for basis set superposition error (BSSE), *AD* is the set of Cartesian coordinates defining the structure of the complex, E_{AD}^{AD} is the energy of the hydrogen bound complex, and E_{A}^{AD} and E_{D}^{AD} are the energies of the acceptor (A) and donor (D), respectively. The subscripts (A and D) denote the Cartesian coordinates that define the geometry of molecules A and D. The superscripts (AD) denote the basis set of the AD complex used in the optimization. The BSSE arises from the artificial energy stabilization of donor and acceptor as they approach each other in the hydrogen bound complex. During energy minimization, each molecule in the hydrogen-bound complex utilizes extra basis functions from the other, thus artificially lowering its own energy.

To correct for this error, the counterpoise procedure was used.[21] As an example, to calculate the energy of a specific hydrogen bound hydrogen donor D, all the basis functions of the hydrogen-bound acceptor A at the atomic positions of A are made available to D while ignoring the charges of electrons and nuclei on A. The BSSE is evaluated by taking the difference

$$E_{BSSE}(D) = E_D^{AD} - E_D^D \qquad (4.2)$$

where $E_{BSSE}(D)$ is the artificial stabilization afforded to D by the additional basis sets in the hydrogen-bound complex. The same procedure is applied to A utilizing the basis functions of D.
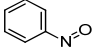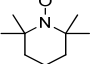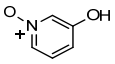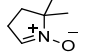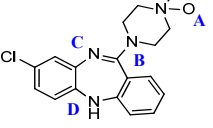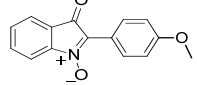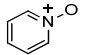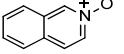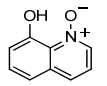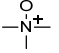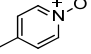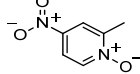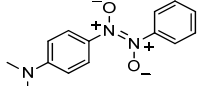
4.3 <u>Results and Discussion</u>

Protonated primary, secondary, and tertiary *N*-oxides and other heteroatom-containing moieties were introduced into the mass spectrometer via ESI and allowed to interact with dimethylamine (DMA) while trapped in the linear quadrupole ion trap (LQIT) and their reaction products were analyzed. Proton affinities and hydrogen-bond energies were calculated for a number of the protonated analytes and their complexes with DMA, respectively, in order to understand their observed reactivity toward DMA. Finally, the residence time of DMA in the trapping region of the mass spectrometer was examined to determine the cycle time of the experiment and verify DMA's usefulness in HPLC methodologies incorporating multiple neutral reagents introduced consecutively during an HPLC analysis.

4.3.1 Reactivity of Dimethylamine (DMA) Toward Protonated *N*-Oxides
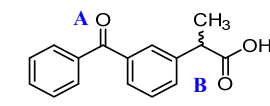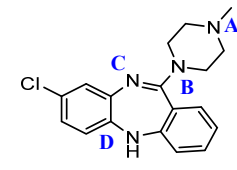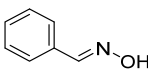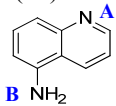
Analytes were protonated via ESI. DMA was introduced into the trapping region of the mass spectrometer through a pair of pulsed valves (i.e., A and B). Parameters used for the pulsed valve experiments are shown in Figure 4.1. Trapped ions were allowed to interact with DMA for 500 ms before all ions were ejected and detected. DMA was found to react with protonated aliphatic and aromatic tertiary *N*-oxide analytes (M) by formation of an $[M + H]^+$ + DMA adduct (Table 4.1), which was not formed for many other protonated analytes (Table 4.2). A typical reaction can be seen in Figure 4.2. When no DMA is in the trapping region of the instrument, only the protonated trimethylamine *N*-oxide is observed. However, after DMA is temporarily introduced into the trapping region of the mass spectrometer, it reacts with protonated trimethylamine *N*-oxide forming an adduct with a m/z-value 45 units greater than that of the analyte ion. This ion signal gradually tapers in abundance as DMA is pumped away by the vacuum system.

Table 4.1 *N*-Oxides, Their PAs, (in kcal mol^{-1}), Reactions of Their Protonated Forms with DMA (PA^a = 222 kcal mol^{-1}), and Their Branching Ratios in a Linear Quadrupole Ion Trap Mass Spectrometer.

Analyte (M)	(m/z of [M+H]$^+$)	Proton Affinity (PA) (kcal mol^{-1})	Observed Reaction (yield %)[a]
	108	204[b]	Proton transfer to DMA (55)
	157	210.9[b]	[M + H]$^+$ + DMA (3)
	112	219.4[c]	[M + H]$^+$ + DMA (85)
	114	221.2[d]	[M + H]$^+$ + DMA (98)
	343	236.7[c] (**A**) 220.2[c] (**B**) 237.3[c] (**C**) 216.9[c] (**D**)	[M + H]$^+$ + DMA (24)
	254	220.6[c]	[M + H]$^+$ + DMA (52)
	96	220.7[b]	[M + H]$^+$ + DMA (91)
	146	227.6[d]	[M + H]$^+$ + DMA (84)
	162	234.7[c]	[M + H]$^+$ + DMA (10)
	76	235[b]	[M + H]$^+$ + DMA (20)
	110	225.5[d]	[M + H]$^+$ + DMA (41)
	155	206.3[c]	[M + H]$^+$ + DMA (45)
	258	242.0[c]	[M + H]$^+$ + DMA (89)

[a] Yield was measured relative to precursor ([M + H]$^+$) abundance. [b] PA value from reference 17. [c] Calculated at the B3LYP/6-31++G(d,p) level of theory. [d] PA value from reference 10.

Table 4.2 Reactions Observed for Various Protonated Analytes with Different PAs with DMA (PA[a] = 222 kcal mol^{-1}) in a Linear Quadrupole Ion Trap Mass Spectrometer.

Analyte (m/z of [M+H]$^+$)	Proton Affinity (PA) (kcal mol^{-1})	Observed Reaction (yield %)[a]
Ethyl acetate (89)	200[b]	Proton transfer to DMA (28)
Acetonitrile (42)	186[b]	Proton transfer to DMA (63)
Ethanol (47)	186[b]	Proton transfer to DMA (74)
Diethyl ether (75)	198[b]	Proton transfer to DMA (81)
Acetone (59)	194[b]	Proton transfer to DMA (97)
Propionaldehyde (59)	187.9[b]	Proton transfer to DMA (15)
Hexanoic acid (117)	188.2[c]	Proton transfer to DMA (33)
Heptanoic acid (131)	188.2[c]	Proton transfer to DMA (49)
2-(3-Benzoylphenyl)-propionic acid (255)	212.0[c] (**A**) 199.6[c] (**B**)	[M + H]$^+$ + DMA (60)[d]
Clozapine (327)	228.4[c] (**A**) 223.9[c] (**B**) 239.4[c] (**C**) 218.1[c] (**D**)	No observed reaction[d]
Benzaldehyde oxime (122)	210.2[c]	Proton transfer to DMA (41)
Pyridine (80)	222.3[b]	[M + H]$^+$ + DMA (1)
5-Aminoquinoline (145)	231.5[c] (**A**) 210.7[c] (**B**)	[M + H]$^+$ + DMA (5)

[a] Yield was measured relative to precursor ([M + H]$^+$) abundance. [b] PA value from reference 17. [c] Calculated at the B3LYP/6-31++G(d,p) level of theory. [d] Low mass cut-off of the instrument prevented observation of ions <50 m/z.
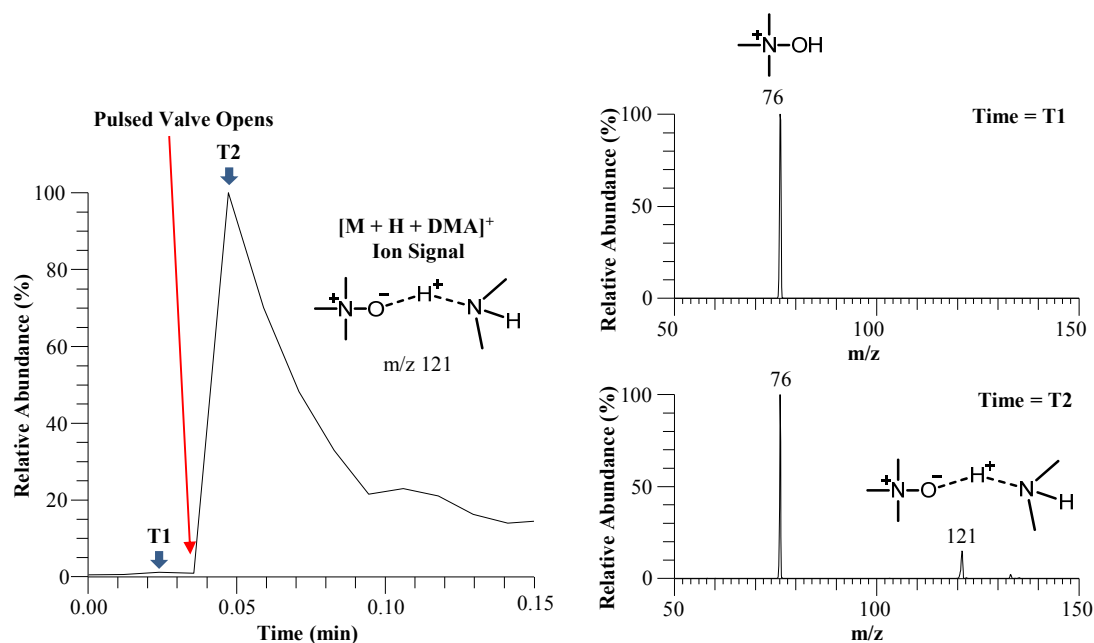
Figure 4.2 Reaction of protonated trimethylamine *N*-oxide (m/z 76) with DMA as a function of time. The extracted ion chromatogram represents the abundance of the [M + H]$^+$ + DMA ion (m/z 121) where M = trimethylamine *N*-oxide (left). At time T1, before DMA has entered into the trapping region of the instrument, only protonated trimethylamine *N*-oxide (m/z 76) is observed (top right). At time T2, the pulsed valve has opened, allowing DMA to enter the trapping region of the instrument, which enables the formation of a stable hydrogen bound complex with m/z value 45 units greater (m/z 121) than the m/z value of protonated trimethylamine *N*-oxide (bottom right).

In the previous studies of reactivity of TDMAB toward protonated tertiary *N*-oxides, collision-activated dissociation (CAD) of the diagnostic adduct – CH$_3$OH products was found to result in the cleavage of the nitrogen-oxygen bond, yielding an immonium ion from the amino moiety of the *N*-oxide analyte (Scheme 4.2).[10] However, CAD of the DMA adducts of protonated tertiary *N*-oxide analytes results in the loss of DMA to yield the protonated analyte. Hence, no structural information is obtained from this experiment. The most plausible explanation for this observation is that the DMA adduct is a hydrogen-bound complex of the protonated analyte and DMA (Scheme 4.3). The wide range of PAs

for analytes (206 – 242 kcal mol^{-1}) that form an adduct with DMA indicates that adduct

formation is fairly independent of PA (Table 4.1; Table 4.2, entry 9). However, protonated

analytes having proton affinities more than 20 kcal mol^{-1} below that of DMA did react by

proton transfer exclusively (Table 4.2). Interestingly, protonated tertiary *N*-oxide 2-methyl-

4-nitropyridine 1-oxide (PA = 206 kcal mol^{-1}) (Table 4.1, entry 12) reacts with DMA by

formation of an adduct while protonated nitrosobenzene (PA = 204 kcal mol^{-1}) (Table 4.1,

entry 1) does not despite of having a similar proton affinity. Additionally, protonated *N,N*-

dimethyl-4-(1,2-dioxido-2-phenyldiazenyl)benzenamine (Table 4.1, entry 12) forms the

adduct with DMA yet has a calculated proton affinity 20 kcal mol^{-1} higher than DMA.

Thus, the hydrogen-bonding energy between DMA and protonated analytes was

investigated to determine whether the formation of a stable adduct correlates with strong

hydrogen bond formation. The energy of a typical hydrogen bond is generally less than 12

kcal mol^{-1} for neutral molecules but has been shown previously to be greater than 30 kcal

mol^{-1} for several ionized hydrogen bond acceptors.[22]
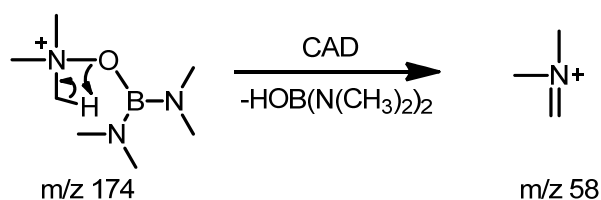
Scheme 4.2 CAD of the TDMAB – methanol adduct ion with tertiary *N*-oxides.
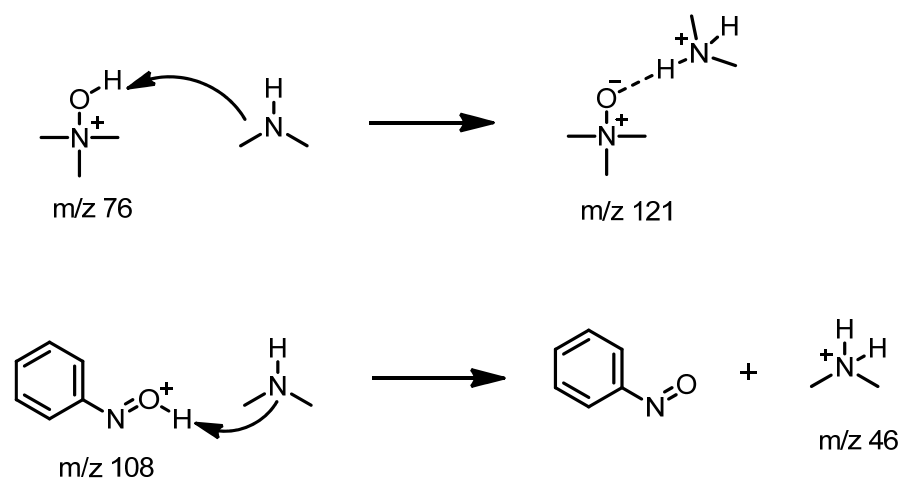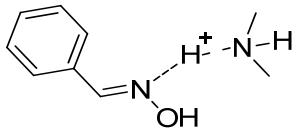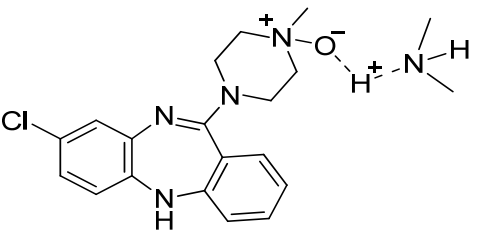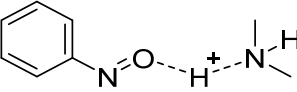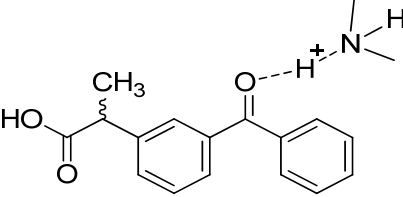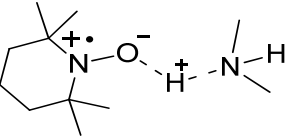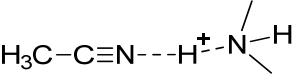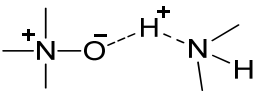
Scheme 4.3 Reactions of DMA with protonated tertiary *N*-oxides and primary *N*-oxides.

Hydrogen-bonding energies (ΔE_{int}) between hydrogen bond donors and acceptors were calculated using Density Functional Theory (DFT) at the B3LYP/6-31++G(d,p) level of theory (Table 4.3). These hydrogen-bonding energies were compared to the difference in proton affinity (ΔPA) between the analyte and DMA to determine the relationship between hydrogen bond formation and proton transfer. Values of ΔPA that are negative indicate an exothermic proton transfer reaction between the protonated analyte and DMA as seen in Table 4.3. The hydrogen-bonding energy (ΔE_{int}, energy released as a result of hydrogen bond formation) was found to be more energetically favorable than proton transfer for all protonated analytes that react with DMA to produce a stable adduct. The results are best represented visually by the use of the Brauman potential energy diagrams[23] as shown in Figure 4.3. The geometries of all hydrogen bound complexes minimized to complex C during the DFT calculations, even for analytes with proton affinity greater than that of DMA, such as trimethylamine *N*-oxide (PA[17] = 235 kcal mol^{-1}) and clozapine-4'-*N*-oxide (PA = 236.7 kcal mol^{-1}). This finding indicates either a single-well potential energy

surface or possibly a shallow barrier between intermediates B and C, a common result for strongly hydrogen bonding donor/acceptor pairs.[22,24] Further, this suggests that the energy of complex B is higher than that of C if such a minimum exists on the potential energy surface at all. Formation of a hydrogen-bound complex was only observed when the transition from C to D was endothermic which is easily measured by taking the difference $\Delta PA - \Delta E_{int}$ as shown in Table 4.3. Positive values indicate hydrogen bond formation is more favorable than proton transfer.

Table 4.3 Calculated Hydrogen Bonding Energies (ΔE_{int}), Calculated Proton Affinity Differences (ΔPA = proton affinity of analyte – proton affinity of DMA), and Free Energy Changes Going from Intermediate C to D ($\Delta PA - \Delta E_{int}$) for Various $[M + H]^+$ + DMA Hydrogen Bound Complexes.

$[M + H]^+$ + DMA Adduct	ΔPA^a (kcal mol^{-1})	ΔE_{int}^b (kcal mol^{-1})	$\Delta PA - \Delta E_{int}$ (kcal mol^{-1})	$[M + H]^+$ + DMA Adduct	ΔPA^a (kcal mol^{-1})	ΔE_{int}^b (kcal mol^{-1})	$\Delta PA - \Delta E_{int}$ (kcal mol^{-1})
Benzaldehyde oxime	-11.8	-6.3	-5.5	Clozapine-4'-N-oxide	14.7	-26.1	40.8
Nitrosobenzene	-18.0	-13.4	-4.6				
TEMPO	-11.1	-15.0	3.9	Ketoprofen	-10.0	-12.5	2.5
Trimethylamine N-oxide	13.0	-25.0	38.0	Acetonitrile	-36.0	-13.8	-22.2

[a] ΔPA = proton affinity of analyte (M) - proton affinity of dimethylamine (DMA), calculated at the B3LYP/6-31++G(d,p) level of theory.

[b] Calculated at the B3LYP/631++G(d,p) level of theory according to equation 1.
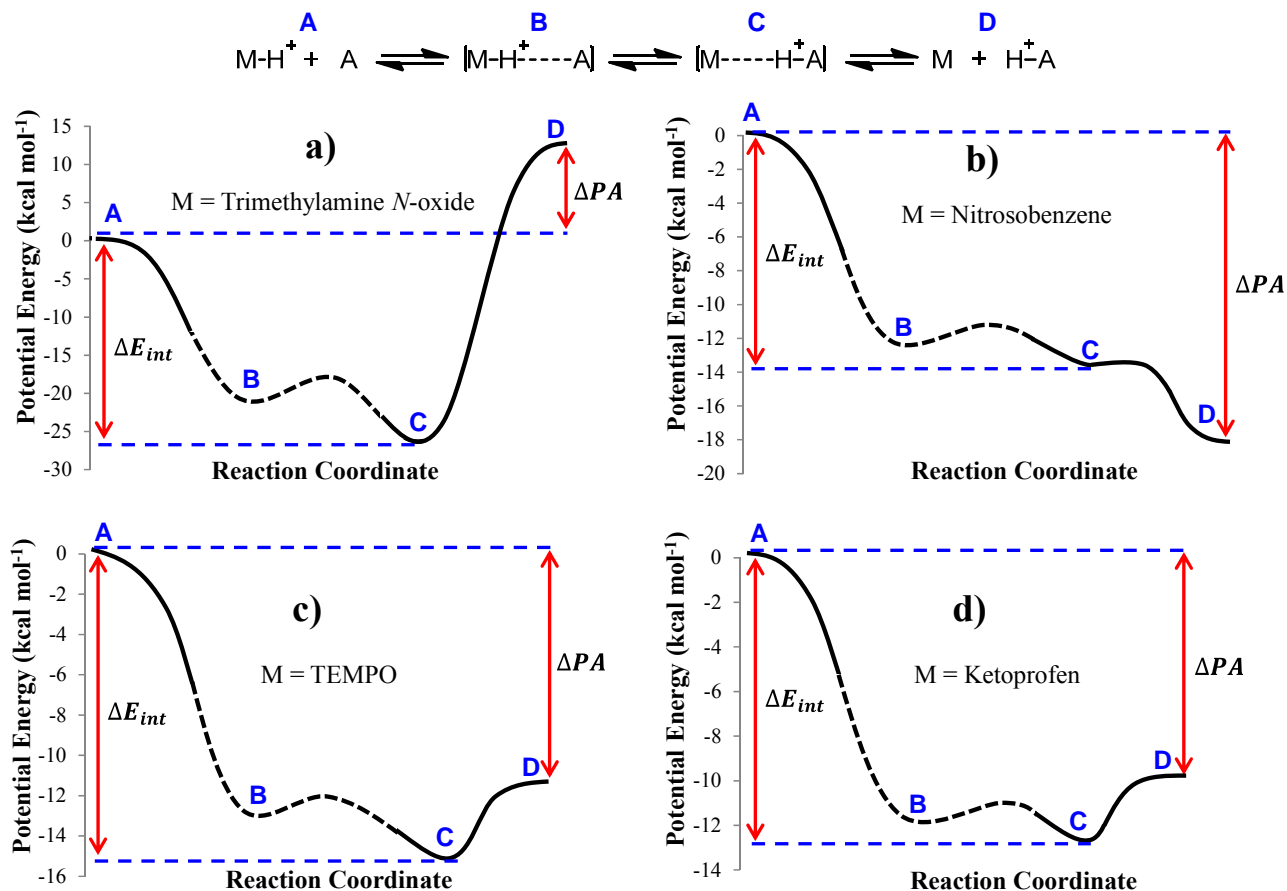
Figure 4.3 Potential energy profiles for proton transfer from protonated trimethylamine *N*-oxide (top left), nitrosobenzene (top right), TEMPO (bottom left), and ketoprofen (bottom right) to DMA. The unknown portion of the energy profile is represented by a dashed line. ΔE_{int} was calculated at the B3LYP/6-31++G(d,p) level of theory using the counterpoise procedure. Proton affinities were calculated at the B3LYP/6-31++G(d,p) level of theory. ΔPA was calculated as the difference in the proton affinity of DMA and the analyte (M).

Cessation of the reaction at the hydrogen bound complex (intermediuate C, Figure 4.3) for tertiary *N*-oxides suggests that there is considerable collisional cooling of the ions with helium in the linear ion trap.[25] Otherwise, we would expect all reactions with a negative ΔPA value to proceed to proton transfer. Helium serves as a buffer gas in the linear quadrupole ion trap cooling ions to improve trapping efficiency and resolution.[25] Additionally, some of the hydrogen bonding energy may be lost as a result of radiative cooling (spontaneous emission of infrared photons).[26] In order to test this idea, an ion-molecule reaction between protonated 4-nitro-2-picoline *N*-oxide (PA = 206 kcal mol^{-1}) (Table 4.1, entry 6) and DMA was carried out in a dual-cell Fourier-transform ion cyclotron resonance mass spectrometer in the absence of any buffer gas. This experiment was carried out by generating protonated 4-nitro-2-picoline *N*-oxide in one of the two cells followed by transferring the resulting ions to the clean cell to react with DMA. The results indicated that only proton transfer occurred in the absence of a buffer gas. Hence, collisional cooling appears to be more influential in removing excess energy resulting from complex formation.

The final step of the proton transfer reaction pathway, formation of proton transfer products D from intermediate C, was found to be endothermic for all protonated analytes that yield an adduct with DMA (Table 4.3). On the other hand, when the dissociation of intermediate C to yield proton transfer products (D) is exothermic, an adduct was not observed for those reactions ($\Delta E_{int} - \Delta PA$ = "-" value) . For example, nitrosobenzene, a primary *N*-oxide, has a calculated hydrogen bonding energy (ΔE_{int}) of -13.4 kcal mol^{-1}, however, the proton transfer reaction is energetically more favorable by -4.6 kcal mol^{-1} making proton transfer the desired pathway for this system. As seen in Table 4.3, the transition from intermediate C to D for the secondary *N*-oxide TEMPO was calculated to

be endothermic ($\Delta E_{int} - \Delta PA = 3.9$) as well which suggests that adduct formation is energetically more favorable than proton transfer. However, formation of the hydrogen bound complex was found to be slow (Table 4.1, entry 2). This is likely the result of steric hindrance due to the four methyl groups adjacent to the *N*-oxide functionality (Table 4.3, entry 3).

The reactivity of protonated clozapine and clozapine-4'-*N*-oxide with DMA was examined (Table 4.1, entry 5 and Table 4.2, entry 10). Clozapine is an atypical antipsychotic drug for the treatment of schizophrenia symptoms. particularly beneficial because of its efficacy on treatment-resistant patients.[27] Clozapine-4'-*N*-oxide is a metabolite of clozapine that has been found to be completely inactive, thus its presence in the drug ultimately reduces the plasma concentration of the active drug clozapine after ingestion.[28,29] Therefore, it is important to be able to identify clozapine-4'-*N*-oxide in drug samples. The presence of the tertiary *N*-oxide functionality in protonated clozapine-4'-*N*-oxide (but not in protonated clozapine) is clearly revealed after reaction with DMA by the appearance of a product ion with a m/z value 45 units greater than that of the analyte ion (Table 4.1, entry 5).

4.3.2 Reactivity of DMA With Other Types of Protonated Analytes

The specificity of reactions of DMA was further investigated by testing its reactivity toward protonated O- and N-containing analytes that do not contain the *N*-oxide functionality (Table 4.2). Proton transfer was observed exclusively for most analytes. However, protonated 2-(3-benzoylphenyl)propionic acid (ketoprofen) reacted with DMA by formation of a hydrogen-bound complex (Table 4.2, entry 9). The potential energy

surface shown in Figure 4.3 indicates proton transfer is less favorable than formation of a hydrogen-bound complex. Isolation of the $[M + H]^+$ + DMA adduct of ketoprofen was attempted in order to subject the ion to CAD for structure determination, but the adduct was found to be too unstable to be isolated. This indicates a rather low barrier to dissociation of the $[M + H]^+$ + DMA adduct of ketoprofen to yield proton transfer products (Figure 4.3d). Conversely, all hydrogen bound complexes of DMA with tertiary *N*-oxides were capable of being efficiently isolated. Protonated clozapine showed no reactivity with DMA, however, the low mass range cut-off of the instrument prevented the observation of a proton transfer reaction. Basic analytes such as pyridine and 5-aminoquinoline did form a hydrogen-bound complex with DMA but the yields were low (≤5%) indicating the reaction was slower than DMA reactions with *N*-oxides (Table 4.2, entry 12 & 13).

4.3.3 Residence Time of DMA in the Ion Trap

Unwanted ion-molecule reactions may persist for long periods after introducing reagents with low boiling points into the trapping region of a mass spectrometer. Thus, the residence time of DMA in the trapping region of the mass spectrometer was experimentally determined. In order to measure this, DMA was introduced into the trapping region of the LQIT using the pulsed valve system and allowed to react with protonated methanol dimer (generated by ESI operating in positive mode) while the instrument scanned continuously. Protonated methanol dimer reacts with DMA by proton transfer only. As seen in Figure 4.4, the abundance of protonated DMA rises while the abundance of protonated methanol dimer decreases simultaneously. The abundance of protonated DMA fell below 5% relative

to protonated methanol dimer after 20 seconds in the trapping region of the mass spectrometer.
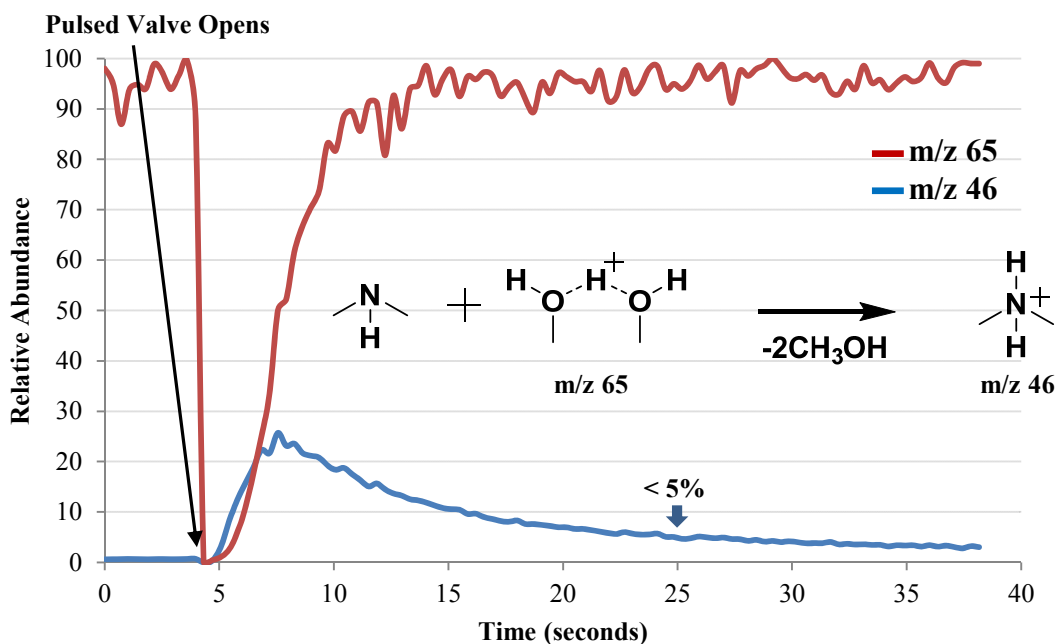
Figure 4.4 Selected ion monitoring of protonated methanol dimer and DMA during the proton transfer reaction in the LQIT. When the pulsed valve closest to the LQIT opens, DMA enters the trapping region of the instrument and reacts with protonated methanol dimer by abstracting a proton. This is evident from the sharp decrease in the abundance of protonated methanol dimer (m/z 65) with a simultaneous increase in the abundance of protonated DMA (m/z 46). After 19.8 seconds the abundance of protonated DMA fell below 5% abundance relative to protonated methanol dimer indicating near complete removal of DMA by the vacuum system.

4.4 Conclusions

A selective ion-molecule reaction, exclusive formation of a stable adduct upon reaction with dimethylamine (DMA), has been identified for protonated tertiary and secondary aliphatic and aromatic *N*-oxides in a linear quadrupole ion trap mass spectrometer. The structure of this adduct was discovered to be a hydrogen-bound complex

of the protonated analyte and DMA. Calculated hydrogen bonding energies between the hydrogen bond donor and acceptor within the complex were found to explain the reactivity of DMA toward protonated secondary and tertiary *N*-oxides and one aromatic ketone (ketoprofen). Formation of a gas-phase hydrogen-bound complex occurred for analytes whose proton transfer reaction was higher in energy than the complex. In contrast, other protonated O- and N-containing analytes were not observed to react with DMA, react only slowly as indicated by lower yield of the complex, or react exclusively by proton transfer to DMA. Thus, the presence of other functionalities does not affect the reactivity of DMA towards the above mentioned *N*-oxides in most cases. Additionally, the PA of these analytes had little influence on their reactivity toward DMA as indicated by the wide range of PAs for tertiary *N*-oxides that, after protonation, form a stable adduct with DMA. However, the above method does not yield additional structural information specific to each analyte upon isolation of the hydrogen-bound complexes with DMA followed by CAD. Dissociation of the complex yields the protonated analyte or protonated DMA. Currently, we are studying DMA reactions with protonated sulfoxides, sulfones, and some hydroxylamines.

The ability of DMA to distinguish protonated clozapine from protonated clozapine-4'-N-oxide suggests that this reagent is applicable to the analysis of drug metabolites with several functionalities. Also, this reagent can be used in many different types of reagent inlet systems since it is volatile and has a short residence time in the vacuum region of a mass spectrometer. This also enables the utilization of this reagent in multi-ported inlet systems designed for the nearly simultaneous use of several different reagents on a chromatographic time scale.[18]

4.5 <u>References</u>

1.   Bickel, M. H. *Pharmacol. Rev.* **1969**, *21*, 325.

2.   Rose, J.; Castagnoli, N. *Med. Res. Rev.* **1983**, *3*, 73.

3.   Ashby, J.; Tennant, R. W. *Mutat. Res.* **1988**, *204*, 17.

4.   Ashby, J.; Tennant, R. W.; Zeiger, E.; Stasiewicz, S. *Mutat. Res.* **1989**, *223*, 73.

5.   García, M. T.; Campos, E.; Ribosa, I. *Chemosphere* **2007**, *69*, 1574.

6.   Krzywda, S.; Jaskólski, M.; Gdaniec, M.; Dega-Szafran, Z.; Grundwald-Wyspiańska, M.; Szafran, M.; Dauter, Z.; Davies, G. *J. Mol. Struct.* **1996**, *375*, 197.

7.   Amundson, L. M.; Eismin, R. J.; Reece, J. N.; Fu, M.; Habicht, S. C.; Mossman, A. B.; Shea, R. C.; Kenttämaa, H. I. *Energy Fuels* **2011**, *25*, 3212.

8.   Jarrell, T. M.; Marcum, C. L.; Sheng, H.; Owen, B. C.; O'Lenick, C. J.; Maraun, H.; Bozell, J. J.; Kenttamaa, H. I. *Green Chem.* **2014**, *16*, 2713.

9.   McRae, G.; Monreal, C. M. *Anal. Bioanal. Chem.* **2011**, *400*, 2205.

10.   Duan, P.; Gillespie, T. A.; Winger, B. E.; Kenttämaa, H. I. *J. Org. Chem.* **2008**, *73*, 4888.

11.   Moneti, G.; Pieraccini, G.; Favretto, D.; Traldi, P. *J. Mass Spectrom.* **1999**, *34*, 1354.

12.   Duan, P.; Fu, M.; Gillespie, T. A.; Winger, B. E.; Kenttämaa, H. I. *J. Org. Chem.* **2009**, *74*, 1114.

13.   Eismin, R. J.; Fu, M.; Yem, S.; Widjaja, F.; Kenttämaa, H. I. *J. Am. Soc. Mass Spectrom.* **2012**, *23*, 12.

14.   Eismin, R.; Fu, M.; Yem, S.; Widjaja, F.; Kenttämaa, H. *J. Am. Soc. Mass Spectrom.* **2012**, *23*, 12.

15.   Mazzoni, V.; Bradesi, P.; Tomi, F.; Casanova, J. *Magn. Reson. Chem.* **1997**, *35*, S81.

16.   Bøjstrup, M.; Petersen, B. O.; Beeren, S. R.; Hindsgaul, O.; Meier, S. *Anal. Chem.* **2013**, *85*, 8802.

17.   Hunter, E. P. L.; Lias, S. G. *J. Phys. Chem. Ref. Data* **1998**, *27*, 413.

18. Jarrell, T.; Riedeman, J.; Carlsen, M.; Replogle, R.; Selby, T.; Kenttämaa, H. *Anal. Chem.* **2014**, *86*, 6533.

19. Frisch, M. J.; Trucks, G. W.; Schlegel, H. B.; Scuseria, G. E.; Robb, M. A.; Cheeseman, J. R.; Scalmani, G.; Barone, V.; Mennucci, B.; Petersson, G. A.; Nakatsuji, H.; Caricato, M.; Li, X.; Hratchian, H. P.; Izmaylov, A. F.; Bloino, J.; Zheng, G.; Sonnenberg, J. L.; Hada, M.; Ehara, M.; Toyota, K.; Fukuda, R.; Hasegawa, J.; Ishida, M.; Nakajima, T.; Honda, Y.; Kitao, O.; Nakai, H.; Vreven, T.; J. A. Montgomery, J.; Peralta, J. E.; Ogliaro, F.; Bearpark, M.; Heyd, J. J.; Brothers, E.; Kudin, K. N.; Staroverov, V. N.; Keith, T.; Kobayashi, R.; Normand, J.; Raghavachari, K.; Rendell, A.; Burant, J. C.; Iyengar, S. S.; Tomasi, J.; Cossi, M.; Rega, N.; Millam, J. M.; Klene, M.; Knox, J. E.; Cross, J. B.; Bakken, V.; Adamo, C.; Jaramillo, J.; Gomperts, R.; Stratmann, R. E.; Yazyev, O.; Austin, A. J.; Cammi, R.; Pomelli, C.; Ochterski, J. W.; Martin, R. L.; Morokuma, K.; Zakrzewski, V. G.; Voth, G. A.; Salvador, P.; Dannenberg, J. J.; Dapprich, S.; Daniels, A. D.; Farkas, O.; Foresman, J. B.; Ortiz, J. V.; Cioslowski, J.; Fox, D. J.; Revision C.01 ed.; Gaussian Inc.: Wallingford CT, 2010.

20. Scheiner, S. *Hydrogen Bonding: A Theoretical Perspective*; Oxford University Press: New York, 1997.

21. Boys, S. F.; Bernardi, F. *Mol. Phys.* **1970**, *19*, 553.

22. Chen, J.; McAllister, M. A.; Lee, J. K.; Houk, K. N. *J. Org. Chem.* **1998**, *63*, 4611.

23. Brauman, J. I. *J. Mass Spectrom.* **1995**, *30*, 1649.

24. Nelson, J. H.; Nathan, L. C.; Ragsdale, R. O. *J. Am. Chem. Soc.* **1968**, *90*, 5754.

25. Stafford, G. C.; Kelley, P. E.; Syka, J. E. P.; Reynolds, W. E.; Todd, J. F. J. *Int. J. Mass Spectrom. Ion Proc.* **1984**, *60*, 85.

26. Sleno, L.; Volmer, D. A. *J. Mass Spectrom.* **2004**, *39*, 1091.

27. Kane, J.; Honigfeld, G.; Singer, J.; Meltzer, H. *Arch. Gen. Psychiatry* **1988**, *45*, 789.

28. Olianas, M. C.; Dedoni, S.; Ambu, R.; Onali, P. *Eur. J. Pharmacol.* **2009**, *607*, 96.

29. Pirmohamed, M.; Williams, D.; Madden, S.; Templeton, E.; Park, B. K. *J. Pharmacol. Exp. Ther.* **1995**, *272*, 984.

CHAPTER 5. HIGH PERFORMANCE LIQUID CHROMATOGRAPHY/MASS
SPECTROMETRY METHOD FOR DISTINGUISHING ISOMERIC
SACCHARIDES: A STUDY OF EPIMERIC 1,6-ANHYDROSUGARS

5.1 Introduction

Levoglucosan (1,6-anhydro-β-D-glucopyranose) is a major final product of fast
pyrolysis of biomass, starch, and cellulose.[1-3] Two epimers of levoglucosan, mannosan
(1,6-anhydro-β-D-mannopyranose) and galactosan (1,6-anhydro-β-D-galactopyranose),
are also commonly observed in biomass pyrolysis products containing levoglucosan.[4-8]
These compounds are typically studied by gas-chromatography coupled with mass
spectrometry (GC-MS).[9] However, this method often requires derivatization of the analytes
and generally produces fragment ions upon ionization thus complicating their mass
spectra.[10] GC-MS is useful for analyzing thermally stable molecules but is less adequate
for analyzing molecules present in biomass pyrolysis products due to the high temperatures
required for the analysis.[11-14]

Liquid chromatography coupled with mass spectrometry (LC-MS) is a versatile
technique for biomass pyrolysis product analysis due to its ability to separate and ionize
carbohydrate mixtures without the need for high temperatures or analyte derivatization.[15]
Gentle ionization of analytes in LC-MS experiments may be achieved via electrospray
ionization (ESI) provided a suitable ionization reagent can be identified. A good ionization
reagent yields one predominant ion-type without causing excessive fragmentation of the

analyte ion. Due to the numerous labile bonds in mono- and oligosaccharides , some LC-MS methods still employ derivatization prior to ionization in order to avoid excessive fragmentation of the analyte ions.[16] On the other hand, alkali metal cations (e.g., Li^+, Na^+) have been found to be effective in generating stable adducts of underivatized oligosacharrides by ESI without inducing fragmentation.[17-19] In these studies, monolithiated isomeric dissacharides and oligosaccharides were subjected to collision-activated dissociation thus revealing linkage positions of the glycosidic bonds.

In the current study, we report the utility of LC-MS incorporating Al^{3+} ion as a gentle ionization reagent for studying epimeric 1,6-anhydrosugars. These species have not previously been studied by this method and are of relative importance due to their abundance as products from pyrolysis of cellulosic biomass.[3,20] Additionally, the structures of these species were examined using density functional theory calculations to understand how Al^{3+} binds with saccharides since this information may pertain to future uses of Al^{3+} as an important ionization reagent. CAD of the formed complexes was investigated as a method for distinguishing isomeric 1,6-anhydrosugar complexes with Al^{3+} based on differences in their fragmentation spectra. Finally, the method was tested with a product mixture derived from pyrolysis of cellobiose to determine its ability to identify levoglucosan within a complex mixture.

5.2 Experimental

Solvents used for HPLC-coupled mass spectrometric analysis were LC-MS grade and used without further purification. Aluminum trichloride was purchased from Acros Organics at a purity of ≥99%. Formic acid (97%) was purchased from Alfa Aesar and used

as is for doping all LC-MS grade solvents used in the study. 1,6-Anhydro-β-D-glucopyranose (levoglucosan), 1,6-anhydro-β-D-galactopyranose (galactosan), and 1,6-anhydro-β-D-mannopyranose (mannosan) were purchased from Carbosynth with purity ranging from 97-99%. Feedstocks used for the fast-pyrolysis experiments were 50 μm microcrystalline cellulose and D-(+)-cellobiose (>99.0%, ~50 μm) from Sigma Aldrich (St. Louis, MO).

The fast-pyrolysis experiments were conducted using a high-pressure, cyclone-type, fast-pyrolysis reactor system. The detailed description of this reactor is available in the literature.[21] The pyrolysis experiments were performed at ~500 °C pyrolysis temperature at a total inert pressure of 27 bar (25 bar helium and 2 bar nitrogen). The feed flow rate was ~0.5 g min^{-1} and experimental run time was ~1 hour. The vapor residence time in the fast-pyrolysis reactor was ~2 seconds. The liquid products from the cellulose and cellobiose fast-pyrolysis experiments were analyzed with the techniques, as explained below.

Standards were prepared by dissolving 2.5 mg of the anhydrosugar in 3 mL of an aqueous 0.1% formic acid solution to produce a final analyte concentration of 5 mM. Pyrolysis-oil samples were prepared by dissolving 40 mg of liquid in 3 mL aqueous 0.1% formic acid solution. These solutions were placed in 1 mL sample vials suitable for the Finnigan Surveyor Plus HPLC system. 2.5 mg AlCl$_3$ was dissolved in 3 mL of an aqueous 0.1% formic acid in water solution to produce a final concentration of 6 mM. However, concentrations as high as 12 mM AlCl$_3$, at the same syringe flow rate, did not noticeably alter results.

All analytes were introduced into the mass spectrometer by ESI operating in positive-ion mode. Source conditions for these experiments were as follows: (capillary temperature: 275 ^{0}C; sheath gas flow: 80 a.u.; auxillary gas flow: 30 a.u.; spray voltage: +3 kV; capillary voltage: 11 V; tube lens: 65 V). The trapping region of the instrument was maintained at ~10^{-5} Torr by a triple-inlet turbomolecular pump as measured by an ion gauge. The HPLC and LQIT were controlled by the Xcalibur 2.0 software and LTQ Tune Plus interface. HPLC runs involved injection of 25 µL of sample solution onto a 300 X 7.8 mm Phenomenex Rezex ROA-organic acid analytical column. The Surveyor AS column oven control maintained the column at a constant 60 ^{0}C during the LC separation. Separations were performed isocratically using a 0.1% formic acid in water mobile phase at a flow rate of 400 µL min^{-1} with the total runtime being 30 minutes per analysis. Aluminum trichloride solution was loaded into a Hamilton 500 µL, Model 1750 C-XP SYR, gastight syringe and t-infused with the LC eluent at a constant flow rate of 10 µL min^{-1} via the LQIT syringe pump. Full schematic of the experimental setup can be seen in Figure 5.1.

Density functional theory (DFT) combined with the hybrid generalized gradient approximation functional developed by Becke, Lee, Yang, and Parr (B3LYP)[22-24] was used to compute the optimized geometries of the $2(M-H^+)^- + Al^{3+}$ analyte species. This popular method uses the Becke88 exchange functional combined with the Lee—Yang—Parr (LYP) correlation functional. The local minima predicted by this method were confirmed by computing the vibrational frequencies which were used to obtain the zero-point energies and thermal enthalpies ($H_{298} - E_0$) for the three analytes. The contracted double basis set 6-31++G(d,p)[25] was used for the approximation of molecular orbitals. Enthalpy differences

(ΔE_e^o) were calculated as the difference in the corrected enthalpies of product $[2(M - H^+)^-$ + Al(III)] and reactant [2M] where M = 1,6-anhydrosugar. ΔE_e^o was used to compare relative binding enthalpies between the three sugars with levoglucosan as the reference ($\Delta E_e^o = 0$). All calculations were performed using the Gaussian 09 software suite (Revision C.01).[26]
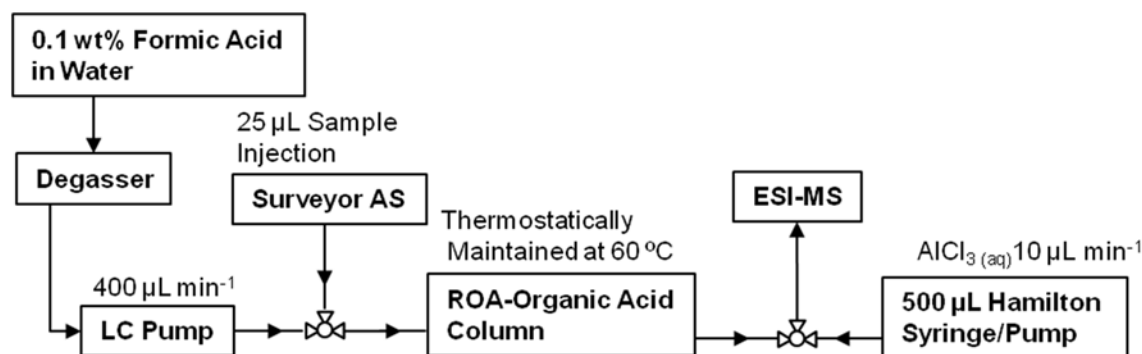
Figure 5.1 LC-MS scheme for AlCl₃ experiments. The surveyor autosampler (AS) injects 25 µL of a 5mM aqueous solution of the pyrolysis-oil sample onto the ROA-organic acid column. LC-MS grade water doped with 0.1% formic acid is pumped by the LC pump through the column which separates constituents in the sample. This processed sample stream is mixed with AlCl₃(aq) soltuion via tee connector and fed into the electrospray ionization (ESI) source of the mass spectrometer where the constituents are analyzed in real time by the linear quadrupole mass spectrometer (LQIT-MS).

5.3 Results and Discussion

In order to assess Al^{3+} for its ability to distinguish isomers in raw pyrolysis-oil samples, levoglucosan (LG) and two of its epimers were chosen for evaluation—galactosan (GS) & mannosan (MN). The mixture of these compounds was subjected to separation by reversed-phase ion-exchange HPLC using an isocratic elution medium consisting of 0.1% (v/v) formic acid in water. The column chosen for this separation was a Rezex ROA-organic acid column (chosen because of its ability to separate carbohydrates). HPLC eluent

was allowed to mix with AlCl$_3$ solution via tee connector which allowed dissolved Al^{3+}$_{(aq)}$ cations to react with analytes eluting from the column (Figure 5.1). This allowed for the generation of Al^{3+} complexes with analyte ions which were subjected to isolation and CAD experiments (MS^2). Mass spectra from the fragmentation of analyte complexes were used for distinguishing the isomers of LG. DFT calculations were used to obtain structures for the Al^{3+} complexes with 1,6-anhydrosugars and to determine which structural properties affect their binding enthalpies.

5.3.1 HPLC-MS of Al^{3+} Complexes with 1,6-Anhydrosugars

Aluminium complexes in solution have been studied before using ESI and within the list of thermodynamically stable monomeric species there are three main aluminium hydroxides [Al(OH)]$^{2+}$, [Al(OH)$_2$]$^+$, and [Al(OH)$_3$]^0. [27,28] These species are formed by the hydrolysis of [Al · (H$_2$O)$_x$]$^{n+}$ and is the reason aqueous AlCl$_3$ solutions are always found to be acidic as shown in Scheme 5.1.

$$[Al(H_2O_x)]^{3+} \rightleftharpoons [Al(OH)_n(H_2O)_{x-n}]^{2+} + H^+$$

Scheme 5.1 Equilibrium of aquaaluminum complexes in solution.

The full mass spectrum of only the eluent with tee infused AlCl$_{3(aq)}$ reveals an abundant tetravalent metal-ion complex with formic acid and water (m/z 153) (Figure 5.2). Upon elution of LG, GS and MN from the column, a bidentate Al^{3+} complex [2(M − H) + Al]$^+$ (m/z 349) was formed. Retention times for each analyte were determined from the chromatogram of ion intensities for the m/z 349 ion. This "extracted" ion chromatogram

(XIC) is generated by monitoring the ion of interest (m/z 349) as a function of time and performing a data-mining process using the Xcalibur software. GS was found to separate well from LG and MN however, LG and MN co-eluted (Figure 5.3). Thus, each of the three anhydrosugars were analyzed by HPLC-MS individually and subjected to CAD experiments for comparison (Figure 5.4). A particularly interesting observation is the large difference in signal intensity produced by Al^{3+} complexes of GS with respect to LG and MN.
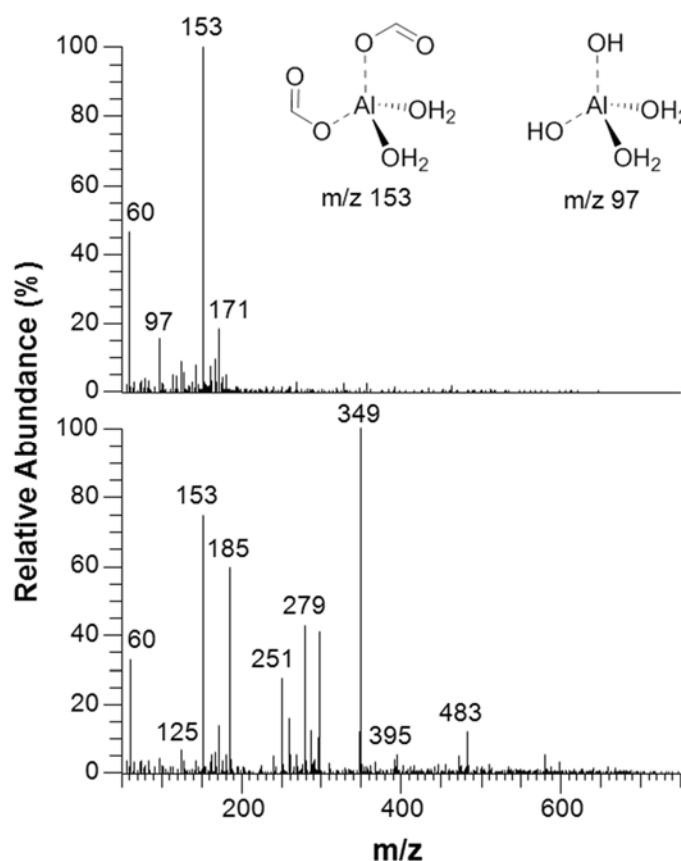
Figure 5.2 Full mass spectrum of 0.1% (v/v) formic acid eluent at retention time 4.88 min. The dominant Al^{3+} species is a tetrahedral coordination complex with two deprotonated formic acid molecules and two water molecules (m/z 153) (top). Full mass spectrum of LG at retention time 19.32 min (bottom) showing the $[2(M - H) + Al]^+$ ion (m/z 349).
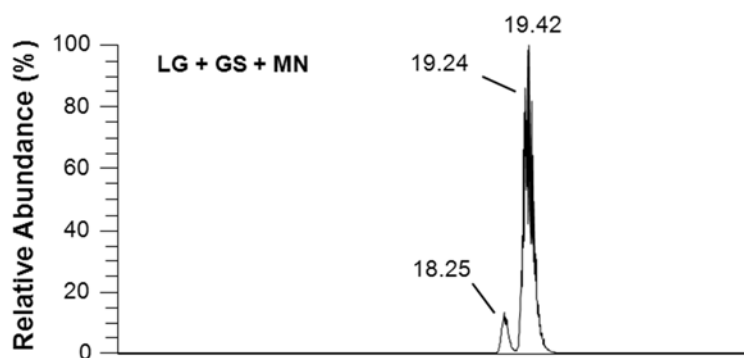
Figure 5.3 Extracted ion chromatogram of 1,6-anhydrosugar epimers, levoglucosan (LG), galactosan (GS), and mannosan (MN) corresponding to the $[2(M-H)+Al]^+$ ion (m/z 349) (M = LG, GS, or MN).
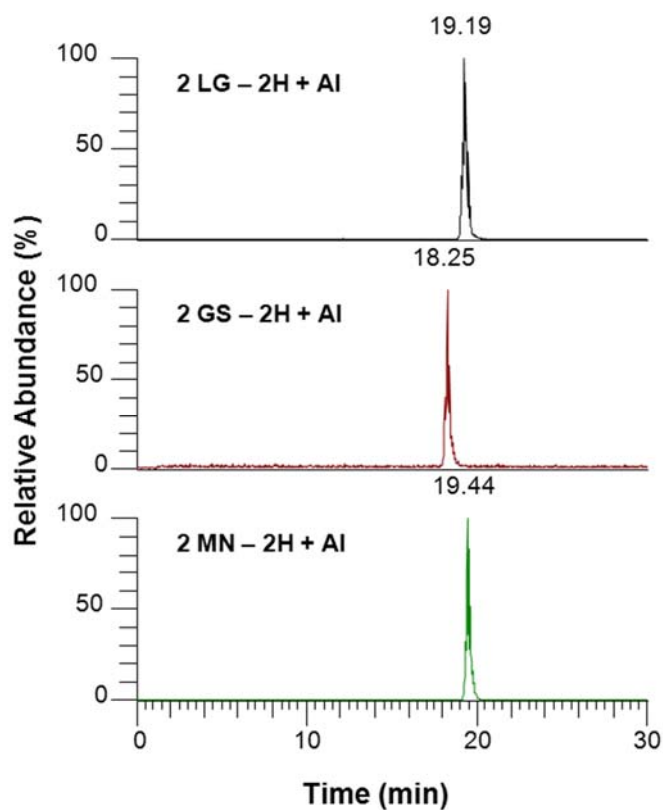
Figure 5.4 Individual extracted ion chromatograms (XIC) for the $[2(M-H)+Al]^+$ ion (m/z 349) signal. XIC of Al^{3+} product with levoglucosan (top), galactosan (middle), and mannosan (bottom).

5.3.2 Geometries of Al^{3+} Complexes with 1,6-Anhydrosugars

To explain the differences in signal intensity for the anhydrosugars examined, each of the Al^{3+} complexes were examined computationally at the B3LYP/6-31++G(d,p) level of theory to obtain energy minimized structures and calculate binding enthalpies. Structural features were compared among analyte complexes to investigate the cause for difference in binding enthalpy among the complexes. LG was found to form two stable complexes with Al^{3+}: pseudo-tetrahedral and pseudo-octahedral (Figure 5.5). The pseudo-tetrahedral isomer of LG $[2(M - H) + Al]^+$ is only marginally higher in energy (<1 kcal mol^{-1}) suggesting that both of these two isomers form in solution. Conversely, DFT calculated structures of Al^{3+} complexes of GS and MN were found to possess only the pseudo-tetrahedral configuration. The tetrahedral configuration of the Al^{3+} complexes produced by the eluent (formic acid & water) were also found to be lower in energy relative to other configurations. Two major configurations exist for coordination number 4—tetrahedral and square planar. Geometry optimizations of the square planar analogs of the $[Al(OH)_2(H_2O)_2]^+$ ion (m/z 97) failed to converge to a local minimum with the prescribed structure but instead converged to the pseudo-tetrahedral structure as the nearest minimum in the potential energy surface (PES). Thus, single point energies of the square planar analogs were calculated and compared to the pseudo-tetrahedral analogs for each solvent-metal complex which revealed an unfavorable energetic difference for the square planar configuration. This suggests the tetrahedral configuration of Al^{3+} complexes is also preferable for non-chelating ligand types (Figure 5.5).
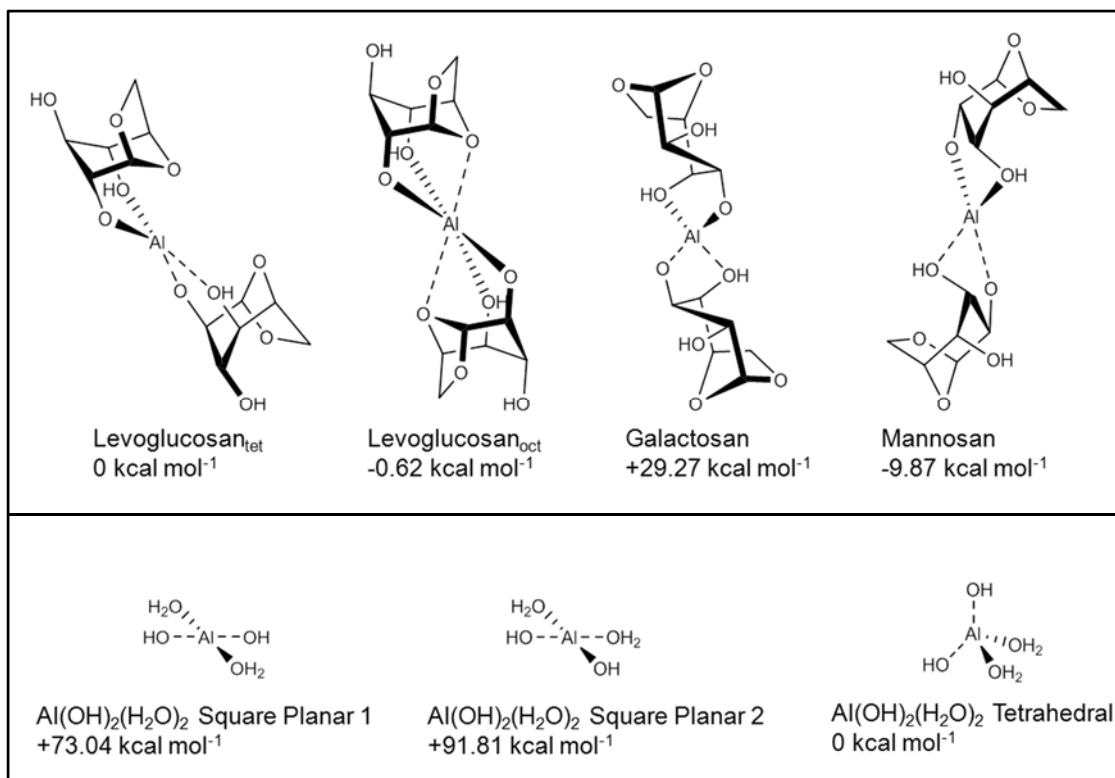
Figure 5.5 Equilibrium geometries of $[2(M - H) + Al]^+$ anhydrosugar complexes and the relative binding enthalpies (LG_{tet} = 0 kcal mol^{-1}) calculated at the UR-DFT/B3LYP/6-31++G(d,p) level of theory (top). Same level of theory applied to solvent complexes ($Al(OH)_2(H_2O)_2$ tetrahedral = 0 kcal mol^{-1}) (bottom).

For each isomer of anhydrosugar $[2(M - H) + Al]^+$ complex to conform to the tetrahedral structure, the two bidentate ligands must twist by ~90° relative to each other. GS also binds in this manner as well except that the C6 ring of the GS ligand contorts to adopt a boat conformation contrary to its unbound form which prefers the lower energy chair conformation. Steric hindrance may prevent galactosan from binding as efficiently as LG and MN with Al^{3+} and may play a role in the decreased ion current produced for this analyte. In addition to the stereo-selectivity of the Al^{3+} ion in each complex, the tetrahedral bond angles obtained from equilibrium geometries were found to be disproportionate.

Angle x_1 which represents the angle between deprotonated hydroxyls (DPH) in the complexes was found to be wider when compared to the angle between the non-deprotonated hydroxyls (NDH) (Table 5.1). MN has the largest x_1 angle and actually adopts the disphenoidal (see-saw) geometry. GS has the largest x_2 angle edging closer to the square planar configuration than the other complexes, which, has already been to shown to be higher in energy for the formic acid and water complexes with Al^{3+}. LG_{tet} (Figure 5.5) adopts a tetrahedral configuration that has similar bond angles as the calculated structure of $[Al(OH)_2(H_2O)_2]^+$. This may be an indication of the steric freedom offered by 1,3-coordination of the two coordinated hydroxyls in LG to the Al^{3+} metal center.

Table 5.1 Tetrahedral Angles of Selected $[2(M - H) + Al]^+$ Complexes.
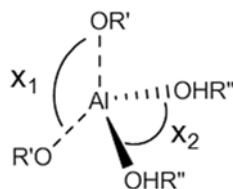
R' = C [LG, GS, & MN], H [Al(OH)$_2$(H$_2$O)$_2$]
R" = C [LG, GS, & MN], H [Al(OH)$_2$(H$_2$O)$_2$]

$2(M - H)^- + Al^{3+}$	Degree (angle)	
M	x_1	x_2
Al(OH)$_2$(H$_2$O)$_{2\,tet}$	144.718	100.058
Levoglucosan$_{tet}$	141.667	95.579
Galactosan	141.103	114.634
Mannosan	173.133	102.207

The relevant energies corresponding to the tetrahedral angles between DPH and NDH were revealed by performing a relaxed potential energy scan of these two coordinates

in the water complex $[Al(OH)_2(H_2O)_2]^+$. Relaxed scans were performed by constraining the bond angle (x_1 or x_2) then optimizing the structure to the nearest minimum. Modification of the bond angle x_1 results in increased potential energy due to Van Der Waals forces between the electron-rich oxygen atoms. However, the increase in energy is rather gradual in the range of bond angles between135-144 degrees and only corresponds to an increase of ~0.3 kcal mol^{-1} for LG and GS when compared to the equilibrium value. The energy actually begins to level off approaching the x_1 equilibrium bond angle of 144.718 degrees but begins to rise slowly as it approaches linearity. For MN this involves an 8 kcal mol^{-1} increase in potential energy along the x_1 coordinate but as we will soon see this increased energy seems to be mitigated by a favorable binding enthalpy. Potential energy was found to increase more rapidly for the x_2 scan corresponding to the angle between NDH's. Still the effect is only marginal even for GS which has an x_2 angle ~10 degrees tighter than the equilibrium value. Potential energy increases for GS are <1.5 kcal mol^{-1} and not likely to contribute to the overall energy profile in a major way.

5.3.3 Influence of Binding Enthalpy on Relative Response Factor f_i

In addition to geometry optimization calculations, binding enthalpies were computed and compared for each complex by calculating the sum of electronic and thermal enthalpies ($H_{298} - E_0$) for the unbound sugars (M) then taking the difference between this value and the calculated value for each complex:

$$\triangle E_e^0 = E_e^0([2(M - H^+) + Al^{3+}]^+ - 2E_e^0(M) \qquad (5.1)$$

Energies were set relative to the LG $[2(M - H) + Al]^+$ complex ($\Delta E_e^o = 0$). This information was related to the relative response factor f_i for each analyte:

$$f_i = \frac{A_i}{A_{LG}} \tag{5.2}$$

where A_{LG} is the integrated peak area from the XIC for the LG $[2(M - H) + Al]^+$ analyte. A_i represents the integrated peak area of each analyte species. Table 5.2 contains the results of this comparison which shows good agreement between theory and experiment. GS, whose enthalpy of formation is less favorable by nearly 30 kcal mol^{-1}, has a response factor f_i only 14% that of LG. MN rather has a lower enthalpy of formation relative to LG by nearly 10 kcal mol^{-1} which agrees with the increased response factor for MN relative to LG.

Table 5.2 Comparison of Relative Binding Enthalpies with the Relative Response Factor f_i

$2(M - H)^- + Al^{3+}$	B3LYP 6-31++G(d,p)	Peak Area	Relative Response Factor
M	ΔE_e **(kcal/mol)**	a.u.	f_i
Levoglucosan$_{tet}$	0	26302550	1
Levoglucosan$_{oct}$	-0.62		
Galactosan	29.27	3553851	0.1351
Mannosan	-9.87	38414387	1.4605

5.3.4 1,6-Anhydrosugar Epimer Identification in Pyrolysis Oil

Obvious differences in the CAD mass spectra shown in Figure 5.6 make distinguishing LG epimers facile by this method. LG does not contain the fragment

pertaining to loss of glyoxal ($C_2H_2O_2$) as MN does and GS is disproportionately favorable to loss of formaldehyde and water (m/z 301). Fragmentation pathways have been shown to be regiospecific in literature when charged sites, such as a DPH group, adopt different orientations.[29] The primary fragmentation pathway of LG $[2(M - H) + Al]^+$ is loss of a C4 fragment $C_4H_6O_3$ differing from GS & MN which readily lose water instead (Table 5.3). Comparison CAD spectra from pyrolysis-oil (Figure 5.7), produced by the pyrolysis of cellulose, with that of LG unequivocally confirms the identity of the major isomer present in the sample to be LG with no other isomers present above 5% relative abundance. However, the pyrolysis of cellobiose yields two additional LG isomers with different retention times (Figure 5.10). The primary isomer produced by this method is still LG with the other two isomers totaling <10% abundance relative to LG. Eluen **B** fragments to yield the ions of m/z 331, 283, 247, and 205 in approximately the same relative abundances as LG (peak **A**) but the product ions of m/z 321, 265, and 185 are unique. Additionally the loss of $C_2H_2O_2$ (m/z 291) appears to be more facile for **B** in comparison to LG which produces only 3.5% relative abundance of this product ion. CAD spectra for eluen **C** is more simple in comparison to previous analytes studied suggesting perhaps the structure has fewer fragmentation pathways available to it or that the three major products ($P^+ - H_2O$; CO; CH_2O_2) have low barriers to formation.
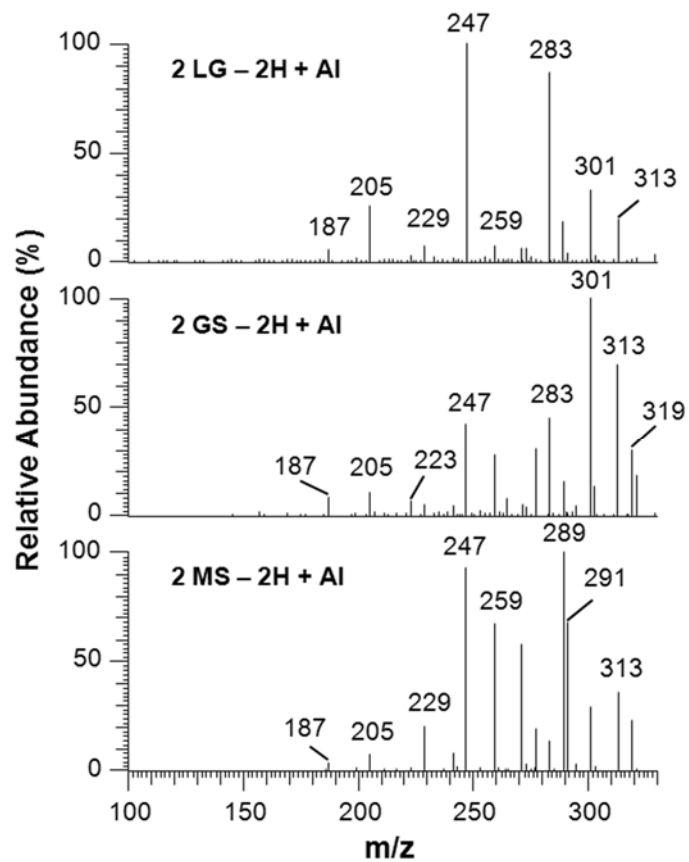
Figure 5.6 Comparison of MS^2 CAD spectra for $[2(M - H) + Al]^+$ complexes of LG, GS, and MN.

Table 5.3 MS^2 CAD Fragment Ions Formed from $[2(M - H) + Al]^+$ Ions.
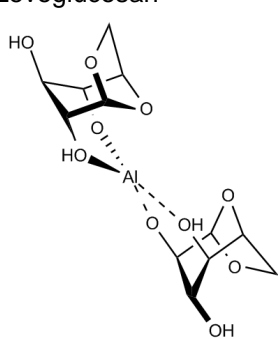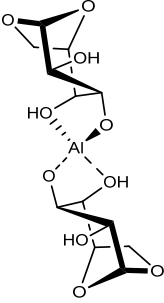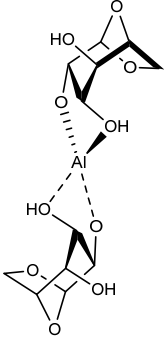
Complex (P$^+$)	m/z	Fragment Ions
Levoglucosan	247	P$^+$ – C$_4$H$_6$O$_3$
	283	P$^+$ – CH$_2$O – 2H$_2$O
	331	P$^+$ – H$_2$O
	301	P$^+$ – CH$_2$O – H$_2$O
	205	P$^+$ – C$_6$H$_8$O$_4$
	289	P$^+$ – C$_2$H$_4$O$_2$
	313	P$^+$ – 2H$_2$O
	259	P$^+$ – C$_3$H$_6$O$_3$
	271	P$^+$ – C$_2$H$_6$O$_3$
	273	P$^+$ – C$_2$H$_4$O$_3$
	229	P$^+$ – C$_4$H$_6$O$_3$ – H$_2$O
	187	P$^+$ – Levoglucosan
	291	P$^+$ – C$_2$H$_2$O$_2$

Table 5.3 (continued)

Complex (P⁺)	m/z	Fragment Ions
Galactosan	331 $P^+ - H_2O$ 301 $P^+ - CH_2O - H_2O$ 313 $P^+ - 2H_2O$ 247 $P^+ - C_4H_6O_3$ 283 $P^+ - CH_2O - 2H_2O$	
Mannosan	331 $P^+ - H_2O$ 247 $P^+ - C_4H_6O_3$ 289 $P^+ - C_2H_4O_2$ 259 $P^+ - C_3H_6O_3$ 291 $P^+ - C_2H_2O_2$ 271 $P^+ - C_2H_6O_3$ 313 $P^+ - 2H_2O$ 301 $P^+ - CH_2O - H_2O$	

*Products with relative abundances <5% are not included. Fragment molecules are ordered from those having the highest abundance to those with the lowest abundance.
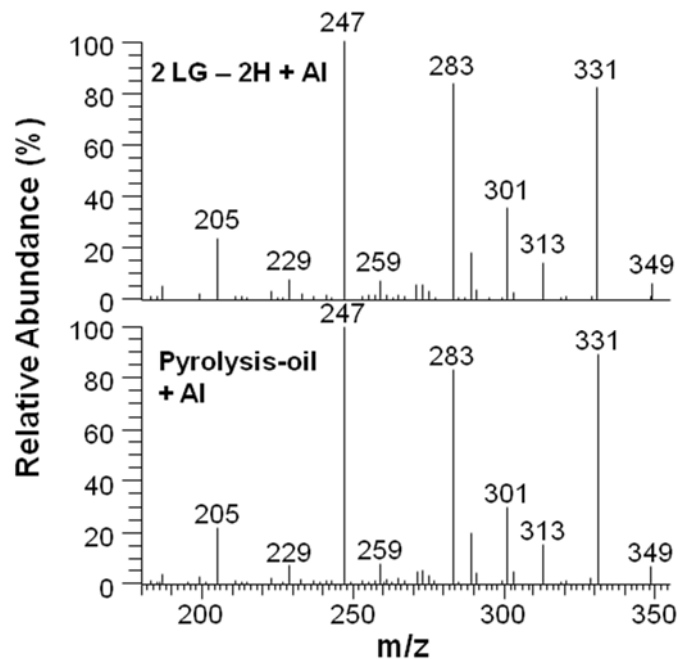
Figure 5.7 MS^2 CAD spectra comparison for LG (top) and pyrolysis-oil (bottom) [2(M – H) + Al]$^+$ complexes. Levoglucosan is the major isomer present in pyrolysis-oil.
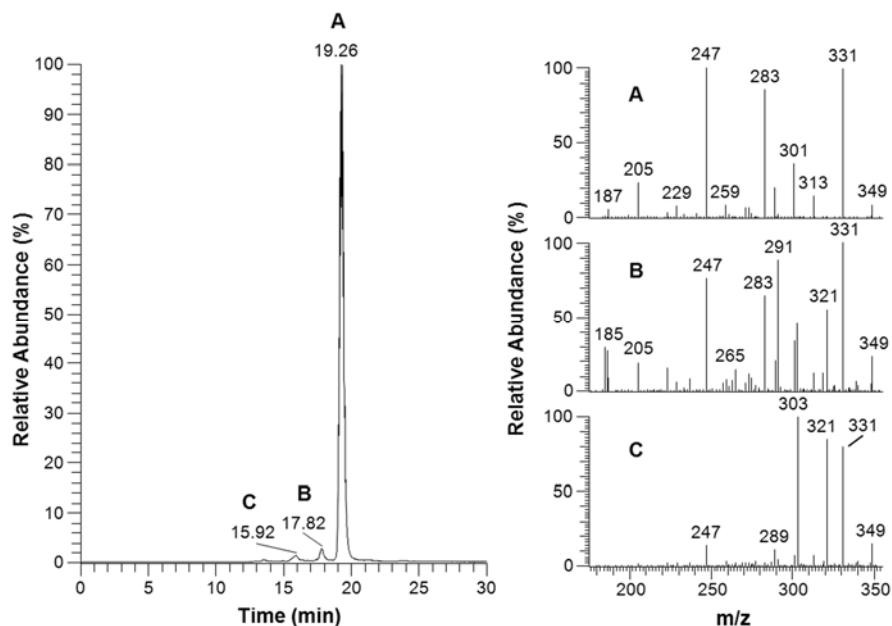
Figure 5.8 Oil from the pyrolysis of cellobiose by using a cyclone reactor. The extracted ion chromatogram of ions of m/z 349 (left). CAD (MS^2) spectra of ionized A-C (right).

5.4 <u>Conclusions</u>

The utility of a novel HPLC/MS method has been demonstrated for the separation and distinction of isomeric anhydrosugars. A ROA-organic acid column, utilizing a 0.1% formic acid (v/v) eluent, achieved baseline separation of GS from LG and MN however, a variety of columns may be supplemented depending on the nature of the saccharides being examined. The energetic properties affecting analyte binding with Al^{3+} has been explored and was found to describe the relative differences in binding enthalpy. Coordination variances of the aluminum/analyte complexes of epimeric anhydrosugars affects their fragmentation behavior facilitating differentiation based on MS^2 results. This gentle ionization technique displayed no obvious signs of fragmentation and although many Al^{3+} species are generated, only one product was dominant in every case. The ability of this method to distinguish between isomers in a real pyrolysis-oil mixture suggests it can be used as a analytical method for assisting pyrolysis reactor design and development for which the tailoring of end products is desired. Additionally, identification of final products from the pyrolysis of cellobiose may be used to improve mechanistic understanding of pyrolysis reactions.

5.5 <u>References</u>

1.   Radlein, D. S. T. A. G.; Grinshpun, A.; Piskorz, J.; Scott, D. S. *J. Anal. Appl. Pyrolysis* **1987**, *12*, 39.

2.   Wolff, I. A.; Olds, D. W.; Hilbert, G. E. *Starke* **1968**, *20*, 150.

3.   Kuzhiyil, N.; Dalluge, D.; Bai, X.; Kim, K.; Brown, R. *ChemSusChem* **2012**, *5*, 2228.

4.   Simoneit, B. R. T. *Appl. Geochem.* **2002**, *17*, 129.

5.   Simoneit, B. R. T.; Schauer, J. J.; Nolte, C. G.; Oros, D. R.; Elias, V. O.; Fraser, M. P.; Rogge, W. F.; Cass, G. R. *Atmos. Environ.* **1999**, *33*, 173.

6.   Fabbri, D.; Torri, C.; Simoneit, B. R. T.; Marynowski, L.; Rushdi, A. I.; Fabiańska, M. J. *Atmos. Environ.* **2009**, *43*, 2286.

7.   Puxbaum, H.; Caseiro, A.; Sánchez-Ochoa, A.; Kasper-Giebl, A.; Claeys, M.; Gelencsér, A.; Legrand, M.; Preunkert, S.; Pio, C. *J. Geophys. Res. Atmos.* **2007**, *112*, D23S05.

8.   Alfarra, M. R.; Prevot, A. S. H.; Szidat, S.; Sandradewi, J.; Weimer, S.; Lanz, V. A.; Schreiber, D.; Mohr, M.; Baltensperger, U. *Environ. Sci. Technol.* **2007**, *41*, 5770.

9.   Simoneit, B. R. T.; Elias, V. O. *Mar. Pollut. Bull.* **2001**, *42*, 805.

10.   Hsu, C.-L.; Cheng, C.-Y.; Lee, C.-T.; Ding, W.-H. *Talanta* **2007**, *72*, 199.

11.   Mullen, C. A.; Boateng, A. A. *Energy Fuels* **2008**, *22*, 2104.

12.   Mullen, C. A.; Boateng, A. A.; Hicks, K. B.; Goldberg, N. M.; Moreau, R. A. *Energy Fuels* **2009**, *24*, 699.

13.   James, P. D.; Stefan, C. *Energy Fuels* **1997**, *11*.

14.   Hélène, A.; Christian, R. *Fuel Sci. Tech. Internat.* **1990**, *8*.

15.   Piot, C.; Jaffrezo, J.-L.; Cozic, J.; Pissot, N.; Haddad, I. E.; Marchand, N.; Besombes, J.-L. *Atmos. Meas. Tech.* **2012**, *5*, 141.

16.   McRae, G.; Monreal, C. M. *Anal. Bioanal. Chem.* **2011**, *400*, 2205.

17.   Zhou, Z.; Ogden, S.; Leary, J. A. *J. Org. Chem.* **1990**, *55*, 5444.

18.   Harvey, D. J. *J. Mass Spectrom.* **2000**, *35*, 1178.

19.   Hofmeister, G. E.; Zhou, Z.; Leary, J. A. *J. Am. Chem. Soc.* **1991**, *113*, 5964.

20.   Aho, A.; Kumar, N.; Eranen, K.; Holmbom, B.; Hupa, M.; Salmi, T.; Murzin, D. Y. *Int. J. Mol. Sci.* **2008**, *9*, 1665.

21.   Venkatakrishnan, V. K.; Degenstein, J. C.; Smeltz, A. D.; Delgass, W. N.; Agrawal, R.; Ribeiro, F. H. *Green Chem.* **2013**.

22.   Becke, A. D. *Phys. Rev. A* **1988**, *38*, 3098.

23.   Becke, A. D. *J. Chem. Phys.* **1996**, *104*, 1040.

24.   Lee, C.; Yang, W.; Parr, R. G. *Phys. Rev. B* **1988**, *37*, 785.

25.   Krishnan, R.; Binkley, J. S.; Seeger, R.; Pople, J. A. *J. Chem. Phys.* **1980**, *72*, 650.

26.   Frisch, M. J.; Trucks, G. W.; Schlegel, H. B.; Scuseria, G. E.; Robb, M. A.; Cheeseman, J. R.; Scalmani, G.; Barone, V.; Mennucci, B.; Petersson, G. A.; Nakatsuji, H.; Caricato, M.; Li, X.; Hratchian, H. P.; Izmaylov, A. F.; Bloino, J.; Zheng, G.; Sonnenberg, J. L.; Hada, M.; Ehara, M.; Toyota, K.; Fukuda, R.; Hasegawa, J.; Ishida, M.; Nakajima, T.; Honda, Y.; Kitao, O.; Nakai, H.; Vreven, T.; J. A. Montgomery, J.; Peralta, J. E.; Ogliaro, F.; Bearpark, M.; Heyd, J. J.; Brothers, E.; Kudin, K. N.; Staroverov, V. N.; Keith, T.; Kobayashi, R.; Normand, J.; Raghavachari, K.; Rendell, A.; Burant, J. C.; Iyengar, S. S.; Tomasi, J.; Cossi, M.; Rega, N.; Millam, J. M.; Klene, M.; Knox, J. E.; Cross, J. B.; Bakken, V.; Adamo, C.; Jaramillo, J.; Gomperts, R.; Stratmann, R. E.; Yazyev, O.; Austin, A. J.; Cammi, R.; Pomelli, C.; Ochterski, J. W.; Martin, R. L.; Morokuma, K.; Zakrzewski, V. G.; Voth, G. A.; Salvador, P.; Dannenberg, J. J.; Dapprich, S.; Daniels, A. D.; Farkas, O.; Foresman, J. B.; Ortiz, J. V.; Cioslowski, J.; Fox, D. J.; Revision C.01 ed.; Gaussian Inc.: Wallingford CT, 2010.

27.   Sarpola, A.; Hietapelto, V.; Jalonen, J.; Jokela, J.; Laitinen, R. S. *J. Mass Spectrom.* **2004**, *39*, 423.

28.   Baes, C. F.; Messmer, R. E. *The Hydrolysis of Cations*; John Wiley & Sons Inc, 1976.

29.   Rannulu, N.; Cole, R. *J. Am. Soc. Mass Spectrom.* **2012**, *23*, 1558.

CHAPTER 6. CHARACTERIZATION OF ASPHALTENE DEPOSITS BY USING MASS SPECTROMETRY AND RAMAN SPECTROSCOPY

6.1 <u>Introduction</u>

The precipitation of asphaltenes in oil transfer pipelines and refinery equipment is a global problem which has exacerbated in recent years with the partial depletion of lighter "sweet" crude oil in oil reservoirs.[1,2] Asphaltenes are the heaviest fraction of crude oil and are procedurally defined as being soluble in toluene but insoluble in *n*-alkanes.[3] Since asphaltenes are defined by their solubility rather than a well-defined molecular structure, they represent a complicated mixture consisting of molecules with many different structures and functionalities. In general, asphaltenes have been shown to contain molecules with polycondensed aromatic rings possessing alkyl chains and sometimes heteroatoms (S, N, and to a lesser extent O) and/or metals.[4] Self-association of asphaltenes is thought to be the step preceding precipitation and it has been shown to be related to the structures of asphaltenes.[5,6] In particular, the aromaticity has been correlated with self-association behavior.[5] Furthermore, the lengths of their alkyl chains influences their stability in crude oil, with longer alkyl chains resulting in decreased rate of precipitation.[6] As the utilization of deepwater oil-gas resources becomes an important strategy for prolonged energy solutions, prevention and remediation of asphaltene deposits will play a vital role in ensuring the safe operation of offshore drilling stations.[7] Thus, a better

understanding of the molecular structures of asphaltenes in oil deposits is imperative for researchers to develop improved methods for controlling asphaltene deposition.[8,9]

The propensity of asphaltenes to aggregate has been shown to be partially dependent on the average diameter of the polycondensed aromatic sheet of their structures which can be studied by Raman spectroscopy.[10] Average molecular dimensions of a polycondensed aromatic sheet can be estimated from the integrated intensities of graphitic bands in the Raman spectra of asphaltenes.[11,12] These bands arise from the microcrystalline planar structure of the graphite-like condensed aromatic sheets of asphaltenes. Variation in the diameter of the aromatic sheet has been observed for asphaltenes from different geological origins, with most falling in the 10-20 Å range.[10,12] Smaller diameters have been correlated with greater stability of the asphaltenes in crude oil.[10] Thus, examination of the aromatic sheet size of asphaltenes derived from oil deposits is essential for understanding the types of asphaltene structures that participate in deposition.

Additional characterization of the molecular structures of asphaltenes in crude oil deposits may be obtained with the use of mass spectrometry. Alkyl chain lengths, aromatic core sizes, and molecular weight distributions (MWDs) can be estimated from mass spectrometric analysis of ionized asphaltenes.[13,14] Tandem mass spectrometry (MS^n) is well suited for studying complicated mixtures such as asphaltenes due to its ability to probe ions of individual constituents without prior separation.[15] This requires an ionization method that produces a single ion type per analyte to prevent convolution of the mass spectrum. Recently, carbon disulfide was shown to dissolve asphaltene model compounds and yield only molecular ions ($M^{+\bullet}$) upon ionization when operating the instrument in positive ion mode.[14,16]

In this study, Raman spectroscopy and mass spectrometry experiments were carried out on *n*-heptane precipitated asphaltenes derived from crude oil deposits originating from a Wyoming oil well with known deposition issues. The diameter of the aromatic sheets of the asphaltenes were estimated from the integrated intensities of the graphitic bands in their Raman spectrum. Alkyl chain lengths, approximate aromatic core sizes, and molecular weight distributions (MWD) were determined via tandem mass spectrometry experiments carried out in a Thermo Scientific linear quadrupole ion trap (LQIT).

6.2 Experimental

Crude oil deposits were provided by Nalco Champion. They were derived from the Thompson Fee 2-35 oil well in Wyoming. Carbon disulfide (99.9%) used in the mass spectrometric measurements was purchased from Alfa Aesar and used as received.

Asphaltenes were extracted from crude oil deposit by adding 1 g of the sample to 40 mL of *n*-heptane and stirring at 60 °C for 2 hours followed by storing in dark at room temperature overnight. The resulting mixture was passed through a membrane with 0.45 μm pore size to collect precipitated asphaltenes. The filtrate was washed with 5 mL *n*-heptane and dried under vacuum. The total yield of asphaltenes was 32.7 wt % of the original sample.

Raman spectra were collected with a single-point Raman microspectrometer (λ_{ex} = 532 nm) at the Advanced Analytical Instrumentation Center (AAIC) at the Department of Chemistry at Purdue University. The homemade Raman microscope features a 532-nm DPSS laser (SLOC GL532RM-100) with a peak power of 100 mW. The laser beam was collimated into an optical fiber coupled to the Raman head, equipped with a Semrock 532

MaxLine® laser-line filter and a notch filter. Olympus LMPlan Fl (20x/0.40) or a Nikon E Plan (100x/0.90) objectives were used; the laser power at the sample was measured to be 2.0 mW. The back-reflected light passed through the notch filter and was fiber-coupled to an Acton Research SpectraPro 300i with a 3-grating turret (300, 1200 and 1800 BLZ). For the experiments in this study the 300 BLZ grating was used. The light was then projected onto a Roper Scientific LN/CCD 1340/400-EHRB/1 CCD (charge-coupled device). Data was collected using WinSpec software.

Origin 9.1 software was used to process Raman spectroscopic data. The data were baseline corrected and fitted with a Gaussian function utilizing a three peak fitting scheme. Peak positions were determined from the peak centers at half-maximum.

The asphaltenes were dissolved in carbon disulfide (3 mg/mL) and introduced into the APCI via a syringe pump at a flow rate of 10 μL min^{-1}. APCI source conditions were set as follows: vaporizer temperature: 300 $^{\circ}$C; capillary temperature: 275 $^{\circ}$C; N_2 sheath gas flow: 40 a.u. (arbitrary units); N_2 auxiliary gas flow: 10 a.u.; corona discharge current: 5 μA; capillary voltage: 10 V; and tube lens voltage: 60 V. Molecular ions of varying *m/z* value were isolated and subjected to CAD. An isolation window of 2 Da (selected *m/z* value $\pm$ 1) and a collision energy of 40 arbitrary units was used. The instrument's automated tuning feature was used to optimize mass measurements for ions with *m/z* values in the range from 50 up to 1500.

6.3 <u>Results and Discussion</u>

Asphaltenes derived from crude oil deposits were studied using Raman spectroscopy and mass spectrometry. The Raman spectrum of asphaltenes resembles Raman spectra of

microcrystalline graphite-like materials due to the presence of polycondensed aromatic structures in these samples, thus allowing the use of the Tuinstra and Koenig equation[17] to estimate the size of the polynuclear aromatic structure (PNA). Two frequency bands in the Raman spectrum are typically studied, the G band near 1580 cm^{-1} and the D1 band near 1350 cm^{-1}. The G band arises from the stretching vibration of sp^2 C-C bonds within an ordered PNA structure. In-plane defects and heteroatoms alter the vibrational modes of the sp^2 carbons in the aromatic rings and give rise to the D1 band. In other words, the D1 band arises from vibrational modes occurring at the periphery of a microcrystalline structure, such as the edge of a polycondensed aromatic ring system like those found in asphaltenes.[18] Since the intensity of the D1 band increases linearly with the number of atoms in the periphery, it is possible to estimate the size of this microcrystalline structure.[11,17] Information about the alkyl substituents on these PNA structures, such as the approximate total number of carbons in alkyl side chains, were obtained using mass spectrometry. Prior mass spectrometric studies of ionized asphaltene model compounds have shown that collision-activated dissociation (CAD) of their ions can be used to determine the number of carbons in alkyl substituents and the number of fused aromatic rings in the PNA core.[14,19]

Mass spectrometry experiments were performed by dissolving the oil deposit asphaltenes in carbon disulfide (CS$_2$), ionizing them via positive ion mode APCI, and measuring their mass spectra. The APCI/CS$_2$ method has been shown to produce stable molecular ions (M$^{+\bullet}$) for asphaltene model compounds.[16] The molecular weight distribution (MWD) was obtained from the measured mass spectrum of ionized asphaltenes and used to determine the average molecular weight (AVG MW) according to Equation 6.1. Tandem mass spectrometry (MS$^{\text{n}}$) experiments were performed on isolated ions to

estimate the approximate maximum total number of carbons in all alkyl chains. This was accomplished by subjecting several isolated ions of varying *m/z* values to CAD experiments and counting the number of carbons in the eliminated alkyl radical(s) that produced the fragment ion with the lowest *m/z* value with an abundance greater than 1% (relative to the most abundant ion in the mass spectrum). The approximate size of the largest PNA core was estimated by determining the maximum number of fused aromatic rings necessary to reach the *m/z* value of the fragment ion discussed above (with methylenes possibly still remaining on the PNA core after elimination of alkyl chains via benzylic and other cleavages).

$$\text{AVG MW} = \frac{\sum (m/z) \times \text{area (all peaks)}}{\sum \text{area (all peaks)}} \qquad (6.1)$$

6.3.1 Raman Spectroscopy of Oil Deposit Asphaltenes

The diameter of the aromatic sheet of oil deposit asphaltenes was measured by Raman spectroscopy via determination of G and D1 bands' integrated intensities by using the Tuinstra and Koenig equation (eq. 6.2).[17]

$$\text{Aromatic sheet diameter, } L_a \left(\text{Å}\right) = 44 \, I_G / I_{D1} \qquad (6.2)$$

The integrated intensities I_G (G band) and I_{D1} (D1 band) are sensitive to the crystallite size L_a. Equation 6.2 may be used to estimate L_a as long as the G band is within an applicable wavenumber range of 1575-1610 cm^{-1}. The baseline corrected Raman spectrum of oil

deposit asphaltenes can be seen in Figure 6.1. Three peaks were used to fit the overall spectrum profile by using the Gaussian function. Starting peak positions chosen for the fitting scheme were 1350, 1580, and 1600 cm^{-1} corresponding approximately to D1, G, and D2 vibrational modes. The D2 band is the result of an intravalley process which connects lines of a circle around the K point of a Brillouin zone.[20] It has been suggested to arise from the edge structure of a graphene-like molecule adjacent to the reference PNA molecule, although its physical attribute is still not fully understood.[11] Thus, evaluation of the aromatic sheet diameter by Equation 6.2 should only involve D1 and G band intensities.
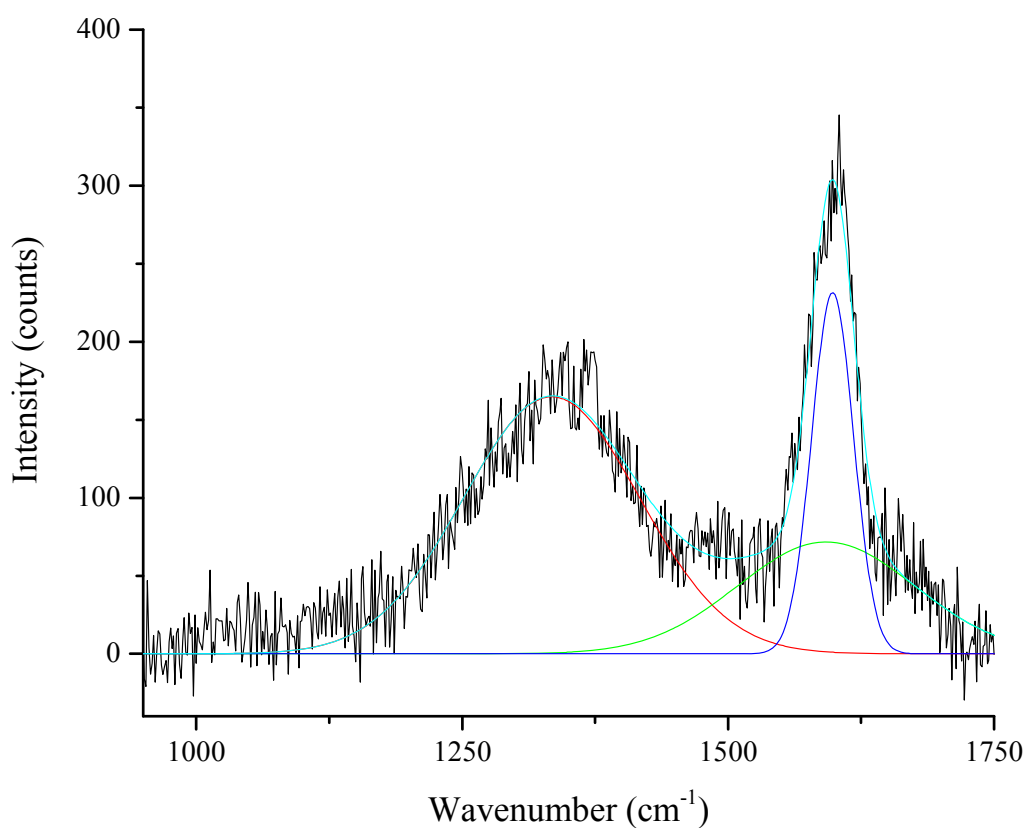
Figure 6.1 Baseline corrected Raman spectrum of oil deposit asphaltenes fitted with the Gaussian function by using three peaks.

The fitted peak positions for D1, G, and D2 bands were found to be 1334 cm^{-1}, 1592 cm^{-1}, and 1598 cm^{-1}, respectively. Evaluation of Equation 6.2 by using the integrated intensities of D1 and G bands indicates an average aromatic sheet diameter (L$_a$) of 19.27 Å. The L$_a$ value is larger than those found for asphaltenes derived from crude oil samples from various geological locations.[12] Heptane precipitated asphaltenes from crude oil originating from Alaska, Mexico, Canada, and Saudi Arabia were studied previously by Raman spectroscopy and observed to have L$_a$ values in the range 15.2-18.8 Å when using the Gaussian function to fit their spectral profiles.[12] The larger L$_a$ value for this sample would suggest that asphaltenes derived from crude oil deposits have larger PNA structures than asphaltenes derived from bulk oil. As reported previously, larger L$_a$ values correlate with lower asphaltene stability, likely as a result of increased self-association among the asphaltene molecules.[10] In other words, a greater number of fused rings in the PNA structure facilitates self-association behavior and thus increases the rate of precipitation of asphaltenes.

6.3.2 Mass Spectrometric Analysis of Asphaltenes in Crude Oil Deposit

The mass spectrum measured for ionized oil deposit asphaltenes can be seen in Figure 6.2. The observed MWD ranges from 150 Da up to 1050 Da, with an AVG MW of 497 Da. These values are lower than MWDs and AVG MWs of petroleum asphaltenes studied previously.[21] Recently, similar studies conducted in our laboratories using the APCI/CS$_2$ mass spectrometry method found a MWD ranging from 275 Da up to 1500 Da and an AVG MW of ~700 Da for oil derived petroleum asphaltenes.[13] On the other hand,

coal asphaltenes were found to have a MWD ranging from 200 Da up to 800 Da and an AVG MW of ~450 Da,[13] values that are in better agreement with the results reported here for oil deposit asphaltenes. Differences in the molecular structures of petroleum and coal asphaltenes were probed via CAD of their molecular ions in a previous study.[13] Coal asphaltenes were shown to have a higher ratio of aromatic carbons to alkane carbons than petroleum asphaltenes, independent of the molecular weight.[13] Thus, several ions with different m/z values were isolated from ionized oil deposit asphaltenes and subjected to CAD to examine the number of carbons in their alkyl side chains and to estimate the number of fused aromatic rings that comprise their PNA core structure.
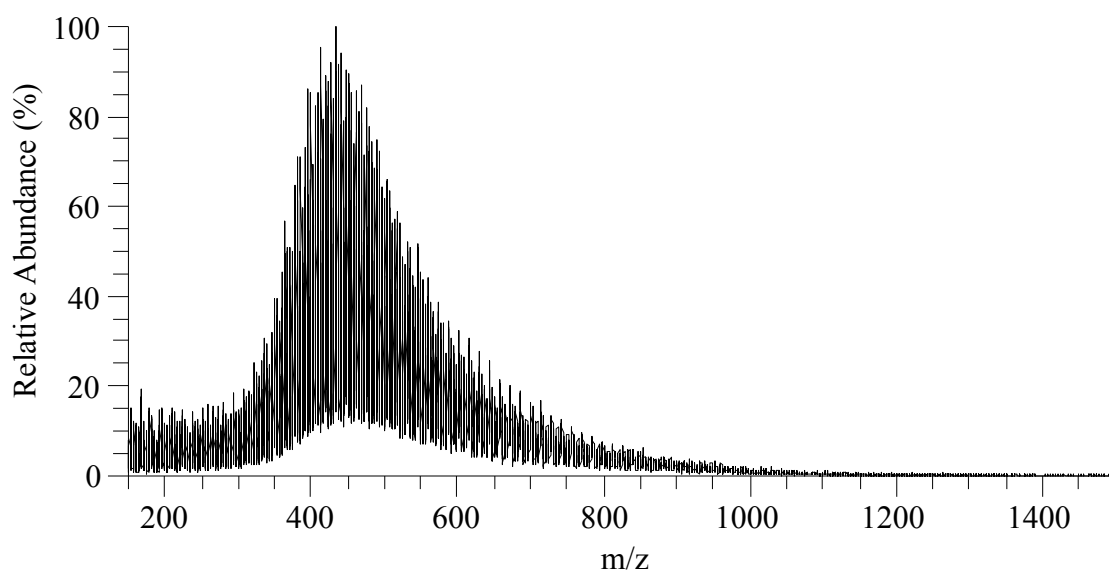
Figure 6.2 APCI/CS$_2$ mass spectrum of oil deposit asphaltenes.

The CAD mass spectrum of ions of m/z 432 ± 1 derived from oil deposit asphaltenes can be seen in Figure 6.3. This CAD mass spectrum is similar to those measured earlier for ionized petroleum and coal asphaltenes, wherein the abundances of fragment ions formed

via large alkyl radical cleavages are lower than the abundances of fragment ions formed via smaller alkyl radical cleavages.[13] Ions of *m/z* 432 ± 1 appear to have a maximum total number of 5 carbons in their alkyl side chains and an aromatic core that consists of no more than 8 fused aromatic rings. CAD mass spectra were also measured for other ions with *m/z* values ranging from 250 Da to 800 Da since this range comprises the most abundant ions, as indicated by the mass spectrum (Figure 6.2). A summary of the results can be seen in Table 6.1. The maximum total number of carbons in the alkyl side chains was found to increase with the *m/z* value of the ion. Ions with *m/z* values near the arithmetic mean *m/z* value of 497 contain larger PNA cores than ions with higher and lower *m/z* values. Since ions of *m/z* 432 are among the most abundant ions among ionized oil deposit asphaltenes, this result indicates that molecules with larger aromatic cores and shorter alkyl chains may participate more in asphaltene deposition than molecules with smaller cores and longer alkyl chains. This result is in excellent agreement with the Raman results discussed above which indicate oil deposit asphaltene molecules contain a large average PNA core structure and with earlier studies[5,6] which found that asphaltenes with large PNA cores and short alkyl chains precipitate out of crude oil more readily.
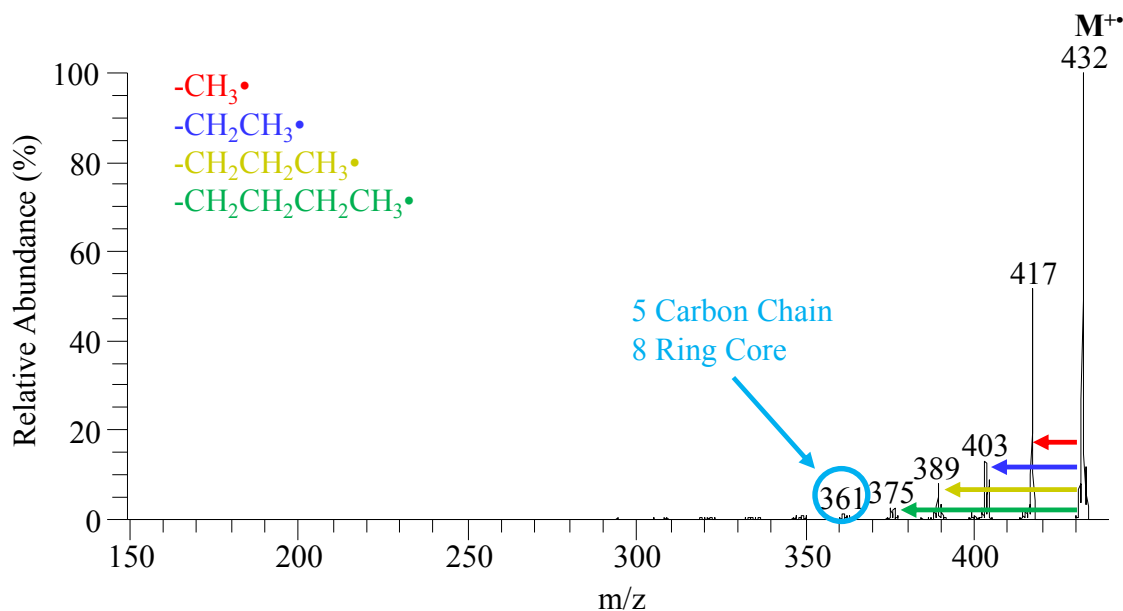
Figure 6.3 CAD mass spectrum measured for ions of *m/z* 432 ± 1 derived from oil deposit asphaltenes.

Table 6.1 Molecular Weight Distribution (MWD) and Average Molecular Weight (AVG MW) Measured for Molecules in Oil Deposit Asphaltenes, And the Estimated Total Number of Carbon Atoms in All Side Chains and Estimated Largest Aromatic Core Sizes, Given for Ions with Selected *m/z* Values.

MWD	AVG MW	Ion of *m/z*	Carbons in side chains	Estimated number of aromatic rings
150-1050	497	256	6	2
		326	5	4
		432	5	8
		548	15	7
		612	16	9
		704	35	4
		800	40	4

6.4 Conclusions

Raman spectroscopic and tandem mass spectrometric analysis of *n*-heptane precipitated asphaltenes derived from crude oil deposits revealed structural information

about the molecular architecture of asphaltenes that participate in oil deposition. The integrated intensities of D1 and G graphitic bands in the Raman spectrum of oil deposit asphaltenes were evaluated using the Tuinstra and Koenig equation which revealed an average aromatic sheet diameter of 19.27 Å for these molecules. This value is larger than previously reported values for petroleum asphaltenes derived from crude oil suggesting that asphaltenes with larger polycondensed aromatic systems are more important participants in oil deposition. Mass spectrometric determination of the molecular weight distribution (MWD) of oil deposit asphaltenes (evaporated and ionized via positive ion mode APCI) was observed to be in the 150 Da to 1050 Da range with an average molecular weight of 497 Da. The MWD of petroleum asphaltenes was shown previously[13] to be from 275 Da up to 1500 Da when utilizing the same ionization and mass spectrometric method. This indicates that the propensity for asphaltenes to precipitate is independent of their molecular weight and likely to be dependent on their structures. The structures of oil deposit asphaltenes were further investigated by tandem mass spectrometry based on collision-activated dissociation (CAD) of their ions. CAD mass spectra of selected ions with different *m/z* values showed that the most abundant constituents (as indicated by the mass spectrum) had ~8 fused aromatic rings and a maximum total number of approximately 5 to 15 carbons in their alkyl chains whereas petroleum asphaltenes have ~8 fused aromatic rings and ~22 total carbons in their side chains as reported in literature.[13] While the size of the aromatic core was shown to be the similar for petroleum and oil deposit asphaltenes, the shorter alkyl side chains for oil deposit asphaltenes possibly contributes to the increased deposition of these molecules via self-association of their aromatic rings. The estimated maximum number of carbons in the alkyl side chains was found to increase steadily from

5 to 40 carbons with increasing *m/z* value of the ion, although ions with alkyl chains containing >30 carbons were observed in drastically lower abundance relative to ions with fewer carbons in their alkyl chains. Large aromatic cores and short alkyl chains have previously been correlated[5,6] with asphaltene instability in crude oil. The results reported here for the most abundant constituents in oil deposit asphaltenes agree with that conclusion.

6.5 <u>References</u>

1.   Ten, T. F.; Chilingarian, G. V. *Asphaltenes and Asphalts, 2*; 1 ed.; Elsevier Science: Los Angeles, 2000.

2.   Leontaritis, K. J. *Fuel Sci. Tech. Internat.* **1996**, *14*, 13.

3.   Mullins, O. C. *Annu. Rev. Anal. Chem.* **2011**, *4*, 393.

4.   Mullins, O. C.; Sheu, E. Y.; Hammami, A.; Marshall, A. G. *Asphaltenes, Heavy Oils, and Petroleomics*; 1 ed.; Springer: New York, NY, 2007.

5.   León, O.; Rogel, E.; Espidel, J.; Torres, G. *Energy Fuels* **1999**, *14*, 6.

6.   Ibrahim, H. H.; Idem, R. O. *Energy Fuels* **2004**, *18*, 1038.

7.   Akbarzadeh, K.; Huo, Z.; Broze, G. *World Oil* **2010**, *231*, 7.

8.   Groenzin, H.; Mullins, O. C. *Energy Fuels* **2000**, *14*, 677.

9.   Akbarzadeh, K.; Hammami, A.; Kharrat, A.; Zhang, D.; Allenson, S.; Creek, J.; Kabir, S.; Jamaluddin, A.; Marshall, A. G.; Rogers, R. P.; Mullins, O. C.; Solbakken, T. *Oilfield Review* **2007**, *19*, 22.

10. Daaou, M.; Bendedouch, D.; Bouhadda, Y.; Vernex-Loset, L.; Modaressi, A.; Rogalski, M. *Energy Fuels* **2009**, *23*, 5556.

11. Bouhadda, Y.; Bormann, D.; Sheu, E.; Bendedouch, D.; Krallafa, A.; Daaou, M. *Fuel* **2007**, *86*, 1855.

12. Abdallah, W. A.; Yang, Y. *Energy Fuels* **2012**, *26*, 6888.

13. Hurt, M. R.; Borton, D. J.; Choi, H. J.; Kenttämaa, H. I. *Energy Fuels* **2013**, *27*, 3653.

14. Jarrell, T. M.; Jin, C.; Riedeman, J. S.; Owen, B. C.; Tan, X.; Scherer, A.; Tykwinski, R. R.; Gray, M. R.; Slater, P.; Kenttämaa, H. I. *Fuel* **2014**, *133*, 106.

15. de Hoffmann, E. *J. Mass Spectrom.* **1996**, *31*, 129.

16. Owen, B. C.; Gao, J.; Borton, D. J.; Amundson, L. M.; Archibold, E. F.; Tan, X.; Azyat, K.; Tykwinski, R.; Gray, M.; Kenttämaa, H. I. *Rapid Commun. Mass Spectrom.* **2011**, *25*, 1924.

17. Tuinstra, F.; Koenig, J. L. *J. Chem. Phys.* **1970**, *53*, 1126.

18.   Jawhari, T.; Roid, A.; Casado, J. *Carbon* **1995**, *33*, 1561.

19.   Borton, D.; Pinkston, D. S.; Hurt, M. R.; Tan, X.; Azyat, K.; Scherer, A.; Tykwinski, R.; Gray, M.; Qian, K.; Kenttämaa, H. I. *Energy Fuels* **2010**, *24*, 5548.

20.   Cançado, L. G.; Pimenta, M. A.; Neves, B. R. A.; Dantas, M. S. S.; Jorio, A. *Phys. Rev. Lett.* **2004**, *93*, 247401.

21.   Hortal, A. R.; Hurtado, P.; Martinez-Haya, B.; Mullins, O. C. *Energy Fuels* **2007**, *21*, 2863.

CHAPTER 7. COLLISION-ACTIVATED DISSOCIATION OF IONIZED ASPHALTENE MODEL COMPOUNDS CONTAINING TERMINAL AND INTERNAL ALKYNE FUNCTIONALITIES

7.1 Introduction

Asphaltenes are the most aromatic constituent of crude oil. They are procedurally defined as the fraction of petroleum that is soluble in toluene but insoluble in n-alkane solvents.[1] Asphaltenes are deleterious to the petroleum industry as a result of their ability to stabilize water-in-oil emulsions, clog reservoir pipelines, and foul catalysts used during petroleum upgrading.[2-5] These problems are likely to become a greater concern for the petroleum industry due to the diminishing availability of light crude oil thus requiring heavier crude oil that is higher in asphaltene content be used more frequently as feedstock in petroleum refineries. Also, due to the difficulties in upgrading asphaltenes, they currently have only limited uses, including delayed coking (an inefficient method for producing distillates) and paving roads.[4,6] In order to address above issues and extract more value from asphaltenes, a better understanding of their structures is imperative.[4,7]

Methods such as time-resolved fluorescence depolarization, NMR, EPR, UV-vis, Taylor diffusion, and diffuse reflectance infrared spectroscopy have been used previously to investigate the structures of asphaltenes.[8-13] However, due to the complexity of asphaltenes, these methods can only provide bulk information (average structural information) rather than information on individual molecules. Based on these studies,

asphaltenes are primarily aromatic hydrocarbons containing alkyl substituents and may possess various heteroatoms, such as sulfur, nitrogen, and oxygen, as well as some trace metals, such as vanadium and nickel.[1] Asphaltenes have never been fully separated into its individual components thus details about structures of individual molecules are still obscure.[1,9,14]

Tandem mass spectrometry is well suited for the analysis of complicated mixtures due to its ability to provide molecular level characterization of individual ionized constituents without prior separation.[15-17] Tandem mass spectrometry involves multiple stages of ion isolation followed by dissociation or other reactions to provide structural information on ions.[18] Analysis of asphaltenes by mass spectrometry can be challenging due to the absence of readily ionizable functional groups.[19,20] However, recently carbon disulfide (CS_2) was identified as a suitable solvent and ionization reagent for asphaltene model compounds when using APCI.[21] CS_2 dissolves asphaltenes and ionizes them to yield only molecular ions when operating APCI in positive mode.

Recently, collision-activated dissociation (CAD) of molecular ions of asphaltene model compounds containing saturated alkyl side chains was performed in a linear quadrupole ion trap (LQIT) mass spectrometer.[22] Analysis of the MS/MS (MS^2) and MS/MS/MS (MS^3) spectra of these ionized compounds provided valuable new information about the fragmentation behavior of molecular ions of aromatic compounds but fragmentation behavior of these ions was found to be different from asphaltene molecular ions.[15] For example, as shown in Figure 7.1, CAD of the molecular ion of 1,6-dodecylpyrene yields a facile cleavage of the α bond (also known as a benzylic cleavage) relative to the aromatic ring system yielding a fragment ion with mass-to-charge (m/z) 355

as the major product. Isolation of this fragment ion and subjecting the ion to another stage of fragmentation results in a charge-driven process yielding a fully conjugated carbocation and an alkene (Figure 7.1). CAD of asphaltene molecular ions also results in cleavage of alkyl radicals in the MS^2 experiment. However, isolation of fragment ions from the MS^2 experiment and subjecting them to further fragmentation results in additional alkyl radical cleavages rather than cleavage of alkenes. Additionally, CAD of asphaltene molecular ions yields multiple fragment ions that decrease in abundance with m/z.[15] A careful review of crude oil formation may be useful in identifying new synthesis targets for asphaltene model compounds which portray similar fragmentation behavior upon CAD of their molecular ions as ionized asphaltenes.

Hydrocarbon pyrolysis has been hypothesized to be responsible for the formation of crude oil at the high temperatures and pressures where it is formed.[23] An understanding of the pyrolysis mechanisms that produce aromatic hydrocarbons in crude oil may be useful in predicting plausible structures for asphaltenes. Mechanisms of hydrocarbon pyrolysis have been the subject intense scrutiny.[24-26] In these studies, alkynes were discovered to be important precursors in the complex chemical reactions that produce aromatic hydrocarbons. Furthermore, growth of the aromatic rings into polycyclic aromatic hydrocarbons in some of these processes involves alkyne substituted aromatic hydrocarbons as intermediates.[25] This would suggest the molecular structure of some asphaltene constituents may contain C-C triple bonds. However, probing the structures of asphaltenes to identify specific structural features, such as the presence of C-C triple bonds, is difficult due to the complexity of asphaltenes.[1,27] Spectroscopic methods, such as NMR and IR, are not sensitive to alkyne funtionalities due to long relaxation times in NMR and

weak absorbance in IR. Hence, C-C triple bonds have currently not been identified in asphaltenes.[28]

In this study, synthetic model compounds containing alkyne, alkene, or alkyl functionalities were ionized via APCI/CS_2 to generate molecular ions and subjected to multiple stages of isolation/fragmentation (MS^n). Elucidation of the fragmentation behavior of these ions is expected to generate new insight into the types of structural features that give rise to the fragmentation behavior of real ionized asphaltenes. Hence, the fragmentation behavior of molecular ions of asphaltenes from a Maya asphaltene sample were also investigated for comparison. Mechanisms are proposed for some of these fragmentation processes. Detailed quantum chemical calculations were performed to explain the observed fragmentation behavior of the molecular ion of one alkyne functionalized aromatic hydrocarbon.
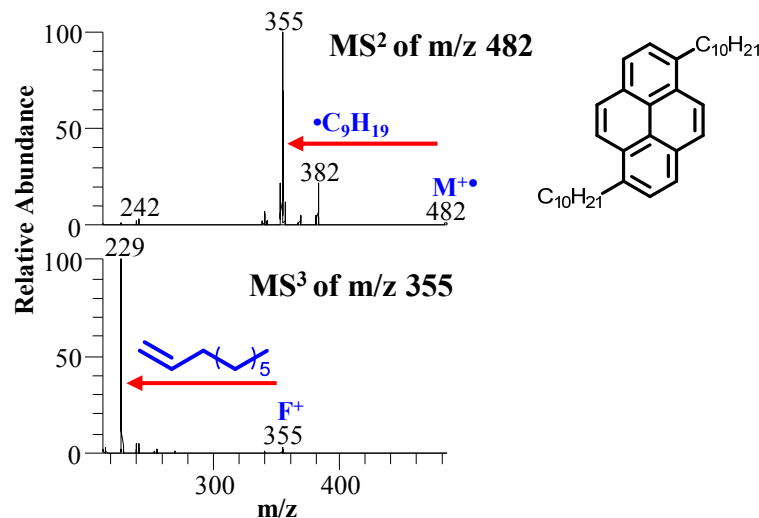
Figure 7.1 MS$^{2-3}$ spectra of the molecular ion of 1,6-didecylpyrene results in the cleavage of the bond α to the aromatic ring system (top). This fragmentation produces a carbocation (m/z 355) and an alkyl radical as its products. CAD of the alkyl cleavage product ion (m/z 355) generates another carbocation and an alkene through a charge-driven rearrangement (bottom).

7.2 Experimental

Synthesis methods of asphaltene model compounds are described in Chapter 3 of this dissertation, including their NMR spectra, exact mass values, and melting points. CS$_2$ (>99%) used in the MS^n studies was purchased from Sigma-Aldrich (St. Louis, MO).

Asphaltene model compounds were dissolved in CS$_2$ at a concentration of 1 mM and introduced into the APCI ion source at a flow rate of 10 µL/min via direct infusion. The APCI source settings were: vaporizer temperature 300 °C, discharge voltage and

current 4 kV and 4.5 μA, respectively, capillary voltage 20 V, and tube lens voltage <55 V. Vaporization and ionization occurred in the APCI source with the assistance of N_2 as sheath and auxiliary gas at flow rates of 40 arbitrary units and 10 arbitrary units, respectively. Ionization of alkyl aromatic compounds by APCI with CS_2 solvent yields stable molecular ions ($M^{+\bullet}$).[21] An isolation window of 2 m/z (selected m/z ±1) with CAD energy of 10 – 30 arbitrary units and a q value of 0.25 was used for all CAD experiments. Abundances of product ions from MS^n experiments were determined relative to the most abundant ion in the mass spectrum (base peak) and normalized to 100 %.
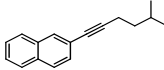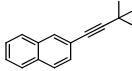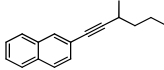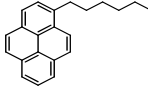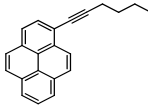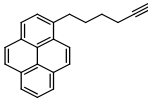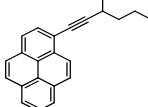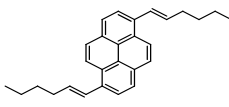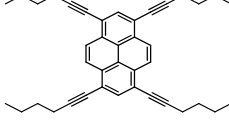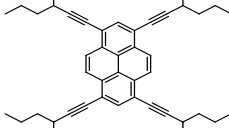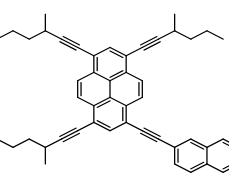
Geometries and zero-point energies for all stationary points in the minimum energy pathways of 2-(hex-1-yn-1-yl)naphthalene molecular ion were calculated at the B3LYP/6-31++G(d,p) level of theory by using the Gaussian 09 suite of programs.[29] Frequency calculations were performed to verify stationary points as energy minimums and to provide zero-point vibrational energy corrections. Minimum energy structures have no imaginary frequencies. Transition states structures were located using the Synchronous Transit-Guided Quasi-Newton Method which is requested with the QST2 or QST3 keyword. The energies reported in this paper are Gibbs free energies.

7.3 <u>Results and Discussion</u>

Maya asphaltenes were dissolved in CS_2 and ionized via APCI to generate molecular ions which were subjected to multiple stages of isolation followed by fragmentation by CAD to obtain MS^n spectra. The fragmentation behavior of these ions was studied and compared with the fragmentation behavior of molecular ions of synthetic alkyne, alkene, and alkyl functionalized aromatic hydrocarbons to investigate the types of structural

features that may be present in real asphaltenes. Table 7.1 lists the model compounds that were synthesized and studied. A total of 11 compounds were synthesized according to the procedures described in Chapter 3 of this dissertation. These synthetic model compounds were evaporated and ionized using the APCI/CS_2 method. All compounds produced an abundant molecular ion which was subjected to fragmentation via CAD, followed by isolation of fragment ions and subjecting them to further CAD/isolation steps. Fragmentation reactions are described below in detail for several model compounds studied.

Table 7.1 Compound Identifiers, Molecular Weights, and Structures for the Model Compounds Studied.

Compound	MW	Structure
1	222.32	
2	208.30	
3	222.32	
4	286.41	
5	282.38	
6	282.38	
7	296.40	
8	366.54	
9	522.76	
10	578.87	
11	634.89	

7.3.1 Tandem Mass Spectrometry of Ionized Maya Asphaltenes

The APCI/CS$_2$ method has been shown previously to be a suitable method for ionizing asphaltenes to produce molecular ions without causing fragmentation.[15] A sample of Maya asphaltenes was dissolved in CS$_2$ (1 mg/mL), ionized via positive-mode APCI, and introduced into the linear quadrupole ion trap mass spectrometer (LQIT). Ionization of these asphaltenes by the APCI/CS$_2$ method generates ions in the LQIT with a distribution of m/z values with the most abundant ions near m/z values of 600. Ions of m/z 578 ($\pm$ 1 m/z) were isolated and subjected to CAD to study their fragmentation reactions. As shown in Figure 7.2, the dissociation of the molecular ion of m/z 578 yields a distribution of fragment ions that are separated by 14 m/z units and decrease in abundance with their size. The fragment ion due to loss of a methyl radical was isolated and subjected to further CAD to yield a MS^3 spectrum. Fragmentation of this [M-methyl]$^+$ product results in another methyl cleavage reaction. Continuing this process for the MS^n experiments, methyl cleavages were observed at every stage of CAD until total loss of ion signal. This type of fragmentation behavior is unusual because it involves the generation of odd-electron fragments from even-electron ions, a violation of the "even-electron rule".[30,31]
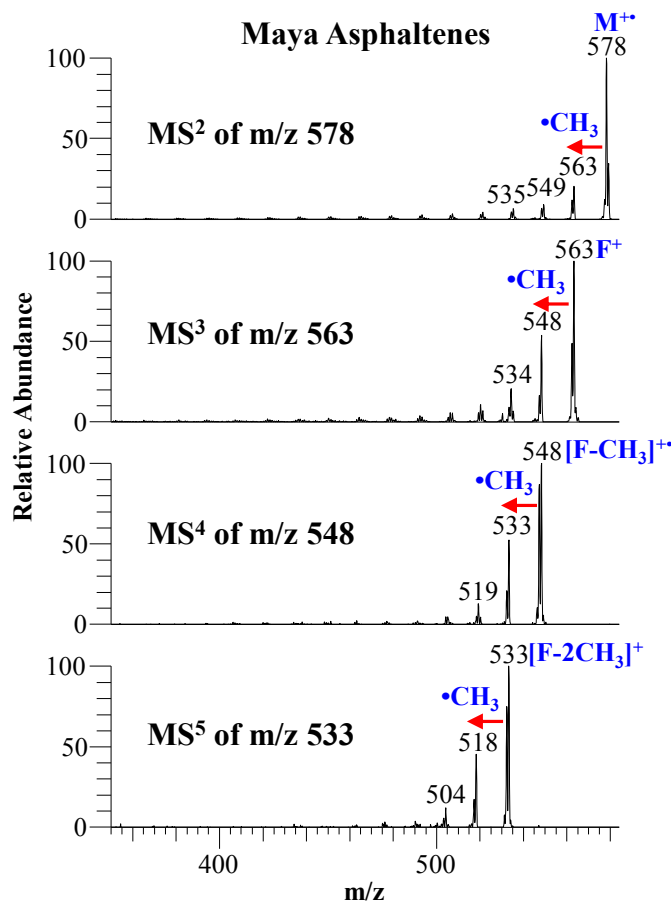
Figure 7.2 MS$^{2-5}$ spectra for molecular ions of Maya asphaltenes at m/z 578.

7.3.2 Fragmentation Reactions of Ionized Alkyne Substituted Naphthalene Compounds

Naphthalene represents the simplest PAH and may be expected to be an intermediate in the pyrolytic reactions that produce larger conjugated PAH molecules from crude oil components while it is deep within the ground. Compounds **1**, **2**, and **3** were ionized, isolated, and subjected to CAD using identical collisional energies so their CAD mass spectra could be compared (Figure 7.3). Loss of methyl radical is a major fragmentation pathway for each of these ions. The position of the methyl on the side chain greatly influences the distribution of products upon CAD of **1**$^{+\bullet}$ and **3**$^{+\bullet}$. Cleavage of methyl

and propyl radical are dominant in the MS^2 spectrum of the molecular ion of compound **1**. Conversely, the abundance of fragment ions decreases with their size upon CAD of **3**$^{+\bullet}$, similar to CAD of molecular ions of asphaltenes. Upon isolation of the methyl loss fragment ion ($[M-CH_3]^+$) followed by CAD, each ion dissociates to cleave an additional methyl radical. This type of fragmentation is a clear violation of the "even-electron rule" for singlet cations.[31] Furthermore, the MS^3 spectra of the $[M-CH_3]^+$ fragment for ions **1** and **3** are identical suggesting these ions undergo rearrangement to form a common intermediate upon CAD. Upon CAD, **2**$^{+\bullet}$ dissociates exclusively by radical-driven processes upon CAD of the $[M-CH_3]^+$ fragment whereas the fragment ions of **1** and **3** also dissociate by loss of ethylene and propylene. This likely indicates that increased branching in the alkyne side chain lowers the activation barrier to radical-driven dissociation reactions that produce odd-electron fragments from even-electron ions.
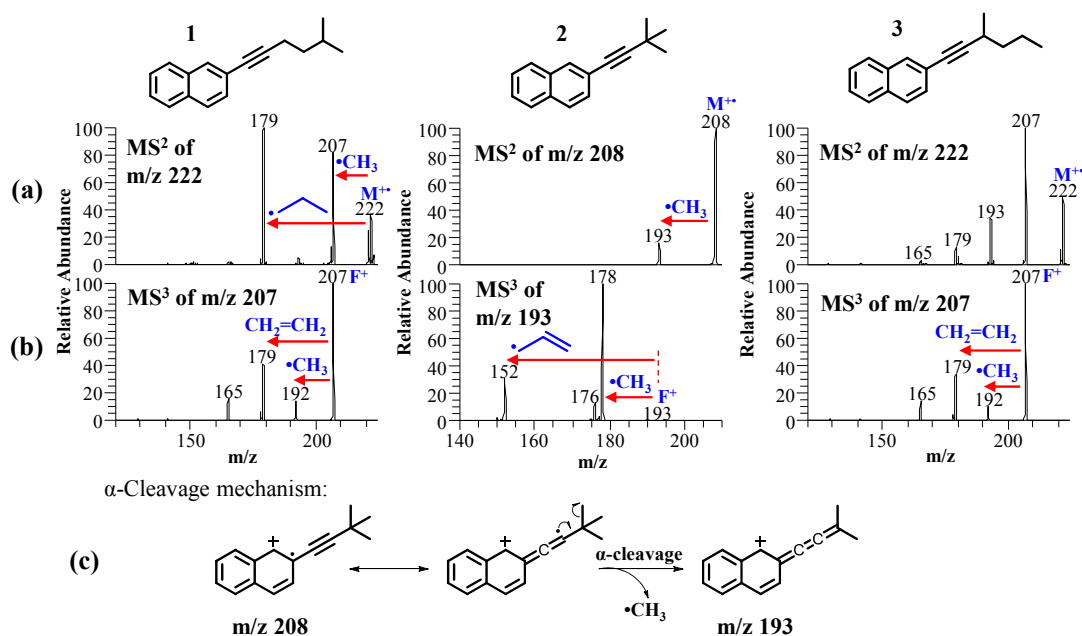
Figure 7.3 MS$^{2-3}$ spectra of $\mathbf{1^{+\bullet}}$, $\mathbf{2^{+\bullet}}$, and $\mathbf{3^{+\bullet}}$ and the proposed major fragmentation pathway of $\mathbf{2^{+\bullet}}$. **(a)** CAD (collision energy 15) of $\mathbf{1^{+\bullet}}$, $\mathbf{2^{+\bullet}}$, and $\mathbf{3^{+\bullet}}$ of m/z 222, 208, and 222, respectively; **(b)** CAD (collision energy 20) of the [M-CH$_3$]$^+$ fragment of ions of m/z 207, 193, and 207. **(c)** Dissociation mechanism for the α bond cleavage reaction of $\mathbf{2^{+\bullet}}$.

7.3.3 Fragmentation Reactions of Mono Substituted Pyrene Compounds

Pyrene was used as a model for larger PAHs that are known to also exist in asphaltenes.[1] An increasing number of condensed rings in the PAH lowers the ionization potential[32] and further stabilizes the charge upon ionization through increased delocalization. Hence, the fragmentation behavior is also affected. Four mono substituted pyrene compounds were studied: an alkyl substituted pyrene (compound **4**), alkyne substituted pyrene, one conjugated to the π-electron system of the aromatic rings (compound **5**) and one deconjugated (compound **6**), and an alkyne substituted pyrene possessing a methyl branch α to the triple bond (compound **7**). Each of these compounds readily forms an abundant molecular ion upon ionization using the APCI/CS$_2$ method. The

only observable fragmentation pathway of **4**$^{+\bullet}$ is benzylic bond cleavage to eliminate the alkyl chain (Figure 7.4a). Interestingly, the molecular ions of alkyne substituted pyrene compounds **5** and **6** both dissociate by cleavage of methyl, ethyl, and ethylene in addition to α bond cleavage to eliminate propyl (Figure 7.4b and 7.4c). These cleavages occur despite lacking methyl or ethyl functional groups α to the π-electron system whereby an alpha bond cleavage may be expected to occur readily. Furthermore, the triple bond in **6** is not conjugated with the aromatic system but rather at the terminus of the alkyl substituent. Thus, dissociation of **6**$^{+\bullet}$ must occur via complex rearrangement initiated by an interaction of the triple bond with the aromatic ring system (Figure 7.4f). Otherwise we would expect benzylic bond cleavage to be the dominant fragmentation pathway as it is for **4**$^{+\bullet}$. Additionally, the abundance of fragment ions decreases with m/z upon CAD of **5**$^{+\bullet}$ with the exception of the α bond cleavage product (Figure 7.4b, m/z 239). This type of fragmentation behavior is remarkably similar to CAD fragmentation patterns exhibited by molecular ions of asphaltenes.
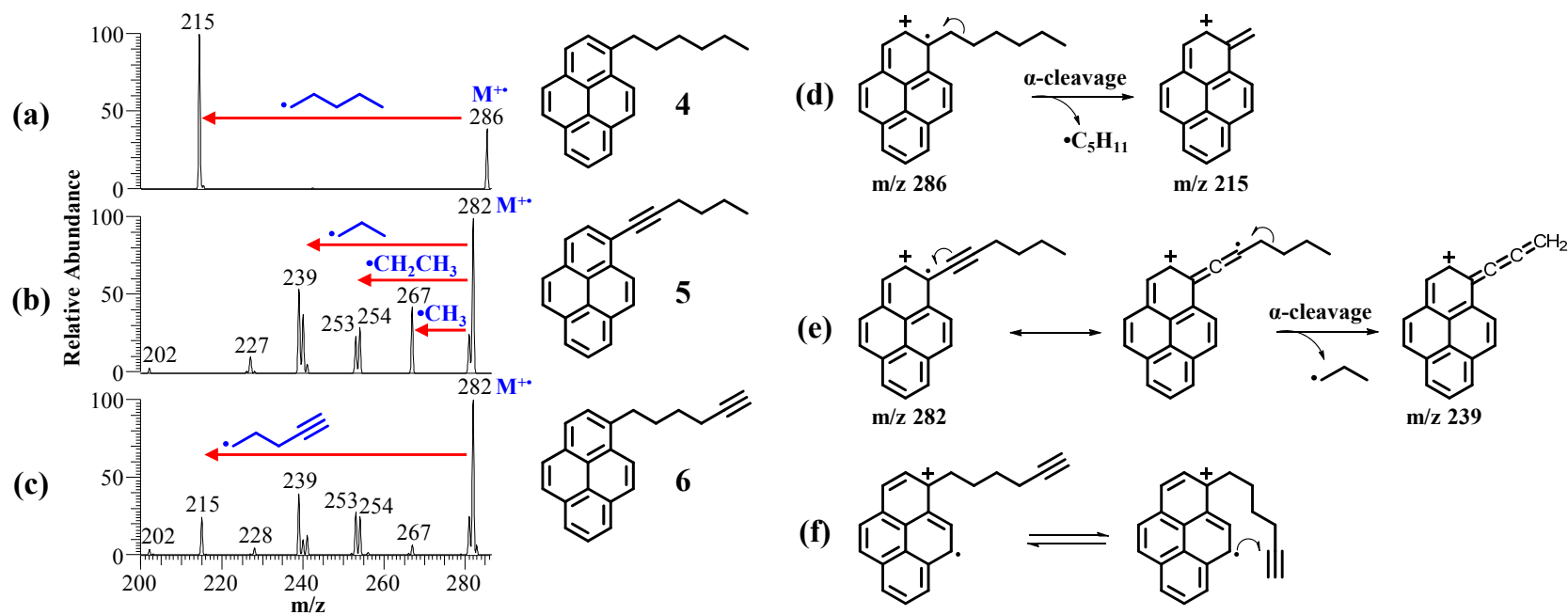
Figure 7.4 MS^2 spectra of **4$^{+\bullet}$**, **5$^{+\bullet}$**, and **6$^{+\bullet}$** and proposed major fragmentation reactions: **(a-c)** CAD (collision energy 20) of **4$^{+\bullet}$**, **5$^{+\bullet}$**, and **6$^{+\bullet}$** of m/z 286, 282, and 282, respectively; **(d)** α bond cleavage reaction of the molecular ion of hexylpyrene (compound **4**); **(e)** α bond cleavage reaction of the molecular ion of 1-(hex-1-yn-1-yl)pyrene (compound **5**); **(f)** proposed rearrangement of the molecular ion of 1-(hex-5-yn-1-yl)pyrene (compound **6**) prior to dissociation.

In order to explain the observed dissociation processes of **5**$^{+\bullet}$ upon CAD, several fragmentation mechanisms were examined using density functional theory (DFT) calculations to identify the minimum energy pathway (MEP) leading to the cleavage of methyl, ethyl, and propyl radical from **5**$^{+\bullet}$. DFT calculations scale as N^4, where N is the number of occupied orbitals. Thus, naphthalene was used as a surrogate for pyrene to simplify the calculation of the MEP. The proposed fragmentation mechanisms and MEPs for cleavage of methyl, ethyl, and propyl are shown in Scheme 7.1 and Figure 7.5, respectively. Methyl and ethyl cleavages are initiated by a hydride shift from the α carbon relative to the alkyne at a calculated barrier of 38 kcal mol^{-1}. Dissociation of the α bond relative to the radical site yields an ethyl cleavage fragment ion with an overall calculated barrier of 43.9 kcal mol^{-1} for this process. Conversely, the molecular rearrangements leading to cleavage of a methyl radical occur below the dissociation threshold for ethyl cleavage. Hence, cleavage of a methyl radical from the molecular ion of 2-(hex-1-yn-1-yl)naphthalene is kinetically more favorable than ethyl cleavage. This result is in excellent agreement with the MS^2 spectrum of **5**$^{+\bullet}$ (Figure 7.4b) which shows [M-methyl]$^+$ fragment ions in higher relative abundance than [M-ethyl]$^+$ fragment ions. Furthermore, cleavage of propyl radical by α bond cleavage has a calculated barrier of 36.9 kcal mol^{-1}, indicating this pathway is the most favorable of the three investigated mechanisms. This is also supported by the CAD results of **5**$^{+\bullet}$ which shows a higher abundance of the [M-propyl]$^+$ fragment ion relative to fragment ions due to methyl and ethyl cleavages. Facile cleavage of the C-C bond α to the alkyne suggests that the addition of a methyl substituent on the carbon α to the alkyne should result in higher abundance of the [M-methyl]$^+$ fragment ion, thus, producing a distribution of fragment ions' abundances in overall better agreement

with CAD spectra of molecular ions of real asphaltenes. The CAD spectrum of $3^{+\bullet}$ corroborates this notion. Thus, a pyrene analog of **3** was synthesized, ionized using the APCI/CS$_2$ method and studied by CAD to determine if the molecular ions of larger aromatic ring systems fragment differently despite possessing an identical substituent.
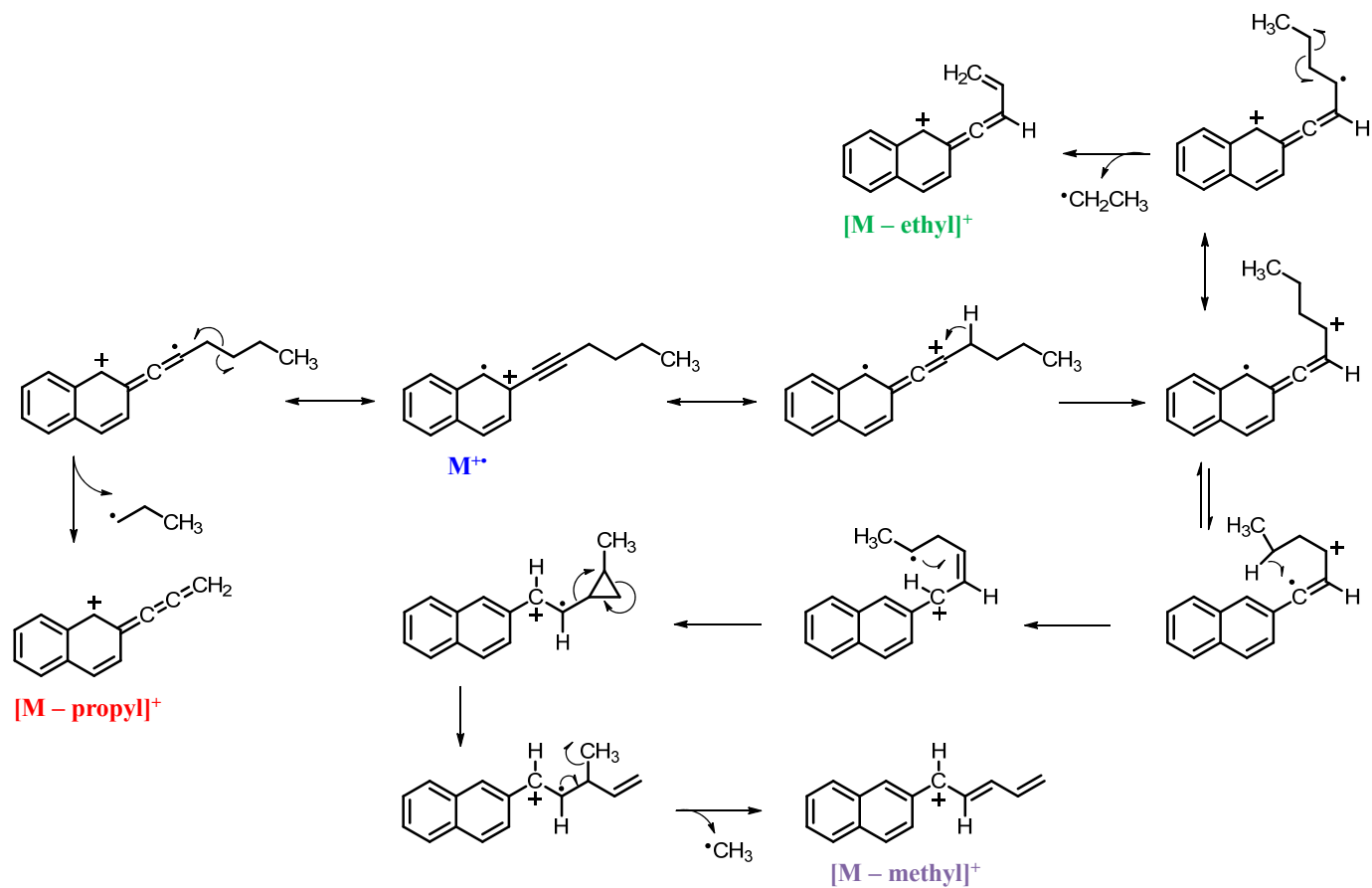
Scheme 7.1 Proposed mechanisms for the cleavages of methyl, ethyl, and propyl from the molecular ion of 2-(hex-1-yn-1-yl)naphthalene
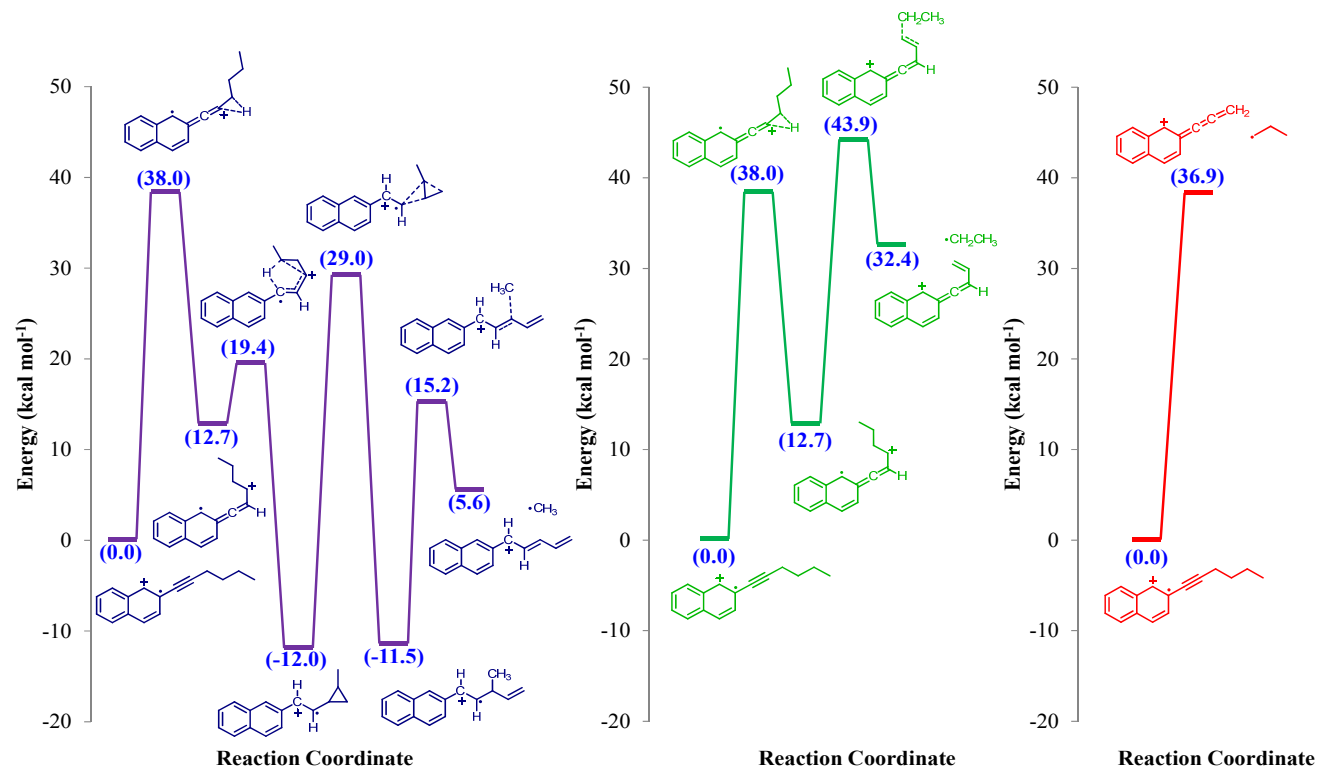
Figure 7.5 Calculated minimum energy pathways (bottom) at the B3LYP/6-31G++(d,p) level of theory. Mechanism details: cleavage of propyl radical from the molecular ion of 2-(hex-1-yn-1-yl)naphthalene occurs directly by dissociation of the C-C bond α to the alkyne (calculated barrier = 36.9 kcal mol^{-1}). Methyl and ethyl cleavages possibly occur through a common intermediate produced by a hydride shift to the carbon β to the aromatic ring (calculated barrier = 38 kcal mol^{-1}). Cleavage of the bond α to the π-electron system would produce the [M-ethyl]$^+$ fragment ion (calculated barrier = 43.9 kcal mol^{-1}). However, a 1,5 H-shift and ring-closure would produce a methylcyclopropane intermediate at a significantly lower calculated barrier of 19.4 kcal mol^{-1}. Ring-opening of the methylcyclopropane intermediate followed by cleavage of methyl would yield the [M-methyl]$^+$ fragment ion with an overall calculated barrier of 38 kcal mol^{-1}.

Upon CAD of **7**$^{+\bullet}$, cleavage of methyl radical occurred more readily than ethyl and propyl (Figure 7.6a). The abundances of fragment ions relative to the parent ion (m/z 296) are lower than what was observed for the CAD of **3**$^{+\bullet}$ despite utilizing identical collisional energies. This is likely due to an increase in available vibrational modes for pyrene than naphthalene and the ability to release energy in the form of IR light.[33] The fragment ion pertaining to cleavage of methyl radical was isolated and subjected to further CAD (MS^3) resulting in cleavage of methyl, ethyl, ethylene, and propylene (Figure 7.6b). Cleavages of methyl and propylene from the [M-methyl]$^+$ fragment ion are more facile than what was observed upon CAD of **3**$^{+\bullet}$ indicating a lower activation barrier for these fragmentations. Thus, alkyne substituted naphthalene and pyrene can be distinguished based on differences in the CAD of their molecular ions.
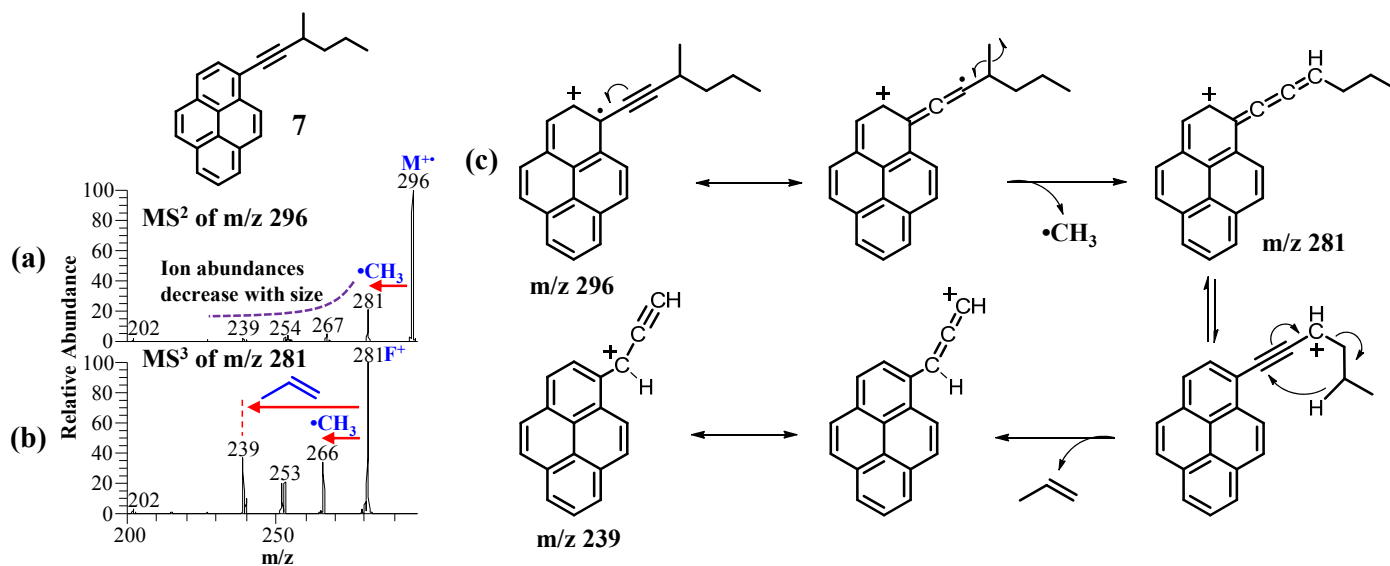
Figure 7.6 MS$^{2-3}$ spectra of **7$^{+\bullet}$** and proposed major fragmentation reactions: **(a)** MS^2 spectrum of **7$^{+\bullet}$** (m/z 296); **(b)** MS^3 spectrum of the [M-CH$_3$]$^+$ fragment ion of **7$^{+\bullet}$** (m/z 281); **(c)** Proposed fragmentation reactions of **7$^{+\bullet}$**. α bond cleavage yields the [M-CH$_3$]$^+$ fragment ion followed by charge-driven rearrangement resulting in the cleavage of propylene. Isolation of this fragment ion (m/z 239) followed by CAD yielded no further fragmentation.

7.3.4 Fragmentation Reactions of Ionized Alkene Substituted Pyrene

In addition to alkyne substituted aromatics, one alkene substituted pyrene was studied. CAD of the molecular ion of 1,6-di((*E*)-hex-1-en-1-yl)pyrene (compound **8**) yields a distribution of fragment ions separated by 12-14 m/z units (Figure 7.7a). Cleavage of methyl, ethyl, and propyl is observed but the abundances of their ions did not in general decrease with m/z. The abundance of the fragment ion pertaining to cleavage of methyl is lower than most of the other fragment ions in the spectrum including the fragment ions generated from ethyl and propyl cleavages indicating a high activation barrier. This type of fragmentation behavior is in poor agreement with CAD spectra of molecular ions of asphaltenes. Furthermore, isolation of the methyl cleavage fragment ion and subjecting the ion to further CAD does not produce an additional methyl cleavage fragment ion. The differences in fragmentation of the molecular ion of an alkene substituted aromatic hydrocarbon may be due to the double bond functionality which may undergo reaction with the aromatic rings as shown in Figure 7.7d.
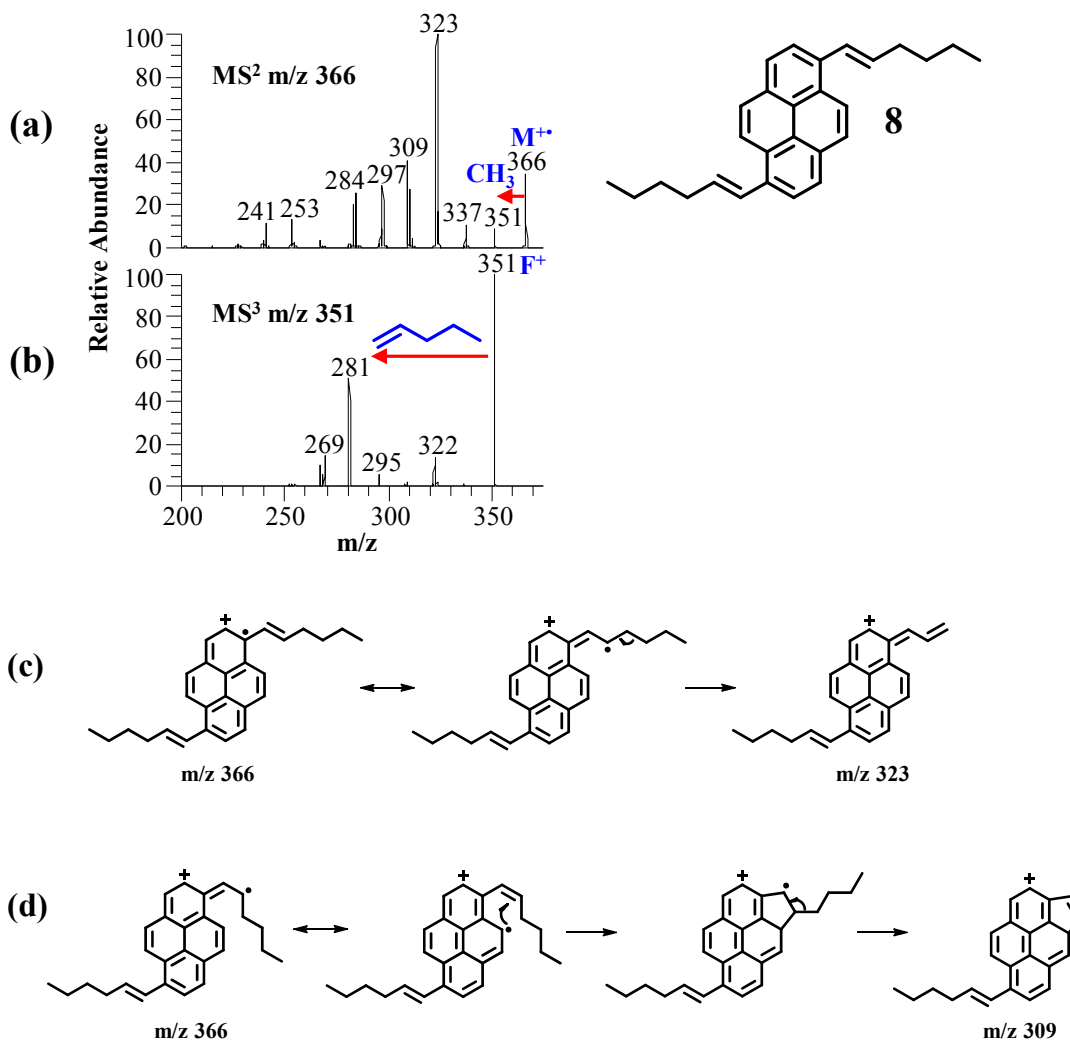
Figure 7.7 MS$^{2\text{-}3}$ spectra for the molecular ion of **8** and proposed major fragmentation reactions: **(a)** CAD (collision energy 15) of M$^{+\bullet}$ of **8** of m/z 366; **(b)** CAD (collision energy 15) of the [M-CH$_3$]$^+$ fragment of **8** of m/z 351; **(c)** cleavage of propyl radical occurs by α bond cleavage relative to the π-electron system to yield the [M-propyl]$^+$ fragment ion of m/z 323; **(d)** radical initiated ring closure followed by α bond cleavage produces the [M-butyl]$^+$ fragment ion of m/z 309.

7.3.5 Fragmentation Reactions of Ionized Tetra Substituted Pyrene Compounds

The fragmentation behavior of three ionized tetra-substituted pyrene compounds was studied. These compounds contain the pyrene core which consists of four fused aromatic rings. Compound **9** possesses the linear alkyne substituent while compounds **10**

and **11** contain the analogous branched alkyne (3-methylhexyne) that was also examined in **3⁺˙** and **7⁺˙**. Compound **11** possesses a 2-ethynylnaphthalene substituent in place of one 3-methylhexynyl group which was ionized and studied by CAD to determine the effect of increased π-bond conjugation on fragmentation of molecular ions of branched alkyne substituted aromatic hydrocarbons. The MS^{2-3} spectra of molecular ions **9-11** can be seen in Figure 7.8. Cleavage of propyl is the dominant fragmentation pathway for each of the three molecular ions upon CAD. Methyl and ethyl cleavages are also observed but are less favored. Conversely, CAD of **7⁺˙,** shown earlier, also affords a fragment pertaining to propyl cleavage but in strikingly lower abundance relative to the fragment ion due to cleavage of methyl. Additionally, the higher abundance of the fragment ion due to cleavage of propyl from **11⁺˙** compared to **10⁺˙** suggests that π-bond conjugation afforded by the 2-ethynylnaphthalene substituent lowers the activation barrier to α bond cleavage. Thus, each additional alkyne substituent provides an additional conjugated π-bond, further stabilizing the radical and charge in the molecular ion and further favoring the α cleavage pathway. Hence, CAD of **10⁺˙** favors cleavage of propyl radical whereas CAD of **7⁺˙** does not.
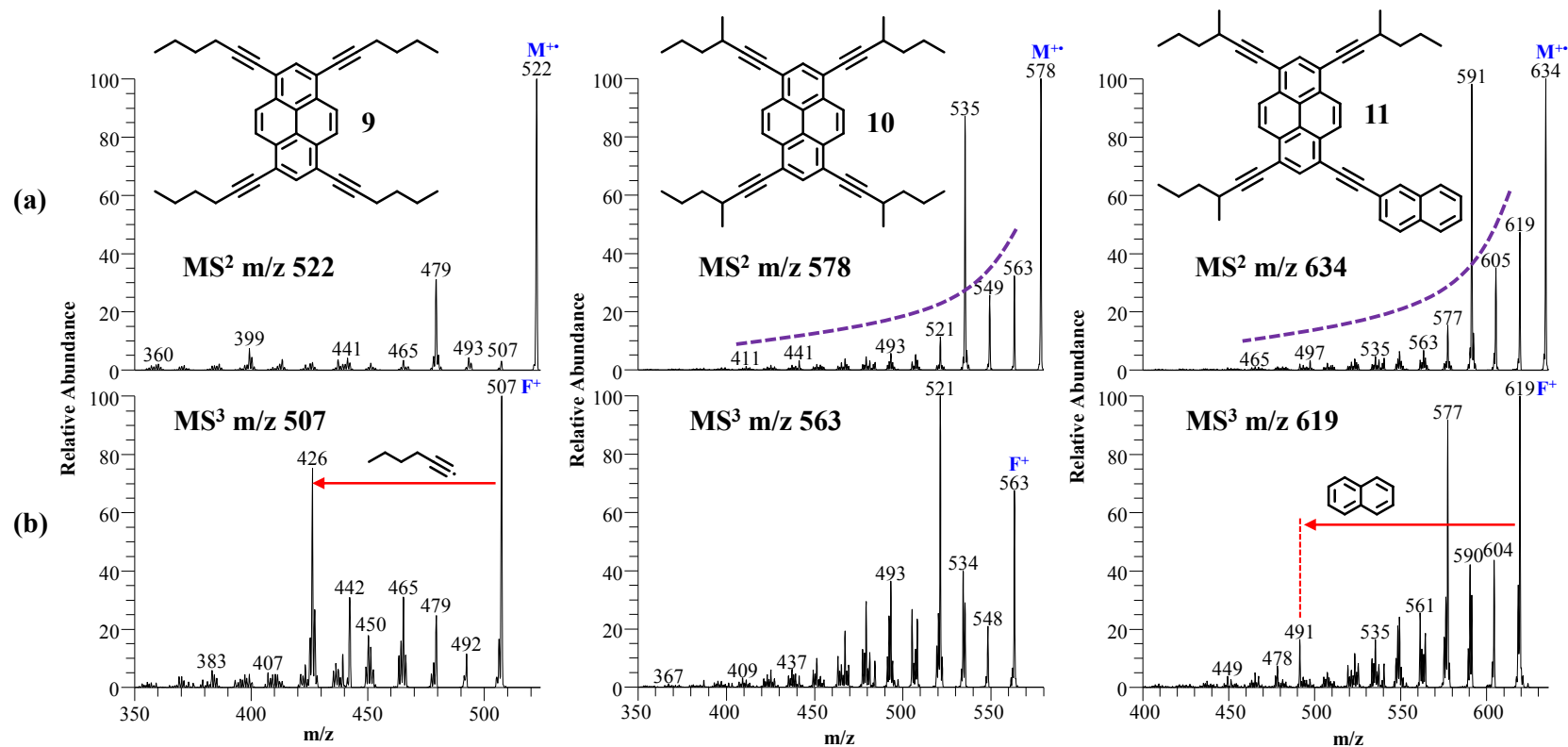
Figure 7.8 MS$^{2-3}$ spectra of **9**$^{+•}$, **10**$^{+•}$, and **11**$^{+•}$. **(a)** CAD (collision energy 15) of **9**$^{+•}$, **10**$^{+•}$, and **11**$^{+•}$ (m/z 522, 578, and 634, respectively); **(b)** CAD (collision energy 20) of the [M-CH$_3$]$^+$ fragment of **9**$^{+•}$, **10**$^{+•}$, and **11**$^{+•}$ (m/z 507, 563, and 619, respectively).

The addition of a methyl to the α carbon of the alkyne substituent results in an increased abundance of the [M-methyl]$^+$ fragment ion upon CAD of **7**$^{+\bullet}$ due to an additional available alpha cleavage pathway whereby methyl radical is cleaved. However, the increase in abundance of the [M-ethyl]$^+$ fragment ion that is also observed for these ions is less obvious. A closer look at the fragmentation pathway leading to cleavage of ethyl (Scheme 7.2) indicates that the additional methyl group on the side chain may afford extra stabilization to the radical after the initial hydride shift preceding ethyl cleavage. This extra stabilization likely increases the resonance contribution of the resonance structure possessing a radical localized on the tertiary carbon α to the dissociating bond. Hence, a higher abundance of the [M-ethyl]$^+$ fragment ion is observed upon CAD in these cases.
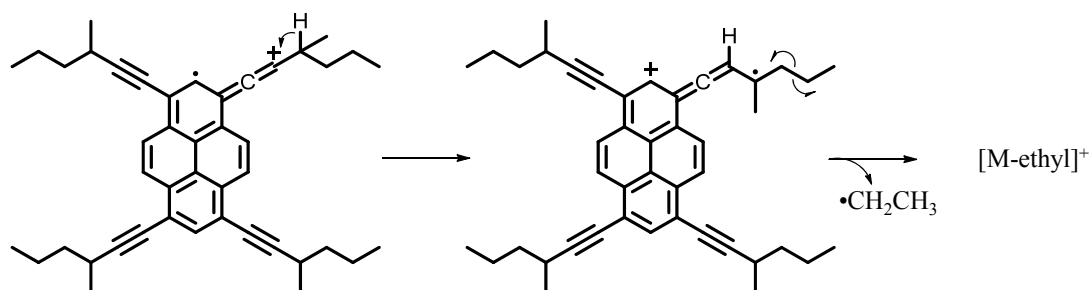
Scheme 7.2 Proposed mechanism for the cleavage of ethyl from **10**$^{+\bullet}$. One resonance structure, wherein the radical is localized on a tertiary carbon, may help facilitate the cleavage of an ethyl radical via dissociation of the α bond relative to the radical site.

Molecular ions of **10** and **11** were found to fragment by cleavage of methyl, ethyl, propyl, and butyl and the abundance of the fragment ions resulting from these cleavages decrease with m/z (Figure 7.8a). This fragmentation behavior is similar to real ionized asphaltenes, with the exception of the fragment ion resulting from α cleavage ([M-propyl]$^+$). However, CAD of **9**$^{+\bullet}$ generates a distribution of fragment ions in relatively similar

abundances. As stated earlier, increased π-bond conjugation alters the fragmentation behavior by favoring the α-cleavage pathway. The additional alkyne substituents increases the number of conjugated π-bonds in the molecule. Thus, CAD of $\mathbf{5^{+\bullet}}$, which possesses only a single alkyne substituent, results in greater relative abundances of higher mass fragment ions. Isolation of the [M-methyl]$^+$ fragment ion and subjecting it to further CAD generates MS^3 spectra that are unique to each ionized model compound. Facile cleavage of the alkyne substituent occurs for the fragment ion of m/z 507 (compound **9**, Figure 7.8b) whereas propyl cleavage is still the dominant fragmentation pathway for $\mathbf{10^{+\bullet}}$ and $\mathbf{11^{+\bullet}}$. CAD of the fragment ion pertaining to cleavage of methyl from $\mathbf{11^{+\bullet}}$ (m/z 619) is more favorable than for $\mathbf{10^{+\bullet}}$ indicating a lower activation barrier. Cleavage of a molecule of MW 128 Da (naphthalene) also occurs upon CAD of ion of m/z 619 indicating hydrogen scrambling in the ion, possibly via hydride shift reactions, prior to dissociation.

A side by side comparison of the MS$^{2\text{-}5}$ spectra of CAD spectra of Maya asphaltene molecular ions and $\mathbf{11^{+\bullet}}$ shows appreciable agreement. Each stage of CAD yields additional fragment ions resulting from methyl cleavage. Additionally, the abundance of fragment ions tends to decrease with m/z for $\mathbf{11^{+\bullet}}$ and Maya asphaltene molecular ion of m/z 618. Notable exceptions are the cleavage of propyl from ion of m/z 619 (MS^3) and m/z 604 (MS^4) for $\mathbf{11^{+\bullet}}$ (Figure 9). These results suggest that ionized branched alkyne substituted aromatic hydrocarbons are a good candidate for real ionized asphaltenes and may be a major contributor to the dissociation reactions that are characteristic of ionized asphaltenes.
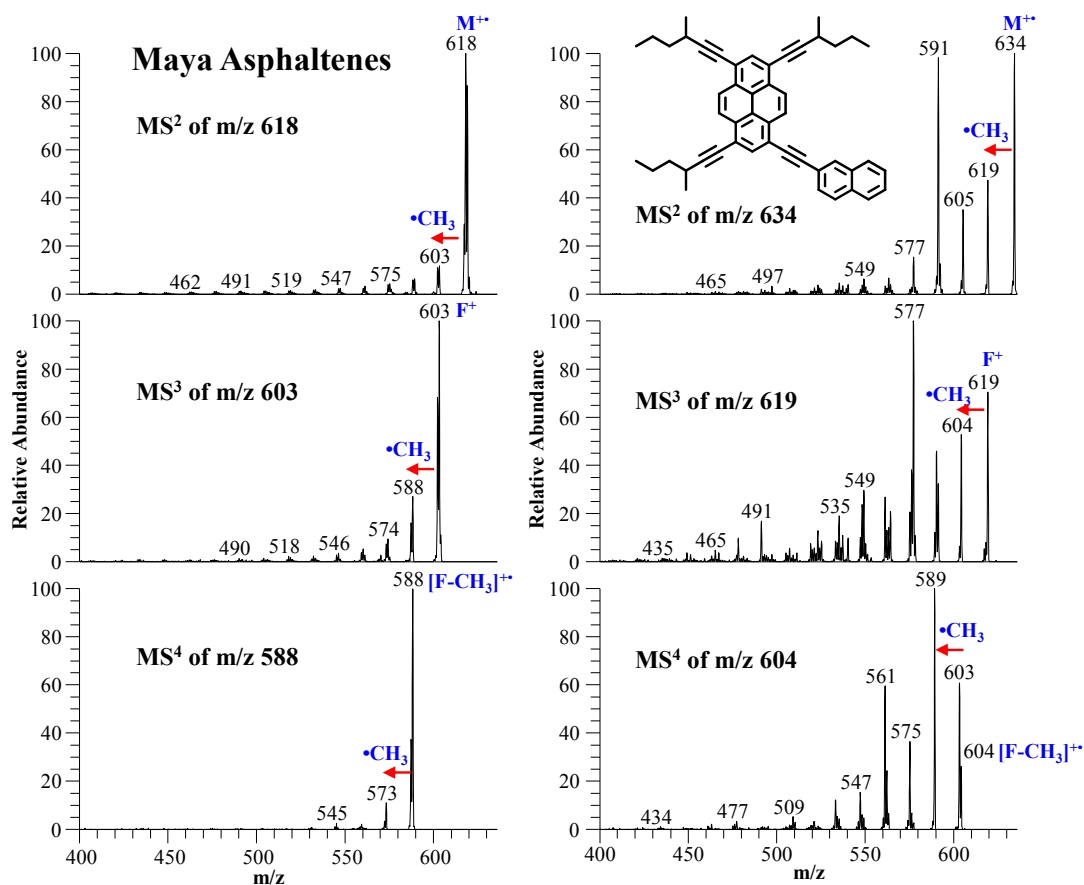
Figure 7.9 MS$^{2-4}$ spectra of Maya asphaltene ion of m/z 618 (left) and **11**$^{+•}$ (right). CAD collision energy 20.

7.4 Conclusions

CAD reactions of molecular ions of asphaltenes have been shown to yield fragment ions due to cleavage of methyl, ethyl, propyl, and butyl and the abundances of their fragment ions decrease with m/z. Additionally, subsequent CAD of these fragment ions yields a similar pattern wherein methyl cleavage is the dominant fragmentation pathway followed by ethyl, propyl, then butyl. Moreover, dissociation of the molecular ions of asphaltenes generates even-electron fragment ions that continue to dissociate by radical cleavages upon CAD in violation of the even-electron rule. Molecular ions of alkyne

substituted aromatic hydrocarbons were shown to fragment in a manner similar to molecular ions of real asphaltenes, i.e., generation of odd-electron fragment ions from even-electron fragment ions. Bond cleavage α to the alkyne functionality was found to be the dominant fragmentation pathway for all molecular ions of compounds containing linear alkynyl substituents. Molecular ions of compounds containing a methyl α to the triple bond yield methyl, ethyl, and propyl cleavages upon CAD and the abundance of fragment ions decrease with m/z similar to CAD of molecular ions of real asphaltenes. However, one molecular ion possessing a methyl group γ to the triple bond did not fragment in this manner. This suggests that the position of the methyl group plays an important role in the fragmentation behavior of molecular ions of alkyne substituted aromatic hydrocarbons and possibly molecular ions of asphaltenes. The molecular ion of an alkene substituted aromatic hydrocarbon was shown to fragment upon CAD to yield fragment ions that are separated by 14 m/z but the abundances of these fragment ions did not in general decrease with m/z. Fragment ions due to cleavage of propyl and butyl were observed in higher abundance than fragment ions due to cleavage of methyl and ethyl. Molecular ions of compounds containing four alkynyl substituents favored the α-cleavage pathway possibly as a result of increased charge and radical delocalization afforded by the additional π-bonds of the alkynyl groups.

The cleavage of an intact naphthalene molecule upon CAD of one fragment ion containing the 2-ethynylnaphthalene substituent suggests that hydrogen scrambling occurs

prior to dissociation of these ions. Finally, MS^n experiments of the molecular ion of 1,3,6-tris(3-methylhex-1-yn-1-yl)-8-(naphthalen-2-ylethynyl)pyrene show excellent agreement with MS^n experiments of molecular ions of real asphaltenes.

7.5 <u>References</u>

1.   Mullins, O. C. *Annu. Rev. Anal. Chem.* **2011**, *4*, 393.

2.   Mullins, O. C.; Sheu, E. Y.; Hammami, A.; Marshall, A. G. *Asphaltenes, Heavy Oils, and Petroleomics*; 1 ed.; Springer, 2007.

3.   Ancheyta, J.; Betancourt, G.; Marroquín, G.; Centeno, G.; Castañeda, L. C.; Alonso, F.; Muñoz, J. A.; Gómez, M. T.; Rayo, P. *Applied Catalysis A: General* **2002**, *233*, 159.

4.   Ten, T. F.; Chilingarian, G. V. *Asphaltenes and Asphalts, 2*; 1 ed.; Elsevier Science: Los Angeles, 2000.

5.   Czarnecki, J.; Tchoukov, P.; Dabros, T.; Xu, Z. *Can. J. Chem. Eng.* **2013**, *91*, 1365.

6.   Derakhshesh, M.; Eaton, P.; Newman, B.; Hoff, A.; Mitlin, D.; Gray, M. R. *Energy Fuels* **2013**, *27*, 1856.

7.   Mullins, O. C. *SPE J* **2008**, *13*, 48

8.   Badre, S.; Carla Goncalves, C.; Norinaga, K.; Gustavson, G.; Mullins, O. C. *Fuel* **2006**, *85*, 1.

9.   Andrews, A. B.; Edwards, J. C.; Pomerantz, A. E.; Mullins, O. C.; Nordlund, D.; Norinaga, K. *Energy Fuels* **2011**, *25*, 3068.

10.   Calemma, V.; Iwanski, P.; Nali, M.; Scotti, R.; Montanari, L. *Energy Fuels* **1995**, *9*, 225.

11.   Ruiz-Morales, Y.; Wu, X.; Mullins, O. C. *Energy Fuels* **2007**, *21*, 944.

12.   Wargadalam, V. J.; Norinaga, K.; Iino, M. *Fuel* **2002**, *81*, 1403.

13.   Christy, A. A.; Dahl, B.; Kvalheim, O. M. *Fuel* **1989**, *68*, 430.

14.   Groenzin, H.; Mullins, O. C. *Energy Fuels* **2000**, *14*, 677.

15.   Hurt, M. R.; Borton, D. J.; Choi, H. J.; Kenttämaa, H. I. *Energy Fuels* **2013**, *27*, 3653.

16.   de Hoffmann, E. *J. Mass Spectrom.* **1996**, *31*, 129.

17. de Hoffmann, E.; Stroobant, V. *Mass Spectrometry: Principles and Applications*; 3rd ed.; Wiley-Interscience: West Sussex, England, 2007.

18. Busch, K. L.; Glish, G. L.; McLuckey, S. A. *Mass Spectrometry/Mass Spectrometry: Techniques and Aplications of Tandem Mass Spectrometry*; VCH Publishers: New York, 1988.

19. Gaspar, A.; Zellermann, E.; Lababidi, S.; Reece, J.; Schrader, W. *Anal. Chem.* **2012**, *84*, 5257.

20. Kim, Y.; Kim, S. *J. Am. Soc. Mass Spectrom.* **2010**, *21*, 386.

21. Owen, B. C.; Gao, J.; Borton, D. J.; Amundson, L. M.; Archibold, E. F.; Tan, X.; Azyat, K.; Tykwinski, R.; Gray, M.; Kenttämaa, H. I. *Rapid Commun. Mass Spectrom.* **2011**, *25*, 1924.

22. Jarrell, T. M.; Jin, C.; Riedeman, J. S.; Owen, B. C.; Tan, X.; Scherer, A.; Tykwinski, R. R.; Gray, M. R.; Slater, P.; Kenttämaa, H. I. *Fuel* **2014**, *133*, 106.

23. Braun, R.; Burnham, A. *Chemical Reaction Model for Oil and Gas Generation from Type I and Type II Kerogen*, Lawrence Livermore National Laboratory, 1993.

24. Kislov, V. V.; Sadovnikov, A. I.; Mebel, A. M. *J. Phys. Chem. A* **2013**, *117*, 4794.

25. Richter, H.; Howard, J. B. *Progr. Energy Combust. Sci.* **2000**, *26*, 565.

26. Winans, R. E.; Tomczyk, N. A.; Hunt, J. E.; Solum, M. S.; Pugmire, R. J.; Jiang, Y. J.; Fletcher, T. H. *Energy Fuels* **2007**, *21*, 2584.

27. Hortal, A. R.; Hurtado, P.; Martinez-Haya, B.; Mullins, O. C. *Energy Fuels* **2007**, *21*, 2863.

28. Scotti, R.; Montanari, L. In *Structures and Dynamics of Asphaltenes*; Mullins, O., Sheu, E., Eds.; Springer US: 1998, p 79.

29. Frisch, M. J.; Trucks, G. W.; Schlegel, H. B.; Scuseria, G. E.; Robb, M. A.; Cheeseman, J. R.; Scalmani, G.; Barone, V.; Mennucci, B.; Petersson, G. A.; Nakatsuji, H.; Caricato, M.; Li, X.; Hratchian, H. P.; Izmaylov, A. F.; Bloino, J.; Zheng, G.; Sonnenberg, J. L.; Hada, M.; Ehara, M.; Toyota, K.; Fukuda, R.; Hasegawa, J.; Ishida, M.; Nakajima, T.; Honda, Y.; Kitao, O.; Nakai, H.; Vreven, T.; J. A. Montgomery, J.; Peralta, J. E.; Ogliaro, F.; Bearpark, M.; Heyd, J. J.; Brothers, E.; Kudin, K. N.; Staroverov, V. N.; Keith, T.; Kobayashi, R.; Normand, J.; Raghavachari, K.; Rendell, A.; Burant, J. C.; Iyengar, S. S.; Tomasi, J.; Cossi, M.; Rega, N.; Millam, J. M.; Klene, M.; Knox, J. E.; Cross, J. B.; Bakken, V.; Adamo, C.; Jaramillo, J.; Gomperts, R.; Stratmann, R. E.; Yazyev, O.; Austin, A. J.; Cammi, R.; Pomelli, C.; Ochterski, J. W.; Martin, R. L.; Morokuma, K.; Zakrzewski, V. G.; Voth, G. A.; Salvador, P.; Dannenberg, J. J.; Dapprich, S.; Daniels, A. D.; Farkas, O.; Foresman, J. B.; Ortiz, J. V.; Cioslowski, J.; Fox, D. J.; Revision C.01 ed.; Gaussian Inc.: Wallingford CT, 2010.

30. Karni, M.; Mandelbaum, A. *Org. Mass Spectrom.* **1980**, *15*, 53.

31. Cooks, R. G. *Org. Mass Spectrom.* **1969**, *2*, 481.

32. Matsen, F. A. *J. Chem. Phys.* **1956**, *24*, 602.

33. Sleno, L.; Volmer, D. A. *J. Mass Spectrom.* **2004**, *39*, 1091.

CHAPTER 8. MOLECULAR REARRANGEMENTS OF DIPHENYLMETHANE
RADICAL CATION UPON COLLISION-ACTIVATED DISSOCIATION IN A
LINEAR QUADRUPOLE ION TRAP MASS SPECTROMETER

8.1 Introduction

The molecular ions ($M^{+\bullet}$) of diphenylmethane (DPM) and its derivatives have been

the subject of study for many years.[1-3] The diphenylmethyl group, also known as

benzhydryl, is a common carbon skeleton found in numerous therapeutic drugs such as

nervous system stimulants, anticholinergics, and antihistaminics.[4-6] Peculiar to the mass

spectra of DPM is the cleavage of a methyl radical upon dissociation of its molecular ion.[1-3,7,8] The mechanism of this process involves an obscure rearrangement which has been

investigated previously by Bowie *et. al.* by studying the decompositions of the molecular

ions of several ^{2}H- and ^{13}C-labelled derivatives of DPM.[9,10] Comparison of the $[M - {}^xCH_{3-n}D_n]^+$ (x = 12 or 13; n = 1-3) product ratios with calculated product ratios indicate complete

carbon and hydrogen scrambling prior to dissociation. Furthermore, metastable defocusing

experiments show the elimination of methyl radical to be a slow process ($\tau = 10^{-7} - 10^{-3}$ s)

characterized by a low activation barrier—conditions favorable for scrambling processes

involving many rearrangements.[9] The work of Bowie and coworkers suggests dissociation

of DPM$^{+\bullet}$ may involve passage through a methylbiphenyl intermediate (Scheme 8.1) before

cleavage of methyl radical. Metastable ion ratios of ^{2}H-labeled derivatives of a, b, and c

(Scheme 8.1) show these ions scramble to the same extent in addition to having very similar

mass spectra when subjected to the same electron ionization potential. However, the minimum energy pathways (MEPs) leading to cleavage of methyl radical from these ions have not been fully explored.
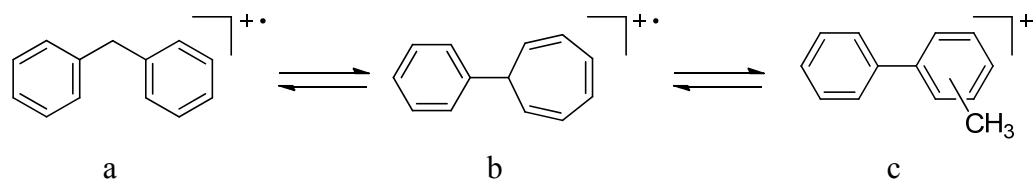
Scheme 8.1 Isomerization of diphenylmethane radical cation.

On the other hand, the unimolecular reactions of toluene radical cation ($TOL^{+\bullet}$) have been studied quite extensively and found to exhibit carbon and hydrogen scrambling by processes similar to those proposed for ionized DPM.[11] $TOL^{+\bullet}$ and cycloheptatriene ($CHT^{+\bullet}$) are shown to interconvert rapidly at the dissociation threshold for cleavage of a hydrogen atom[12] similar to the interconversion process a $\rightleftharpoons$ b (scheme 1) proposed by Bowie and coworkers for $DPM^{+\bullet}$.[9] However, unlike $DPM^{+\bullet}$, $TOL^{+\bullet}$ does not readily dissociate by loss of methyl radical. Hence, further investigation of the unimolecular reactions of $DPM^{+\bullet}$ are needed to elucidate the MEP for the methyl radical cleavage process.

Previous investigations of $DPM^{+\bullet}$ were conducted using double-focusing mass spectrometers and electron ionization (EI).[9,10] Precursor ions generated in these experiments possess internal energies in excess of the activation barrier for dissociation, defined as *kinetic shift*. This is necessary to induce fragmentation of the ion within the timescale of the experiment. Hence, unimolecular dissociation reactions involving multiple rearrangements are well suited for trapping instruments due to the longer activation times

that can be provided during experiments conducted with these instruments. Thus, mass spectrometry experiments conducted in this work were performed in a linear quadrupole ion trap (LQIT) mass spectrometer utilizing collision-activated dissociation (CAD). CAD is considered a "slow heating" method wherein activation occurs via inelastic collisions with an inert gas over a time period longer than the unimolecular reaction rates.[13] Hence, CAD is well suited for dissociation reactions involving multiple rearrangements such as the scrambling reactions of DPM$^{+•}$. A series of ^{2}H- and ^{13}C-labelled derivatives of DPM were studied to determine the extent of carbon and hydrogen scrambling. High level theoretical calculations were performed to elucidate the MEP leading to cleavage of methyl radical from DPM$^{+•}$. Additionally, potential isomers of [DPM – CH$_3$]$^+$ such as [biphenyl – H]$^+$, [biphenylene + H]$^+$, and [3-phenyltoluene – CH$_3$]$^+$ were subjected to CAD to identify a possible structure of the final product ion upon loss of methyl radical and to determine the validity of the proposed MEP.

8.2 Experimental

All compounds were dissolved in CS$_2$ (~1 mg/mL) with the exception of biphenylene which was dissolved in hexane (~1 mg/mL). The resulting solutions were introduced into the APCI source (vaporizer temperature 300 °C, discharge voltage and current 3-5 kV and 2-6 μA, respectively, capillary voltage 10-48 V, tube lens ≤40 V) and vaporized with the assistance of N$_2$ sheath (40 arbitrary units) and auxiliary (10 arbitrary units) gas. Tube lens voltage was maintained at or below 40 V since higher voltages induced fragmentation of ions before reaching the trap resulting in reduced ion signal. Ionization of aromatic molecules by the APCI/CS$_2$ method have been shown to produce

molecular ions ($M^{+\bullet}$) when operating the instrument in positive mode.[14] Ions were accumulated in the LQIT and subjected to collision-activated dissociation (CAD) for the MS/MS (MS[2]) and MS/MS/MS (MS[3]) experiments. For these experiments, ions were subjected to the excitation waveform for 30 ms. A q value of 0.25 was used for CAD experiments involving the molecular ions of 3-phenyltoluene, DPM, and [2]H- and ^{13}C-labelled derivatives of DPM. However, the $[DPM - CH_3]^+$ product and its isomers required higher-energy collisions to induce fragmentation, thus a q value of 0.50 was used for these studies. Ion abundances reported in the MS[2-3] spectra are averages of at least 60 scans.
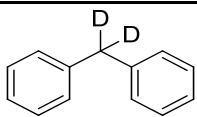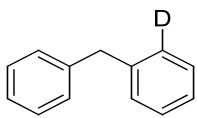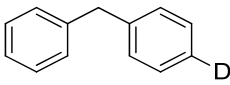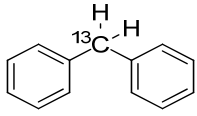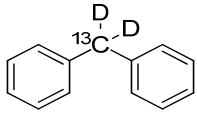
The minimum energy pathway (MEP) leading to loss of a methyl radical from the molecular ion of DPM was obtained using the hybrid density functional developed by Becke, Lee, Yang, and Parr[15] (B3LYP) in the spin-unrestricted formalism with the cc-pVTZ[16] (correlation consistent-polarized valence triple-ζ) basis set. All calculations were carried out using the Gaussian 09 suite of programs.[17] Frequency calculations were performed to obtain zero-point energy (ZPE) corrections, 298 K thermal contributions to the energy, and to verify all stationary points as either minima or transition states. Minimum energy structures do not contain imaginary frequencies whereas transition states contain a single imaginary frequency pertaining to the vibrational mode involved in the transition.

8.3 Results and Discussion

Elucidation of the methyl cleavage reaction for $DPM^{+\bullet}$ involved CAD of isotope labeled derivatives of $DPM^{+\bullet}$, computational modeling, and CAD of relevant $[DPM - CH_3]^+$ isomers. First, the degree of carbon and hydrogen scrambling preceding

fragmentation of DPM$^{+\bullet}$ was evaluated by analyzing molecular ions of ^{2}H- and ^{13}C-labelled derivatives of DPM which were studied in a linear quadrupole ion trap (LQIT) mass spectrometer using collision-activated dissociation (CAD) of their molecular ions. Product ratios pertaining to loss of CH_3, CH_2D, CHD_2, $^{13}CH_3$, $^{13}CH_2D$, and $^{13}CHD_2$ from the molecular ions of compounds in Table 8.1 were measured and compared to their calculated ratios based on statistical scrambling of their ions. Molecular orbital calculations were performed to elucidate the minimum energy pathway (MEP) leading to the cleavage of methyl radical from DPM$^{+\bullet}$. CAD of ionized compounds hypothesized for the [DPM – CH$_3$]$^+$ product ion were performed to probe its structure and determine the validity of the proposed MEP.

Table 8.1 Names, Molecular Weights, and Structures of ^{2}H- and ^{13}C-Labelled Diphenylmethane Derivatives.

Compound	MW	Structure
(1,1-^{2}H$_2$)Diphenylmethane	170.11	
(2-^{2}H$_1$)Diphenylmethane	169.10	
(4-^{2}H$_1$)Diphenylmethane	169.10	
(1-^{13}C)Diphenylmethane	169.10	
(1-^{13}C,1,1-^{2}H$_2$)Diphenylmethane	171.11	

8.3.1 Collision-Activated Dissociation of Ionized ^{2}H- and ^{13}C-Labelled Diphenylmethane

Derivatives

In order to investigate the extent of hydrogen and carbon scrambling for the molecular ion of DPM preceding loss of methyl radical, ^{2}H- and ^{13}C-labelled derivatives of DPM were synthesized (see Chapter 3), dissolved in CS_2 (~1 mg/mL), ionized via positive mode APCI, and subjected to CAD in the LQIT. All compounds produced an abundant molecular ion ($M^{+\bullet}$) using the APCI/CS_2 method. An activation time of 30 ms was chosen since it is considerably longer than the unimolecular reaction rates of $DPM^{+\bullet}$ as reported ealier.[9] Upon CAD, cleavage of CH_3, CH_2D, $^{13}CH_3$, CHD_2, $^{13}CH_2D$, and/or $^{13}CHD_2$ occurred for these compounds and the abundances of the resulting product ions corresponding to these losses were measured. The product ratios were compared to calculated ratios based on statistical scrambling without kinetic isotope effects included. As can be seen in Table 8.2, the observed product ratios from cleavage of methyl radical with and without a label are very close in value to the calculated product ratios corresponding to each loss. This indicates $DPM^{+\bullet}$ undergoes complete hydrogen and carbon scrambling in the LQIT prior to cleavage of methyl radical. Further, the higher observed product ratios corresponding to cleavage of an unlabeled methyl (CH_3) from the molecular ions of all ^{2}H-labeled DPM compounds suggests the kinetic isotope effect is implicated in the rearrangement of these ions thus indicating all hydrogens lose their positional identity prior to cleavage of methyl radical.

Table 8.2 Calculated Versus Observed Product Ratios for the $[M - X]^+$ (X = CH$_3$, CH$_2$D, ^{13}CH$_3$, CHD$_2$, ^{13}CH$_2$D, or ^{13}CHD$_2$) Ions Obtained from the CAD Spectra of Ionized ^{2}H- and ^{13}C-Labelled Diphenylmethane Compounds.

| | [M - X]$^+$ Product Ratios (Calculated[a] : Observed) | | | |
| | | X | | |
M	CH$_3$	CH$_2$D or ^{13}CH$_3$	CHD$_2$ or ^{13}CH$_2$D	^{13}CHD$_2$
Diphenylmethane	(1 : 1)	-	-	-
(1,1-^{2}H$_2$)Diphenylmethane	(0.545 : 0.580)	(0.409 : 0.379)	(0.045 : 0.041)	-
(2-^{2}H$_1$)Diphenylmethane	(0.750 : 0.765)	(0.250 : 0.235)	-	-
(4-^{2}H$_1$)Diphenylmethane	(0.750 : 0.768)	(0.250 : 0.232)	-	-
(1-^{13}C)Diphenylmethane	(0.909 : 0.904)	(0.091 : 0.096)	-	-
(1-^{13}C,1,1-^{2}H$_2$)Diphenylmethane	(0.496 : 0.532)	(0.421 : 0.396)	(0.079 : 0.067)	(0.004 : 0.005)

[a] Values calculated assuming statistical H/D and ^{13}C/^{12}C scrambling with no isotope effects.

8.3.2 Calculated Minimum Energy Pathway for Cleavage of Methyl Radical

The minimum energy pathway (MEP) proposed for cleavage of methyl radical from the molecular ion of DPM was investigated at the B3LYP/cc-pVTZ level of theory. The MEP presented in Figure 8.1 summarizes the results of the computational study. The intermediates derived from earlier work by Bowie and coworkers (Scheme 8.1) were used to guide development of the MEP since prior evidence[7,9,10] implicates their involvement in the rearrangement. Based on Scheme 8.1, methyl radical cleavage may occur directly from the methylbiphenyl ion via C-C scission of the methyl group, however, the final product ion has been suggested by some to be a condensed ring structure such as protonated biphenylene ion.[2,18] Thus, pathways leading to both products were calculated and compared.
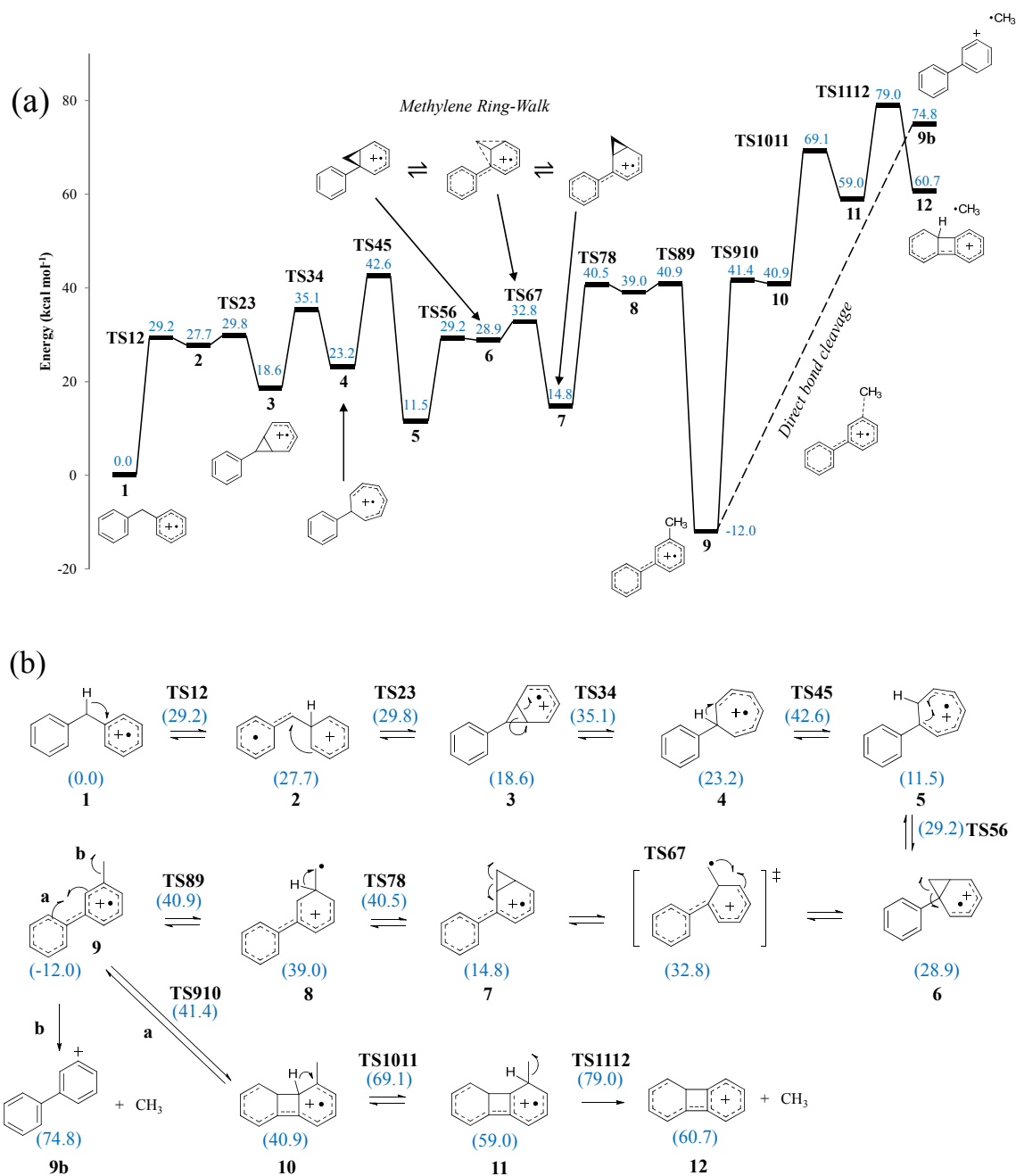
Figure 8.1 Relative free energy (in kcal mol^{-1}) profiles calculated at the B3LYP/cc-pVTZ level of theory for the rearrangement of DPM$^{+\bullet}$ and subsequent cleavage of methyl radical. (a) Schematic potential energy diagram with identifiers for all stationary points and energies (relative to DPM$^{+\bullet}$). (b) Proposed rearrangement of DPM$^{+\bullet}$ showing all minimum energy structures and one transition state including energies.

As shown in Figure 8.1, the rearrangement is initiated by a 1,2 H-shift from the methylene bridge carbon to the *ipso*-position of one of the phenyl rings via a barrier of 29.2 kcal mol^{-1}. Next, ring closure to form the phenylnorcaradiene (PNCD) radical cation **3** occurs via a low barrier of 2.1 kcal mol^{-1} (29.8 kcal mol^{-1} relative to DPM$^{+\bullet}$) followed by ring expansion to generate a phenylcycloheptatriene (PCHT) radical cation intermediate **4** with a total barrier of 35.1 kcal mol^{-1}. This process (**1→4**) is analogous to the mechanism proposed by Hoffman[19] in 1974 for the stepwise skeletal rearrangement of TOL$^{+\bullet}$ to CHT$^{+\bullet}$. Alternatively, PCHT$^{+\bullet}$ may also be formed via 1,3 H-shift followed by intramolecular cyclization and ring expansion as proposed by Dewar and Landman.[20] However, the 1,3 H-shift of a methylene bridge hydrogen in DPM$^{+\bullet}$ to the *ortho*-position of one of the phenyl rings was found to possess a barrier of 47.5 kcal mol^{-1}, more than 12 kcals higher than the Hoffman pathway for this system. In the next step following formation of intermediate **4**, another 1,2 H-shift from the C1 carbon (formerly the methylene bridge carbon) to the *ortho*-position in the CHT ring followed by ring closure generates another PNCD$^{+\bullet}$ intermediate (**6**) via a barrier of 19.4 kcal mol^{-1} (42.6 kcal mol^{-1} relative to DPM$^{+\bullet}$). [1,5]-sigmatropic rearrangement of **6** yields yet another PNCD$^{+\bullet}$ structure at a barrier of just 3.9 kcal mol^{-1} relative to **6**. The successive formation of PNCD$^{+\bullet}$ intermediates wherein the CH$_2$ group circumabulates the ring is commonly referred to as the methylene ring-walk or norcaradiene walk and is likely an important process contributing to the scrambling of carbon and hydrogen below the dissociation threshold.[21,22] According to the Hoffman mechanism, interconverstion between norcaradiene structures involves a distonic ion intermediate wherein the radical is localized on the exocyclic methylene group. However, a distonic ion intermediate was unable to be found between PNCD$^{+\bullet}$ intermediates **6** and **7**

despite a careful search suggesting only the concerted pathway is probable for the **6→7** rearrangement. Previously, the concerted methylene ring-walk for TOL[+•] was investigated and found to possess a much higher barrier than the stepwise pathway involving a distonic ion intermediate.[22] Moreover, a transition state for the conversion of **7** to **8b** also could not be found despite a careful search indicating the step-wise pathway is the most favorable for this rearrangement. This would suggest steric influence from the *o*-phenyl group (relative to the shifting methylene unit) prevents the formation of a stable distonic ion intermediate and thus favoring the concerted pathway for the **6→7** rearrangement but not for 1,2-shifts wherein the methylene unit is *meta* or *para* to the phenyl group.

The final step in the pathway to formation of a methylbiphenyl radical ion intermediate (**9**) involves a 1,2 H-shift to the exocyclic methylene group (**8→9**). This results in a significant gain in internal energy by nearly 53 kcals mol^{-1} as a result of the increased delocalization of the radical and charge. From this stage in the MEP, methyl cleavage may occur by two competing mechanisms, one involving the formation of a biphenylene ion (**9→12**) and the other by direct bond cleavage (**9→9b**). Following pathway **a** (Figure 8.1), methyl cleavage can occur by ring closure to the methylbiphenylene structure **10** followed by 1,2 H-shift and finally C-C scission of the methyl bond to yield a conjugated protonated biphenylene product ion with an overall barrier of 79.0 kcals mol^{-1}. On the other hand, the biphenyl ion **9b** may be obtained directly by cleavage of methyl radical from intermediate **9** via a lower barrier of 74.8 kcals mol^{-1}, a 4.2 kcals mol^{-1} savings. Thus, CAD of [biphenylene + H][+], [biphenyl − H][+], and [3-phenyltoluene − CH₃][+] were compared to the CAD of [DPM − CH₃][+] to verify the

computational results and determine which product is produced upon cleavage of methyl radical from $DPM^{+\bullet}$.

8.3.3 Collision-Activated Dissociation of Relevant $[DPM - CH_3]^+$ Isomers

Diphenylmethane, 3-phenyltoluene, and biphenyl were dissolved in CS_2 (~1 mg/mL), ionized via positive mode APCI, and subjected to CAD. Biphenylene was dissolved in hexane (~1 mg/mL) and ionized via positive mode APCI to generate protonated biphenylene ion which was also subjected to CAD using the same experimental conditions. The product ion $[DPM - CH_3]^+$ (mass-to-charge (m/z) 153) was subjected to CAD and compared to the CAD of $[biphenyl - H]^+$, $[3\text{-phenyltoluene} - CH_3]^+$, and $[biphenylene + H]^+$ which are isomeric ions of m/z 153. A higher q value of 0.5 was required for the CAD experiments due to the greater stability of these ions. As shown in Figure 8.2, $[biphenyl - H]^+$ and $[3\text{-phenyltoluene} - CH_3]^+$ yield identical CAD spectra as $[DPM - CH_3]^+$, however, $[biphenylene + H]^+$ does not. All spectra show several hydrogen loss products with cleavage of 1 and 3 hydrogens being dominant. However, the CAD spectra of $[biphenylene + H]^+$ shows an additional product pertaining to loss of acetylene (M − 26). Furthermore, relative abundances of hydrogen loss products for the CAD spectra of $[biphenylene + H]^+$ do not compare appreciably to the other ions in the study. Also, the $[biphenylene + H]^+$ ion shows greater stability than the other isomeric ions as indicated by a higher relative abundance of its parent ion despite being subjected to identical collision energy. These results would suggest pathway **9→9b** is preferred over **9→12,** as shown in Figure 8.1, due to near perfect agreement between the product distributions for $[DPM - CH_3]^+$ and $[biphenyl - H]^+$. These results agree with the MEP for cleavage of methyl radical from

DPM$^{+\bullet}$ (Figure 8.1) following pathway **b** (**9→9b**) and suggest a deprotonated biphenyl ion

is the final product.
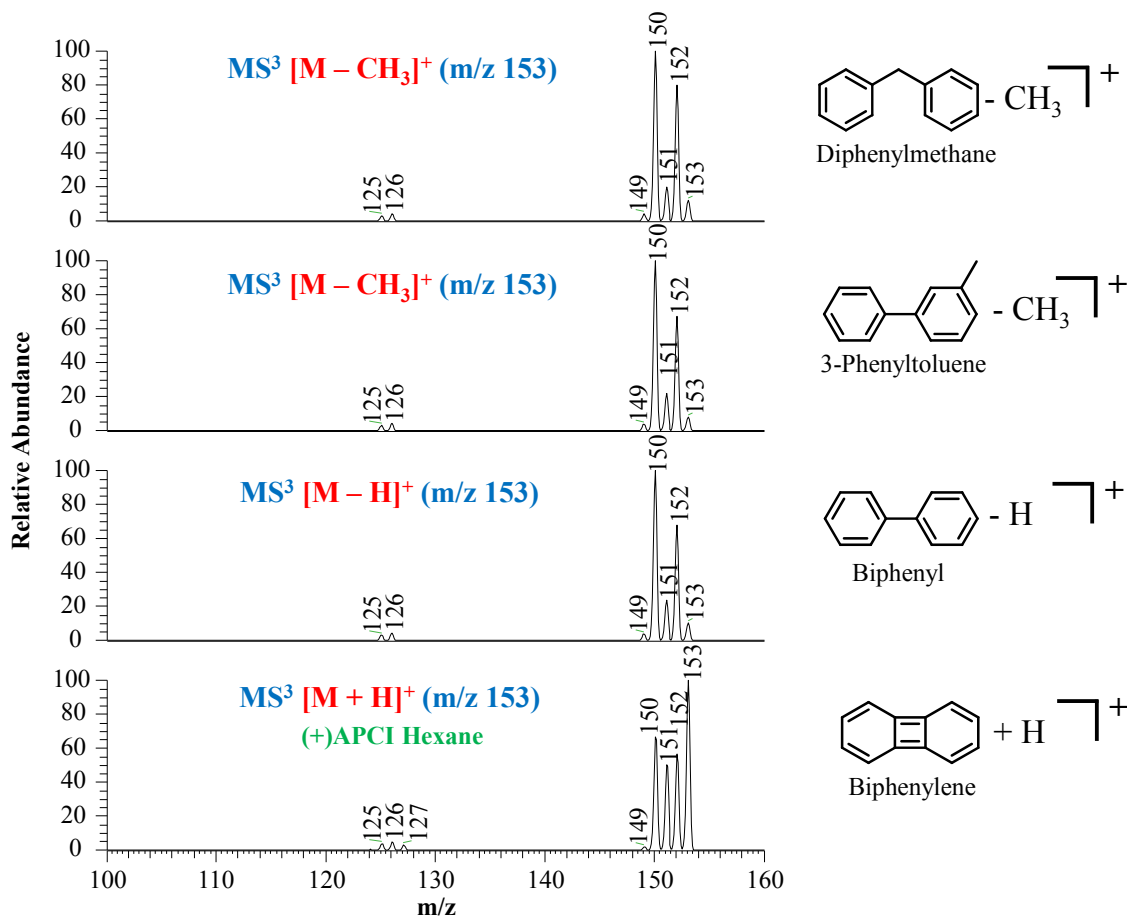
Figure 8.2 CAD spectra of [DPM – CH$_3$]$^+$, [3-phenyltoluene – CH$_3$]$^+$, [biphenyl – H]$^+$, and [biphenylene + H]$^+$, using a *q* value of 0.5 and collision energy 40.

8.4 Conclusions

The examination of the MEP for cleavage of methyl radical from the molecular ion

of DPM by theoretical calculations, CAD of molecular ions of ^{2}H- and ^{13}C-labeled

derivatives of DPM, and CAD of isomeric ions of [DPM – CH$_3$]$^+$, show that methyl

cleavage from DPM$^{+\bullet}$ occurs through a methylbiphenyl radical cation intermediate to yield a deprotonated biphenyl product ion. Product ion ratios from the CAD of molecular ions of ^{2}H- and ^{13}C-labeled derivatives of DPM indicate this process occurs with complete carbon and hydrogen scrambling. This corroborates earlier mass spectrometric investigations of DPM$^{+\bullet}$ which indicated all carbons and hydrogens lose their positional identity upon dissociation. Theoretical calculations show that the isomerization of DPM$^{+\bullet}$ to PCHT$^{+\bullet}$ and then to methylbiphenyl radical cation via ring contraction of the seven-membered CHT ring to a norcaradiene radical cation is a plausible rearrangement pathway. The norcaradiene radical cation intermediates may convert to other norcaradiene radical cations via ring opening of the three-membered ring to a distonic ion intermediate in which the exocyclic methylene is *meta* or *para* to the phenyl ring or directly if the phenyl ring is *ortho* to the shifting methylene where steric influence by the phenyl ring favors a concerted 1,2-shift. These 1,2-shifts of methylene around the phenyl ring are plausible pathways for DPM$^{+\bullet}$ isomerization below the dissociation threshold and thus contribute to randomization of carbon and hydrogen. Cessation of the methylene ring walk occurs via H-shift to the exocyclic methylene yielding a methylbiphenyl radical cation. Calculations indicate the cleavage of methyl occurs by direct bond cleavage of the C-C bond between methyl and the biphenyl ion. Formation of a methylbiphenylene radical cation prior to cleavage of methyl results in a product ion that is lower in energy upon loss of methyl but the barrier is higher than the direct bond cleavage pathway by 4.2 kcal mol^{-1}. CAD of isomeric ions of [DPM – CH$_3$]$^+$ show that a deprotonated biphenyl ion is a more plausible structure for the final product upon loss of methyl from DPM$^{+\bullet}$ which agrees well with the calculated MEP.

8.5 <u>References</u>

1.   Meyerson, S.; Drews, H.; Fields, E. K. *J. Am. Chem. Soc.* **1964**, *86*, 4964.

2.   Eland, J. H. D.; Danby, C. J. *J. Chem. Soc.* **1965**, 5935.

3.   Johnstone, R. A. W.; Millard, B. J. *Z. Naturforsch., A: Phys. Sci.* **1966**, 604.

4.   Minzenberg, M. J.; Carter, C. S. *Neuropsychopharmacol* **2008**, *33*, 1477.

5.   Chancellor, M. B.; de, M. F. *Geriatrics* **2007**, *62*, 15.

6.   Portnoy, J. M.; Dinakar, C. *Expert Opin. Pharmacother.* **2004**, *5*, 125.

7.   Williams, D. H.; Ward, R. S.; Cooks, R. G. *J. Chem. Soc. B* **1968**, 522.

8.   Meyerson, S.; Hart, H.; Leitch, L. C. *J. Am. Chem. Soc.* **1968**, *90*, 3419.

9.   Bowie, J. H.; White, P. Y.; Bradshaw, T. K. *J. Chem. Soc., Perkin Trans. 2* **1972**, *0*, 1966.

10.   Bradshaw, T. K.; Bowie, J. H.; White, P. Y. *J. Chem. Soc. D* **1970**, *0*, 537.

11.   Baldwin, M. A.; McLafferty, F. W.; Jerina, D. M. *J. Am. Chem. Soc.* **1975**, *97*, 6169.

12.   Rylander, P. N.; Meyerson, S.; Grubb, H. M. *J. Am. Chem. Soc.* **1957**, *79*, 842.

13.   McLuckey, S. A.; Goeringer, D. E. *J. Mass Spectrom.* **1997**, *32*, 461.

14.   Owen, B. C.; Gao, J.; Borton, D. J.; Amundson, L. M.; Archibold, E. F.; Tan, X.; Azyat, K.; Tykwinski, R.; Gray, M.; Kenttämaa, H. I. *Rapid Commun. Mass Spectrom.* **2011**, *25*, 1924.

15.   Becke, A. D. *Phys. Rev. A* **1988**, *38*, 3098.

16.   Dunning, T. H. *J. Chem. Phys.* **1989**, *90*, 1007.

17. Frisch, M. J.; Trucks, G. W.; Schlegel, H. B.; Scuseria, G. E.; Robb, M. A.; Cheeseman, J. R.; Scalmani, G.; Barone, V.; Mennucci, B.; Petersson, G. A.; Nakatsuji, H.; Caricato, M.; Li, X.; Hratchian, H. P.; Izmaylov, A. F.; Bloino, J.; Zheng, G.; Sonnenberg, J. L.; Hada, M.; Ehara, M.; Toyota, K.; Fukuda, R.; Hasegawa, J.; Ishida, M.; Nakajima, T.; Honda, Y.; Kitao, O.; Nakai, H.; Vreven, T.; J. A. Montgomery, J.; Peralta, J. E.; Ogliaro, F.; Bearpark, M.; Heyd, J. J.; Brothers, E.; Kudin, K. N.; Staroverov, V. N.; Keith, T.; Kobayashi, R.; Normand, J.; Raghavachari, K.; Rendell, A.; Burant, J. C.; Iyengar, S. S.; Tomasi, J.; Cossi, M.; Rega, N.; Millam, J. M.; Klene, M.; Knox, J. E.; Cross, J. B.; Bakken, V.; Adamo, C.; Jaramillo, J.; Gomperts, R.; Stratmann, R. E.; Yazyev, O.; Austin, A. J.; Cammi, R.; Pomelli, C.; Ochterski, J. W.; Martin, R. L.; Morokuma, K.; Zakrzewski, V. G.; Voth, G. A.; Salvador, P.; Dannenberg, J. J.; Dapprich, S.; Daniels, A. D.; Farkas, O.; Foresman, J. B.; Ortiz, J. V.; Cioslowski, J.; Fox, D. J.; Revision C.01 ed.; Gaussian Inc.: Wallingford CT, 2010.

18. Kuck, D. *Mass Spectrom. Rev.* **1990**, *9*, 187.

19. Hoffman, M. *Z Naturforsch* **1974**, *29*, 1077.

20. Dewar, M. J. S.; Landman, D. *J. Am. Chem. Soc.* **1977**, *99*, 2446.

21. Grutzmacher, H. F.; Harting, N. *Eur. J. Mass Spectrom.* **2003**, *9*, 327.

22. Norberg, D.; Larsson, P.-E.; Salhi-Benachenhou, N. *J. Phys. Chem. A* **2008**, *112*, 4694.

VITA

VITA

James Steven Riedeman was born in Indianapolis, IN on April 29, 1983. At an early age, he dreamed of becoming an architect after witnessing his father sketching the blueprint for a house that would later become their home. However, some point during his time at Doe Creek Middle School he became fascinated with science. For a science class presentation he demonstrated the electrolysis of water by producing hydrogen and oxygen above two graphite electrodes connected to a lantern-style battery. However, upon graduating New Palestine High School in New Palestine, IN in 2001, his family had been hit with financial difficulties due to a decline in his father's health and change of employment status. Thus, at the age of eighteen he began working as a product selector for Atlas Logistics Retail Services, a distribution facility for Kroger stores across the mid-west. Although the job provided a stable income, James did not find the tasks of his work to be mentally stimulating. Thus, on a whim he applied to the University of Indianapolis (Uindy) in 2005 declaring Computer Information Systems as his major area of study. During this time he continued to work for Atlas Logistics Retail Services as a part-time employee. After one and a half years of study at Uindy he also did not find his major area of study to be satisfying and thus began taking chemistry classes due to a suggestion from his sister Mary Riedeman. James found the field of chemistry to be incredibly fascinating and thus changed his major area of study to chemistry in 2007. He couldn't imagine a more

satisfying career path than solving chemistry-related problems. Hence, upon graduating *magna cum laude* from Uindy in 2010 with a B.S. in chemistry, he applied to Purdue University to pursue a Ph.D. in organic chemistry. Once accepted into Purdue University, he moved to West Lafayette, IN in 2010 and began searching for a research group. He initially sought to join a research group engaging in total synthesis but found Dr. Hilkka I. Kenttämaa's group to be more suiting due to her multidisciplinary approach to research and her high enthusiasm for solving chemistry-related problems. He was and still is very grateful that she gave him the opportunity to conduct research in her group. He quickly developed an interest in gas-phase ion chemistry and methodologies for investigating the structures of molecules within complex mixtures such as asphaltenes. James was awarded the Robert R. Squires Scholarship in 2013. In December 2014, he earned a Ph.D. in chemistry from Purdue University.

LIST OF PUBLICATIONS

LIST OF PUBLICATIONS

1.   Sheng, H., Williams, P. E., Tang, W., Riedeman, J. S., Zhang, M., Kenttämaa, H. I. "Identification of the Sulfone Functionality in Protonated Analytes via Ion/Molecule Reactions in a Linear Quadrupole Ion Trap Mass Spectrometer**."** *J. Org. Chem.* 2014, *79*, 2883.

2.   Jarrell T. M., Jin, C., Riedeman, J. S., Owen B. C., Tan X., Azyat K., Tykwinski R., Gray M., Kenttämaa, H. I. "Elucidation of structural information achievable for asphaltenes via collision-activated dissociation of their molecular ions in MSn experiments: A model compound study." *Fuel* 2014, *133*, 106.

3.   Jarrell, T. M., **Riedeman, J. S.**, Carlson, M. Replogle, R. Selby, T., Kenttämaa, H. I. "Multi-Ported Pulsed Valve Interface for a Linear Quadrupole Ion Trap Mass Spectrometer to Enable Rapid Screening of Multiple Functional-Group Selective Ion-Molecule Reactions." *Anal. Chem.* 2014, *86*, 6533.

4.   Jarrell, T. M., **Riedeman, J. S.**, Kenttämaa, H. I. "Gas-phase reactions of a novel chemical ionization reagent, $ClMn_2^+$, with polar and nonpolar analytes in a linear quadrupole ion trap." *Int. J. Mass Spectrom.* 2014.

Identification of the Sulfone Functionality in Protonated Analytes via Ion/Molecule Reactions in a Linear Quadrupole Ion Trap Mass Spectrometer

Huaming Sheng,[†] Peggy E. Williams,[†] Weijuan Tang,[†] James S. Riedeman,[†] Minli Zhang,[‡] and Hilkka I. Kenttämaa*[,†]

[†]Department of Chemistry, Purdue University, West Lafayette, Indiana 47907, United States

[‡]AstraZeneca, Boston, Massachusetts 02130, United States

Ⓢ *Supporting Information*

ABSTRACT: A tandem mass spectrometric method is presented for the rapid identification of drug metabolites that contain the sulfone functional group. This method is based on a gas-phase ion/molecule reaction of protonated sulfone analytes with trimethyl borate (TMB) that yields a diagnostic product ion, adduct-Me_2O, at high reaction efficiency. A variety of compounds with different functional groups, such as sulfoxides, hydroxylamines, N-oxides, anilines, phenol, an aliphatic amine, and an aliphatic alcohol, were examined to probe the selectivity of this reaction. Except for protonated sulfones, most of the protonated compounds react very slowly or not at all with TMB. Most importantly, none of them give the adduct-Me_2O product. A mechanism that explains the observed selectivity is proposed for the diagnostic reaction and is supported by quantum chemical calculations. The reaction was tested with the anti-inflammatory drug sulindac and its metabolite, sulindac sulfone, which were readily distinguished. The presence of other functionalities in addition to sulfone was found not to influence the diagnostic reactivity.
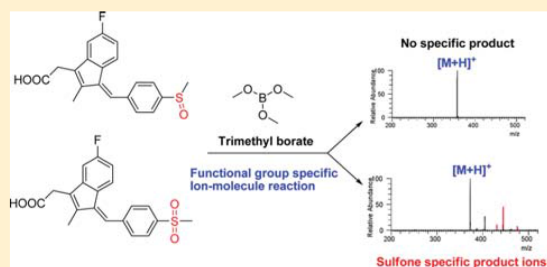
■ INTRODUCTION

Oxidation of sulfur functionalities to sulfones is an important biotransformation pathway for many drugs.[1] Rapid identification of these drug metabolites is crucial because some of them have been reported to cause idiosyncratic drug reactions and they often go undiscovered until after the postmarketing stage.[2] However, the detection of these metabolites in the highly complex plasma is challenging for many analytical methods, such as NMR, FT-IR, and X-ray crystallography, because of their small quantity and because of stability issues of some metabolite molecules.[3] Tandem mass spectrometric methods involving collisionally activated dissociation (CAD) have been widely used for structure elucidation of unknown compounds directly in mixtures.[4] However, only a few CAD studies have been published on ionized sulfones. Some sulfones, such as deprotonated N-phenyl benzenesulfonamides, have been reported to lose SO_2 upon CAD.[5] Moreover, other oxidation products of N and S atom-containing drugs, such as sulfoxides, hydroxylamines, and N-oxides, may have the same molecular weight as the sulfone, which makes it difficult to identify the sulfone functionality unambiguously.[6]

Tandem mass spectrometric methods based on ion/molecule reactions hold great promise for being able to provide information useful in the identification of specific functional groups in analytes.[7] Our group has successfully developed methods based on ion/molecule reactions to identify several functionalities, such as epoxide,[8a] carboxylic acid,[8b] amido,[8c] polyol,[8d] primary, secondary and tertiary amino,[8e] hydroxyl,[8f] and N-oxide functionalities.[8g,h] In the work presented here, gas-phase ion/molecule reactions of trimethyl borate (TMB) are demonstrated to allow the differentiation of the protonated sulfone functionality from many other functional groups, including sulfoxide, hydroxylamino, N-oxide, aniline, amino, hydroxyl, and phenol functionalities. The reaction specificity is also demonstrated using a sulfoxide-containing anti-inflammatory drug, sulindac, and its metabolite, sulindac sulfone.

■ RESULTS AND DISCUSSION

Trimethyl borate (TMB) is known to deprotonate many protonated oxygen functionalities followed by addition of the analyte to the boron center and elimination of methanol (adduct-MeOH; Scheme 1).[8a,9,10] However, in order for the first proton transfer to occur within the gas-phase collision complex, the proton affinity (PA) of the analyte cannot be more than 10 kcal/mol greater than that of TMB (195 kcal/mol).[9] TMB was chosen to be the reagent to differentiate sulfones from sulfoxides and N-oxides because its PA is close to the PAs of sulfones (193−205

Scheme 1. Proposed Mechanism for Reaction of a Protonated Sulfone with TMB to Form Adduct and Adduct-MeOH
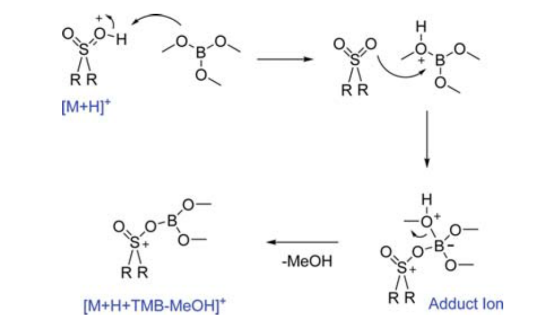
kcal/mol, Table 1), somewhat lower than the PAs of hydroxyl-amines (205−216 kcal/mol; Table 2), and substantially lower than the PAs of sulfoxides (215−220 kcal/mol; Table 1) and N-oxides (~220 kcal/mol; Table 2). Therefore, TMB is expected to react readily, as shown in Scheme 1, with protonated sulfones but not as readily with protonated hydroxylamines, sulfoxides, and N-oxides.

The reactions of TMB with many protonated model compounds with different functional groups, including sulfone, sulfoxide, hydroxylamino, N-oxide, aniline, amino, hydroxyl, and phenol, were examined in a linear quadruple ion trap mass spectrometer (LQIT). As shown in Table 1, most protonated sulfone model compounds react with TMB at high efficiencies (~100%) by predominant formation of the adduct-MeOH ion (Table 1), as expected. The lower reaction efficiency measured for protonated N-hydroxybenzenesulfonamide is explained by its relatively high PA (211.2 kcal/mol, Table 1).

For protonated sulfones, such as protonated methyl phenyl sulfone, additional product ions besides the adduct-MeOH ion were observed. These are a stable TMB adduct ion and, most importantly, adduct-Me_2O ion (Figure 1), which is diagnostic for protonated sulfones. No adduct-Me_2O product ion was found for any other protonated model compound studied here (Tables 1 and 2). On the basis of the literature, however, some protonated epoxides yield the adduct-Me_2O ion with a branching ratio ranging from 3 to 10% in the same instrument and under the same conditions as those used here (the other product is adduct-MeOH).[8a] Protonated epoxides can be distinguished from sulfones based on the lack of formation of TMB adduct ions for the epoxides.[8a] Therefore, the formation of adduct-Me_2O ions together with TMB adduct ions can be used to distinguish sulfones from all other compounds considered here.

A possible mechanism for the formation of adduct-Me_2O ion for protonated sulfones is shown in Figure 2. This mechanism is initiated by proton transfer from the analyte to the boron compound, just like the methanol elimination mechanism shown in Scheme 1. Nucleophilic addition of the sulfone to the boron center leads to the methanol elimination product as shown in Scheme 1. However, we propose that in some cases the sulfone instead undergoes nucleophilic substitution at the carbon atom of the protonated methoxy group and a methyl-transfer reaction takes place followed by nucleophilic substitution at the same carbon atom by a methoxy substituent of TMB, leading to another methyl cation transfer (Figure 2). The methyl cation affinities of TMB and sulfones are likely to be similar because of their similar PA values[8h] and hence these reactions should be nearly thermoneutral. Nucleophilic substitution has a more
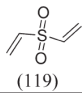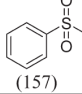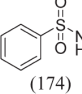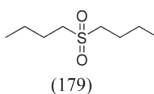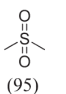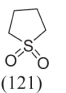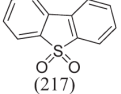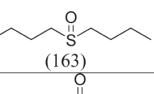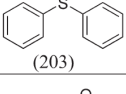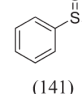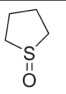
constrained TS than addition reactions, which explains why this pathway is minor compared to methanol elimination. Addition of the sulfone to the boron center in TMB with a methylated methoxy group has a very low calculated barrier (0.25 kcal/mol; Figure 2), and it is estimated to be exothermic by 1 kcal/mol. Elimination of dimethyl ether from this adduct also has a very low barrier (1.8 kcal/mol) and is exothermic by about 3 kcal/mol (Figure 2). Scheme S1 in the Supporting Information shows an analogous mechanism for the formation of adduct-Me_2O for a protonated epoxide, propylene oxide, with PA = 192.0 kcal/mol, which is close to that of TMB and sulfones.

On the basis of previous research,[11] protonated compounds containing oxygen functionalities other than sulfone, such as ethers, ketones, carboxylic acids, and esters, only yield adduct-MeOH product ions with TMB, and they are formed as shown in Scheme 1. Here, the same was found to be true for protonated sulfoxides (Table 1) and hydoxylamines (Table 2), which also have substantially lower reaction efficiencies than protonated sulfones. Hence, sulfones are distinguished from sulfoxides and hydroxylamines based on the formation of the Me_2O elimination product for protonated sulfones only and based on their substantially greater reaction efficiencies. Protonated N-oxides are readily differentiated from sulfones, sulfoxides and hydroxyl-amines since they are unreactive toward TMB, as reported before.[8h] The observation of the Me_2O elimination product only for protonated sulfones (and some protonated epoxides) may be partially explained by their lower nucleophilicity compared to sulfoxides, N-oxides, and hydroxylamines (nucleophilicity commonly correlates[8h] with PA). Addition of the more nucleophilic analytes to the boron center of protonated TMB is likely to be exothermic enough to cause immediate elimination of methanol. However, for sulfones, this addition may be reversible. Furthermore, sulfones have very large dipole moments[16] (>4 D; comparable to those[16] of sulfoxides and N-oxides), which means that ion/molecule complexes containing a neutral sulfone lay low in energy, have a long lifetime, and contain excess internal energy. This likely enables a neutral sulfone to undergo competitive attack at both the boron atom and the most electrophilic methyl group in protonated TMB, ultimately resulting in elimination of both methanol as well as dimethyl ether (Scheme 1 and Figure 2).

The reactivity of TMB toward a protonated aliphatic amine and an alcohol as well as phenol and two anilines was also examined. As shown in Table 2, the protonated amine and the protonated anilines react only slowly with TMB (efficiencies <7%) via exclusive formation of a stable adduct (likely as shown in Scheme 1), whereas protonated butanol reacts rapidly by exclusive proton transfer (because of its low PA; 188.8 kcal/mol[16]). Protonated phenol (with PA close to that of TMB; Table 2) also transfers a proton to TMB, but, in addition, it forms a stable adduct and the MeOH elimination product (see Scheme 1 for both reactions). These findings suggests that formation of a stable adduct (just like the MeOH elimination product) is preceded by proton transfer from the protonated analyte to TMB because the adduct was observed only for analytes whose PAs are similar or greater than that of TMB (Tables 1 and 2). This finding is in agreement with the mechanisms shown in Scheme 1 and Figure 2. In summary, the protonated sulfone functional group can be easily differentiated from amino, aniline, hydroxyl, and phenol moieties via its formation of the adduct-Me_2O ion.

The application of this method for the identification of a sulfone metabolite of a sulfoxide drug was demonstrated using sulindac, a nonsteroidal anti-inflammatory drug, and its

Table 1. Reaction Efficiencies and Products (*m/z* Values and Branching Ratios) for Reactions of Protonated Sulfones and Sulfoxides with TMB (PA = 195 kcal/mol)[a]
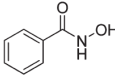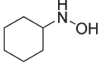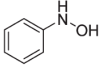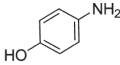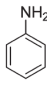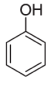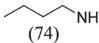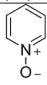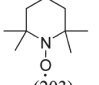
Reagent (m/z of [M+H]$^+$)	PA[b] (kcal/mol)	Product ions (m/z) and branching ratios		Reaction efficiency
(119)	206.3	Adduct–MeOH (191)	85%	107%
		Adduct–Me$_2$O (177)	10%	
		Adduct (223)	5%	
(157)	201.4	Adduct–MeOH (225)	87%	107%
		Adduct–Me$_2$O (215)	10%	
		Adduct (261)	3%	
(174)	211.6	Adduct–MeOH (246)	74%	57%
		Adduct–Me$_2$O (232)	12%	
		Adduct (278)	14%	
(179)	203.7	Adduct–MeOH (251)	89%	118%
		Adduct–Me$_2$O (237)	9%	
		Adduct (281)	1%	
(95)	193.5	Adduct–MeOH (167)	83%	101%
		Adduct–Me$_2$O (153)	8%	
		Adduct (199)	3%	
		Proton Transfer (105)	6%	
(121)	198.3	Adduct–MeOH (193)	79%	111%
		Adduct–Me$_2$O (179)	14%	
		Adduct (225)	7%	
(217)	205.0	Adduct–MeOH (289)	89%	104%
		Adduct–Me$_2$O (276)	10%	
		Adduct (321)	1%	
(163)	220.1	Adduct–MeOH (235)	100%	0.7%
(203)	222.5	Adduct–MeOH (275)	100%	0.4%
(141)	219.8	Adduct–MeOH (213)	100%	0.9%
(104)	219.6	Adduct–MeOH (177)	64%	2%
		Adduct (209)	36%	

[a]Ref 9. [b]PA calculated at the B3LYP/6-31G(d) level of theory.

metabolite, sulindac sulfone (Figure 3). As expected, protonated sulindac sulfone reacts quickly (with 44% efficiency) with TMB to give TMB adduct, adduct-MeOH, and adduct-Me$_2$O, whereas protonated sulindac reacts slowly (10% efficiency) with TMB and only shows a small amount of adduct-MeOH product ion. Their reactivities and product ions are similar to the analogous compounds in Table 1. However, when sulindac and sulindac sulfone were protonated and subjected to CAD, both of these molecules fragment by losses of water, carbon dioxide, and methyl radical, with no fragmentations indicative of either a sulfoxide or a sulfone functionality.

Lastly, it is important to note that a reactivity diagnostic of a sulfone functionality was observed for reactions of TMB with two protonated compounds with more than one functionality, *N*-hydroxybenzenesulfonamide and sulindac sulfone. These findings indicate that the diagnostic reactivity is not quenched by the presence of additional functionalities, although the reaction efficiency may depend on the functionalities present in the analyte.

Table 2. Reaction Efficiencies and Products (*m/z* Values and Branching Ratios) Formed in Reactions between Protonated Hydroxylamines, N-Oxides, Anilines, an Aliphatic Amine, an Aliphatic Alcohol, and Phenol with TMB (PA = 195 kcal/mol)[a]

Reagent (m/z of [M+H]⁺)	PA[b] (kcal/mol)	Product ions (m/z) and branching ratios		Reaction efficiency
(138)	211.7	Adduct–2MeOH (178)	45%	6%
		Adduct (242)	29%	
		Adduct–MeOH(228)	26%	
(116)	215.9	Adduct (220)	100%	4%
(110)	204.6	Adduct (214)	100%	1%
(110)	212.9	Adduct (214)	100%	1%
(94)	209.4	Adduct (198)	100%	2%
(95)	194.6	Adduct–MeOH (167)	85%	5%
		Adduct (199)	3%	
		Proton Transfer (105)	12%	
(75)	187.6	Proton Transfer (105)	100%	60%
(74)	220.9	Adduct (178)	100%	1%
(96)	219.2	No reaction		No reaction
(203)	--	No reaction		No reaction

[a]Ref 9. [b]PA calculated at the B3LYP/6-31G(d) level of theory.

■ CONCLUSIONS

The ability to use functional-group-selective ion/molecule reactions in a linear quadrupole ion trap mass spectrometer to identify compounds with the sulfone functionality has been demonstrated. All protonated sulfone model compounds were found to react with TMB to form the diagnostic product ion, adduct-Me₂O, at high efficiency. Other protonated compounds, including sulfoxides, hydroxylamines, and N-oxides, react with TMB only very slowly or not at all via adduct formation or MeOH elimination from the adduct, and none of them give the adduct-Me₂O product ion. Similar results were obtained for anilines and an aliphatic amine. Phenol yields a proton-transfer product in addition to the adduct-MeOH product and the stable adduct. Protonated butanol differs from the other ions studied in that it rapidly and exclusively transfers a proton to TMB because of its high acidity. On the basis of the literature,[8a] some protonated epoxides form the adduct-Me₂O product ion but can be differentiated from sulfones because of the lack of formation of a stable adduct. The sulfone-selective reactivity was observed even in the presence of additional functionalities. A mechanism is proposed that rationalizes the selectivity of the addition/Me₂O elimination reaction for protonated sulfones and that is supported by quantum chemical calculations. Lastly, the results obtained for sulindac and sulindac sulfone suggest that this method is applicable to sulfone-containing drugs and drug metabolites.

The Journal of Organic Chemistry
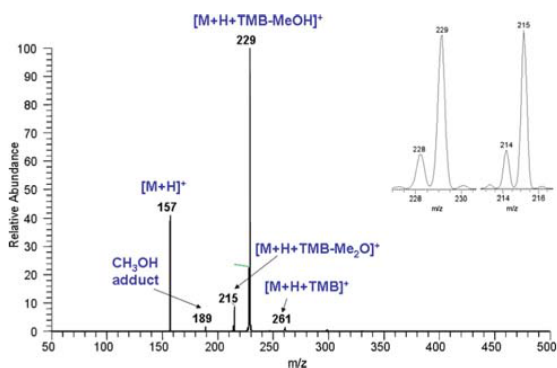
Figure 1. Mass spectrum measured after 30 ms reaction of protonated methyl phenyl sulfone (m/z 157) with TMB. The most abundant product ion (m/z 229) corresponds to adduct-MeOH. The other two product ions of TMB correspond to the adduct-Me$_2$O (m/z 215) and TMB adduct (m/z 261). The presence of boron in ions of m/z 229 and 215 was verified by the presence of ^{10}B isotope peaks. Ion of m/z 189 corresponds to a methanol adduct (verified by using ethanol as a solvent instead of methanol and observing a 14 unit shift in the m/z value).

■ EXPERIMENTAL SECTION

Chemicals. All chemicals were purchased and used without further purification.

Instrumentation. All mass spectrometry experiments were performed using a linear quadruple ion trap (LQIT) equipped with an APCI source. Sample solutions were prepared at analyte concentrations ranging from 0.01 to 1 mg/mL in methanol. An integrated syringe drive directly infused the solutions into the APCI source at a rate of 20 μL/min. In the APCI source (operated in positive ion mode), the vaporizer and capillary temperatures were set at 400 and 265 °C, respectively. The sheath gas (N$_2$) flow was maintained at about 30 arbitrary units. The voltages for the ion optics were optimized for

each analyte by using the tune feature of the LTQ Tune Plus interface. The detection mass range was from m/z 50 to 500. The manifold used to introduce reagents into the helium buffer gas line was first described by Gronert.[12,13] A diagram of the exact manifold used in this research was published by Habicht et al.[8b] TMB was introduced into the manifold via a syringe pump maintained at a flow rate of 5 μL/h. A known amount of He (0.8 L/h) was used to dilute TMB. The syringe port and surrounding area were heated at ~70 °C to ensure evaporation of TMB. Before entering the trap, the He/reagent mixture was split using two Granville—Phillips leak valves instead of the standard flow splitter. This allowed for better control over the amount of the mixture introduced into the instrument. One leak valve was set to establish a helium pressure of ~3 mTorr in the ion trap by allowing ~2 mL/min of the mixture into the trap,[14] whereas the other leak valve controlled the amount of flow diverted to waste. A typical nominal pressure of TMB in the trap during the experiments was 0.38×10^{-5} Torr. After the experiments were completed each day, the manifold was isolated from the instrument and placed under vacuum to remove any remaining reagent.

Kinetics. During the ion/molecule reactions, the reagent (TMB) was present at a constant pressure, and its concentration was in excess of that of the ion of interest. Hence, these reactions follow pseudo-first-order kinetics. The reaction efficiencies (efficiency = ($k_{reaction}/k_{collision}$)100 = the fraction of ion/molecule collisions that results in the formation of products) were determined by measuring each reaction's rate (IM) (by monitoring the abundance of the protonated analyte as a function of time for up to 1 s) and the rate of the highly exothermic proton-transfer reaction (PT) between protonated methanol and the reagent (TMB) under identical conditions on the same day. Assuming that this exothermic proton-transfer reaction proceeds at a collision rate ($k_{collision}$) that can be calculated, the efficiencies of the ion/molecule reactions can be obtained using eq 1. This equation is based on the ratio of the slopes ($k_{reaction}$[TMB] = slope (IM) and $k_{collision}$[TMB] = slope (PT); [TMB] = TMB concentration) of the plots of the natural logarithm of the relative abundance of the reactant ion versus reaction time for the ion/molecule (IM) and exothermic proton-transfer (PT) reactions (thus eliminating the need to know [TMB]), masses of the ion (M_i), neutral reagent (M_n), and methanol ($M_{(PT)}$), and the nominal pressure of the neutral reagent

Figure 2. Proposed mechanism for reaction of a protonated sulfone with TMB to form adduct-Me$_2$O and the calculated (B3LYP/6-31G(d,p)) free-energy surface for the second step (left) and the last two steps (right) of the mechanism.

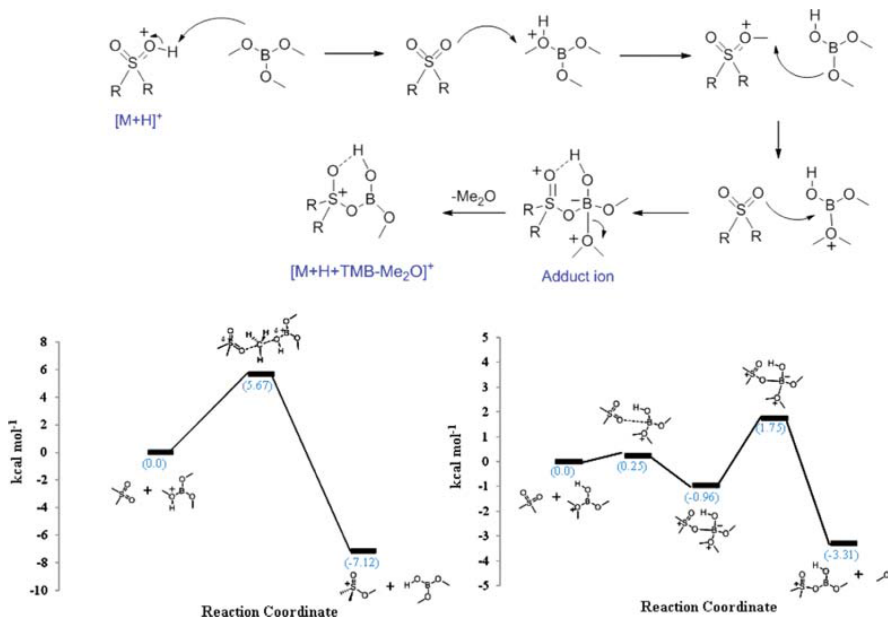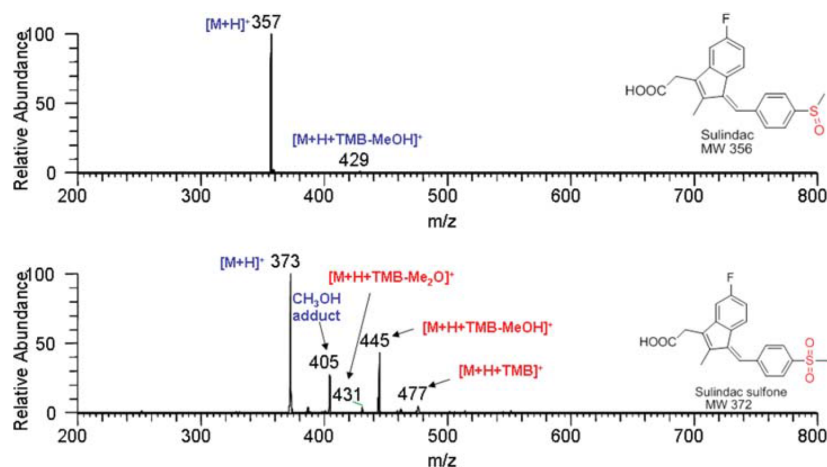**Figure 3.** Upper mass spectrum was measured after 1 s reaction of protonated sulindac with TMB. Lower mass spectrum was measured after 100 ms reaction of protonated sulindac sulfone with TMB. The ion of m/z 405 in the bottom spectrum corresponds to a methanol adduct, which was confirmed by using ethanol as the solvent instead of methanol and observing a 14 unit shift in the m/z value.

during the ion/molecule reaction ($P_{n(IM)}$) and the proton-transfer reaction ($P_{n(PT)}$).

$$\text{efficiency} = \frac{\text{slope(IM)}}{\text{slope(PT)}} \left(\frac{M_i(M_{(PT)} + M_n)}{M_{(PT)}(M_i + M_n)} \right)^{1/2} \left(\frac{P_{n(PT)}}{P_{n(IM)}} \right) 100 \tag{1}$$

Computational Studies. The Gaussian 03 suite of programs was used for all calculations.[15] Proton affinities were calculated at the B3LYP/6-31G(d) level of theory. For protonation of an oxygen site, protonated methanol was used as the Brønsted acid in isodesmic reaction schemes.[16] For protonation of the phenyl ring, protonated benzene[16] was used as the reference acid. For protonation of a nitrogen site, ammonium[16] was used as the reference acid. An excellent agreement of the calculated values with experimental data, where available, was found. For example, methyl phenyl sulfone, dimethyl sulfone, diphenyl sulfoxide, and methyl phenyl sulfoxide have calculated PAs of 201.4, 193.5, 222.5, and 219.8 kcal/mol, whereas the experimentally[17] determined values are 200.0, 193.5, 218.8, and 214.9 kcal/mol. The free-energy surfaces shown in Figure 2 were calculated at the B3LYP/6-31G(d,p) level of theory.

■ ASSOCIATED CONTENT

ⓢ Supporting Information

Proposed mechanism for reaction of a protonated epoxide with TMB to form adduct-Me₂O and dtailed computational data. This material is available free of charge via the Internet at http://pubs.acs.org.

■ AUTHOR INFORMATION

Corresponding Author
*E-mail: hilkka@purdue.edu.

Notes
The authors declare no competing financial interest.

■ ACKNOWLEDGMENTS

■ REFERENCES

(1) Holland, H. L. *Nat. Prod. Rep.* **2001**, *18*, 171.

(2) (a) Zuniga, F. I.; Loi, D.; Ling, K. H.; Tang-Liu, D. D. *Expert Opin. Drug Metab. Toxicol.* **2012**, *8*, 467. (b) Chen, X.; Hussain, S.; Parveen, S.; Zhang, S.; Yang, Y.; Zhu, C. *Curr. Med. Chem.* **2012**, *19*, 3578.

(3) (a) Caslavska, J.; Thormann, W. *J. Chromatogr. A* **2011**, *1218*, 588. (b) Bhave, D. P.; Muse, W. B., 3rd; Carroll, K. S. *Infect. Disord.: Drug Targets* **2007**, *7*, 140. (c) Dibbern, D. A., Jr.; Montanaro, A. *Ann. Allergy, Asthma, Immunol.* **2008**, *100*, 91.

(4) Cooks, R. G.; Busch, K. L.; Glish, G. L. *Science* **1983**, *222*, 273.

(5) (a) Hibbs, J. A.; Jariwala, F. B.; Weisbecker, C. S.; Attygalle, A. B. *J. Am. Soc. Mass Spectrom.* **2013**, *24*, 1280. (b) Lam, W.; Ramanathan, R. *J. Am. Soc. Mass Spectrom.* **2002**, *13*, 345.

(6) Coleman, M. D. *Human Drug Metabolism: An Introduction*, 2nd ed.; John Wiley & Sons: Hoboken, NJ, 2010.

(7) Osburn, S.; Ryzhov, V. *Anal. Chem.* **2013**, *85*, 769.

(8) (a) Eismin, R. J.; Fu, M.; Yem, S.; Widjaja, F.; Kenttämaa, H. I. *J. Am. Soc. Mass Spectrom.* **2012**, *23*, 12. (b) Habicht, S. C.; Vinueza, N. R.; Archibold, E.; Duan, P.; Kenttämaa, H. I. *Anal. Chem.* **2008**, *80*, 3416. (c) Campbell, K. M.; Watkins, M. A.; Li, S.; Fiddler, M. N.; Winger, B.; Kenttämaa, H. I. *J. Org. Chem.* **2007**, *72*, 3159. (d) Somuramasami, J.; Winger, B. E.; Gillespie, T. A.; Kenttämaa, H. I. *J. Am. Soc. Mass Spectrom.* **2010**, *21*, 773. (e) Fu, M.; Eismin, R. J.; Duan, P.; Li, S.; Kenttämaa, H. I. *Int. J. Mass Spectrom.* **2009**, *282*, 77. (f) Fu, M.; Duan, P.; Gao, J.; Kenttämaa, H. I. *Analyst* **2012**, *137*, 5720. (g) Duan, P.; Fu, M.; Gillespie, T. A.; Winger, B. E.; Kenttämaa, H. I. *J. Org. Chem.* **2009**, *74*, 1114. (h) Duan, P.; Gillespie, T. A.; Winger, B. E.; Kenttämaa, H. I. *J. Org. Chem.* **2008**, *73*, 4888.

(9) Fu, M.; Duan, P.; Li, S.; Eismin, R. J.; Kenttämaa, H. I. *J. Am. Soc. Mass Spectrom.* **2009**, *20*, 1251.

(10) Watkins, M. A.; Winger, B. E.; Shea, R. C.; Kenttämaa, H. I. *Anal. Chem.* **2005**, *77*, 1385.

(11) Habicht, S. C.; Vinueza, N. R.; Amundson, L. M.; Kenttämaa, H. I. *J. Am. Soc. Mass Spectrom.* **2011**, *22*, 520.

(12) Gronert, S. *J. Am. Soc. Mass Spectrom.* **1998**, *9*, 845.

(13) Gronert, S. *Mass Spectrom. Rev.* **2005**, *24*, 100.

(14) Schwartz, J. C.; Senko, M. W.; Syka, J. E. P. *J. Am. Soc. Mass Spectrom.* **2002**, *13*, 659.

(15) Frisch, M. J.; Trucks, G. W.; Schlegel, H. B.; Scuseria, G. E.; Robb, M. A.; Cheeseman, J. R.; Montgomery, J. A., Jr.; Vreven, T.; Kudin, K. N.; Burant, J. C.; Millam, J. M.; Iyengar, S. S.; Tomasi, J.; Barone, V.; Mennucci, B.; Cossi, M.; Scalmani, G.; Rega, N.; Petersson, G. A.; Nakatsuji, H.; Hada, M.; Ehara, M.; Toyota, K.; Fukuda, R.; Hasegawa, J.; Ishida, M.; Nakajima, T.; Honda, Y.; Kitao, O.; Nakai, H.; Klene, M.; Li, X.; Knox, J. E.; Hratchian, H. P.; Cross, J. B.; Bakken, V.; Adamo, C.; Jaramillo, J.; Gomperts, R.; Stratmann, R. E.; Yazyev, O.; Austin, A. J.;

Cammi, R.; Pomelli, C.; Ochterski, J. W.; Ayala, P. Y.; Morokuma, K.; Voth, G. A.; Salvador, P.; Dannenberg, J. J.; Zakrzewski, V. G.; Dapprich, S.; Daniels, A. D.; Strain, M. C.; Farkas, O.; Malick, D. K.; Rabuck, A. D.; Raghavachari, K.; Foresman, J. B.; Ortiz, J. V.; Cui, Q.; Baboul, A. G.; Clifford, S.; Cioslowski, J.; Stefanov, B. B.; Liu, G.; Liashenko, A.; Piskorz, P.; Komaromi, I.; Martin, R. L.; Fox, D. J.; Keith, T.; Al-Laham, M. A.; Peng, C. Y.; Nanayakkara, A.; Challacombe, M.; Gill, P. M. W.; Johnson, B.; Chen, W.; Wong, M. W.; Gonzalez, C.; Pople, J. A. *Gaussian 03*, revision C.02; Gaussian, Inc.: Wallingford, CT, 2003.

(16) Hunter, E. P.; Lias, S. G. Proton Affinity Evaluation. In *NIST Chemistry WebBook, NIST Standard Reference Database Number 69*; Linstrom, P. J., Mallard, W. G., Eds.; National Institute of Standards and Technology: Gaithersburg, MD, 2013.

(17) Buncel, E.; Decouzon, M.; Formento, A.; Gal, J. F.; Herreros, M.; Li, L.; Maria, P. C.; Koppel, I.; Kurg, R. *J. Am. Soc. Mass Spectrom.* **1997**, *8*, 262.

ELSEVIER

Elucidation of structural information achievable for asphaltenes via collision-activated dissociation of their molecular ions in MS^n experiments: A model compound study

CrossMark

Tiffany M. Jarrell [a], Chunfen Jin [a], James S. Riedeman [a], Benjamin C. Owen [a], Xiaoli Tan [c], Alexander Scherer [b], Rik R. Tykwinski [b], Murray R. Gray [c], Peter Slater [d], Hilkka I. Kenttämaa [a],*

[a] Department of Chemistry, Purdue University, USA
[b] Department of Chemistry and Pharmacy & Interdisciplinary Center of Molecular Materials (ICMM), University of Erlangen-Nuremberg, Germany
[c] Department of Chemical and Materials Engineering, University of Albert, Canada
[d] ConocoPhillips Company, USA

HIGHLIGHTS

- Methodology will facilitate the elucidation of the structures of asphaltenes.
- Unique fragmentation shown for island and archipelago structures.
- Distinguishable characteristics: alkyl chain lengths and sizes of aromatic cores.
- Fragmentation influenced by presence of nitrogen.
- No influence from the presence of sulfur.

ARTICLE INFO

ABSTRACT

Despite extensive studies of the asphaltene fraction of petroleum, the molecular structures of asphaltenes remain a highly debated topic. Tandem mass spectrometry is the only technique that allows the examination of the structures of individual asphaltene molecules due to the extreme complexity of asphaltenes. Recently, atmospheric pressure chemical ionization (APCI) using CS_2 as the reagent was demonstrated to produce abundant and stable molecular ions for polyaromatic hydrocarbons with long alkyl chains. Hence, coupling APCI/CS_2 with tandem mass spectrometry appears to be a promising method for the examination of the structures of molecules in asphaltenes. However, the fragmentation pathways of the molecular ions of large alkyl aromatic compounds are not well understood. In order to address this issue, a detailed examination of the collision-activated dissociation reactions of the molecular ions and several of their fragment ions (MS^n experiments) was carried out for several model compounds of asphaltenes. The results show that information on various structural aspects of asphaltenes can be obtained from these experiments, such as alkyl chain lengths and sizes of aromatic cores. Based on these results, MS^2 experiments may provide enough information to determine approximate core sizes for molecules with archipelago structures. However, the number of ion isolation and collision-activated dissociation (CAD) experiments needed to elucidate maximum structural information for molecules with island structures depends on the number of carbon chains on the aromatic core.

© 2014 Elsevier Ltd. All rights reserved.

1. Introduction

Asphaltenes are a subset of molecules in crude oil whose structural elucidation has proven difficult [1–3]. They comprise the fraction of petroleum that is soluble in toluene but insoluble in n-alkanes [4] and can correspond to up to 20% of crude oil [5]. The elucidation of the structures of the molecules in asphaltenes has far reaching implications [3] since asphaltenes clog pipes used for transportation of crude oil and poison catalysts used in refining [1,6–11]. Further, only few uses exist for asphaltenes, including expensive upgrading to distillates [12], road construction [13] and recently proposed use in organic electronic materials [14,15].

In order to be able to efficiently address the above problems, a better understanding of the structures of the predominant molecules is essential [1,3,16].

Archipelago and island structures have been proposed for asphaltenes [4,17]. Archipelago structures are defined as two or more fused aromatic rings that are connected with alkyl chains [18]. In contrast, the island structures only have one core of fused aromatic rings and may contain external alkyl chains. Both proposed structures also may contain saturated rings [17]. The island structure has received strong support from studies using methods such as time resolved fluorescence depolarization, Taylor diffusion, and NMR pulsed field gradient measurements [3,7,19–24]. However, evidence in support of the existence of archipelago structures has been obtained from studies using NMR spectroscopy and average structural parameter calculations [7,25] FT-ICR MS/MS experiments [26], and thermal cracking [27]. Despite these studies, conflicting consensus exists on the structures of asphaltenes due to the variation of the analytical techniques used [5]. For example, a recent study suggested that spectroscopic methods may lack the ability to distinguish island and archipelago structures [1]. Further, asphaltenes comprise very complex mixtures, which prevent the determination of the structures of individual molecules by most analytical techniques.

Tandem mass spectrometry (MS^n) is uniquely suited for complex mixture analysis because it allows for direct molecular level characterization of individual components without prior separation [28–30]. Tandem mass spectrometry (MS^n) employs at least two stages of mass analysis (MS/MS) in order to examine a particular ion of interest by isolation followed by dissociation or other reactions before mass analysis. Dissociation reactions of fragment ions and their fragment ions can be examined using MS/MS/MS and MS/MS/MS/MS experiments, respectively. MS also is attractive due to its high speed and great sensitivity [28]. However, complex mixtures can only be analyzed with confidence when an appropriate ionization method is available [31]. The ionization method must produce only one ion type containing the intact analyte without fragmentation or aggregation for all analytes present to prevent convolution of the mass spectrum.

Asphaltenes are notoriously difficult to introduce into mass spectrometers and ionize due to their limited volatility, lack of ionizable functionalities and facile aggregation and degradation after ionization [5,21,32–34]. Recently, atmospheric pressure chemical ionization (APCI) combined with CS_2 reagent was demonstrated [9] to be especially well suited for evaporation and ionization of asphaltenes since it has no bias to more polar analytes and it produces only one ion type, molecular ion (M$^{+\cdot}$), for all asphaltene model compounds studied [9]. In addition, it has been demonstrated that laser desorption/laser ionization of analytes relevant to asphaltenes produces molecular ions with minimal fragmentation for the majority of analytes studied [33,34]. These methods allow for the determination of the molecular weight and elemental composition of all analytes present. However, structural information can only be obtained via tandem mass spectrometry experiments wherein the molecular ions are isolated and subjected to collision-activated dissociation (CAD) or other reactions [8,28].

Previous studies on CAD of protonated asphaltene model compounds have revealed useful structural information [8]. In sharp contrast, CAD of the molecular ions of asphaltene model compounds has not been explored. However, better understanding on these processes is required to be able to make proper structural conclusions based on fragmentation reactions observed for molecular ions derived from asphaltenes. In this study, a representative set of model compounds (Tables 1 and 2) of asphaltenes was ionized by APCI/CS_2 and subjected to multiple stages of consecutive ion isolation and CAD events (MS^n experiments) in order to

Table 1
Labels and structures for the asphaltene model compounds studied.

Label	Structure
Naphthalene	
Biphenylene	
Diphenylacetylene	
Anthracene	
Pyrene	
Chrysene	
Coronene	
THN	
DHP	
DHA	
DDP	
THP	
TDP	

improve the fundamental understanding of fragmentation/structure relationships for molecular ions of asphaltenes.

2. Materials and methods

2.1. Chemicals

DDP, TDP, THP, KS-140, KS-152, KS-P4P, P-mPhP, KS-100, KS-115, KS-136, P26PP, PB, ABA, P-3,5pyrP, and P-2,5pyr-3-Mep were provided by Professor Murray Gray [35]. Diphenylacetylene was purchased from Alfa Aesar (Ward Hill, MA). Coronene (97%), 1,2,3,4-tetrahydronaphthalene (99%), pyrene (99%), 9,10-dihydrophenanthrene (94%), 9,10-dihydroanthracene (97%), biphenylene (99%), chrysene (98%), diphenylacetylene (99%), anthracene (97%), and the solvent CS_2 (>99.9%) were purchased from Sigma–Aldrich (St. Louis, MO). Naphthalene (>95%) was purchased from Fisher Scientific.

2.2. Instrumentation

All the model compounds were dissolved in CS_2 at 1 mM concentration, and the solutions were directly injected into the ion source with a spray flow rate of 5 μl/min. The N_2 sheath gas and auxiliary gas were used with a flow rate of <40 arbitrary units and <10 arbitrary units, respectively, to maintain a stable spray. All CAD studies were performed in a linear quadrupole ion trap

Table 2
Labels and structures for the archipelago model compounds studied.

Label	Structure
KS-P4P	
KS-152	
P-mPhP	
KS-140	
KS-115	
KS-136	
PB	
P-3,5pyrP	
P26PP	
ABA	
P-2,5pyr-3-Mep	
KS-100	

(LQIT) mass spectrometer (Thermo Scientific, San Jose, CA, USA). The instrument was equipped with an atmospheric-pressure chemical ionization (APCI) source and operated in positive ion mode. The settings for the ionization conditions were as follows: vaporizer temperature 300 °C, Corona discharge voltage and current, 5 kV and 5 μA, respectively, and the transfer capillary voltage and tube lens voltage 10–20 V and 50–70 kV, respectively. The moderate capillary and tube lens voltages were used to prevent fragmentation of the molecular ions.

The molecular ions were isolated with a total isolation window width of m/z 1.0 centered at the molecular ion's m/z-value. A narrow isolation window was used to prevent inclusion of interfering ions with similar m/z-values. Any width smaller than m/z 1.0 resulted in the loss of ion signal. The isolated ions were kinetically excited at a q value of 0.25 or 0.40 for CAD (MS^2 experiment). In the

LQIT, CAD is a slow heating method wherein ions are subjected to multiple low-energy collisions with the helium buffer gas over a relatively long period of time. A dipolar supplementary excitation pulse with a frequency matching the ions' secular frequency was used to increase the ions' kinetic energy for 30 ms. Upon collisions with the helium buffer gas, the kinetic energy is converted into internal energy to induce dissociation. A q value of 0.25 was selected to ensure efficient trapping of small fragment ions. However, to induce fragmentation for those molecular ions requiring higher energy collisions, the q value was increased to 0.4, as noted in the Tables. In MS^3 experiments, major fragment ions produced from the molecular ions in the MS^2 experiments were isolated, one after each other, and subjected to CAD. This was followed by isolation of the fragment ions' major fragment ions and subjecting them to CAD (MS^3), followed by isolation and fragmentation of their fragment ions (MS^4), until no more fragmentation was observed. The MS^n product ions' relative abundances are given as averages of values measured using at least 30 scans (only product ions with relative abundances above 10% are reported).

When using Thermo Scientific LQIT, the kinetic energy of the excited ions is defined by "normalized collision energy" on a scale from 0% to 100%. The exact collision energies are unknown. However, the q value also plays an essential role in CAD experiments. The q value chosen greatly influences the amount of kinetic energy that the ion of interest gains. At higher q values, ions oscillate at a higher frequency and hence have higher kinetic energies, resulting in more fragmentation upon collisions with helium.

3. Results and discussion

A total of 25 aromatic compounds were studied using positive-ion mode APCI/CS$_2$ and MS^n experiments in a linear quadrupole ion trap (LQIT) mass spectrometer. The compounds studied include island and archipelago structures containing only carbons and hydrogens, and archipelago type compounds with nitrogen or sulfur heteroatoms. In agreement with a previous study [9], all compounds studied were found to produce stable molecular ions upon APCI/CS$_2$. After isolation of the molecular ions in the mass spectrometer, they were subjected to CAD, followed by isolation of many of their fragment ions and subjecting them to CAD, and so on. CAD experiments were continued until no fragment ions were visible. When no fragmentation was observed, the q value of the ion trap was increased to induce higher energy collisions in order to further probe the structures of the ions. Structurally informative fragment ions were obtained for all of the analytes studied. A detailed discussion of the fragmentation reactions observed for the asphaltene model compounds is provided below.

3.1. Fragmentation reactions of completely conjugated molecular ions with Island structures

The molecular ions of many of the island compounds without saturated moieties, i.e., coronene, pyrene, chrysene, anthracene, and naphthalene, did not fragment under the lowest energy conditions used. At a higher q value, the molecular ions of coronene, pyrene and chrysene lose several H$_2$ molecules or H atoms in a consecutive manner (Fig. 1, Table S1). H$_2$ loss is the most facile fragmentation for these three analytes. Coronene and chrysene molecular ions exhibit four consecutive H$_2$ losses, while pyrene molecular ion exhibits three. For all island type analytes with more than three aromatic rings and no alkyl chains, H$_2$ loss is the predominant fragmentation reaction observed. Pyrene molecular ion exhibits additional, slower losses of acetylene in MS$^{3-5}$, diacetylene in MS$^{4-5}$, and triacetylene in MS^5 experiments (Table S1). Naphtha-
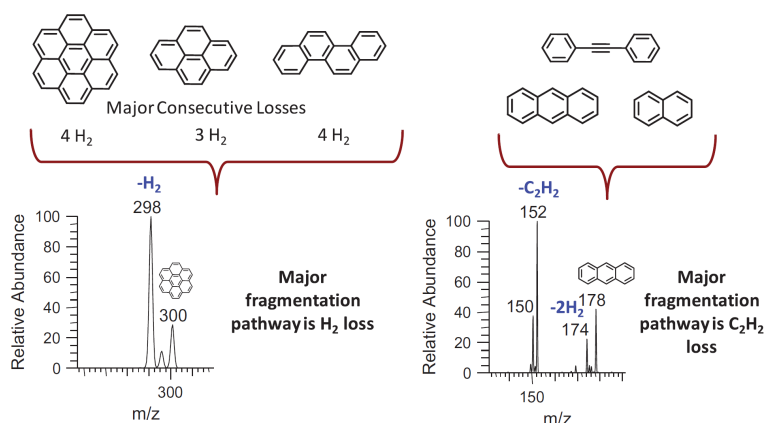
Fig. 1. Major fragmentation pathways for molecular ions of island model compounds without alkyl substituents or saturated rings.

lene and anthracene exhibit a facile loss of acetylene in MS^2 experiments (Fig. 1).

In addition to above compounds, fragmentation reactions of the molecular ion of diphenylacetylene were explored. No fragmentation was observed upon low-energy CAD. Upon increasing the q value, fragmentations involving loss of an acetylene or a hydrogen molecule occurred (Fig. 1). Upon further CAD of the fragment ions and their fragment ions *etc.* in MS^{3-5} experiments, additional losses of acetylene and hydrogen molecules took place until no further fragmentation was observed (Table S1). This fragmentation is reminiscent of that observed for molecular ions of anthracene and naphthalene. In sharp contrast to all above compounds, and despite also being fully conjugated, ionized biphenylene readily undergoes fragmentation via loss of C_6H_4 without the use of higher-energy conditions. The strained linkages between the aromatic rings may drive this facile fragmentation (Fig. 2, Table S1). This is the only fully conjugated system whose molecular ions did not require higher-energy conditions to obtain fragmentation.

3.2. Fragmentation reactions of molecular ions with Island structures containing saturated rings

In addition to fully conjugated compounds, three compounds containing aromatic rings fused with saturated rings were studied: 9,10-dihydrophenanthrene, 9,10-dihydroanthracene, and 1,2,3,4-

tetrahydronaphthalene. Due to the presence of a saturated ring, fragmentation pathways with lower barriers are accessible for the molecular ions of these compounds (Fig. 2, Table S2). Hence, they fragment under low energy conditions. CAD of the molecular ions of 1,2,3,4-tetrahydronaphthalene occurs via a retro-Diels–Alder reaction to lose ethylene. Upon isolation of the fragment ion and subjection to CAD at low-energy conditions, loss of acetylene was observed, like for the compounds without saturated moieties (Table S2). No further fragmentation was observed at normal or increased q values, suggesting that the fragment ions formed are very stable. For the molecular ions of 9,10-dihydrophenanthrene and 9,10-dihydroanthracene, methyl radical loss was observed (Fig. 2). This appears to be a characteristic fragmentation for compounds containing a methylene or ethylene bridge between two aromatic rings. Upon increasing the q value, fragmentation reminiscent of the compounds without saturated moieties, *i.e.*, losses of acetylene, diacetylene, and hydrogen, was observed for both analytes, suggesting fragmentation of the aromatic core.

The results discussed above allow the compounds with no saturated rings to be distinguished from compounds with saturated rings via CAD of their molecular ions. The former systems can be identified by the higher q value required to obtain fragmentation and by the losses of acetylene and hydrogen molecules. The need for a higher q value for fragmentation of fully conjugated molecules is most likely due to their high activation energies for frag-
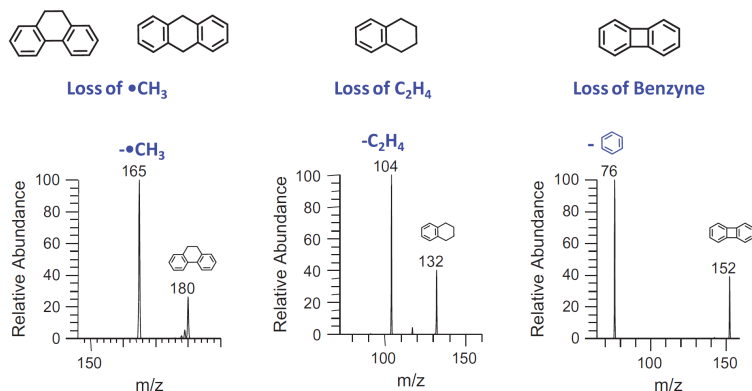

Fig. 2. Major fragmentation pathways for molecular ions of island model compounds with saturated rings but without alkyl substituents.

mentation as well as their ability to undergo IR emission [36]. On the other hand, molecular ions containing saturated rings undergo facile fragmentation by loss of methyl or ethylene at lower energies. Molecular ions containing aromatic rings with a bridging methylene show methyl loss in MS[2] experiments while molecular ions with a cyclohexane ring fused with an aromatic ring undergo a facile loss of ethylene.

3.3. Fragmentation reactions of molecular ions with Island structures containing alkyl chains

Three compounds that meet the criteria of having an island structure with alkyl substituents were examined. Each compound has a core containing four fused aromatic rings with two or more alkyl chains attached. Each of these compounds forms a stable molecular ion upon APCI/CS$_2$ and readily undergoes fragmentation upon CAD. The primary fragmentation pathway for these molecular ions is the elimination of most of one alkyl chain as an alkyl radical via a benzylic bond cleavage (Scheme 1, Table S3). For example, for DDP, $\cdot$C$_9$H$_{19}$ is readily eliminated from one of the two ten-carbon long alkyl chains. Upon further isolation and CAD (MS^3), most of the second carbon chain is eliminated as an alkene (C$_9$H$_{18}$) to yield the fragment ion of m/z 229. Upon further CAD, no further fragmentation was observed under low energy conditions. At a higher q value, hydrogen atoms and hydrogen molecules are lost consecutively (Table S6). No methyl loss was observed. This fragmentation behavior allows for counting of the carbon chains and determination of their lengths by using MS^3 experiments. For compounds with additional carbon chains, such as TDP and THP, a similar trend was observed (Scheme 1, Table S3). The molecular ions of TDP with four ten-carbon alkyl chains and THP with four six-carbon alkyl chains fragment by loss of $\cdot$C$_9$H$_{19}$ and $\cdot$C$_5$H$_{11}$, respectively. Upon isolation of these fragment ions and subjecting them to CAD, followed by the isolation of their fragment ions and subjecting them to CAD, and with this repeated until no more fragmentation was observed (MS^5 experiments), all the remaining alkyl chains are cleaved as alkenes (with one less carbon than in the alkyl chain), one after each other (Scheme 1). Each benzylic bond cleavage after the first one likely leaves a methyl group on the aromatic core. Once two or three alkyl chains have been cleaved off so that the fragment ion contains one or two methyl groups (and one methy-
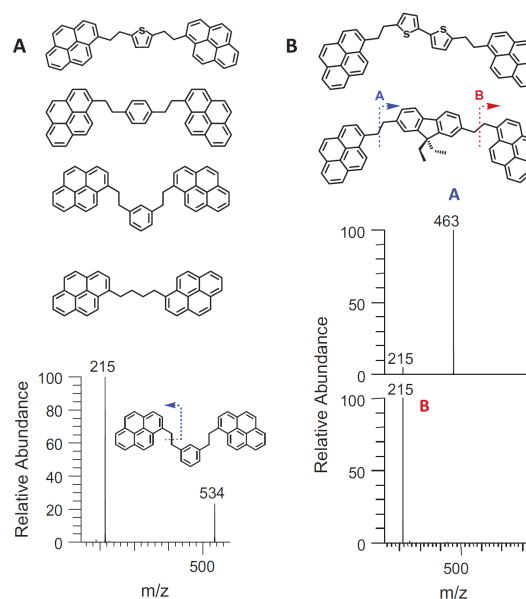
Fig. 3. Major fragmentation pathways for molecular ions of archipelago model compounds containing no heteroatoms except for sulfur atoms.

lene), a facile loss of $-$CH$_3$ was observed. In addition to the loss of alkenes via benzylic bond cleavages, a slower process of cleaving the entire carbon chain as an alkene, *i.e.*, C$_{10}$H$_{20}$ and C$_6$H$_{12}$ for TDP and THP, respectively, was observed. After the loss of each of these alkenes, no methyl group is left on the aromatic core.

Based on above trends, specific structural aspects of island compounds can be elucidated via the fragmentation of their molecular ions. The number of alkyl chains can be counted using MS^n experiments. In addition, the number of carbons in the alkyl chains can be determined by the masses of the neutral molecules lost upon fragmentation. Finally, for compounds with four alkyl chains, a fac-
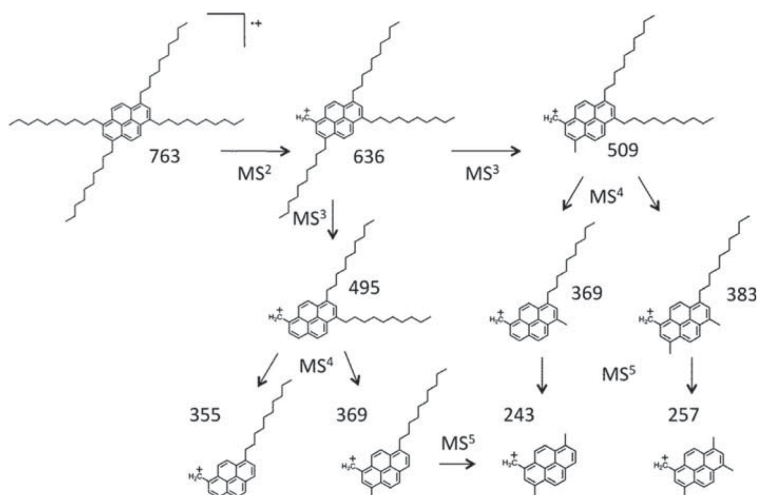
Scheme 1. Fragmentation pathways for the molecular ion of TDP upon consecutive CAD.
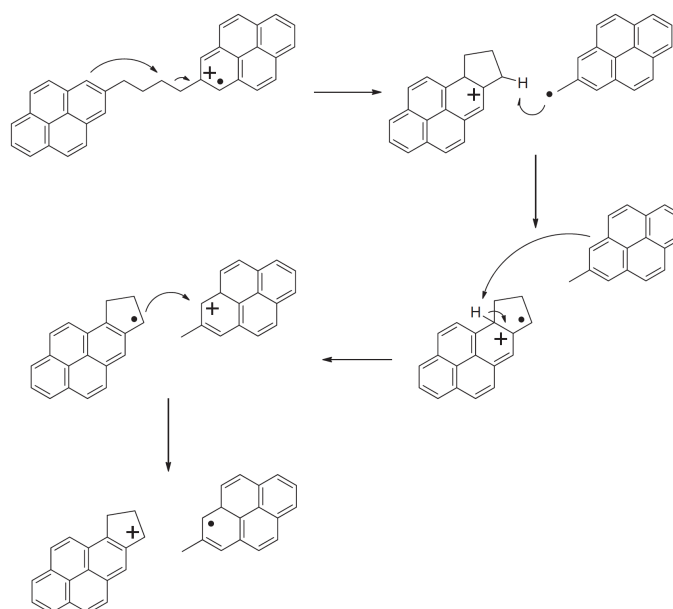
Scheme 2. Proposed mechanism for the loss of pyrene from the molecular ion of KS-P4P.
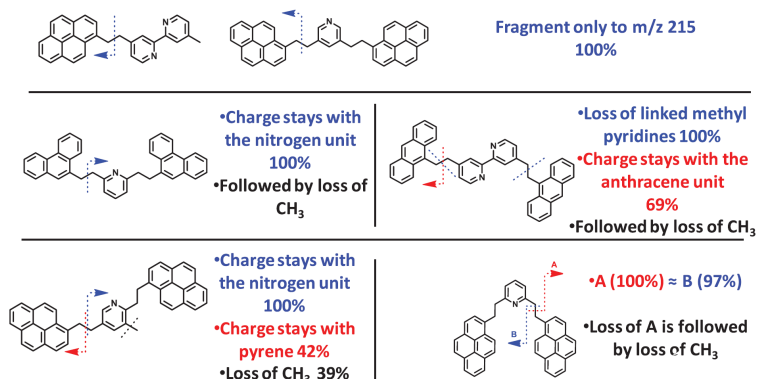
Fig. 4. Major and notable fragmentation pathways for molecular ions of archipelago model compounds containing nitrogen atoms.

ile methyl loss was observed after a series of benzylic cleavages leaves one or two methyl groups on the aromatic core.

To further probe the structures of the fragment ions discussed above, some of them were subjected to CAD under high-energy conditions (using a larger q-value). For example, the fragment ions of m/z 243 and 257 produced during fragmentation of the molecular ions of THP and TDP (Table S6) were examined this way. The fragment ion of m/z 243 contains a pyrene ring with two residual methyl groups and a methylene. Upon CAD at a higher q value, the ion undergoes $\cdot CH_3$ loss as well as a consecutive $\cdot H$ loss. Further isolation of the ion formed upon $\cdot CH_3$ loss and subjecting it to CAD yields primarily the loss of H_2 accompanied by a slow loss of acetylene. Only one methyl loss was observed. This fragmentation is indicative of a fully conjugated core system. The fragment ion of m/z 257 contains a pyrene ring with three residual methyl groups

and a methylene group. Upon CAD, the ion undergoes loss of $\cdot CH_3$ and consecutively loss of $\cdot H$ (Table S6). Upon CAD, the ion formed upon loss of $\cdot CH_3$ loses an additional $\cdot CH_3$ due to the additional methyl group on the aromatic core.

3.4. Fragmentation reactions of molecular ions with Archipelago structures containing no heteroatoms

Four hydrocarbons that meet the definition of having an archipelago structure, all containing pyrene cores, were studied (Table S4). Each compound forms a stable molecular ion upon ionization. The molecular ions of the two isomeric compounds studied, P-mPhP and KS-152, exhibit identical fragmentation. Hence, the location of the linkage of the larger pyrene cores to the connecting benzene ring (*meta* vs. *para*) does not appear to influence

T.M. Jarrell et al. / Fuel 133 (2014) 106–114
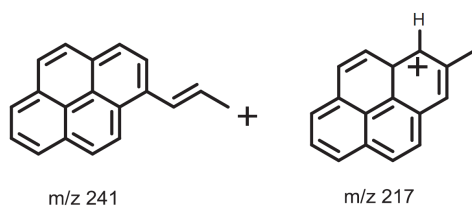
Scheme 3. Proposed structures for two fragment ions of the molecular ion of KS-P4P.

fragmentation. Doubly benzylic cleavage between the pyrene and benzene rings leads to the characteristic fragment ion of m/z 215 (Fig. 3A). Using high-energy conditions, the fragment ion of m/z 215 can be further fragmented via loss of a hydrogen molecule and acetylene, as expected (Table S6). The fragment ion of m/z 215 was observed for all molecular ions of the archipelago type analytes containing pyrene, demonstrating the better ability of the pyrene ring than the benzene ring to stabilize the charge. For example, the molecular ion of KS-140 fragments via benzylic cleavage to lose the pyrene moiety as $\cdot C_{17}H_{11}$ (Fig. 3B, Table S4). After further isolation and fragmentation of the resulting fragment ion, the smaller aromatic core system originally linking the two pyrene rings undergoes benzylic cleavage, resulting in the formation of the fragment ion of m/z 215.

The fragment ion of m/z 215 is formed via a benzylic cleavage also for molecular ions of KS-P4P with two pyrene rings connected by an alkyl chain, butylene (Fig. 3A, Table S4). Additional fragment ions were also observed for the molecular ions of KS-P4P since these ions do not contain the especially fragile doubly benzylic bond as the other archipelago compounds discussed above. For example, an abundant fragment ion of m/z 241 is formed (Table S4). The formation of this ion may occur via cyclization of the alkyl bridge (Scheme 2). Isolation of this ion and subjecting it to CAD results in the loss of a methyl radical, which supports the structure proposed for the fragment ion of m/z 241 in Scheme 3.

For archipelago systems, benzylic cleavages of the alkyl bridges occur readily and are characteristic of the archipelago structure. Identification of the smallest fragment ion that does not fragment further reveals the approximate mass of the largest core (or the one most able to stabilize the charge) in archipelago molecules. This can be determined by subtracting thirteen units from the fragment ion's m/z-value to account for the residual methylene group. For example, the fragment ion of m/z 215 is shown to be indicative of an archipelago system with a pyrene core (Table S4). This ion contains a pyrene ring with a residual methylene group. The fragment ion's m/z-value (215) minus the mass of CH (13 Da) yields the mass of the pyrene core (202 Da). The same approach can be utilized for other aromatic core sizes. An archipelago structure containing coronene, chrysene, or anthracene cores would be expected to yield major fragment ions of m/z 313, 241, and 191, respectively. This approach cannot be applied to island analytes
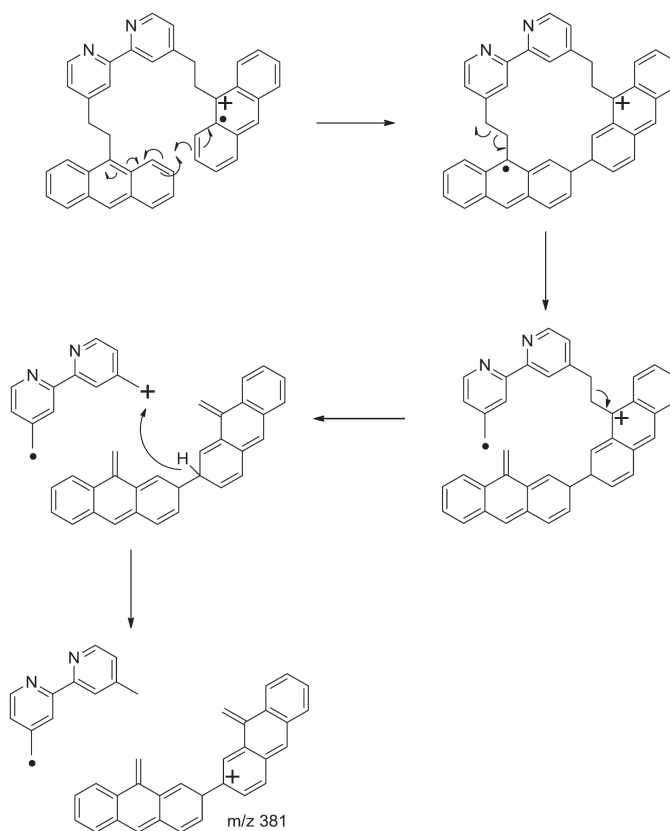
Scheme 4. Proposed mechanism for formation of the fragment ion of m/z 381 of the molecular ion of ABA.

since the number of residual methyl groups would depend on the number of alkyl chains present.

3.5. Fragmentation reactions of molecules with Archipelago structures containing heteroatoms

In order to study some likely variants of archipelago structures, molecular ions of such compounds containing thiophene and pyridine rings were examined (Table S5). For the molecular ions of compounds containing pyrene cores, including KS-115, PB, KS-136 and P-3,5pyrP (Table S5), only the fragment ion of m/z 215 (indicative of a pyrene core) was observed. The sulfur atom appears to have no influence on the fragmentation of the molecular ions containing sulfur (Fig. 3). The same is true for two of the nitrogen containing compounds, P-3,5pyrP and PB (Fig. 4, Table S5).

In contrast to the nitrogen compounds discussed above, the remaining nitrogen containing archipelago compounds studied yield more than one fragment ion. For example, the molecular ions of an isomer of P-3,5pyrP, KS-100, exhibit several fragment ions in addition to the ion of m/z 215. Upon fragmentation, the molecular ions of KS-100 have an approximately equal probability of the charge staying with the pyridine (97%) or with the pyrene unit (100%) (Fig. 4, Table S5). This phenomenon does not occur when a phenyl ring is present instead of the pyridine ring (Fig. 3, Table S4). Furthermore, it does not occur when the ethylene bridges connecting the pyridine ring to the pyrene cores are in the 3- (P-3,5pyrP) or 4-positions (PB) in the pyridine ring instead of the 2-position, with the exception of ABA (Fig. 4, Table S5). These findings suggest that the nitrogen atom facilitates the homolytic bond scission of the C–C bond in the 2-position, possibly by anchimeric assistance and formation of an aziridinium cation.

When the charge stays with the pyridine unit upon fragmentation of the molecular ions of KS-100 to produce the fragment ion of m/z 320, additional structural information can be obtained upon further CAD. Upon CAD, the fragment ion of m/z 320 loses $\cdot CH_3$ and $\cdot C_5H_7N$.

The molecular ions of P-2,5pyr-3-Mep show similar fragmentation as KS-100 (Fig. 4, Table S5). However, for P-2,5pyr-3-Mep, the probability of the charge staying with the pyrene unit is lower (42%). Furthermore, methyl radical loss was observed due to the presence of a methyl group on the pyridine ring. Methyl loss was also observed when the fragment ion of m/z 334 is further fragmented. This can be used as an identification tool for unknown analytes. The molecular ions of the compound with the phenanthrene core, P26PP, yield an ion of m/z 296 as the most abundant fragment ion. It is formed via benzylic cleavage of the linking alkane. For this analyte, the charge stays solely with the nitrogen substituent. The phenanthrene substituent is less likely to retain the charge than pyrene due to its smaller size. Upon further CAD, two consecutive $\cdot CH_3$ losses were observed. The molecular ion of a similar analyte, ABA, contains two anthracene rings bridged by two pyridines. As expected, an ion of m/z 191, corresponding to anthracene with a methylene group, was observed due to the anthracene core (Table S5). When the fragment ion of m/z 191 was subjected to CAD under higher energy conditions (using a higher q value), loss of hydrogen molecules and acetylene were observed (Table S6). A surprising fragment ion of m/z 381 was also observed (Fig. 4, Table S5). Formation of this ion corresponds to a rearrangement reaction wherein both pyridine rings are lost as $\cdot C_{12}H_{11}N_2$, possibly as shown in Scheme 4.

4. Conclusions

The CAD fragmentation patterns obtained in MS^n experiments for molecular ions and their fragment ions of 25 model compounds of asphaltenes (evaporated and ionized by positive-ion mode APCI with CS_2 reagent) have been shown to facilitate the elucidation of their structural features. Losses of characteristic neutral molecules were observed for each analyte type discussed, i.e., analytes containing different types of island or archipelago structures. Molecular ions derived from analytes with an island structure containing no saturated moieties lose hydrogen and acetylene but only under high-energy conditions. Molecules with island structures containing alkyl chains can be identified due to sequential and facile losses of the alkyl chains via α-cleavages from their molecular ions. This allows for the determination of the length and number of alkyl chains as well as the size of the core. Molecules with archipelago structures without nitrogen can be identified via the observation of characteristic fragment ions that correspond to the masses of the individual cores. Determination of the degree of unsaturation of the lost neutral molecules reveals them to be aromatic. The integration of sulfur into the archipelago structures had no effect on the fragmentation reactions observed. On the other hand, the integration of nitrogen into the archipelago system had a great influence on the fragmentation of the molecular ions of some compounds but not all. The fragmentation behavior depends on the proximity of the nitrogen atom in the center ring to the cleaving bonds. Finally, fragmentation of molecular and fragment ions that do not undergo fragmentation under normal operating conditions was achieved by increasing the operating q value during CAD. For example, this allows for probing of the structure of the aromatic core of asphaltenes. The analytical methodology discussed here will facilitate the elucidation of the structures of the molecules in asphaltenes.

Acknowledgement

Appendix A. Supplementary material

Supplementary data associated with this article can be found, in the online version, at http://dx.doi.org/10.1016/j.fuel.2014.04.040.

References

[1] Alvarez-Ramírez F, Ruiz-Morales Y. Island versus archipelago architecture for asphaltenes: polycyclic aromatic hydrocarbon Dimer theoretical studies. Energy Fuels 2013;27:791–1808.
[2] Hurt MR, Borton DJ, Choi H, Kenttämaa HI. Comparison of molecules' structures in coal and petroleum asphaltenes by using mass spectrometry. Energy Fuels 2013;27:3653–8.
[3] Mullins O. Review of the molecular structure and aggregation of asphaltenes and petroleomics. SPE J 2008;13:48–57.
[4] Mullins OC. The asphaltenes. Annu Rev Anal Chem 2011;4:393–418.
[5] Gaspar A, Zellermann E, Lababidi S, Reece J, Schrader W. Impact of different ionization methods on the molecular assignments of asphaltenes by FT-ICR mass spectrometry. Anal Chem 2012;84:5257–67.
[6] Ancheyta J, Betancourt G, Marroqun G, Centeno G, Castañeda LC, Alonso F, et al. Hydroprocessing of Maya heavy crude oil in two reaction stages. Appl Catal A 2002;233:159–70.
[7] Andrews AB, Edwards JC, Pomerantz AE, Mullins OC, Nordlund D, Norinaga K. Comparison of Coal-derived and petroleum asphaltenes by 13 C nuclear magnetic resonance, DEPT, and XRS. Energy Fuels 2011;25:3068–76.
[8] Borton D, Pinkston D, S., Hurt MR, Tan X, Azyat K, et al. Molecular structures of asphaltenes based on the dissociation reactions of their ions in mass spectrometry. Energy Fuels 2010;24:5548–59.
[9] Owen B, Gao J, Borton D, Amundson L, Archibold E, Tan X, et al. Carbon disulfide reagent allows the characterization of nonpolar analytes by atmospheric pressure chemical ionization mass spectrometry. Rapid Commun Mass Spectrom 2011;25:1924–8.
[10] Vega SS, Urbina RH, Covarrubias MV, Galeana CL. The zeta potential of solid asphaltene in aqueous solutions and in 50:50 water+ethylene glycol (v/v) mixtures containing ionic surfactants. J Petrol Sci Eng 2009;69:174–80.
[11] Yen T. The realms and definitions of asphaltenes. Amersterdam, The Netherlands: Elsevier Science B.V; 2000.
[12] Gray MR. Consistency of asphaltene chemical structures with pyrolysis and coking behavior. Energy Fuels 2003;17:1566–9.
[13] Yen TF, Chilingarian GV. Asphaltenes and asphalts, 2. Amersterdam, The Netherlands: Elsevier Science B.V; 2000.

T.M. Jarrell et al. / Fuel 133 (2014) 106–114

[14] Dilabio GA, Mackie I, Dettman HD. Asphaltene Components as Organic Electronic Materials, in US Patent 20,130,043,462, 2013.
[15] Idris M, Okoro LN. The effects of asphaltenes on petroleum processing. Eur Chem Bull 2013;2:393–6.
[16] Hortal AR, Hurtado P, Martínez-Haya B, Mullins OC. Molecular-weight distributions of coal and petroleum asphaltenes from laser desorption/ionization experiments. Energy Fuels 2007;21:2863–8.
[17] Groenzin H, Mullins OC. Molecular size and structure of asphaltenes. Pet Sci Technol 2001;19:219–30.
[18] Gray MR, Tykwinski RR, Stryker JM, Tan X. Supramolecular assembly model for aggregation of petroleum asphaltenes. Energy Fuels 2011;25:3125–34.
[19] Badre S, Goncalves CC, Norinaga K, Gustavson G, Mullins OC. Molecular size and weight of asphaltene and asphaltene solubility fractions from coals, crude oils and bitumen. Fuel 2006;85:1–11.
[20] Groenzin H, Mullins OC. Molecular size and structure of asphaltenes from various sources. Energy Fuels 2000;14:677–84.
[21] Mullins OC, Martínez-Haya B, Marshall AG. Contrasting perspective on asphaltene molecular weight. Energy Fuels 2008;22:1765–73.
[22] Mullins OC, Sabbah H, Eyssautier J, Pomerantz AE, Barré L, Andrews AB, et al. Advances in asphaltene science and the Yen-Mullins model. Energy Fuels 2012;26:3986–4003.
[23] Rubinstein I, Spyckerelle C, Strausz OP. Pyrolysis of asphaltenes: a source of geochemical information. Geochim Cosmochim Acta 1979;43:1–6.
[24] Ruiz-Morales Y, Wu X, Mullins OC. Electronic absorption edge of crude oils and asphaltenes analyzed by molecular orbital calculations with optical spectroscopy. Energy Fuels 2007;21:944–52.
[25] Morgan T, George A, Alvarez-Rodriguez P, Millan M, Herod A, Kandiyoti R. Estimating molecular masses of petroleum-derived fractions: high mass (>2000 μ) materials in maltenes and asphaltenes from maya crude oil. J Chromatogr A 2010;1217:3804–18.
[26] Podgorski DC, Corilo YE, Nyadong L, Lobodin VV, Bythell BJ, Robbins WK, et al. Heavy petroleum composition. 5. Compositional and structural continuum of petroleum revealed. Energy Fuels 2012;27:1268–76.
[27] Rueda-Velásquez RI, Freund H, Qian K, Olmstead WN, Gray MR. Characterization of asphaltene building blocks by cracking under favorable hydrogenation conditions. Energy Fuels 2012;27:1817–29.
[28] de Hoffmann ES. Mass spectrometry: principles and applications. 3rd ed. West Sussex, England: Wiley and Sons; 2007.
[29] Skoog DA, Holler FJ, Crouch SR. Principles of instrumental analysis. Belmont, CA: Thomson Brooks/Cole; 2007.
[30] Watson JT, Sparkman OD. Introduction to mass spectrometry: instrumentation, applications, and strategies for data interpretation. 4th ed. West Sussex, England: Wiley & Sons; 2008.
[31] Cooks RG, Busch KL, Glish GL. Mass-spectrometry – analytical capabilities and potentials. Science 1983;222:273–91.
[32] Kim Y, Kim S. Improved abundance sensitivity of molecular ions in positive-ion APCI MS analysis of petroleum in toluene. J Am Soc Mass Spectrom 2010;21:386–92.
[33] Sabbah H, Morrow A, Pomerantz A, Zare R. Evidence for Island structures as the dominant architecture of asphaltenes. Energy Fuels 2011;25:1597–604.
[34] Wu Q, Pomerantz A, Mullins O, Zare R. Minimization of fragmentation and aggregation by laser desorption laser ionization mass spectrometry. J Am Soc Mass Spectrom 2013;24:1116–22.
[35] Tan X, Fenniri H, Gray MR. Pyrene derivatives of 2,2′-bipyridine as models for asphaltenes: synthesis, characterization, and supramolecular organization†. Energy Fuels 2008;22.
[36] Pinkston DS, Duan P, Gallardo VA, Habicht SC, Tan XL, Qian KN, et al. Analysis of asphaltenes and asphaltene model compounds by laser-induced acoustic desorption/Fourier transform ion cyclotron resonance mass spectrometry. Energy Fuels 2009;23:5564–70.

analytical chemistry

Multiported Pulsed Valve Interface for a Linear Quadrupole Ion Trap Mass Spectrometer to Enable Rapid Screening of Multiple Functional-Group Selective Ion−Molecule Reactions

Tiffany Jarrell, James Riedeman, Mark Carlsen, Randall Replogle, Tim Selby, and Hilkka Kenttämaa*

Department of Chemistry, Purdue University, West Lafayette, Indiana 47907, United States

ABSTRACT: Ion−molecule reactions provide a powerful tool for structural elucidation of ionized pharmaceutical analytes in tandem mass spectrometry. However, all previous interfaces for the introduction of reagents for ion−molecule reactions have utilized a single reagent approach. In this study, a multiported pulsed valve system was designed and characterized for rapid introduction of three neutral reagents into a linear quadrupole ion trap. Additionally, automatic triggering was used to allow for the introduction of the reagents on a chromatographic time scale. This system enables automatic, high throughput screening of complex mixtures by using at least three different ion−molecule reactions. Further, rapid testing of new neutral reagents is also possible.

Multiple Ion-Molecule Reactions
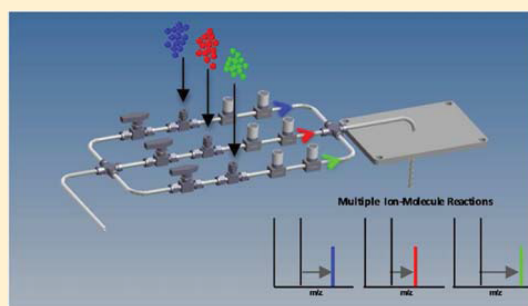
Mass spectrometry (MS) is a powerful technique well suited for the analysis of complex mixtures due to its ability to rapidly provide valuable information on molecules in mixtures without prior separation.[1−3] MS is used to obtain molecular mass and elemental composition information.[4] The tandem MS (MS^n; $n \geq 2$) technique, usually coupled with collision-activated dissociation (CAD), is commonly used to provide insight into the structural aspects of isolated ionized analytes.[5−11] However, CAD does not always allow definitive determination of the elemental connectivity of ionized molecules.[5] Another MS^n technique based on ion−molecule reactions of isolated analyte ions can be used to obtain more in-depth structural information.[12−16]

Ion−molecule reactions have been used to identify unique structural features in many ionized analytes, such as small organic compounds, lipids, drug metabolites, and biopolymers.[15−26] However, ion−molecule reactions are often underutilized in tandem mass spectrometry laboratories, likely due to the required modification to the mass spectrometry hardware that allows introduction of neutral reagents into a reaction region.[15] Both continuous and pulsed introduction of a neutral reagent can be performed.[15] The continuous flow approach is a well-established technique wherein the neutral reagent is introduced throughout the entire experiment into a triple quadrupole, pentaquadrupole or Fourier transform ion cyclotron resonance (FT-ICR) mass spectrometer or a three-dimensional or linear quadrupole ion trap.[13,14,27−33] This approach is essential for measuring ion−molecule reaction rates and efficiencies.[14] However, it is almost always limited to the introduction of only one neutral reagent at a time due to reagents' different volatilities,[13,24] and this neutral reagent can interfere with further MS^n experiments based on CAD due to

unwanted ion−molecule reactions.[34] To avoid this interference, pulsed valves can be used to introduce reagents for an optimal period of time.[15,32,33,35−37] The pulsed valve approach has been shown previously to be compatible with FT-ICR and three-dimensional quadrupole ion trap instruments.[32,33,35−37] Later, this technique was successfully coupled with liquid chromatography (LC)/MS/MS and used to rapidly identify analytes in peptide mixtures.[38]

However, it should be emphasized that all above pulsed valve systems only utilized a single reagent port,[15,32,33,35−37] although the nature of the pulsed valve approach allows multiple reagents to be introduced sequentially. This experiment would facilitate the examination of several ion−molecule reactions for the purpose of screening for different functional groups nearly simultaneously.

This paper presents an automated multiported pulsed valve inlet system that allows the rapid, sequential introduction and reintroduction of three neutral reagents into a commercial linear quadrupole ion trap instrument by simply attaching the interface to the existing hardware. The pulsed valve interface allows the examination of three different ion−molecule reactions of the ionized components of complex mixtures as they are eluting from a high-performance liquid chromatograph. The performance of the pulsed valve system was evaluated using previously described ion−molecule reactions.[19,24,26,39]
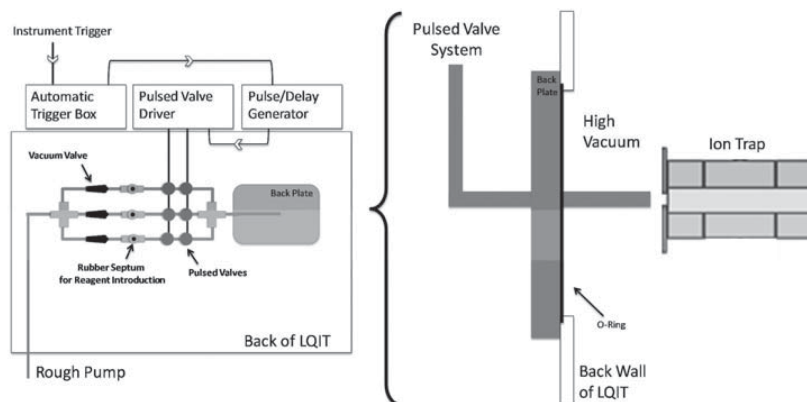
Figure 1. Experimental setup for the pulsed valve interface.

■ EXPERIMENTAL SECTION

Materials. Trimethyl amine *N*-oxide (97%), 4-picoline *N*-oxide (98%), 5,5-dimethylamine *N*-oxide (97%), nitrosobenzene (97%), isoquinoline *N*-oxide (98%), 8-hydroxyquinoline *N*-oxide (98%), caffeine (>95%), clozapine (>98%), clozapine *N*-oxide (>95%), benzoic acid (99.5%), trimethyl borate (99%), dimethylamine (99%), 2-methoxypropene (97%), and dimethyl disulfide (99%) were obtained from Sigma-Aldrich. Pyridine *N*-oxide was obtained from Mallinckrodt Chemical Company. High-performance liquid chromatography/mass spectrometry (HPLC/MS) grade water and acetonitrile were purchased from Fisher Scientific (Pittsburgh, PA). All chemicals were used as received. A Zorbax SB-C18 column (4.6 × 250 mm, 5 μm particle size) was purchased from Agilent Technologies.

Instrumentation. All experiments were performed using a Thermo Scientific linear quadrupole ion trap (LQIT) mass spectrometer (LTQ, Thermo Scientific, San Jose, CA, USA) using an electrospray ionization (ESI) source. The instrument was operated using the LTQ Tune Plus interface and Xcalibur 2.1 software. The mass spectrometer was coupled to a Surveyor Plus high-performance liquid chromatograph equipped with a quaternary pump, autosampler, and photodiode array (PDA) detector.

Analyte Introduction by Direct Injection. Some samples were introduced into the ESI source via a syringe drive at a flow rate of 15 μL/min. To facilitate formation of a stable ESI spray, the sample was combined via a tee connector with 50/50 (v/v) methanol/water eluting from a Finnigan Surveyor MS Pump Plus at a flow rate of 200 μL/min. The resulting mixture was introduced into the ESI source. The ESI conditions were set as follows: 3.5 kV spray voltage, 20 (arbitrary units) flow of sheath gas, 10 (arbitrary units) flow of auxiliary gas, and a 275 °C transfer capillary temperature. All ion optic voltages were set using the tune feature of the LTQ Tune Plus interface. The nominal pressure within the ion trap of the instrument, as read by an ion gauge, was maintained at 0.6 × 10⁻⁵ Torr.

High-Performance Liquid Chromatography. For HPLC/MS analysis, all samples were introduced using an autosampler with a full-loop injection volume (25 μL) for high reproducibility. The mobile phase solvents used were 0.01% (m/v) formic acid in water (A) and 0.01% (m/v) formic acid in acetonitrile (B). Formic acid was used as a buffer to encourage protonation upon ESI. A linear gradient was used: 0.00 min, 80% A and 20% B; 23.00 min, 25% A and 75% B; 24.00 min,

5% A and 95% B; 24.99 min, 5% A and 95% B; 25.00 min, 80% A and 20% B; 35.00 min, 80% A and 20% B. After compounds had eluted from the HPLC and had been ionized in the ESI source as described above, the most abundant ion was isolated and allowed to react for 30 ms with introduced neutral reagent(s), which was performed using the data dependent functionality of the Xcalibur software. The 30 ms reaction time is the delay between ion isolation and ejection of the ions into the external detection system.

Reagent Introduction by Using Pulsed Valves. The neutral reagents used in this study were introduced into the ion trap by using six Series 9 pulsed valves with an exit orifice of 0.060 in. (Parker Hannifin Corp., Cleveland, OH). The experimental setup is shown in Figure 1. The hardware consists of three pairs of pulsed valves mounted in parallel on 1/4 in. stainless steel tubing (Figure 1). A pair of pulsed valves was used instead of a single valve to act as a safeguard in the event of a high back pressure in the sample channel. The space between the pulsed valve pair acts as a vacuum baffle. Using a cross connector, each pulsed valve was connected to steel tubing that was connected to the LQIT vacuum chamber via a modified cover plate. Along each channel, a tee connector was used to attach a Swagelok Ultra-Torr fitting holding a rubber septum. The neutral reagents used in this study were introduced via a syringe (∼5 uL) through the rubber septum into the channel.

The timing and width of the electronic pulse used to open each pulsed valve and the delay between the pulses were controlled using a BNC Model 555 pulse/delay generator (Berkley Nucleonics Corp., San Rafael, CA). The generator's channels A−F were used to control pulsed valves A−F, respectively. An example of a standard sequence is shown in Figure 2. The pulsed valves were triggered either manually via a waveform generator or automatically with the LTQ software. Automatic triggering was accomplished via a programmable trigger in the digital board of the LTQ that was controlled via the LTQ Tune Plus software. Using the software, an experimental event, such as ion isolation, acceleration, or detection, can be selected to act as a trigger. A trigger box (JAFCI, Purdue University) was designed to function as an interface between the instrument and the pulse/delay generator as shown in Figure 1.

The reagent was introduced into the instrument by first opening the pulsed valve connected to the sample channel (i.e.,
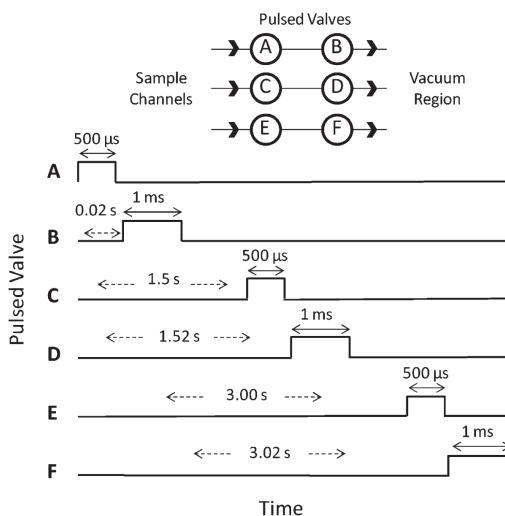
Figure 2. Typical pulsed valve sequence parameters are shown. Pair 1 is composed of pulsed valves labeled A and B, pair 2 is composed of pulsed valves labeled C and D, and pair 3 is composed of pulsed valves labeled E and F. The pulse width of A, C, and E is the time that each pulsed valve is open When A, C, or E is opened, the neutral reagent moves from the sample channel into the space between the pulsed valve pairs (i.e., between A and B). The pulse width of B, D, and F is the time the pulsed valve is open to the mass spectrometer. The pulse delay (dashed arrows) is the delay from the start of the sequence to the time when the designated pulsed valve opens. Each open event for a pulsed valve in a pair is separated by a 20 ms delay, whereas the open events for entire pairs are separated by 1.5 s.

pulsed valve A, C, or E, Figure 2) for a set amount of time to introduce the reagent into the space between the pulsed valves (i.e., between A and B). The time that the pulsed valve was open was defined by the width of the electronic pulse from the pulse/delay generator. Second, the pulsed valve that interfaced the vacuum region of the instrument (i.e., pulsed valve B, D, or F, Figure 2), was opened for a set amount of time (determined by electronic pulse-width) to let the reagent enter the mass spectrometer. A 20 ms delay was set between the open events for the pulsed valves in a pair and a 1.5 s delay was used between the open events of entire pulsed valve pairs (Figure 2). Each pulsed valve was opened using a basic pulsed valve driver built at the Jonathan Amy Facility for Chemical Instrumentation (JAFCI). The output voltage was set to 40 VDC. Finally, each channel was equipped with a ball valve connected to a mechanical pump to enable cleaning of the channel after use (Figure 1).

For experiments using the trigger box, a scan is defined as a complete MS experiment including the events of ion injection, isolation, reaction, and detection. Although several scans were usually performed, the pulsed valves were not triggered in every scan in order to prevent pressure buildup in the instrument. This was achieved as follows. As mentioned above, a specific event within each scan (i.e., ion isolation) was used as a trigger to send an output signal from the LQIT. However, the trigger box intercepted this output signal from the instrument. It was set to only send an output signal to the pulse/delay generator after a designated number of triggers (10–40) had been received (Figure 1). Therefore, the trigger box prevented the pulse valves from opening during every scan. Because the time

it takes to perform a single MS scan is less than 100 ms, triggering once every 10–40 scans (approximately 1–4 s) prevented superfluous pulsing of neutral reagents.

■ RESULTS AND DISCUSSION

The pulsed valve interface was tested via several experiments using known reagents designed to identify specific functionalities in protonated analytes. A single pulsed valve pair as well as all three pairs were manually triggered while using different pulse widths to identify the optimal pulse width for each valve for most efficient monitoring of each ion–molecule reaction. The pulse delays were not varied. After optimization of these parameters, the pulsed valves were operated via automatic triggering from the instrument.

Single Reagent Introduction via a Pulsed Valve Pair. A single pulsed valve pair (shown as A and B in Figure 2) was employed to test the functionality of the pulsed valves in combination with the linear quadrupole ion trap. A known[24] reaction of trimethyl borate (TMB) and a protonated carbonyl compound (benzoic acid) was used to monitor the residence time of the neutral reagent and formation of product ions in the ion trap. Benzoic acid was protonated via ESI. The triggering of the pulses of neutral TMB was manually controlled for this experiment. The pulse widths for pulsed valves A and B (Figure 2) were varied to determine the conditions needed for a minimal residence time of TMB in the trap. The shorter the residence time of the neutral reagent in the trap, the shorter the duty cycles, which is desirable for HPLC experiments. The optimal pulse widths for TMB were found to be 50 μs for pulsed valve A and 1 ms for pulsed valve B. Pulsed valve B was held open longer than pulsed valve A to prevent buildup of the neutral reagent in the reservoir between the pulsed valves, which could result in the introduction of an excess amount of neutral reagent into the ion trap.

Figure 3 shows an average mass spectrum collected across a single reagent pulse and the ion currents of the analyte (protonated benzoic acid of m/z 123) and product ions (protonated analyte + TMB − methanol of m/z 195) as a function of time as TMB was pulsed six times into the mass
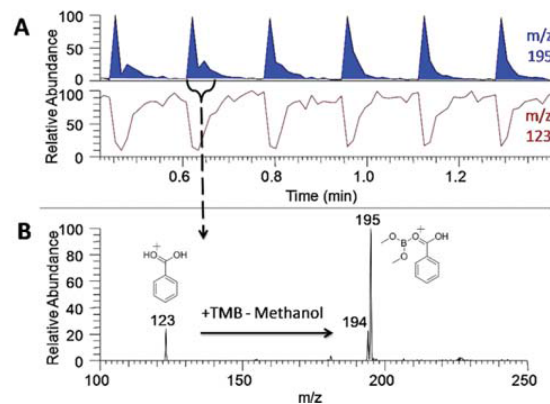

Figure 3. Reaction of protonated benzoic acid (m/z 123) with the neutral reagent trimethyl borate (TMB) introduced via a single pair of pulsed valves. Trimethyl borate was pulsed into the ion trap six times. (A) Extracted ion currents for reactant ions of m/z 123 and product ions of m/z 195 over time. (B) Average mass spectrum measured over one pulse of TMB.
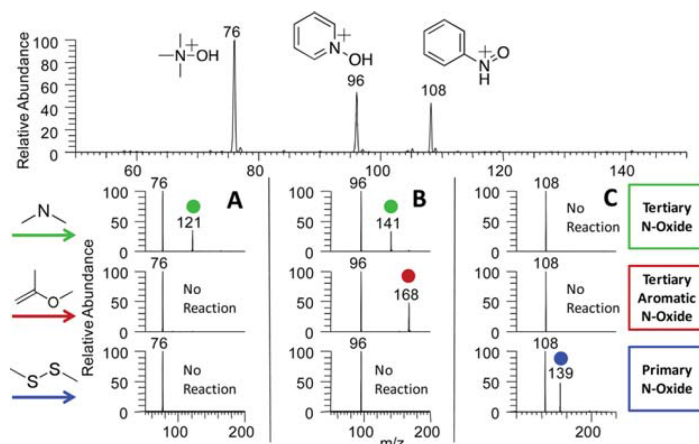
Figure 4. (Top) Mass spectrum of a mixture of trimethylamine, pyridine *N*-oxide, and nitrosobenzene introduced simultaneously and protonated via ESI. (Bottom) Mass spectra measured after the sequential isolation and reaction of each of the protonated analytes, trimethylamine *N*-oxide (column A), pyridine *N*-oxide (column B), and nitrosobenzene (column C), with the neutral reagents dimethylamine, 2-methoxypropene, and dimethyl disulfide pulsed in a consecutive manner into the ion trap. Each reagent was pulsed three times, one time for each ion, for a total of nine pulses.

spectrometer under the optimum conditions. Introduction of the reagent into the trap caused an immediate decrease in the signal for the analyte ion (m/z 123) and increase in the signal for the reaction product (m/z 195). On the basis of the ion current of the reaction product, the residence time of TMB is determined to be approximately 0.1 min (or 6 s). These observations confirm that a single pair of pulsed valves can be used to rapidly study ion–molecule reactions in the LQIT.

Introduction of Multiple Reagents via Three Parallel Sets of Pulsed Valves. Next, all three pulsed valve pairs were used consecutively in a single experiment to fully test the pulsed valve interface. Each pulsed valve pair was manually triggered according to the sequence shown in Figure 2. Each channel was loaded with a different reagent. The three ion–molecule reagents selected are specific to different types of protonated *N*-oxides (Figure 4). Ion–molecule reactions specific for *N*-oxides are of interest due to the limited ability of CAD to identify analytes containing this functionality.[40] First, dimethylamine (DMA) was pulsed into the ion trap to identify protonated tertiary *N*-oxides via a known diagnostic addition reaction (addition of DMA of 45 Da should be observed).[39] Second, 2-methoxypropene (2MP) was pulsed into the trap to identify protonated aromatic tertiary *N*-oxides via a previously published, diagnostic addition reaction (addition of 2MP of 72 Da should be observed).[19] Finally, dimethyl disulfide (DMDS) was used to identify protonated primary *N*-oxides via a previously reported ligand exchange reaction (addition of a fragment of 31 Da should be observed; Scheme 1).[26] A mixture of three *N*-oxide model compounds, including a primary, aliphatic tertiary, and aromatic tertiary *N*-oxide, was introduced at the same time to test the operation of the three pulsed valve pairs. The compounds were ionized via protonation by ESI (Figure 4, top). The protonated *N*-oxides were isolated in a consecutive manner and then allowed to react with the three reagents pulsed into the trap one after the other, for a total of nine pulsed reagent introductions (Figure 4).

The full mass spectrum of the mixture of the ionized model compounds is shown at the top of Figure 4. After each analyte ion was isolated, all three reagents were pulsed in a consecutive manner into the ion trap to react with the isolated ion. This

Scheme 1. Proposed Mechanism for the Reaction of Dimethyl Disulfide with a Protonated Primary *N*-Oxide[a]
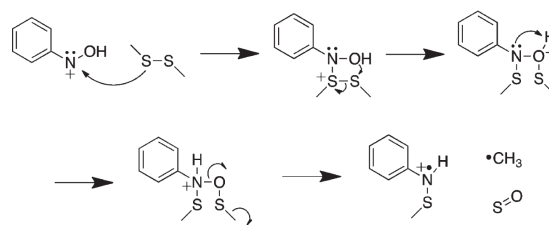
[a]See references 19 and 26.

process was repeated for the remaining two analyte ions, involving a total of nine reagent pulses. In Figure 4, column A shows the mass spectra measured after isolation of the protonated trimethylamine *N*-oxide (76 m/z) followed by reaction with each neutral reagent. The protonated analyte only reacts with DMA due to the presence of a tertiary *N*-oxide functionality in this analyte. Column B shows the mass spectrum measured after isolation of protonated pyridine *N*-oxide (96 m/z) followed by reaction with each neutral reagent. The protonated analyte reacts with two of the reagents, DMA and 2MP, due to the presence of an aromatic tertiary *N*-oxide functionality in this analyte. Finally, column C shows the mass spectrum measured after isolation of protonated nitrosobenzene (108 m/z) followed by reaction with each neutral reagent. The protonated analyte only reacts with DMDS due to the presence of a primary *N*-oxide functionality in this analyte. This set of reactions provides a proof of concept for the use of several neutral reagents to rapidly screen for specific functional groups in molecules in mixtures.

Automatic Triggering of the Pulsed Valve System. The utility of a multiported pulsed reagent inlet system was demonstrated above by manually pulsing the reagents into the ion trap. However, in order to be able to couple the reagent inlet system with HPLC, which is desirable for the analysis of very complex mixtures, automatic triggering of the pulsed valves is necessary. Using the instrument software, the isolation
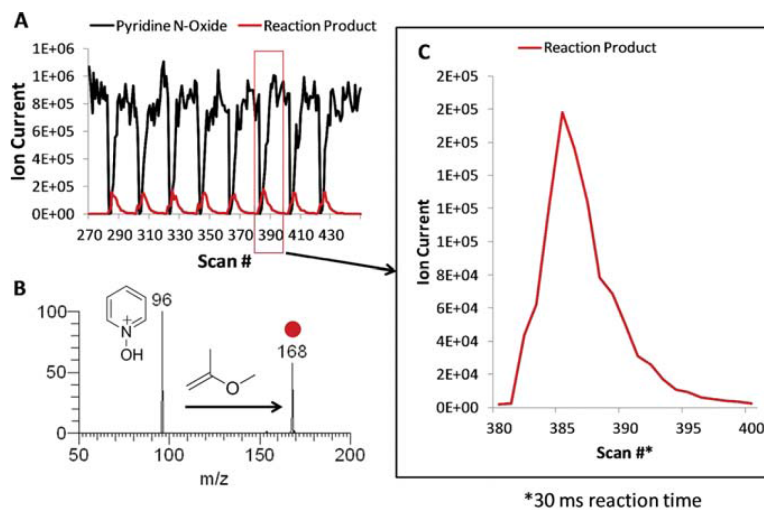
Figure 5. Currents of the analyte (m/z 96) and product (m/z 168) ions for the reaction of protonated pyridine N-oxide (m/z 96) with 2-methoxypropene (2MP) introduced via an automatically controlled pulsed valve pair. (A) The currents of protonated pyridine N-oxide (m/z 96) and the ionic reaction product corresponding to the addition of 2MP (m/z 168) as a function of the number of MS scans. The ion current was recorded over 8 consecutive pulses of 2MP. (B) Average mass spectrum measured over one pulse of 2MP. (C) Zoomed view of the current of the ionic reaction product to show the residence time of neutral 2MP after it was pulsed into the mass spectrometer.
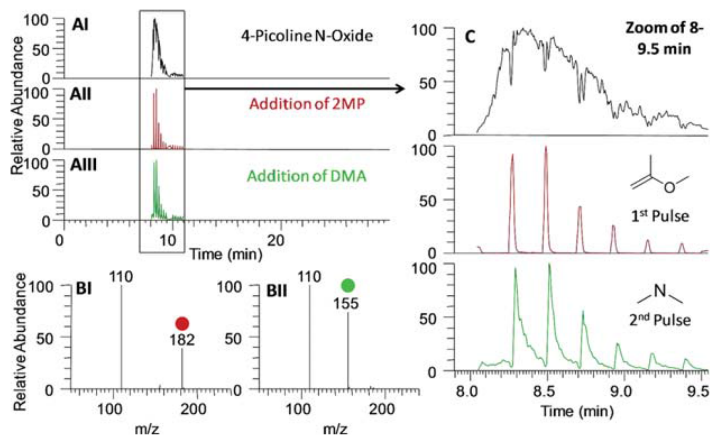

Figure 6. Results obtained for the reactions of three reagents with N-picoline N-oxide as it elutes from HPLC and is ionized via ESI. Currents of the analyte and product ions measured as a function of time for the reaction of protonated 4-picoline N-oxide with two reagents, 2MP and DMA, as well as mass spectra showing the reactant ion and product ion. No product ion was observed for the third reagent, DMDS. (AI) Extracted ion current of protonated 4-picoline N-oxide (m/z 110). (AII) Extracted ion current of the 2MP addition product ion (m/z 182). (AIII) Extracted ion current of the DMA addition product ion (m/z 155). (BI) Average mass spectrum measured during the reaction of protonated 4-picoline N-oxide with 2MP. (BII) Average mass spectrum measured during the reaction of protonated 4-picoline N-oxide with DMA. (C) Zoom of the extracted ion currents measured as a function of time for the analyte and product ions during the elution 4-picoline N-oxide from the HPLC from 8 up to 9.5 min.

event was selected as the trigger event. For every 30 trigger events, the trigger box sent an output signal to the pulse/delay generator to initiate the pulsed introduction of the neutral reagent as described in the Experimental Section. Figure 5 demonstrates the utility of this experimental setup. Protonated pyridine N-oxide (introduced via direct injection and ionized by ESI) was isolated, which triggered the pulsed introduction of the neutral reagent (2MP). The residence time of the neutral reagent is approximately equal to the amount of time it takes to perform 20 scans (about 1 s; Figure 5C). The mass spectra obtained by the scans were averaged to obtain the mass

spectrum shown in Figure 5B. On the basis of these results, the pulsed valve system with automatic triggering is concluded to be suitable for implementation on the HPLC time scale.

Pulsed Reagent Introduction Coupled with HPLC. Ion–molecule reactions using the pulsed valve interface were coupled with HPLC due to the need for separation before MS^n analysis of complex mixtures containing isomeric and isobaric analytes commonly found in pharmaceutical samples. The automatic triggering system described above was tested for the feasibility of analysis on the chromatographic time scale. As the molecules eluted from the HPLC, they were ionized and

introduced into the mass spectrometer. Data dependent scanning was used to select ions for reactions with the neutral reagents. Data dependent scanning involves the instrument automatically selecting the most abundant ions produced by the ion source for further experiments. The selected ions were isolated, which triggered the pulsed valves to introduce three neutral reagents in a consecutive manner for reactions with the isolated ions. The reactions of protonated 4-picoline N-oxide with 2MP, DMA, and DMDS were used to test the experimental setup. Figure 6 shows the mass spectra measured after the reactions of protonated 4-picoline N-oxide with 2MP and DMA as the neutral analyte elutes from an HPLC column (no products were observed for DMDS). Figure 6AI shows the current measured for the analyte ion over time, whereas Figures 6AII and AIII show the currents measured for the addition products of reactions with 2MP and the DMA, respectively. By averaging the mass spectra measured over a single pulse of each neutral reagent, a representative mass spectrum can be obtained for the reactions of protonated 4-picoline N-oxide with 2MP and DMA (Figures 6BI and BII). This experiment demonstrates that reactions of ions with pulsed neutral reagents can be studied on a chromatographic time scale. Further, several well-spaced ion−molecule reaction events were observed over a single chromatographic peak, as seen in Figure 6C. Due to the lower volatility of DMA compared to 2MP, broader pulse widths were observed for DMA. Therefore, a more volatile reagent, such as 2MP, is more compatible with HPLC experiments. DMDS was also pulsed into the ion trap; however, no reaction products were observed for protonated 4-picoline N-oxide.

Finally, 2MP, DMA, and DMDS were used to screen a mixture of model compounds containing different N-oxide functionalities. As each analyte eluted from the column and was ionized, they were isolated and allowed to react with each reagent. Because each reagent forms characteristic reaction products corresponding to a specific increase in mass, the ion currents of product ions corresponding to the addition of 72, 45, and 31 Da to the m/z value of the analyte ions were plotted over time (Figure 7). Figure 7 shows that only analytes with specific functional groups, i.e., aromatic tertiary N-oxide, tertiary N-oxide, or primary N-oxide, react with each of the reagents. For example, protonated nitrosobenzene only undergoes reactions with DMDS, which confirms that it is a primary N-oxide. Therefore, aromatic tertiary N-oxides, tertiary N-oxides, and primary N-oxides can be readily identified within the mixture (Figure 7).

Figure 7. Ion current over time for all ions generated from a mixture of model compounds and reaction product ions during an HPLC separation. Several consecutive pulses of the three neutral reagents 2MP, DMA, and DMDS were employed during elution of each analyte. The gray trace corresponds to the total ion current during the HPLC separation. The green, red, and blue traces correspond to the ion current of the reaction products (addition of 2MP (+72 Da), red; addition of DMA (+45 Da), green; a ligand exchange reaction with DMDS (+31 Da), blue). For clarity, each analyte is marked with a colored dot to indicate which ion−molecule reagents reacted with that analyte. *Protonated 5,5-dimethyl-1-pyrroline reacts with 2MP due to the presence of a C−N double bond at the N-oxide functionality (ref 11).

reactions over an HPLC peak is feasible as long as the reagents used are reasonably volatile. Hence, this approach enables the study of several ion−molecule reactions of many ionized molecules in complex mixtures in a fast and automated manner and thus facilitates high throughput screening of molecules with specific functionalities in complex mixtures. Future work will include optimization of the reagent residence time in the ion trap in order to enable reactions of even more reagents over a single HPLC peak.

■ AUTHOR INFORMATION

Corresponding Author

*Professor Hilkka I. Kenttämaa. Tel: (765) 494-0882. Fax: (765) 494-9421. E-mail: hilkka@purdue.edu.

Notes

The authors declare no competing financial interest.

■ CONCLUSIONS

A multiported pulsed valve inlet system was successfully installed onto a LQIT mass spectrometer and characterized. The pulsed valve system enables fast and efficient successive introduction of three different neutral reagents into the LQIT for the examination of their ion−molecule reactions with mass-selected ions. The setup allows, for example, the rapid screening of three new functional-group selective reagents for a specific protonated analyte or the rapid screening of the presence of three different functionalities in an unknown protonated analyte. Furthermore, by integrating automatic triggering, the neutral reagents were successively introduced on a chromatographic time scale. The examination of three different ion−molecule reactions with five repeats was demonstrated for an ionized analyte while it was eluting from an HPLC. These findings suggest that the examination of at least six different
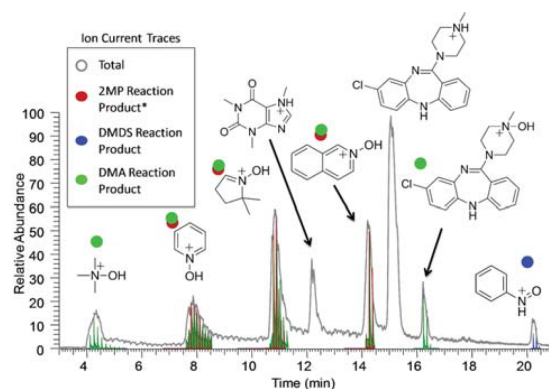
■ ABBREVIATIONS

2MP	2-methoxypropene
CAD	collision-activated dissociation
ESI	electrospray ionization
DMA	dimethylamine
DMDS	dimethyl disulfide
HPLC/MS	high-performance liquid chromatography/mass spectrometry

LC/MS	liquid chromatography/mass spectrometry
LQIT	linear quadrupole ion trap
MS	mass spectrometry
MS^n	tandem mass spectrometry
PDA	photodiode array
TMB	trimethyl borate

■ REFERENCES

(1) Amy, J. W.; Baitinger, W. E.; Cooks, R. G. *J. Am. Soc. Mass Spectrom.* **1990**, *1*, 119.

(2) Cooks, R. G.; Busch, K. L.; Glish, G. L. *Science* **1983**, *222*, 273.

(3) McLafferty, F. W. *Int. J. Mass Spectrom.* **2001**, *212*, 81.

(4) Watson, J. T.; Sparkman, O. D. *Introduction to Mass Spectrometry: Instrumentation, Applications, and Strategies for Data Interpretation*, 4 ed.; Wiley & Sons: West Sussex, England, 2008.

(5) Amundson, L.; Owen, B.; Gallardo, V.; Habicht, S.; Fu, M.; Shea, R.; Mossman, A.; Kenttämaa, H. *J. Am. Soc. Mass Spectrom.* **2011**, *22*, 670.

(6) Amundson, L. M.; Eismin, R. J.; Reece, J. N.; Fu, M.; Habicht, S. C.; Mossman, A. B.; Shea, R. C.; Kenttämaa, H. I. *Energy Fuels* **2011**, *25*, 3212.

(7) Amundson, L. M.; Gallardo, V. A.; Vinueza, N. R.; Owen, B. C.; Reece, J. N.; Habicht, S. C.; Fu, M.; Shea, R. C.; Mossman, A. B.; Kenttämaa, H. I. *Energy Fuels* **2012**, *26*, 2975.

(8) Kaiser, R. E.; Cooks, R. G.; Syka, J. E. P.; Stafford, G. C. *Rapid Commun. Mass Spectrom.* **1990**, *4*, 30.

(9) Mayer, P. M.; Poon, C. *Mass Spectrom. Rev.* **2009**, *28*, 608.

(10) McLuckey, S. A. *J. Am. Soc. Mass Spectrom.* **1992**, *3*, 599.

(11) Wells, J.; McLuckey, S. *Methods Enzymol.* **2005**, *402*, 148.

(12) Brodbelt, J. S. *Mass Spectrom. Rev.* **1997**, *16*, 91.

(13) Gronert, S. *Chem. Rev.* **2001**, *101*, 329.

(14) Gronert, S. *Mass Spectrom. Rev.* **2005**, *24*, 100.

(15) Osburn, S.; Ryzhov, V. *Anal. Chem.* **2013**, *85*, 769.

(16) Eberlin, M. *J. Mass Spectrom.* **2006**, *41*, 141.

(17) Andrew, A. M.; William, R. C.; Günter, K. E. *Int. J. Mass Spectrom.* **1999**, *190*, 195.

(18) Duan, P.; Fu, M.; Gillespie, T.; Winger, B.; Kenttämaa, H. *J. Org. Chem.* **2009**, *74*, 1114.

(19) Duan, P.; Gillespie, T.; Winger, B.; Kenttämaa, H. *J. Org. Chem.* **2008**, *73*, 4888.

(20) Eismin, R.; Fu, M.; Yem, S.; Widjaja, F.; Kenttämaa, H. *J. Am. Soc. Mass Spectrom.* **2012**, *23*, 12.

(21) Fu, M.; Duan, P.; Li, S.; Eismin, R.; Kenttämaa, H. *J. Am. Soc. Mass Spectrom.* **2009**, *20*, 1251.

(22) Gao, H.; Petzold, C. J.; Leavell, M. D.; Leary, J. A. *J. Am. Soc. Mass Spectrom.* **2003**, *14*, 916.

(23) Green, M.; Lebrilla, C. *Mass Spectrom. Rev.* **1997**, *16*, 53.

(24) Habicht, S.; Vinueza, N.; Amundson, L.; Kenttämaa, H. *J. Am. Soc. Mass Spectrom.* **2011**, *22*, 520.

(25) Petzold, C.; Leavell, M.; Leary, J. *Anal. Chem.* **2004**, *76*, 203.

(26) Watkins, M.; WeWora, D.; Li, S.; Winger, B.; Kenttämaa, H. *Anal. Chem.* **2005**, *77*, 5311.

(27) Gronert, S. *J. Am. Soc. Mass Spectrom.* **1998**, *9*, 845.

(28) Habicht, S.; Vinueza, N.; Archibold, E.; Duan, P.; Kenttämaa, H. *Anal. Chem.* **2008**, *80*, 3416.

(29) Eberlin, M. N. *Mass Spectrom. Rev.* **1997**, *16*, 113.

(30) Goode, G. C.; O'Malley, R. M.; Ferrer-Correia, A. J.; Massey, R. I.; Jennings, K. R.; Futrell, J. H.; Llewellyn, P. M. *Int. J. Mass Spectrom. Ion Processes* **1970**, *5*, 393.

(31) Nibbering, N. M. M. *Acc. Chem. Res.* **1990**, *23*, 279.

(32) Carlin, T. J.; Freiser, B. S. *Anal. Chem.* **1983**, *55*, 571.

(33) Sack, T. M.; Gross, M. L. *Anal. Chem.* **1983**, *55*, 2419.

(34) Owen, B. C.; Jarrell, T. M.; Schwartz, J. C.; Oglesbee, R.; Carlsen, M.; Archibold, E. F.; Kenttämaa, H. I. *Anal. Chem.* **2013**, *85*, 11284.

(35) Einhorn, J.; Kenttämaa, H. I.; Cooks, R. G. *J. Am. Soc. Mass Spectrom.* **1991**, *2*, 305.

(36) Emary, W. B.; Kaiser, R. E.; Kenttämaa, H. I.; Cooks, R. G. *J. Am. Soc. Mass Spectrom.* **1990**, *1*, 308.

(37) Coopersmith, B. I.; Yost, R. A. *J. Am. Soc. Mass Spectrom.* **1995**, *6*, 976.

(38) Pyatkivskyy, Y.; Ryzhov, V. *Rapid Commun. Mass Spectrom.* **2008**, *22*, 1288.

(39) Riedeman, J. S.; Jarrell, T. M.; Sheng, H.; Kenttämaa, H. I.; Submitted.

(40) Tong, W.; Chowdhury, S.; Chen, J.; Zhong, R.; Alton, K.; Patrick, J. *Rapid Commun. Mass Spectrom.* **2001**, *15*, 2085.

Gas-phase reactions of a novel chemical ionization reagent, $ClMn_2^+$, with polar and nonpolar analytes in a linear quadrupole ion trap

Tiffany M. Jarrell, James S. Riedeman, Hilkka Kenttämaa *

Department of Chemistry, Purdue University, Brown Building, 560 Oval Dr., West Lafayette, IN 47907, USA

ABSTRACT

A chemical ionization reagent ion, $ClMn_2^+$, has been identified for the analysis of mixtures of organic compounds since it allows ionization of both polar and nonpolar analytes so that only one product ion, $ClMn^+$ adduct of the analyte, is generated without fragmentation. The reagent ion is formed upon ionization of $ClMn(CO)_5$ via corona discharge in an atmospheric pressure chemical ionization source of a linear quadrupole ion trap mass spectrometer. Volatile analytes were introduced into the ion trap via a reagent mixing manifold. Nonvolatile analytes were deposited on a titanium foil and desorbed using laser-induced acoustic desorption (LIAD). Formation of a $ClMn^+$ adduct with no accompanying fragmentation was observed for all analytes, including branched saturated hydrocarbons. Calculations indicate that $ClMn^+$ binds to saturated hydrocarbons via an agostic interaction involving the manganese center and a C—H bond of the analyte. The reagent ion Mn^+ was also investigated. This ion forms a stable adduct with most analytes studied. It binds fairly strongly to saturated hydrocarbons via two agostic interactions with two C—H bonds instead of insertion into a C—H bond. However, it was found to cause fragmentation for alcohols. $ClMn(H_2O)^+$ has been previously shown to ionize most compounds by $ClMn^+$ adduct formation but also to yield molecular ions for amines due to their low ionization energies (<8.3 eV). However, electron transfer was not observed upon ionization of amines with the reagents reported here. The $CpCo^+$ ion has been reported earlier to ionize most saturated hydrocarbons without fragmentation. However, it induces C—C bond cleavages for highly branched alkanes upon ionization. This was not observed for the reagent ions studied here. $ClMn_2^+$ ion is a more universal ionization reagent than Mn^+ and the previously reported reagent ions due to its ability to ionize analytes with low ionization energies without electron transfer and due to the complete lack of fragmentation for all analytes. Furthermore, based on the examination of six very different analytes, it has no significant bias toward specific types of analytes.

© 2014 Elsevier B.V. All rights reserved.

1. Introduction

Mass spectrometry is well suited for analysis of complex mixtures without prior separation [1–3] if careful attention is paid to choosing a suitable ionization method. An ionization method well suited for mixture analysis should ionize different types of analytes by forming only one type of ion per analyte that contains the intact analyte molecule. This should take place without ionization bias or fragmentation to retain molecular weight and structural information and prevent convolution of the mass spectrum [4,5]. Electron ionization is one of the few ionization methods that is capable of ionizing all organic compounds.

Unfortunately, it induces fragmentation for most analytes, thus convoluting the mass spectra. Less fragmentation usually occurs upon traditional chemical ionization (CI) based on proton transfer reactions but the efficiency of ionization and extent of fragmentation both depend on the basicity of the analyte. Electrospray ionization (ESI) and traditional atmospheric pressure chemical ionization (APCI) ionize preferentially the most basic or most acidic analytes. In contrast, the aquachloromanganese(II) cation $[ClMn(H_2O)^+]$ has been previously reported to enable efficient ionization of both polar and nonpolar analytes, including highly branched saturated hydrocarbons, via formation of a $ClMn^+$ adduct without accompanying fragmentation [6–8]. Coupling the $ClMn(H_2O)^+$ reagent ion with laser-induced acoustic desorption (LIAD) enabled mass spectrometric analysis of analytes previously inaccessible to such analysis, such as saturated nonpolar hydrocarbons in base oil fractions [7]. However, $ClMn(H_2O)^+$ was

* Corresponding author. Tel.: +765 494 0882; fax: +765 494 0239.
E-mail address: hilkka@purdue.edu (H. Kenttämaa).

found to ionize analytes with ionization energies less than 8 eV by electron transfer [8]. Therefore, this reagent is not suited for analysis of mixtures containing analytes with low ionization energies. In order to address this issue, gas-phase reactions of two new, less aggressive reagent ions, $ClMn_2^+$ and Mn^+, were studied.

The previous studies on the reagent ion $ClMn(H_2O)^+$ were carried out using an obsolete Fourier-transform ion cyclotron resonance mass spectrometer(FT-ICR) [6–8]. In the study discussed here, a commercially available LQIT and a custom built dual linear quadrupole ion trap [9] (DLQIT) were used in order to take advantage of the faster duty cycles of the LQIT [10]. A variety of volatile analytes were studied to ensure unbiased ionization for both polar and non-polar analytes without fragmentation. In addition, LIAD was used to desorb large nonpolar hydrocarbons for ionization using $ClMn_2^+$ and Mn^+ in order to demonstrate the utility of this approach for analysis of petroleum samples.

2. Experimental

All reactions were examined in either a Thermo Scientific LTQ linear quadrupole ion trap (LQIT) equipped with a pulsed valve sample introduction interface [11] or a dual linear quadrupole ion trap mass spectrometer [9] (DLQIT) equipped with a reagent mixing manifold [12]. The same results were obtained for both instruments. Each instrument was operated using the LTQ Tune Plus interface and was equipped with an atmospheric pressure chemical ionization (APCI) source. Typical APCI parameters were as follows: discharge current, 3–4 μA; sheath gas (N_2) flow, 0 (arbitrary units); auxiliary gas (N_2) flow, 5 (arbitrary units); vaporizer temperature 0 °C; capillary temperature, 275 °C.

$ClMn(CO)_5$ was synthesized using a literature procedure [13] and used as a precursor for the generation of the reagent ions $ClMn_2^+$ and Mn^+. All other reagents were purchased from Sigma–Aldrich and used without additional purification. The reagent ions were generated by allowing $ClMn(CO)_5$ (solid) to sublime from a glass slide inside the ion source at atmospheric pressure and by ionizing the vapors via corona discharge, which formed the ions Mn^+ and $ClMn_2^+$ in ~1:4 abundance. The optimal tube lens voltage (115 V) was found to be higher than standard operating voltages (20–70 V). When using DLQIT equipped with two ion traps, reagent ions were accumulated in the front trap, isolated, and transferred into the back trap for reactions with analytes. In other words, in this experiment, the accumulation and isolation of the reagent ions and the reactions of the reagent ions with the analytes were separated in both time and space (front and back trap). In the LQIT, these events were only separated in time since they both occurred in the same ion trap.

For the DLQIT, all volatile analytes were introduced into the back ion trap of the instrument via the standard helium line by using a previously described reagent mixing manifold [14,15]. Analytes (neat) were introduced into the reagent mixing manifold via a syringe drive operating at a delivery rate of 10 μL/h and then diluted with helium at a flow rate of 600 mL/min. Nonvolatile analytes were introduced via laser-induced acoustic desorption (LIAD) with a fiber optic set-up [16] into the back ion trap of the DQIT, as described previously for LQIT [16]. For the LQIT, volatile analytes were introduced into the ion trap by using a multi-ported pulsed valve sample introduction interface [11]. Analytes (5 μL neat) were introduced into the pulsed valve sample introduction interface manually via a rubber septum by using a syringe. The reagent ions were isolated (2 Da window or ±1 Da) by ejecting all unwanted ions from the ion trap. Each analyte was allowed to react for 30 ms with the isolated reagent ions (either Mn^+ (m/z 55) or $ClMn_2^+$ (m/z 145). The nominal pressure of the ion traps in both

instruments were maintained at 0.5–0.7 × 10^{-5} Torr. Helium was used as the buffer gas within the ion trap. Without isolation of the reagent ion, simple product distributions are not obtained. For mixtures containing analytes with very different concentrations, different ion accumulation times can be employed before examination of the ion-molecule reactions.

Density functional theory (DFT) combined with the hybrid generalized gradient approximation functional developed by Becke, Lee Yang, and Parr [17–19] (B3LYP) was used to compute optimized geometries of $ClMn_2^+$, ethane, the ClMn–ethane$^{+\bullet}$ adduct and the Mn–ethane$^{+\bullet}$ adduct. This method uses the Becke88 exchange functional combined with the Lee–Yang–Parr (LYP) correlation functional. Local minima predicted by this method were confirmed by computing the vibrational frequencies in order to verify the absence of imaginary frequencies. This also provided thermal and zero-point corrections to the calculated energies. The contracted double basis set 6–31 + G(d,p) [20] was used for the approximation of molecular orbitals. Enthalpies were calculated as the energy difference between products and reactants. All calculations were performed using the Gaussian 09 software suite (Revision C.01) [21].

3. Results and discussion

Several different types of analytes, including linear, branched and cyclic alkanes, thiophenes, furans, aromatic compounds, alcohols, ethers, ketones and amines, were used to test the utility of the manganese chemical ionization reagent ions $ClMn_2^+$ and Mn^+. The ions were generated via corona discharge in an atmospheric pressure chemical ionization (APCI) source of a linear quadrupole ion trap. The isolated $ClMn_2^+$ and Mn^+ ions were allowed to react with each of the analytes for 30 ms. Every analyte yielded only one product ion for $ClMn_2^+$ and most of them for Mn^+ (Table 1). This was found to be true for analytes with a wide range of different ionization energies (Table 2). Reactions of $ClMn_2^+$ with the analytes (X) yielded an adduct that had lost Mn ($ClMnX^+$), while reactions of Mn^+ yielded an adduct of Mn^+ ($Mn(X)^+$) for all analytes except for two alcohols that also showed loss of water (Table 2). This is true even for branched alkanes, such as 2,3-dimethylpentane (Table 1), which have been shown to fragment by C—C bond cleavages upon ionization with other fairly gentle reagent ions, such as CpCo$^+$ [22]. Further, this also applies to analytes with low ionization energies [23] (IE; e.g., triethyl amine, IE = 7.5 eV; Table 2), which undergo [8] electron transfer with $ClMn(H_2O)^+$ to produce molecular ions in addition to the desired adducts with $ClMn^+$. Fig. 1 shows an example mass spectrum measured after reaction of a mixture of pentane, ethanol and triethylamine with $ClMn_2^+$ for 30 ms. Only one product ion was formed for each of the analytes. Further, this experiment suggests that there is virtually no ionization bias for very different analytes. Examination of the reaction of an equimolar mixture of tetrahydrofuran and benzene yielded the same conclusions.

Since the $ClMn(H_2O)^+$ reactions reported previously [8] were performed in a different instrument(FT-ICR) from those used here, the reaction of triethylamine with $ClMn(H_2O)^+$ was repeated in the LQIT in order to test whether similar reactivity is observed. Fig. 2 compares reactions of $ClMn(H_2O)^+$ and $ClMn_2^+$ with triethylamine (shown [8] previously to undergo electron transfer upon ionization with $ClMn(H_2O)^+$ in an FT-ICR) in the linear quadrupole ion trap. In agreement with literature, [8] electron transfer was observed for the reaction of $ClMn(H_2O)^+$ with triethylamine to form molecular ions (which react further to produce protonated triethylamine molecules). However, no electron transfer was observed when $ClMn_2^+$ was allowed to react with triethylamine.

Table 1

Product ions (with their m/z-values) formed in reactions of $ClMn_2^+$ and Mn^+ with a variety of polar and nonpolar analytes.
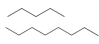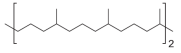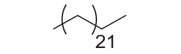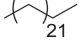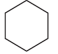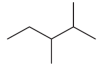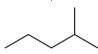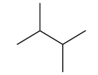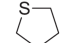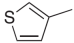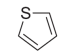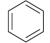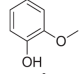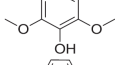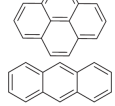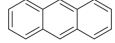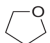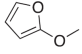
Analyte (MW)	Structure	$ClMn_2^+$ products, m/z	Mn^+ products, m/z
Linear alkanes			
Pentane (72)		Adduct–Mn, 162	Adduct, 127
Octane (114)		Adduct–Mn, 204	Adduct, 169
Squalane (422)		Adduct–Mn, 512	Adduct, 477
Tetracosane (338)		Adduct–Mn, 428	Adduct, 393
Cyclic alkane			
Cyclohexane (80)		Adduct–Mn, 170	Adduct, 135
Branched alkanes			
2,3-Dimethylpentane (100)		Adduct–Mn, 190	Adduct, 155
2-Methylpentane (86)		Adduct–Mn, 176	Adduct, 141
2,3-Dimethylbutane (86)		Adduct–Mn, 176	Adduct, 141
Thiophenes			
Tetrahydrothiophene (88)		Adduct–Mn, 178	Adduct, 143
3-Methylthiophene		Adduct–Mn, 188	Adduct, 153
Thiophene (84)		Adduct–Mn, 174	Adduct, 139
Aromatic			
Benzene (78)		Adduct–Mn, 172	Adduct, 133
Guaiacol (124)		Adduct–Mn, 214	Adduct, 179
Syringol (154)		Adduct–Mn, 244	Adduct, 209
Pyrene (202)		Adduct–Mn, 292	Adduct, 257
Anthracene (178)		Adduct–Mn, 268	Adduct, 233
Furan			
Tetrahydrofuran (72)		Adduct–Mn, 162	Adduct, 127
2-Methylfuran (82)		Adduct–Mn, 172	Adduct, 137
2-Methoxyfuran (98)		Adduct–Mn, 188	Adduct, 153

Table 2
Product ions (with their m/z-values) formed in the reactions of $ClMn_2^+$ and Mn^+ with small organic compounds with various functionalities and differing ionization energies. (IE; obtained from literature[a]).

Analyte (MW)	IE in eV	$ClMn_2^+$products, m/z	Mn^+products, m/z
Triethylamine (101)	7.50	Adduct–Mn, 191	Adduct, 156
Diethylamine (73)	7.90	Adduct–Mn, 163	Adduct, 128
Dimethylamine (45)	8.24	Adduct–Mn, 135	Adduct, 100
Benzyl Alcohol (108)	8.26	Adduct–Mn, 198	Adduct, 163,Adduct–H_2O, 145
Phenol (94)	8.49	Adduct–Mn, 184	Adduct, 149
Methyl *tert*-Butyl Ether (88)	9.24	Adduct–Mn, 178	Adduct, 143
Acetone (58)	9.7	Adduct–Mn, 148	Adduct, 113
Butanal (72)	9.8	Adduct–Mn, 162	Adduct, 127
t-Butanol (74)	9.9	Adduct–Mn, 164	Adduct, 129;Adduct–H_2O, 111
n-Butanol (74)	9.99	Adduct–Mn, 164	Adduct, 129
n-Propanol (60)	10.22	Adduct–Mn, 150	Adduct, 115
Methanol (32)	10.85	Adduct–Mn, 122	Adduct, 87
Ethanol (46)	10.48	Adduct–Mn, 136	Adduct, 101

[a] [19].

The reactions described above were also examined by quantum chemical calculations. Thelowest-energy structures calculated for $ClMn_2^+$ can be seen in Fig. 3B B. The linearMn–Mn–Cl structure is more stable by 24.5 kcal mol^{-1} than the bent Mn–Cl–Mn structure and hence it is likely to be the reagent ion involved in the experiments discussed here. Upon reaction of $ClMn_2^+$ with analytes, Mn is eliminated and a $ClMn^+$ adduct of the analyte molecule generated. $ClMn^+$ contains a coordinatively unsaturated manganese atom with the $d5$ [5] electron configuration. The $d5$ [5] electron configuration is a stablehigh-spin configuration [24]. Thus, the interaction of $ClMn^+$ with analytes may increase the coordination number of manganese but is unlikely to involve oxidative addition. The interaction of $ClMn^+$ with a saturated alkane, ethane, was examined using the B3LYP/6–31G(d,p) level of theory. Based on the calculations, the bonding of $ClMn^+$ with ethane is best described as an agostic interaction of the manganese center with a C—H bond in ethane. An agostic interaction is athree-centertwo-electron bond characterized by a metal (M) M—H bond with a length between 1.8 and 2.3 Å, and an M—H—C angle in the range90–140° [25]. The structure calculated for the $ClMn^+$ adduct with ethane agrees very well with that description (Fig. 3A). Further, two different types of interactions of the reagent ion Mn^+, with the d [4] electron configuration, and ethane were examined. The formation of two agostic interactions of Mn^+ with two C—H bonds in ethane was found to lower the Gibbs free

energy of the system by 16.7 kcal mol^{-1} more than formation of a C—H bond insertion product (Fig. 3C). Hence, C—H bond insertion is not likely to occur for this reagent ion, either.

Finally,collision-activated dissociation (CAD) was used to examine the dissociation reactions of many of the $ClMn^+$ adducts (Table 3). Six of the adducts, those of the saturated hydrocarbons and the smallestoxygen-containing analytes, exclusively or predominantly dissociate to form the neutral analyte and $ClMn^+$ (for methanol, see Scheme 1A). This finding is in agreement with agnostic interactions between $ClMn^+$ and the saturated hydrocarbons, as calculated, and dative bonding between theoxygen-containing analytes and $ClMn^+$ (a dative bond is a dipolar bond where both of the electrons in the bond are donated by the ligand and are typically formed between good Lewis acids and bases, such as a transition metal and a lone pair of electrons [26]). In sharp contrast, CAD of the $ClMn^+$ adducts of ethanol and propanol involves cleavage of the C—O bond and predominant elimination of ethene and propene, respectively, to generate the $ClMn(H_2O)^+$ ion (possibly as shown in Scheme 1B for propanol). However, *t*-butanol adduct fragments by elimination of water. Apparently, at some point during CAD, water and isobutene are generated and they compete for binding with $ClMn^+$. Based on above results, isobutene forms the strongest bond with $ClMn^+$, followed by water,
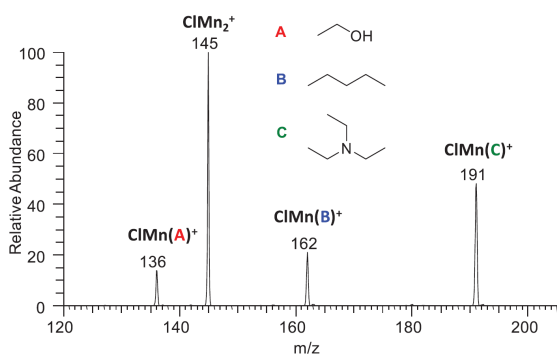

Fig. 1. Mass spectrum measured after reaction of $ClMn_2^+$ with an equimolar mixture of ethanol, pentane, and triethylamine introduced into the back ion trap of DLQIT via an external mixing manifold attached to the helium line. Nearly equal ionization efficiency is observed for these three very different analytes.
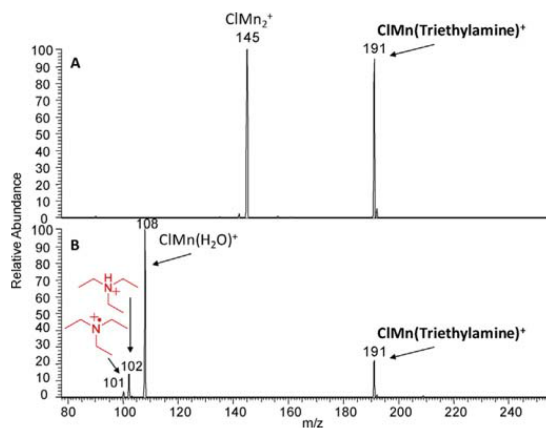

Fig. 2. Mass spectra measured after ion-molecule reactions of triethylamine with (A) $ClMn_2^+$ and (B) $ClMn(H_2O)^+$. Molecular ions of triethylamine generate protonated trimethylamine molecules upon secondary reactions.

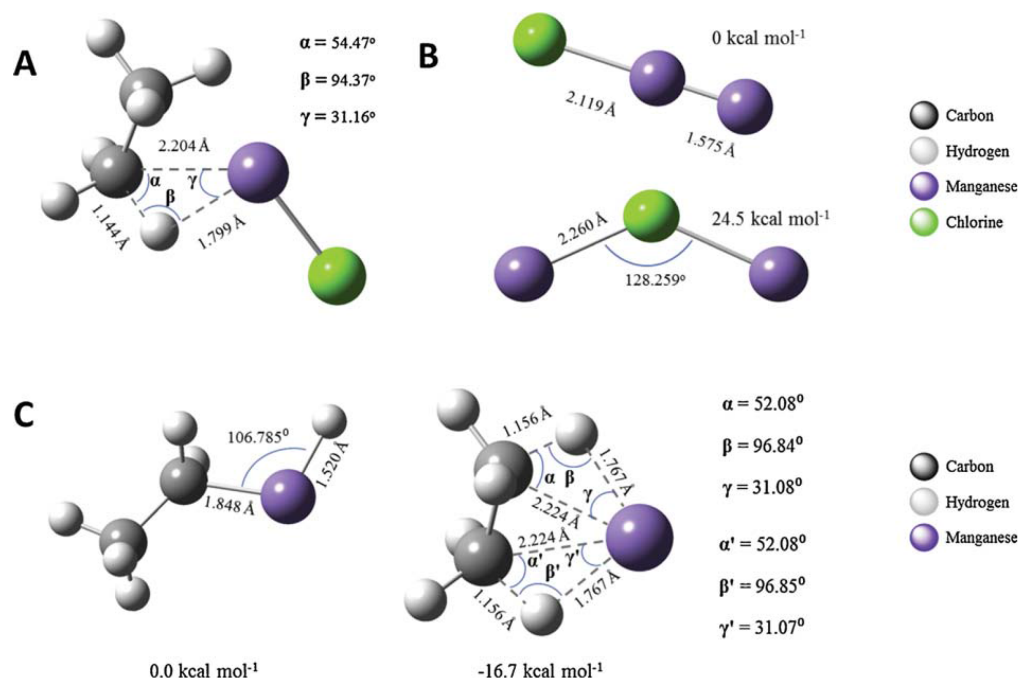**Fig. 3.** (A) Calculated geometry of the $ClMn^+$ adduct of ethane. (B) Isomers of $ClMn_2^+$ and their relative energies. (C) Calculated geometry and relative energy for Mn^+ after insertion into a C—H bond of ethane (left) and for Mn^+ bound to ethane via two agostic interactions (right).

propene and ethene. However, methanol binds even stronger than isobutene since the adduct of methyl *tert*-butyl ether undergoes elimination of isobutene to form $ClMn(CH_3OH)^+$. Cleavage of C—C bonds was observed for the adducts of butanal and tetrahydrofuran: the loss of propene occurred from each adduct to form ClMn $(CH_2O)^+$ (for butanal, possibly as shown in Scheme 1C). Hence, formaldehyde binds stronger to $ClMn^+$ than propene. Interestingly,

the adducts of diethylamine and triethylamine were found to eliminate a hydrogen atom or form the $ClMnH^+$ ion, respectively.

The reasons for many of the above observations are currently unknown. A detailed study is in progress on the fragmentation patterns of $ClMn^+$ adducts of many more analytes in order to be able to make generalizations about the types of structural information available from these experiments.

Table 3
Product ions (with their *m/z* ratios and relative abundances) formed uponcollision-activated dissociation (CAD) of the ionic products of reactions of $ClMn_2^+$ with several analytes (X).

Analyte (X)	MS/MS fragment ions (*m/z*) of $ClMnX^+$ and their relative abundances	
Acetone	$ClMn^+(90)$	100%
Methanol	$ClMn^+(90)$	100%
2-Methylpentane	$ClMn^+(90)$	100%
	$ClMn(H_2O)^+(108)^a$	
	$[(ClMnX)–H]^+(175)$	28%
Thiophene	$ClMn^+(90)$	100%
Cyclohexane	$ClMn^+ (90)$	100%
Benzene	$ClMn^+(90)$	100%
Diethylamine	$[(ClMnX)–H]^+(162)$	100%
Triethylamine	$ClMnH^+(91)$	100%
Ethanol	$ClMn(H_2O)^+(108)$	100%
n-Propanol	$ClMn(H_2O)^+(108)$	100%
	$[(ClMnX)–H_2O]^+(132)$	57%
t-Butanol	$[(ClMnX)–H_2O]^+(146)$	100%
Methyl *tert*-Butyl Ether	$ClMn(CH_3OH)^+(122)$	100%
Butanal	$ClMn(CH_2O)^+(120)$	100%
Tetrahydrofuran	$ClMn(CH_2O)^+(120)$	100%
	$(X–H)^+(71)$	10%

[a] Secondary reaction product due to reaction with water always present in the ion trap.
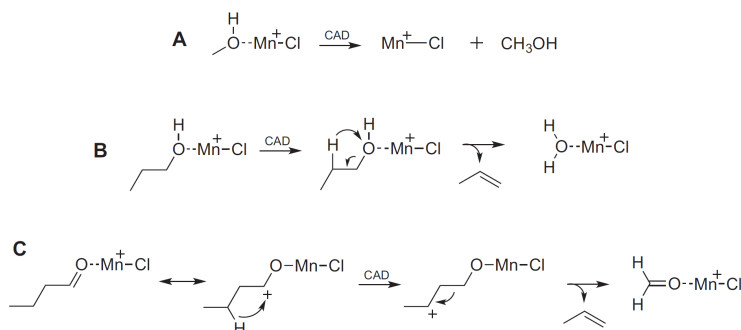
Scheme 1. Proposed mechanisms for the fragmentation of the ClMn⁺ adducts of methanol, propanol and butanal.

4. Conclusions

ClMn$_2$⁺ chemical ionization reagent ion efficiently ionizes various types of analytes, both polar and nonpolar, to exclusively form ClMn⁺ adduct ions, which makes it a promising reagent for mixture analysis. Furthermore, no bias was found for any specific analytes. This reagent is better than the previously reported ClMn (H$_2$O)⁺ and CpCo⁺ reagent ions due to its ability to ionize analytes with low ionization energies without the production of multiple product ions or fragment ions [1–3,27]. Calculations suggest that the adducts of ClMn⁺ with saturated hydrocarbons are bound via a relatively strong agostic interaction of the manganese center with a C—H bond while the adducts with oxygen-containing analytes involve dative bonding. Collision-activated dissociation of the ClMn⁺ adduct ions proceeds via several different pathways, depending on the structure of the analyte. Based on the observed fragmentation reactions, the strength of binding of ClMn⁺ gets weaker in the following order: methanol, isobutene, water, propene, ethane. The reactions of Mn⁺ were also explored with similar results. Based on calculations, Mn⁺ interacts with saturated hydrocarbons via two agostic interactions involving two C—H bonds. However, Mn⁺ is not suited for ionization of alcohols due to their fragmentation upon ionization.

Acknowledgements

References

[1] J.W. Amy, W.E. Baitinger, R.G. Cooks, J. Am. Soc. Mass Spectrom. 1 (1990) 119.
[2] R.G. Cooks, K.L. Busch, G.L. Glish, Science 222 (1983) 273.
[3] F.W. McLafferty, Int. J. Mass Spectrom. 212 (2001) 81.
[4] E. de Hoffmann, V. Stroobant, Mass Spectrometry Principles and Applications, third ed., John Wiley & Sons, Ltd., West Sussex, England, 2007.
[5] J.T. Watson, O.D. Sparkman, Introduction to Mass Spectrometry: Instrumentation, Applications, and Strategies for Data Interpretation, fourth ed., Wiley & Sons, West Sussex, England, 2008.
[6] P. Duan, M. Fu, D. Pinkston, S. Habicht, H. Kenttämaa, J. Am. Chem. Soc. 129 (2007) 9266.
[7] P. Duan, K. Qian, S. Habicht, D. Pinkston, M. Fu, H. Kenttämaa, Anal. Chem. 80 (2008) 1847.
[8] P. Gqamana, P. Duan, M. Fu, V. Gallardo, H. Kenttämaa, Rapid Commun. Mass Spectrom. 26 (2012) 940.
[9] B.C. Owen, T.M. Jarrell, J.C. Schwartz, R. Oglesbee, M. Carlsen, E.F. Archibold, H.I. Kenttämaa, Anal. Chem. 85 (11) (2013) 284.
[10] S.A. McLuckey, J.M. Wells, Chem. Rev. 101 (2001) 571.
[11] T. Jarrell, J. Riedeman, M. Carlsen, R. Replogle, T. Selby, H. Kenttamaa, Anal. Chem. (2014) , doi:http://dx.doi.org/10.1021/ac501034v.
[12] S. Gronert, Mass Spectrom. Rev. 24 (2005) 100.
[13] K.J. Reimer, A. Shaver, M.H. Quick, R.J. Angelici, Inorganic Syntheses: Reagents for Transition Metal Complex and Organometallic Syntheses, 28, John Wiley & Sons, 1990, pp. 154.
[14] S. Habicht, N. Vinueza, E. Archibold, P. Duan, H. Kenttämaa, Anal. Chem. 80 (2008) 3416.
[15] S. Gronert, Chem. Rev. 101 (2001) 329.
[16] S. Habicht, L. Amundson, P. Duan, N. Vinueza, H. Kenttämaa, Anal. Chem. 82 (2010) 608.
[17] C.Y.W. Lee, R.G. Parr, Phys. Rev. B 37 (1988) 785.
[18] A.D. Becke, Phys. Rev. A 38 (1988) 3098.
[19] A.D. Becke, J. Chem. Phys. 104 (1996) 1040.
[20] R. Krishnan, J.S. Binkley, R. Seeger, J.A. Pople, J. Phys. Chem. 72 (1980) 650.
[21] Gaussian 09, C. Revision 01, G.W.T. Frisch, G.E. Scuseria, J.R.C. Robb, V. Scalmani, B. Mennucci, G.A. Petersson, H.N. Caricato, X. Li, H.P. Hratchian, A.F. Izmaylov, J.B.G. Zheng, J.L. Sonnenberg, M. Hada, M. Ehara, K.T.R. Fukuda, J. Hasegawa, M. Ishida, T. Nakajima, Y. Honda, O.K.H. Nakai, T. Vreven, J.A. Montgomery Jr., J.E. Peralta, F.O.M. Bearpark, J.J. Heyd, E. Brothers, K.N. Kudin, V.N.S.T. Keith, R. Kobayashi, J. Normand, K. Raghavachari, A.R.J.C. Burant, S.S. Iyengar, J. Tomasi, M. Cossi, N.R.J.M. Millam, M. Klene, J.E. Knox, J.B. Cross, V. Bakken, C.A.J. Jaramillo, R. Gomperts, R.E. Stratmann, O. Yazyev, A.J.A.R. Cammi, C. Pomelli, J.W. Ochterski, R.L. Martin, K.M.V.G. Zakrzewski, G.A. Voth, P. Salvador, J.J.D.S. Dapprich, A.D. Daniels, O. Farkas, J.B.F.J.V. Ortiz, J. Cioslowski, D.J. Fox, Gaussian, Inc., Wallingford, CT, 2010.
[22] J. Campbell, K. Crawford, H. Kenttämaa, Anal. Chem. 76 (2004) 959.
[23] S.G. Lias, in: P.J. Linstrom, W.G. Mallard (Eds.), NIST Chemistry WebBook, NIST Standard Reference Database Number 69, NIST Mass Spec Data Center, Gaithersburg, MD, 2014.
[24] J.E. Huheey, Inorganic Chemistry Principles of Structure and Reactivity, third ed., Harper & Row: New York, NY, 1983.
[25] M. Brookhart, M.L.H. Green, J. Organomet. Chem. 250 (1983) 395.
[26] IUPAC, Compendium of Chemical Terminology, second ed., Blackwell Science Inc, 1997.
[27] J.L. Campbell, K.E. Crawford, H.I. Kenttämaa, Anal. Chem. 76 (2004) 959.